DOCTOR OF PHILOSOPHY

An Investigation into Hybrid Topology Optimisation of Vehicle Structures

Wilson, Alexis

Award date:
2019

Awarding institution:
Coventry University

An Investigation into Hybrid Topology Optimisation of Vehicle Structures

By

Alexis Wilson

August 2018

A thesis submitted in partial fulfilment of the University's requirements for the Degree of Doctor of Philosophy

Institute for Future Transport and Cities
Coventry University

in collaboration with HORIBA MIRA

Certificate of Ethical Approval

Student:

Alexis Wilson

Project Title:

Hybrid structural algorithm development

This is to certify that the above named student has completed the Coventry University Ethical Approval process and their project has been confirmed and approved as Low Risk

Date of approval:

06 March 2015

Project Reference Number:

P32182

Acknowledgements

I would like to thank my Director of Studies Dr. Jesper Christensen for his commitment, support and infectious enthusiasm for the subject area all the way through this project.

I would like to thank the other members of my supervisory team, Dr. Christophe Bastien from Coventry University and Dr. Waldemar Golinksi from HORIBA-MIRA for the guidance and expertise they have provided me with many times over the course of my work

To the many colleagues and friends, both from Coventry University and HORIBA MIRA, who have provided me with opportunities to discuss my work and general good humour, a big thanks goes out to you. A special mention to Dr. Anthony Baxendale who has coordinated all PhD projects at HORIBA MIRA and provided us with many opportunities to present our work and feel a part of the company. A special mention also to Dr. Madeline Cheah, who answered the many questions I had close to submission and helped ease the process.

Finally, a thank you to my family for their endless support, patience and encouragement for the past four years. I couldn't have done this without them.

Abstract

Finite Element Analysis (FEA) based topology optimisation (TO) is now widely used across a range of industries from civil to automotive engineering. It efficiently identifies the optimal load-path locations (topology) based on a user defined design volume. Current TO algorithms are well developed for linear static applications. A vehicle structure is however significantly different as it exhibits both linear and non-linear deformation during an impact scenario. Throughout this thesis linear and non-linear behaviour refers to both material and geometry. No current state of the art TO software simultaneously considers coupled linear/non-linear behaviour within a single system. The contribution of this thesis is a novel hybrid methodology which combines existing TO algorithms within a single optimisation process to cater for this combined behaviour. After an initial investigation into the capabilities of existing, commercially available TO algorithms, the Variable Density Method (VDM) and Solid Isotropic Material with Penalisation (SIMP) methods were selected for linear behaviour, while a Bi-directional Evolutionary Structural Optimisation (BESO) based method BEETS was selected for non-linear behaviour. A number of hybrid optimisation parameters were created, defined and evaluated via two case studies. The first case study was a 2D plate study which demonstrates the proof-of-concept, and the second case study a Research Council for Automobile Repairs (RCAR) bumper test based study used to critically assess the performance of the methodology applied to a real-world vehicle structure scenario. The results demonstrated that a specific aspect of the developed methodology, the interface parameters, were the most influential upon the resulting topology. It was determined that increasing data exchange between the linear and non-linear solvers improved the structural performance of the optimised topology. Overall, the main conclusion from this PHD is that a hybrid topology optimisation methodology, combining linear and non-linear optimisation within the same process, can be advantageous in certain circumstances, highlighting the importance of work in this field in the pursuit of obtaining lightweight and safe vehicle structures.

Table of Contents

Acknowledgements i

Abstract ii

Abbreviations vi

Table of Figures vii

List of Tables xviii

1. Introduction and background to study 1

2. Literature Review 13

2.1. Mathematical based methods 13

2.2. Heuristic and Meta-Heuristic methods 21

2.2.1. BESO method 22

2.2.2. BEETS Method 34

2.2.3. Hybrid Cellular Automata (HCA) method 39

2.3. Conclusions and gaps 41

3. Investigation into commercially available topology optimisation algorithms 43

3.1. Linear model 51

3.1.1. Optistruct - SPC 51

3.1.2. Optistruct - IR 55

3.1.3. LS-TaSC 65

3.1.4. Conclusion 72

3.2. Non-linear model 73

3.2.1. ESLM 73

3.2.2. LS-TaSC 75

3.2.3. BESO / BEETS 81

3.2.4. Conclusion 88

3.3. Combined linear / non-linear model 89

3.3.1. LS-TaSC 89
3.3.2. BESO / BEETS 96
3.4. Conclusion 102
4. Methodology 103
4.1. Hybrid optimisation: Interface parameters 103
4.2. Hybrid optimisation: Software development 106
4.2.1. Force exchange 109
4.2.2. Hybrid optimisation setup 118
4.2.3. Update HW FE status 119
4.2.4. Zero-length beam stiffness update 121
5. Case study 1: Investigation into hybrid topology optimisation parameters 123
5.1. Hybrid optimisation parameters study 124
5.1.1. Study A - Interface size 133
5.1.2. Study B - Rate of exchange 138
5.1.3. Study C – Linear model optimisation objective/constraint 144
5.1.4. Study D - Interface BC 147
5.1.5. Study E - Linear BC 150
5.1.6. Study F - Interface size / Rate of exchange 152
5.1.7. Study G - Interface size / interface BC definition 159
5.1.8. Study H - Interface size / linear BC 163
5.1.9. Study I - Interface size / linear model optimisation objective/ constraint 165
5.1.10. Study J - Rate of exchange / Interface BC 166
5.1.11. Study K - Rate of exchange / linear BC 171
5.1.12. Study L - Rate of exchange / linear model optimisation objective / constraint 176
5.2. Conclusions 179
6. Case study 2: RCAR bumper impact 188

6.1. Reduced model creation and correlation 191
6.2. Case study hybrid optimisation and modelling parameters 199
6.3. Optimisation results – geometric analysis 206
6.3.1. Crush can configurations 206
6.3.2. Longitudinal configurations 218
6.4. Optimisation results – RCAR bumper test re-analysis 241
6.5. Conclusion 267
7. Future Work 273
7.1.1. Future work – hybrid methodology versatility and robustness 273
7.1.2. Future work – applications of the hybrid methodology 275
8. Conclusions 277
References 280
APPENDIX A - BEETS / Optistruct parameter tests 288
I. Optistruct tests 288
II. BEETS tests 295
APPENDIX B – Hybrid methodology user recommendations 302
APPENDIX C – Ethical Approval review 304

Abbreviations

BC	Boundary Conditions
BEETS	Bi-directional Evolutionary Entropy Tabu search Simulated Annealing
(B)ESO	(Bi-directional) Evolutionary Structural Optimisation
DOF	Degrees of Freedom
ER:	Evolutionary Ratio
ESLM	Equivalent Static Load Method
FE	Finite Element
FEA	Finite Element Analysis
HCA	Hybrid Cellular Automata
IR	Inertia Relief
MEP	Maximum Entropy Principle
NCAP	New Car Assessment Program
RCAR	Research Council for Automobile Repairs
SA	Simulated Annealing
SEA	Specific Energy Absorption
SIMP	Solid Isotropic Material with Penalisation
SPC	Single Point Constraints
TO	Topology Optimisation
TS	Tabu Search
VDM	Variable Density Method

Table of Figures

Figure 1.1 : Example of a typical modern day vehicle structure, edited from Kiani et al. (2014) 1
Figure 1.2 : Deformation of a vehicle front end structure from a rigid wall impact, edited from Grimes et al. (2013) 3
Figure 1.3 : Typical stress-strain curve of metals 4
Figure 1.4 : Example crash pulse of vehicle deceleration (g) during impact (s) (Du Bois et al. 2004) 7
Figure 1.5 : Design cycles with and without optimisation (Adapted from Altair University (2015b)) 9
Figure 1.6 : Different types of structural optimisation (Altair University 2015b) 10
Figure 1.7 : Example of TO result (Christensen et al. 2011) 11
Figure 2.1 : Graph representing the relative density (ρ) vs the structural efficiency (η) for different values of p: (1) p = 1.6; (2) p = 2.2; (3) p = 2.8; (4) p = 3.4; (5) p = 5; (6) p = 1 (Bruns 2005) 15
Figure 2.2 : Simply supported beam example (a) and the resulting checkerboard-patterned topology (b) (Sigmund and Petersson 1998) 16
Figure 2.3 : Solution of simply supported beam with filter applied (Sigmund and Petersson 1998) 16
Figure 2.4 : Function with several local minima (Altair University 2015) 18
Figure 2.5 : Example of multiple starting points (Altair University 2015) 20
Figure 2.6 : Filter scheme for BESO (Huang and Xie 2010) 25
Figure 2.7 : Evolution history of single load cantilever beam optimisation with instabilities Adapted from (Huang and Xie 2007) 26
Figure 2.8 : Evolution history of single load cantilever beam with sensitivity averaging (Huang and Xie 2007) 27
Figure 2.9 : Test example (a) initial design (b) ESO error after 1 iteration (c) optimum design (Zhou and Rozvany 2001) 28
Figure 2.10 : Beam under tensile load optimisation example 32
Figure 2.11 : BESO flowchart (Christensen 2015) 33
Figure 2.12 : BEETS method flowchart, adapted from (Christensen 2015) 38
Figure 3.1 : 2D plate base model 43
Figure 3.2 : Load curve for ESLM optimisation 46
Figure 3.3 : Acceleration curve from dynamic impact scenario 46

Figure 3.4 : IR models setup (a) Model 21 (b) Model 22 (c) Model 23 48
Figure 3.5 : Basic Optistruct setup..... 51
Figure 3.6 : Model 1 density distribution (with simple averaging filter applied)..... 52
Figure 3.7 : Model 2 density distribution (with simple averaging filter applied)..... 53
Figure 3.8 : Model 2 unfiltered density distribution 53
Figure 3.9 : Model 2 von Mises stress distribution (MPa)..... 54
Figure 3.10 : Model 21 density distribution 55
Figure 3.11 : Model 22 density distribution 56
Figure 3.12 : Model 23 density distribution 56
Figure 3.13 : Model 22 unfiltered density distribution 57
Figure 3.14 : Model 2 force sensitivity analysis setup (a) 15° (b) 30° (c) 45° 59
Figure 3.15 : Model 2 sensitivity analysis (a) model 44 (15°) (b) model 45 (30°) (c) model 46 (45°)..... 60
Figure 3.16 : Model 21 sensitivity analysis (a) model 47 (15°) (b) model 48 (30°) (c) model 49 (45°) 61
Figure 3.17 : Model 22 sensitivity analysis (a) model 50 (15°) (b) model 51 (30°) (c) model 52 (45°) 62
Figure 3.18 : Model 23 sensitivity analysis (a) model 53 (15°) (b) model 54 (30°) (c) model 55 (45°)..... 63
Figure 3.19 : Model 56 density distribution 64
Figure 3.20 : Load curve for LS-TaSC optimisation..... 65
Figure 3.21 : Basic LS-TaSC FE model setup..... 66
Figure 3.22 : Model 3 thickness distribution (mm) 67
Figure 3.23 : Model 4 thickness distribution (mm) 67
Figure 3.24 : Model 3 optimisation convergence criteria graph 69
Figure 3.25 : Model 4 von Mises stress distribution (MPa)..... 69
Figure 3.26 : Model 57 thickness distribution (mm) 70
Figure 3.27 : Model 58 with activated SIMP structure at iteration 16 71
Figure 3.28 : Model 58 with SIMP activation optimisation convergence criteria graph. 72
Figure 3.29 : ESLM lowered magnitude density distribution..... 75
Figure 3.30 : Model 9 thickness distribution (mm) 76
Figure 3.31 : Model 10 thickness distribution (mm) 76
Figure 3.32 : Model 11 thickness distribution (mm) 77
Figure 3.33 : Model 12 thickness distribution (mm) 77
Figure 3.34 : Model 9 plastic strain plot 78

Figure 3.35 : Model 59 single section thickness distribution 79
Figure 3.36 : Model 59 single section plastic strain plot 79
Figure 3.37 : Model 60 thickness distribution (mm) 80
Figure 3.38 : Model 60 optimisation convergence criteria graph 80
Figure 3.39 : Final topology (a) Model 24 (b) Model 25 (c) Model 26 82
Figure 3.40 : Final topology model 27 83
Figure 3.41 : Final topology model 28 83
Figure 3.42 : Final topology model 29 83
Figure 3.43 : Topology trends for models 24 - 29 84
Figure 3.44 : Model 27 plastic strain plot 85
Figure 3.45 : Final topology model 30 86
Figure 3.46 : Final topology model 31 86
Figure 3.47 : Final topology model 32 86
Figure 3.48 : Final topology model 33 87
Figure 3.49 : Topology trends for models 30-33 87
Figure 3.50 : Model 17 thickness distribution 90
Figure 3.51 : Model 18 thickness distribution 90
Figure 3.52 : Model 19 thickness distribution 90
Figure 3.53 : Model 20 thickness distribution 91
Figure 3.54 : Model 17 optimised structure FE analysis setup 92
Figure 3.55 : Model 17 optimised for FE analysis plastic strain at t=0.008s 92
Figure 3.56 : Model 17 optimised for FE analysis plastic strain at t = 0.014s 93
Figure 3.57 : Model 61 setup 93
Figure 3.58 : Model 61 thickness distribution 94
Figure 3.59 : Model 61 von Mises stress plot (MPa) 94
Figure 3.60 : Model 62 thickness distribution 95
Figure 3.61 : Model 62 re-analysis plastic strain plot 95
Figure 3.62 : Model 63 thickness distribution 96
Figure 3.63 : Model 63 re-analysis plastic strain plot 96
Figure 3.64 : Final topology (a) model 34 (b) model 35 (c) model 36 97
Figure 3.65 : Final topology model 37 98
Figure 3.66 : Final topology model 38 98
Figure 3.67 : Final topology model 39 98
Figure 3.68 : Model 34 initial von Mises strain distribution 99
Figure 3.69 : Final topology model 40 100

Figure 3.70 : Final topology model 41 100
Figure 3.71 : Final topology model 42 101
Figure 3.72 : Final topology model 43 101
Figure 4.1 : Hybrid optimisation basic FE setup 104
Figure 4.2 : Overall hybrid optimisation algorithm flowchart 106
Figure 4.3 : Force transfer method 1 (a) Non-linear model with main cross section (b) Initial non-linear nodal forces determined from main cross section force (c) Incorrect nodal forces during optimisation process 111
Figure 4.4 : Force transfer method 2 (a) Non-linear model with individual cross sections (b) Incorrect initial non-linear nodal forces determined from individual cross section forces (c) Nodal forces during optimisation process 113
Figure 4.5 : Step 4 "Create cross sections" function flowchart 114
Figure 4.6 : Cross-sectional force sampling rate effect comparison 116
Figure 4.7 : Cross-sectional force sampling rate effect maximum force 117
Figure 4.8 : Step 8 "Hybrid optimisation setup" function flowchart 118
Figure 4.9 : Step 12 "Update HW FE status" function flowchart 120
Figure 5.1 : Initial structure behaviour test FE setup 124
Figure 5.2 : Initial structure plastic strain distribution 125
Figure 5.3 : Interface size study non-linear section 126
Figure 5.4 : Rate of exchange flowchart 127
Figure 5.5 : Config 1 FE setup 128
Figure 5.6 : Config 2 FE setup 128
Figure 5.7 : Config 3 FE setup 129
Figure 5.8 : PS_M01 final topology deformed state 133
Figure 5.9 : PS_M02 final topology deformed state 133
Figure 5.10 : PS_M03 final topology deformed state 134
Figure 5.11 : PS_M04 final topology deformed state 134
Figure 5.12 : Topology trends non-linear section models PS_M01 - PS_M04 134
Figure 5.13 : Topology trends linear section models PS_M01 - PS_M04 135
Figure 5.14 : Model PS_M01 section (2) plastic strain distribution 136
Figure 5.15 : Component internal energy (mJ) of PS_M01 vs time (s) 136
Figure 5.16 : PS_M05 final topology deformed state 138
Figure 5.17 : PS_M06 final topology deformed state 138
Figure 5.18 : PS_M07 final topology deformed state 139
Figure 5.19 : PS_M08 final topology deformed state 139

Figure 5.20 : PS_M09 final topology deformed state 140
Figure 5.21 : PS_M10 final topology deformed state 140
Figure 5.22 : PS_M11 final topology deformed state 140
Figure 5.23 : PS_M12 final topology deformed state 141
Figure 5.24 : Topology trends linear section models PS_M05 - PSM12 141
Figure 5.25 : PS_M06 section (2) plastic strain distribution 142
Figure 5.26 : Component internal energy (mJ) of PS_M06 vs time (s) 143
Figure 5.27 : PS_M13 final topology deformed state 144
Figure 5.28 : Model PS_M13 section (2) plastic strain distribution 145
Figure 5.29 : Component internal energy (mJ) of PS_M13 vs time (s) 145
Figure 5.30 : PS_M13 section (2) iteration 1 element density distribution 146
Figure 5.31 : PS_M13 section (2) iteration 1 von Mises stress (MPa) 146
Figure 5.32 : PS_M14 final topology deformed state 147
Figure 5.33 : PS_M15 final topology deformed state 148
Figure 5.34 : PS_M02 final topology deformed state 148
Figure 5.35 : Topology trends non-linear section for models PS_M02, PS_M14 and PS_M15 148
Figure 5.36 : Topology trends linear section for models PS_M02, PS_M14 and PS_M15 149
Figure 5.37 : PS_M17 section (2) iteration 4 element density distribution 150
Figure 5.38 : PS_M17 section (2) iteration 5 FE setup 151
Figure 5.39 : PS_M22 final topology deformed state 153
Figure 5.40 : Final topologies for (a) PS_M10 and (b) PS_M34 154
Figure 5.41 : Topology trends linear section for Study F Grouping 1 154
Figure 5.42 : PS_M23 final topology deformed state 155
Figure 5.43 : Component internal energy (mJ) of PS_M26 vs time (s) 156
Figure 5.44 : Topology trends linear section for Study F Grouping 2 156
Figure 5.45 : Grouping 3 final topologies deformed state (a) PS_M24 (b) PS_M33 (c) PS_M42 158
Figure 5.46 : Topology trends linear section for Study F Grouping 3 158
Figure 5.47 : Final topologies (a) PS_M04 (b) PS_M45 (c) PS_M48 161
Figure 5.48 : Topology trends non-linear section for Study G 162
Figure 5.49 : Topology trends linear section for Study G 162
Figure 5.50 : PS_M53 (a) iteration 5 result with detached element (b) iteration 6 with detached element deleted 164

Figure 5.51 : PS_M58 section (2) iteration 8 element density distribution 165
Figure 5.52 : PS_M58 section (2) iteration 9 FE setup 166
Figure 5.53 : Model PS_M63 final topology deformed state 168
Figure 5.54 : Topology trends linear section for Study J Grouping 1 169
Figure 5.55 : Grouping 2 final topology deformed state (a) model PS_M71 (b) model PS_M74 170
Figure 5.56 : Topology trends non-linear section for Study J Grouping 2 170
Figure 5.57 : Topology trends linear section for Study J Grouping 2 171
Figure 5.58 : PS_M87 linear section (a) after iteration 4 (b) after iteration 5 174
Figure 5.59 : PS_M101 final topology deformed state 177
Figure 5.60 : Rate of exchange / linear optimisation objective/constraint final topology deformed state (a) PS_M106 (b) PS_M107 (c) PS_M108 177
Figure 5.61 : Graph depicting number of elements in linear section of structure after each hybrid TO iteration 178
Figure 5.62 : Model 2 updated forces FE setup 183
Figure 5.63 : Model 2 updated forces density distribution (with simple averaging filter applied) 183
Figure 5.64 : Model 2 density distribution (with simple averaging filter applied) 184
Figure 5.65 : PS_M10 density distribution (a) Original (b) Updated Forces 185
Figure 5.66 : PS_M10 final iteration topologies (a) Original (b) Updated Forces 185
Figure 5.67 : PS_M10 updated forces final topology deformed state 186
Figure 6.1 : RCAR bumper test engagement measurement (Research Council for Automobile Repairs 2010) 189
Figure 6.2 : RCAR test vehicle bumper height measurement zones (Research Council for Automobile Repairs 2010) 190
Figure 6.3 : 2010 Toyota Yaris sedan original bumper system (a) bumper (b) crush can (c) longitudinal 190
Figure 6.4 : 2010 Toyota Yaris reduced FE model for TO 192
Figure 6.5 : 2010 Toyota Yaris RCAR bumper test energy levels - Full vs reduced model 193
Figure 6.6 : 2010 Toyota Yaris x-axis velocity - Full vs reduced model 193
Figure 6.7 : 2010 Toyota Yaris original crush can geometry 194
Figure 6.8 : 2010 Toyota Yaris simplified crush can geometry 194
Figure 6.9 : 2010 Toyota Yaris original longitudinal geometry (right hand) 195
Figure 6.10 : 2010 Toyota Yaris simplified longitudinals geometry (right hand) 195

Figure 6.11 : Plastic strain plot of initial simplified crush can / longitudinal system 196
Figure 6.12 : Original vs simplified crush can geometry internal energy comparison. 197
Figure 6.13 : 2010 Toyota Yaris RCAR bumper test bumper beam internal energy - full vs reduced model 197
Figure 6.14 : Reduced model connections between crush cans and firewall 198
Figure 6.15 : Case study 2 interface nodes search sphere 199
Figure 6.16 : Yaris longitudinals attachment..... 201
Figure 6.17 : Yaris longitudinals IR FE setup 201
Figure 6.18 : Yaris longitudinals SPC FE setup..... 202
Figure 6.19 : BUS_M01 optimised crush cans (Interface size = 0; Impact velocity = 10 km/h; ER = 5%) – Top = LH crush can, Bottom = RH crush can..... 207
Figure 6.20 : BUS_M02 optimised crush cans (Interface size = 0; Impact velocity = 10 km/h; ER = 2.5%) – Top = LH crush can, Bottom = RH crush can..... 207
Figure 6.21 : BUS_M09 optimised crush cans (Interface size = 1; Impact velocity = 10 km/h; ER = 5%) – Top = LH crush can, Bottom = RH crush can..... 208
Figure 6.22 : BUS_M10 optimised crush cans (Interface size = 1; Impact velocity = 10 km/h; ER = 2.5%) – Top = LH crush can, Bottom = RH crush can..... 208
Figure 6.23 : BUS_M17 optimised crush cans (Interface size = 5; Impact velocity = 10 km/h; ER = 5%) – Top = LH crush can, Bottom = RH crush can..... 209
Figure 6.24 : BUS_M18 optimised crush cans (Interface size = 5; Impact velocity = 10 km/h; ER = 2.5%) – Top = LH crush can, Bottom = RH crush can..... 209
Figure 6.25 : BUS_M49 optimised crush cans (Interface size = 0; Impact velocity = 16 km/h; ER = 5%) – Top = LH crush can, Bottom = RH crush can..... 210
Figure 6.26 : BUS_M50 optimised crush cans (Interface size = 0; Impact velocity = 16 km/h; ER = 2.5%) – Top = LH crush can, Bottom = RH crush can..... 210
Figure 6.27 : BUS_M57 optimised crush cans (Interface size = 1; Impact velocity = 16 km/h; ER = 5%) – Top = LH crush can, Bottom = RH crush can..... 211
Figure 6.28 : BUS_M65 optimised crush cans (Interface size = 5; Impact velocity = 16 km/h; ER = 5%) – Top = LH crush can, Bottom = RH crush can..... 211
Figure 6.29 : BUS_M58 optimised crush cans (Interface size = 1; Impact velocity = 16 km/h; ER = 2.5%) – Top = LH crush can, Bottom = RH crush can..... 212
Figure 6.30 : BUS_M66 optimised crush cans (Interface size = 5; Impact velocity = 16 km/h; ER = 2.5%) – Top = LH crush can, Bottom = RH crush can..... 212
Figure 6.31 : BUS_M02 left hand crush can plastic strain plot 213
Figure 6.32 : BUS_M02 checkerboard affected zone 214

Figure 6.33 : BUS_M02 left hand crush can iteration 1 total strain plots in local element directions (a) Normal X (b) Normal Y (c) Normal Z (d) Shear XY (e) Shear YZ (f) Shear ZX 215
Figure 6.34 : BUS_M50 left hand crush can plastic strain plot 216
Figure 6.35 : BUS_M50 left hand crush can iteration 1 total strain plots in local element directions (a) Normal X (b) Normal Y (c) Normal Z (d) Shear XY (e) Shear YZ (f) Shear ZX 216
Figure 6.36 : BUS_M52 longitudinals iteration 1 element density plot 220
Figure 6.37 : BUS_M52 linear optimisation iteration 1 objective function convergence 220
Figure 6.38 : BUS_M52 right hand longitudinal iteration 2 geometry 221
Figure 6.39 : BUS_M01 iteration 1 longitudinals element density plot 222
Figure 6.40 : BUS_M05 iteration 1 longitudinals element density plot 223
Figure 6.41 : BUS_M05 iteration 1 Von Mises stress plot (MPa) 224
Figure 6.42 : BUS_M01 longitudinals final iteration topologies Top = LH longitudinal, Bottom = RH longitudinal 225
Figure 6.43 : BUS_M05 longitudinals optimised final iteration topologies Top = LH longitudinal, Bottom = RH longitudinal 225
Figure 6.44 : BUS_M16 longitudinals final iteration topologies (Grouping 1) Top = LH longitudinal, Bottom = RH longitudinal 226
Figure 6.45 : BUS_M23 longitudinals final iteration topologies (Grouping 3) Top = LH longitudinal, Bottom = RH longitudinal 227
Figure 6.46 : BUS_M21 longitudinals final iteration topologies (Grouping 2) Top = LH longitudinal, Bottom = RH longitudinal 227
Figure 6.47 : BUS_M53 longtudinals final iteration topology (Grouping 4) Top = LH longitudinal, Bottom = RH longitudinal 228
Figure 6.48 : BUS_M55 longitudinals final iteration topology (Grouping 5) Top = LH longitudinal, Bottom = RH longitudinal 228
Figure 6.49 : BUS_M95 longitudinals final iteration topology (Grouping 6) Top = LH longitudinal, Bottom = RH longitudinal 229
Figure 6.50 : Graph depicting number of elements in longitudinals after each hybrid optimisation iteration (BUS_M16) 233
Figure 6.51 : Graph depicting number of elements in longitudinals after each hybrid optimisation iteration (BUS_M07 and BUS_M55) 234
Figure 6.52 : BUS_M07 iteration 1 linear optimisation input (right hand longitudinal) 235

Figure 6.53 : BUS_M55 iteration 1 linear optimisation input (right hand longitudinal) 235
Figure 6.54 : BUS_M07 iteration 1 element density distribution and Von Mises stress plot 236
Figure 6.55 : BUS_M55 iteration 1 element density distribution and Von Mises stress plot 236
Figure 6.56 : BUS_M07 and BUS_M55 Von Mises stress plot with 160 MPa threshold applied 237
Figure 6.57 : BUS_M25 longitudinals final iteration topologies 239
Figure 6.58 : BUS_M49 longitudinal final iteration topologies 240
Figure 6.59 : BUS_M73 longitudinals final iteration topologies 240
Figure 6.60 : BUS_M25 (BUS_M01) crush cans for re-analysis 243
Figure 6.61 : BUS_M25 longitudinals for re-analysis..... 244
Figure 6.62 : BUS_M23 optimised right hand longitudinal plastic strain plot..... 245
Figure 6.63 : BUS_M04 optimised left hand crush can plastic strain plot..... 246
Figure 6.64 : BUS_M04 optimised right hand crush can plastic strain plot 247
Figure 6.65 : BUS_M04 optimised left hand longitudinal plastic strain plot 247
Figure 6.66 : BUS_M04 optimised right hand longitudinal plastic strain plot..... 248
Figure 6.67 : BUS_M25 optimised left hand crush can plastic strain plot..... 248
Figure 6.68 : BUS_M25 optimised right hand crush can plastic strain plot 249
Figure 6.69 : BUS_M25 optimised left hand longitudinal plastic strain plot 249
Figure 6.70 : BUS_M25 optimised right hand longitudinal plastic strain plot..... 250
Figure 6.71 : BUS_M25 optimised left hand longitudinal localised buckling..... 251
Figure 6.72 : BUS_M35 optimised left hand longitudinal plastic strain plot 254
Figure 6.73 : BUS_M35 optimised right hand longitudinal plastic strain plot..... 254
Figure 6.74 : BUS_M13 optimised left hand longitudinal plastic strain plot 255
Figure 6.75 : BUS_M13 optimised right hand longitudinal plastic strain plot..... 255
Figure 6.76 : BUS_M53 optimised left hand crush can plastic strain plot..... 258
Figure 6.77 : BUS_M53 optimised right hand crush can plastic strain plot 259
Figure 6.78 : BUS_M53 optimised left hand longitudinal plastic strain plot 259
Figure 6.79 : BUS_M53 optimised right hand longitudinal plastic strain plot..... 260
Figure 6.80 : BUS_M53 optimised left hand longitudinal maximum plastic strain area 260
Figure 6.81 : BUS_M83 optimised left hand longitudinal undeformed..... 261
Figure 6.82 : BUS_M83 optimised left hand longitudinal deformed..... 261

Figure 6.83 : BUS_M53 longitudinals Von Mises stress distribution (MPa) at iteration 1 (1) 263
Figure 6.84 : BUS_M53 longitudinals Von Mises stress distribution (MPa) at iteration 1 (2) 263
Figure 6.85 : BUS_M55 longitudinals Von Mises stress distribution (MPa) at iteration 1 (1) 264
Figure 6.86 : BUS_M55 longitudinals Von Mises stress distribution (MPa) at iteration 1 (2) 264
Figure 6.87 : BUS_M53 longitudinals Von Mises stress distribution (MPa) at iteration 2 (1) 265
Figure 6.88 : BUS_M53 longitudinals Von Mises stress distribution (MPa) at iteration 2 (2) 265
Figure 6.89 : BUS_M55 longitudinals Von Mises stress distribution (MPa) at iteration 2 (1) 266
Figure 6.90 : BUS_M55 longitudinals Von Mises stress distribution (MPa) at iteration 2 (2) 266
Figure 6.91 : Original Toyota Yaris crush can with spotwelds 271
Figure 7.1: Example block of solid elements 275
Figure 7.2: Rectangular box-section with internal "cells" (Duddeck et al. 2016) 276
Figure 7.3: Example optimised cross section of thin-walled structure and crashworthiness behaviour 276
Figure A.1 : FE setup for Optistruct parameter tests 288
Figure A.2 : Model 52_1 density distribution 291
Figure A.3 : Model 52_2 density distribution 291
Figure A.4 : Model 52_3 density distribution 292
Figure A.5 : Model 52_4 density distribution 292
Figure A.6 : Model 52_5 density distribution 292
Figure A.7 : Model 52_6 density distribution 293
Figure A.8 : Model 52_7 density distribution 293
Figure A.9 : Model 52_8 density distribution 293
Figure A.10 : Model 52_9 density distribution 294
Figure A.11 : Model 52_10 density distribution 294
Figure A.12 : Final topology model 30 296
Figure A.13 : Final topology model 30_1 297
Figure A.14 : Final topology model 30_2 297

Figure A.15 : Model 30 topology after iteration 4 298
Figure A.16 : Model 30_1 topology after iteration 2 298
Figure A.17 : Model 30_2 topology after iteration 1 298
Figure A.18 : Final topology model 30_3 299
Figure A.19 : Final topology model 30_4 300

List of Tables

Table 2.1 : Advantages / disadvantages of the VDM/SIMP method 21
Table 2.2 : Advantages / Disadvantages of BESO 34
Table 2.3 : Advantages / disadvantages of the BEETS method 39
Table 2.4 : Advantages / disadvantages of the HCA method 41
Table 3.1 : Mild steel and High Strength steel material properties (Christensen 2015) 45
Table 3.2 : Loading parameters 46
Table 3.3 : Case studies summary 49
Table 3.4 : Filter radii used for models 24-26 and 34-36 50
Table 3.5 : Models for linear study 51
Table 3.6 : Optistruct optimisation parameters 52
Table 3.7 : Optistruct sensitivity analysis models 58
Table 3.8 : LS-TaSC optimisation parameters 66
Table 3.9 : Models for non-linear study 73
Table 3.10 : BESO/BEETS optimisation parameters 81
Table 3.11 : BEETS vs LS-TaSC run time comparison 88
Table 3.12 : Models for combined linear/non-linear behaviour study 89
Table 4.1 : Summary of hybrid optimisation functions 108
Table 4.2 : Hybrid optimisation functions names 109
Table 4.3 : Cross-sectional force data sampling rate effect 116
Table 5.1 : Summary of Optistruct parameters for case study 1 123
Table 5.2 : Summary of BEETS parameters for case study 1 123
Table 5.3 : Case study 1 FE model parameters 124
Table 5.4 : Hybrid optimisation plate study models 130
Table 5.5 : Study A re-analysis data 137
Table 5.6 : Study B re-analysis data 143
Table 5.7 : Study C re-analysis data 145
Table 5.8 : Study D re-analysis data 149
Table 5.9 : Study E re-analysis data 151
Table 5.10 : Combined interface size / rate of exchange study groupings 152
Table 5.11 : Study F – Grouping 1 re-analysis data 153
Table 5.12 : Study F - Grouping 2 re-analysis data 155
Table 5.13 : Study F - Grouping 3 re-analysis data 157
Table 5.14 : Study G re-analysis data 160

Table 5.15 : Study H re-analysis data 163
Table 5.16 : Combined rate of exchange / interface BCs groupings 167
Table 5.17 : Study J - Grouping 1 re-analysis data 167
Table 5.18 : Study J - Grouping 2 re-analysis data 169
Table 5.19 : Combined rate of exchange / linear BC groupings 172
Table 5.20 : Study K - Grouping 1 re-analysis results 172
Table 5.21 : Study K - Grouping 2 re-analysis data 173
Table 5.22 : Study K - Grouping 3 re-analysis data 175
Table 5.23 : Study L re-analysis data 176
Table 5.24 : Comparison between interface BC models with identical hybrid TO parameters 181
Table 6.1 : Full and reduced Toyota Yaris model CoG and mass properties 192
Table 6.2 : Hybrid optimisation and modelling parameters for case study 2 203
Table 6.3 : Hybrid optimisation bumper study models 204
Table 6.4 : "Minimise mass" longitudinal geometry trend groupings 226
Table 6.5 : Grouping 1 hybrid optimisation and modelling parameters 229
Table 6.6 : Grouping 2 hybrid optimisation and modelling parameters 229
Table 6.7 : Grouping 3 hybrid optimisation and modelling parameters 230
Table 6.8 : Grouping 4 hybrid optimisation and modelling parameters 230
Table 6.9 : Grouping 5 hybrid optimisation and modelling parameters 230
Table 6.10 : Grouping 6 hybrid optimisation and modelling parameters 230
Table 6.11 : "Minimise mass" longitudinal grouping 7 231
Table 6.12 : Grouping 7 hybrid optimisation and modelling parameters 232
Table 6.13 : RCAR bumper test re-analysis groupings (a) 242
Table 6.14 : RCAR bumper test re-analysis groupings (b) 242
Table 6.15 : RCAR bumper test re-analysis groupings (c) 243
Table 6.16 : RCAR bumper test re-analysis results data (Low Velocity) 245
Table 6.17 : RCAR bumper test volume reduction data (Low Velocity) 252
Table 6.18 : RCAR bumper test re-analysis models hybrid optimisation and modelling parameters (Low Velocity) 253
Table 6.19 : RCAR bumper test volume reduction data (High Velocity) 258
Table 6.20 : RCAR bumper test re-analysis models hybrid optimisation parameters (High Velocity) and maximum plastic strain in longitudinals 262
Table A.1 : Models for Optistruct parameter tests 289
Table A.2 : Optistruct parameter test optimisation run data 290

Table A.3 : Summary of Optistruct parameters for case study 1 295
Table A.4 : Models for BEETS parameter tests 296
Table A.5 : Summary of BEETS parameters for case study 1 301

1. Introduction and background to study

As the automotive vehicle has evolved as a technological concept, its overall structural makeup has also changed dramatically (Genta et al. 2014). The development of the vehicle structure as an entity "can be described by considering three partially overlapping periods"; the separable chassis, the partially integrated body and chassis, and the unitized bodies which make up the majority of vehicle fleets today, and have done since around 1980 (Du Bois et al. 2004). An example of such a structure is given in Figure 1.1. This structure is typically known as a Body-In-White (BIW).

Figure 1.1 : Example of a typical modern day vehicle structure, edited from Kiani et al. (2014)

At this stage, it is important to establish the main function of a BIW structure, and the general associated terms used throughout this thesis.

Aside from acting as a support structure for the vehicle's main components (engine, suspension, etc.), the main objective of a BIW structure is to protect the occupants during an impact scenario. Worldwide statistics show the importance of considering occupant safety; to date, road accidents are the 8th cause of deaths and are projected to become the 5th by 2030 (World Health Organization 2013).

Considering the example of a frontal impact, two main sections of the vehicle can exhibit significantly different behaviours in order to protect the occupants: the "front end" and

the “passenger cell”. The “front end” of the vehicle (sections x2, x9, x10, x11 and x12 from Figure 1.1) is designed to absorb as much of the kinetic energy from the impact as possible through plastic deformation, while remaining stiff enough to avoid any intrusion into the “passenger cell” (the parts behind section x3 in Figure 1.1) where the driver/passengers are located. This passenger cell must protect the occupants from injury from intruding components or a reduction in the interior space, and is therefore designed with maximum stiffness in mind. In engineering terms, the “front end” of the vehicle is designed with the intention of exhibiting highly non-linear responses/deformation, while the “passenger cell” must remain within the linear deformation mode. This will be studied in more detail in the literature review, but these contrasting behaviours are likely to have an impact on the possible uses of structural optimisation.

With the evolution of the automotive industry and its importance to the population, the list of criteria to fulfil in vehicle and BIW design, such as safety criteria, light weighting, emission standards, has grown. The next section will explain in more detail the key criteria.

Vehicle crashworthiness is defined as the ability of a vehicle structure to protect occupants during an impact. This is enabled through plastic deformation to absorb impact energies, while simultaneously keeping the “passenger cell” intact (Du Bois et al. 2004). In order to limit the injuries due to severe deceleration of the vehicle, the aforementioned plastic deformation must be achieved in a controlled manner by the structure. Figure 1.2 Grimes et al. (2013) demonstrates a Finite Element Analysis (FEA) example of plastic deformation as a means of absorbing energy from a frontal rigid wall impact.

Figure 1.2 : Deformation of a vehicle front end structure from a rigid wall impact, edited from Grimes et al. (2013)

Before continuing the analysis of different design criteria for the BIW, this numerical example (Figure 1.2) demonstrates an important aspect to consider in structural optimisation: the modelling of the FE model. The optimisation process will feed off FEA results, and therefore certain aspects of the model could potentially affect the optimisation procedure.

Firstly, the type of analysis used is important, i.e. a static or dynamic analysis. An analysis is considered static when the following parameters are met (Altair University 2015a) :

- The force is static (no time dependency)
- Static equilibrium states are achieved, i.e. the sum of the external forces and moments acting on the structure are zero

For many applications, including in the automotive industry, this type of analysis is largely sufficient for designing components capable of withstanding typical loads. However, in certain contexts including crashworthiness, the loads are time dependent. Therefore, a dynamic analysis is preferable in order to consider time dependency (Altair University 2015a).

The behaviour of the structure is also crucial to the process, specifically whether it is linear or non-linear. Both of these responses have been discussed and identified in

Figure 1.2. In many cases, it is desirable to have a structure or component that remains below the Yield strength threshold of the material when subjected to a certain load. In this case, the structure can be defined as linear as the forces are a linear function of the displacements via the stiffness matrix and by extension the stresses are a linear of function of strain through Hooke's law (Altair University 2015a). However, as mentioned previously, the front end of the vehicle in an impact scenario displays high levels of deformation, and is defined as having non-linear behaviour.

There are two possible types of non-linearity (Altair University 2015a). Firstly, geometric non-linearity where the displacements/deformations are no longer considered infinitesimal and the linear force/displacement relationship is invalid. Buckling is one example of such behaviour, as is contact between two parts as a change in stiffness appears in the contact zone.

Secondly, material non-linearity can be considered when stresses are greater than the Yield limit of the material. The material behaviour past this point can be very different, as shown by the stress-strain curve of Figure 1.3.

Some materials have been removed due to 3rd party copyright. The unabridged version can be viewed in Lancester Library - Coventry University.

Figure 1.3 : Typical stress-strain curve of metals (Christensen et al. 2013)

In Figure 1.3, σ_{yield} is the Yield strength of the material, σ_{UTS} the ultimate tensile strength of the material, ε_E the elastic strain and ε_P the plastic strain. Considering earlier statements, that plastic deformation is the key to absorbing impact energy and the plastic strain area under the curve in Figure 1.3 represents the strain energy, then it is critical to designing for crashworthiness that non-linear material behaviour is defined.

Finally, a combination of both geometric and material non-linear behaviour can be defined.

Before moving on to other modelling aspects of FEA, it is useful at this stage to introduce implicit and explicit FEA solving methods, as they tie quite closely to the static/dynamic and linear/non-linear discussions above. The differences between implicit and explicit FEA stem from the resolution of Newton's second law as stated in equation (1.1) below (Jacob and Goulding 2002):

$$[M]\{\ddot{x}\} + [K]\{x\} = \{f_{ex}\} \tag{1.1}$$

where [M] and [K] are the mass and stiffness matrices, $\{\ddot{x}\}$ the nodal accelerations, $\{x\}$ the nodal displacement and $\{f_{ex}\}$ the external forces. Starting from iteration n, the implicit formulation calculates displacements at the following iteration n+1 as follows (Jacob and Goulding 2002):

$$\left[\frac{4[M]}{\Delta t^2} + [K]\right]\{x\}_{n+1} = \{f_{ex}\}_{n+1} + \frac{4[M]}{\Delta t^2}(2\{x\}_n - \{x\}_{n-1}) + [M](2\{\ddot{x}\}_n + \{\ddot{x}\}_{n-1}) \tag{1.2}$$

where Δt is the timestep between n and n+1. In essence, [M] and [K] need to be formulated before the equilibrium calculation can take place (Jacob and Goulding 2002). If equilibrium is not achieved, then the process can begin again but with a smaller timestep. This results in an increase in computational time. However, this method is "unconditionally stable" (Hellen and Becker 2013), and suited to linear and/or static problems as equilibrium checks are not as frequent, and the timestep can be set quite large.

On the other hand, explicit calculations solve equation (1.1) by rearranging it as follows:

$$[M]\{\ddot{x}\} = \{f_{ex}\} - [K]\{x\} = \{f_{ex}\} - \{f_{int}\} \tag{1.3}$$

The displacements are calculated as follows:

$$x_{n+1} = \Delta t_{n+1}\dot{x}_{n+\frac{1}{2}} + x_n \tag{1.4}$$

Therefore, explicit FEA uses previous or current information to calculate the next timestep, and there is no need for frequent equilibrium checks. This makes it ideal for problems where high levels of non-linearity and/or dynamic loading are present. This is under the condition however that the timestep used is kept relatively small. To

summarise, implicit is more adapted to linear static problems and explicit suited to non-linear dynamic problems.

The boundary conditions (BCs) applied can also influence the analysis results. Typically, Single Point Constraints (SPCs) are used to constrain the FE model at certain points in certain degrees of freedom. Therefore, by effectively blocking movement at those points, reaction forces are created in those constrained points. However, as mentioned in Christensen et al. (2013), this may not accurately reflect the load case applied. If the FE model in Figure 1.2 were considered once again, with the scenario of a rigid wall impacting the vehicle, one possible method of constraining the model using SPCs would be to apply the latter to the wheels, and apply the loading at the front end of the vehicle. However, this would be akin to “gluing” the vehicle to the ground, vastly different to the real life behaviour of the vehicle where it is allowed to move and essentially bounces off the rigid wall once its velocity reaches zero depending on the inertia properties of the vehicle. Inertia Relief (IR) can circumvent this issue. In essence, no constraints are added to the FE model, and instead the FEA process calculates the internal loads necessary to counter the external loading and achieve static equilibrium. This is done by adding additional terms to the stiffness matrix (Christensen et al. 2013). However, IR is used for linear static conditions, and while it more accurately represents the BCs for impact scenarios than SPCs, it is not a complete replacement for using a dynamic analysis.

Overall, this section has focused on highlighting that when creating the FE model, several assumptions can be made, and FEA is inherently an approximation method. This will logically filter down to the optimisation process, which underlines once again that optimisation is a tool to help engineers, and not an “exact science”.

Focusing back on the design criteria, though the structure must absorb as much energy as possible through plastic deformation, it must also prevent any intrusion into the passenger compartment to minimise injuries to the occupants. Therefore, the structure must maintain a certain level of stiffness.

The crashworthiness performance is verified and graded using both regulatory programs (the National Highway Traffic Safety Administration (NHTSA) in the USA and the Vehicle Certification Agency (VCA) in the UK) and consumer assessment programs such as the Euro New Car Assessment Program (NCAP) or Insurance Institute for Highway Safety (IIHS). The ratings awarded by these agencies provide incentives to the manufacturer to design as safe a structure as possible (Euro NCAP 2015). The standards have evolved

and keep on evolving as the landscape of vehicle safety changes. For example, the number of tests has increased over the years, with the introduction of the safety assist criteria and whiplash tests in 2009 (Euro NCAP 2009) and the newly introduced “Frontal Full Width Impact” as of 2015 (Euro NCAP 2015). The four areas assessed consist of Adult Occupant Protection (AOP), Child Occupant Protection (COP), Pedestrian Protection (PP) and Safety Assist (SA). In total, 20 assessment criteria are currently evaluated in the current Euro NCAP ratings, with a scheduled increase to 22 in 2020 (Safety Wissen 2018). Since 2014, the weight factor for SA in the overall vehicle safety rating increased to 20% of the overall score (Euro NCAP 2012). This includes active safety features, which may have a subsequent impact on reducing the weight of the safety structure due to lower impact speeds, and structural optimisation will have a role in achieving these lower weight targets.

The deceleration of a vehicle over time, due to an impact, is characterised by a “crash pulse”. Typically, a crash pulse will resemble that shown in Figure 1.4., which in this instance represents the frontal impact with a fixed barrier (Du Bois et al. 2004).

Figure 1.4 : Example crash pulse of vehicle deceleration (g) during impact (s) (Du Bois et al. 2004)

In order to measure the vehicle deceleration, an accelerometer is placed at the bottom of the B-pillar in the “passenger cell”, crucially in the non-deformable section of the vehicle, as shown in Figure 1.1 and Figure 1.2. The resulting crash pulse is then used as a tool to analyse the impact and validate the crashworthiness of the vehicle. As previously mentioned, the non-linear behaviour of the vehicle “front end” is used to control the impact and avoid/reduce occupant injuries. The crash pulse can be used to monitor this. Essentially, an early acceleration peak and gradual decay is preferred from

an occupant safety point of view (Du Bois et al. 2004). The peak value needs to be below a certain threshold that limits occupant injuries. Generally these injuries are calculated from data collected by accelerometers and load cells placed in Hybrid III dummies, and include the head injury criterion (HIC), or other values taken from the neck, chest or legs for example (Guha et al. 2008). The injury data is then used to evaluate the vehicle using for example Euro NCAP standards, where for instance the HIC value must be below 700 where hard contact is visible (Euro NCAP 2015).

The vehicle structure is subjected to several impact scenarios such as frontal impacts, side impacts, rear impacts or roof crush scenarios. These scenarios may also occur simultaneously, at different impact speeds and different durations.

Lastly, the vehicle compatibility is an important aspect to consider (Van der Sluis 2000). Vehicle compatibility is defined as the behaviour of a vehicle structure when impacting other vehicles of varying masses. An impact between a small city car and an SUV for example would in general result in more damage to the former (Van der Sluis 2000). This can be mitigated by considering the compatibility of its front structure.

The future and evolution of the automotive industry may also have an impact on the layout of vehicle structures. Expanding on the accident prevention systems, or “Safety Assist” (SA) features mentioned in the discussion on Euro NCAP requirements, the future is being driven towards autonomous vehicles (Department for Business Innovation & Skills 2016, Litman 2015) and the potential is for a vast decrease in impact speeds, and therefore the loads travelling through the structure. This would allow for a possible decrease in necessary structural mass to protect the occupants, and optimisation is a key tool in enabling this. On the other hand, vehicle propulsion methods are also evolving such as engine downsizing, hybridisation and fully electric vehicles (Lane 2016) which would modify the mass distribution around the vehicle and therefore the inertia properties. Optimisation could also cater for these considerations in the design process.

Safety considerations have shown to be important in the design process of vehicle structures. Another important aspect somewhat steered by Government policies is emissions reduction (Department for Transport et al. 2015). The UK targeting a reduction of 80% of greenhouse gas emissions by 2050, transport has been identified as a key source of emissions (Department for Transport et al. 2015). The vehicle BIW structure, in particular lightweighting, is an area where design engineers can focus on to achieve those targets. Casadei and Broda (2008) show that a typical 1.6L petrol engine vehicle can provide between 0.27% and 0.32% of fuel economy benefit per percentage of weight

reduction. Lightweighting of vehicle structures also provides a benefit by reducing material usage, which could be considered as reducing emissions associated with material extraction/harvesting and manufacturing.

Considering the above criteria, and that other conditions such as bending/torsional stiffness for road handling, vibration mitigation for ride quality, manufacturing capabilities and costs must also be considered, designing vehicle structures is not an easy task, and a certain level of compromise must be expected. There are two important branches that influence the design of efficient structures: the structural geometry (defined by structural optimisation) and material selection. This PhD will focus on the structural geometry branch.

The previous discussions, examples and standards have led to a common conclusion in terms of designing vehicle structures: optimisation tools offer a solution to obtaining structures that validate or offer the best compromise between different design requirements. The following discussion will introduce in greater detail the “typical” design process (Altair University 2015b), with a focus on how it can be applied to the design of vehicle structures subject to the criteria mentioned in the previous discussions.

Figure 1.5 below depicts how previous design methods without optimisation entailed many redesign loops as a result of physical prototype testing (Altair University 2015b).

Figure 1.5 : Design cycles with and without optimisation
(Adapted from Altair University (2015b))

The introduction of FEA based structural optimisation (Figure 1.5) has played a key role in designing more efficient and lightweight structures in many engineering fields, including automotive. Optimisation tools are also able to design with the criteria previously mentioned in mind, using a system of design objectives (minimising weight for example) and constraints (maximum stress values for example) (Altair Engineering

2009). At the beginning of the design cycle, Figure 1.5 shows that structural optimisation allows for concept ideas to be produced (Figure 1.5 (b)), which can then be fine-tuned further down the design process as opposed to the previous design processes (Figure 1.5 (a)) where initial design ideas were produced from engineering judgment and previous designs. Furthermore, by introducing optimisation into the design cycle, there is a reduction in material costs, with less prototype testing and a reduction in time with quickly obtainable efficient designs (Figure 1.5). One possible downside to CAE based optimisation is the approximation induced through using FEA. However, thanks to modern day computational capabilities coupled with improvements in FEA, those concerns are reduced. Optimisation is therefore a valid tool for designing vehicle structures. The keyword here is “tool”, as mentioned by Altair University (2015b) it does not have engineering judgment which must come from the user. However, in order to obtain design ideas, it is perfectly valid.

There are three main types of structural optimisation used to design efficient structures (Altair University 2015b), the differences between which are displayed in Figure 1.6:

Some materials have been removed due to 3rd party copyright. The unabridged version can be viewed in Lancester Library - Coventry University.

Figure 1.6 : Different types of structural optimisation (Altair University 2015b)

- Size optimisation (“Dimensioning” Figure 1.6): This procedure involves modifying the geometrical parameters of a given structure/part, such as the section area, thickness, or stiffness for spring elements
- Shape optimisation: As its name suggests, shape optimisation modifies the outer boundaries of the structure. Essentially, the nodal coordinates are modified, but there is no modification of the topology (no extra openings or holes)

- Topology optimisation: This process deals with the distribution of material in a given structure. The aim is to efficiently create openings in the structure or even add material in response to given load cases.

The latter, topology optimisation (TO), is generally used as an initial design tool to obtain efficient material distribution from a given set of load cases (Reed 2002, Krog et al. 2011), and an enclosed “design volume” (the design volume is the boundary of possible material locations). From this definition, TO is therefore a tool to be used at the concept design phase from Figure 1.5. A typical result from TO is illustrated in Figure 1.7, which in essence gives the load paths through the structure (Christensen et al. 2011). TO can be embedded into FEA software for linear static optimisation applications, such as the Optistruct solver in the Altair Hyperworks software package (Altair University 2015b).

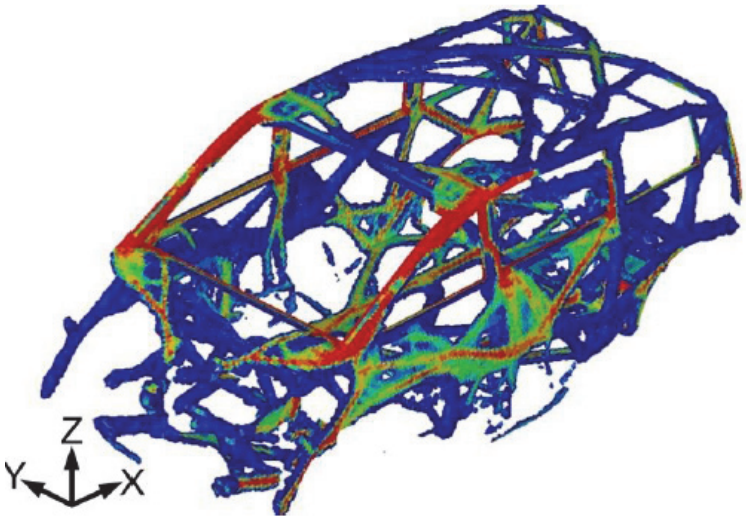

Figure 1.7 : Example of TO result (Christensen et al. 2011)

Size and shape optimisation are then used as a means of fine tuning the design to meet specific requirements (Reed 2002, Krog et al. 2011). Throughout this PhD thesis, the focus will be on TO, and therefore on obtaining initial design ideas. However, as has been previously mentioned, the BIW structure experiences different types of behaviour, and must meet different design targets. To reiterate, the front end of the vehicle exhibits highly non-linear behaviour and the passenger cell exhibits linear deformation. In order to achieve a fully optimum vehicle structure, an optimisation tool or methodology must be able to cater simultaneously for this difference in behaviour and the corresponding requirements previously discussed. The creation of such a tool is the overall aim of this

PhD. The next chapter will therefore analyse the main existing algorithms used in TO and implemented in FEA software. Their advantages and drawbacks will be discussed, focusing on their potential use in a methodology that caters for both linear and non-linear deformations, either on their own or as a combination.

2. Literature Review

This literature review will explore and review the existing optimisation algorithms that focus on structural topology. The algorithms will be explored according to the two main groups, mathematical based algorithms and heuristic/meta-heuristic (experienced based) algorithms. As mentioned in the conclusion to the previous chapter, the methods outlined here are implemented or tied in some way to industry standard, commercially available FEA software. In this instance, the two software selected are Optistruct, a solver part of the Altair Hyperworks software package and typically used in industry for linear static problems through implicit calculations. The other, LS-DYNA, is an explicit solver that is used in industry for crash analysis, and generally problems that exhibit dynamic loading and high levels of non-linearity. Throughout this chapter, wherever mentioned, linear topology optimisation refers to optimisation of structures with linear responses to external loading. Similarly, non-linear topology optimisation refers to a structure exhibiting non-linear responses as a function of the loads.

2.1. Mathematical based methods

The homogenisation method was first developed as a topology optimisation (TO) tool by Bendsøe and Kikuchi (1988). It involves modifying elements, initially defined using porosities, into essentially anisotropic elements. A relation between the material density and mechanical properties would then be determined to evaluate the efficiency of each material. A much more practical technique, needing only one element variable, in this instance the material density, was defined (Bendsøe 1989) and is known as the Variable Density Method (V.D.M.) (Altair Engineering 2009). The latter was then combined with the Solid Isotropic Material with Penalisation (SIMP) method (Zhou and Rozvany 1991, Rozvany et al. 1992). To put into context the development of the VDM/SIMP method, equation (2.1) states the initial problem to be solved. In this instance, the objective is to minimize the compliance of the structure for a given volume constraint (Bendsøe and Sigmund 2003). Assuming a numerical approach is used and the Young's modulus E is constant, the problem amounts to the following:

$$\begin{gathered} min\, \boldsymbol{f}^T \boldsymbol{u} \\ subject\ to: \boldsymbol{K}(E_e)\boldsymbol{u} = \boldsymbol{f} \\ E_e \in E_{add} \end{gathered} \tag{2.1}$$

where ***f*** is the load vector, ***u*** is the displacement vector, ***K*** the stiffness matrix dependent on the element Young's modulus E_e, which itself must be part of the admissible values given in E_{add}. This method uses E_e as the design variable. Initially, to obtain structures containing only solid or void elements, the following modification (equation (2.2)) was applied to the Young's modulus of each element, with the introduction of a discrete variable $l_{\Omega mat}$ (Bendsøe and Sigmund 2003):

$$E_{ijkl} = l_{\Omega mat} E^0_{ijkl}, \quad with\ l_{\Omega mat} = \begin{cases} 1\ if\ material \\ 0\ if\ void \end{cases} \tag{2.2}$$

Here, E^0_{ijkl} is the stiffness tensor of the used isotropic material, and via the discrete variable $l_{\Omega mat}$ defines whether the element in question should be solid or void, based on Finite Element Analysis (FEA) results. However, the issue with using a discrete variable, and reducing Young's modulus to zero for void elements, is the creation of numerical instabilities. The equilibrium equation of FEA $\boldsymbol{K}(E_e)\boldsymbol{u} = \boldsymbol{f}$ from equation (2.1) cannot be solved where there is an absence of a Young's modulus value in the stiffness matrix $\boldsymbol{K}$. This is where the development of the VDM/SIMP method can be traced. Instead of using a discrete variable, a continuous variable which can take any value between x_{min} (a value close, but not equal to 0) and 1, $\rho(x)$, is introduced into the problem. Therefore, $\rho(x)$ effectively represents the relative density of the element. The main issue with a continuous variable, is the appearance of intermediate densities, or otherwise called "grey" elements. In engineering terms, and from a manufacturing point of view, these elements make very little sense, as in TO the aim is to achieve well-defined structures. The SIMP interpolation scheme can alleviate this issue using a penalisation factor p applied as follows (equation (2.3)):

$$E_{ijkl}(x) = \rho(x)^p E^0_{ijkl}, \quad with\ p > 1 \tag{2.3}$$

Usually, a penalty factor of above 3 is chosen to obtain solid/void topologies. Figure 2.1 shows the influence of the penalty factor on the relative density (Bruns 2005):

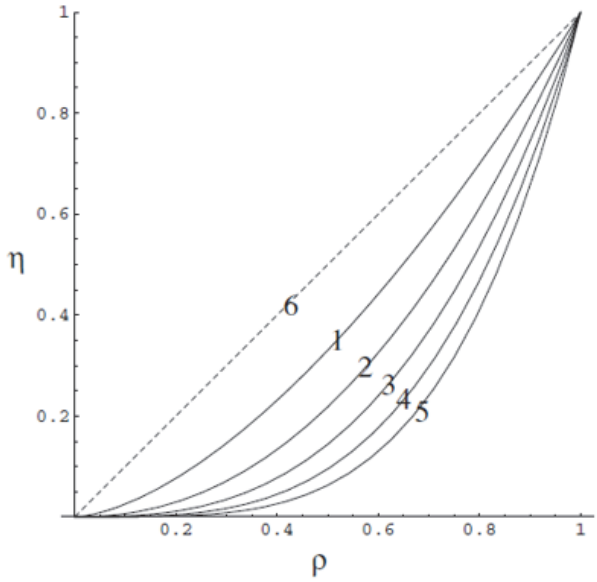

Figure 2.1 : Graph representing the relative density (ρ) vs the structural efficiency (η) for different values of p: (1) p = 1.6; (2) p = 2.2; (3) p = 2.8; (4) p = 3.4; (5) p = 5; (6) p = 1 (Bruns 2005)

In Figure 2.1, ρ represents the density of each element through the material redistribution, and η represents the efficiency of each element, i.e. the effect the density ρ has on the Young's Modulus. Therefore, η from Figure 2.1 corresponds to $\rho(x)^p$ from equation (2.3). For example, with no penalisation, if an element is attributed a density of 0.5, then the density value used in the recalculation of the stiffness tensor $E_{ijkl}(x)$ is 0.5. In essence, an element with half the mass provides half the stiffness. However, with a penalisation factor of three, the density value η drops to 0.125, i.e. the element is 8 times more compliant for half the mass of the original element. This is an "inefficient" use of the material compared to density values of 1 (all the stiffness for all the mass of the element) or close to 0 (low mass for low stiffness). Therefore the VDM methods attempts to redistribute the density towards these 0/1 values.

Despite the vast improvements offered by the VDM/SIMP method compared to the initial homogenisation techniques developed, some initial problems are found to hinder its performance. The first of these is the checkerboard effect. This issue manifests itself through alternating solid/void elements in the structure, as its name suggests much like a checkerboard (Figure 2.2). These type of patterns are due to numerical instabilities in the model, and it is clear they provide little clarity in terms of manufacturing.

Figure 2.2 : Simply supported beam example (a) and the resulting checkerboard-patterned topology (b) (Sigmund and Petersson 1998)

Therefore several techniques were developed to eliminate this problem (Sigmund and Petersson 1998):

- *Smoothing*: A post processing technique, much like image processing, this method simply uses the final topology obtained with checkerboard patterns and smoothes them over, thus obtaining mechanically feasible designs. Whilst a simple method, its main drawback is the fact that it doesn't eliminate the issue itself
- *Higher order finite elements*: This modification includes using more precise finite element (FE) formulations in the structure (for example 8 node shell elements), which would provide a more accurate representation. However, this comes at the cost of vastly increased computational time.
- *Filtering*: The last technique, and the most widespread in its use, is to filter the element sensitivities (effectively the values that decide the efficiency of an element) using the sensitivities of surrounding elements. By using this technique, the checkerboard pattern has been shown to be vastly suppressed (Figure 2.3).

Figure 2.3 : Solution of simply supported beam with filter applied (Sigmund and Petersson 1998)

The second issue relates to mesh dependence. When performing TO on a structure, refining the mesh should not lead to a different layout of material, simply a better definition of the boundaries. However, in the original VDM/SIMP method, this was not the case. Several methods, called “restriction methods”, were developed to eliminate this occurrence. The other advantage of these restriction methods is that most of them simultaneously solve the checkerboard problem. These methods are (Sigmund and Petersson 1998):

- *Perimeter control*: This method consists of limiting the density variation in an iteration. Effectively, this limits the changes that can be made to the boundaries in the structure, as the two are linked (a relative density close to 1 equates to a solid element, whereas a relative density of 0 equates to a void).
- *Global gradient constraint*: The global density function can be constrained using this method. However, a constraint value must be defined for this method by experimentation, as too high a value effectively removes the boundary restrictions (Bendsøe and Sigmund 2003).
- *Local gradient constraint*: Much like the previous method, this method limits the density variation in each point of the structure, in this case the elements. However, when considering the potential size of FE models, it is clear that this method adds too many constraints to the optimisation problem to be a viable solution.
- *Mesh independent filtering*: This method is very similar to the checkerboard filter technique previously discussed. In this case, the neighbouring element sensitivities are weighted so that those closest to the analysed element have more influence. The sensitivities are calculated as demonstrated by equation (2.4):

$$\frac{\widehat{\delta f}}{\delta \rho_k} = (\rho_k)^{-1} \frac{1}{\sum_{i=1}^{N} \widehat{H}_i} \sum_{i=1}^{N} \widehat{H}_i \rho_i \frac{\delta f}{\delta \rho_i} \tag{2.4}$$

where $\frac{\widehat{\delta f}}{\delta \rho_k}$ is the sensitivity of element *k*, $(\rho_k)^{-1}$ is the density of element *k* in the previous optimisation iteration, *N* the number of neighbouring elements and $\widehat{H}_i$ the weight factor defined by equation (2.5):

$$\widehat{H}_i = r_{min} - dist(k, i) \tag{2.5}$$

where *i* is a neighbouring element and r_{min} is a user defined filter zone, within which element sensitivities are taken into account in the calculation. Outside the zone, the weight factor is equal to zero. Whilst this method has been doubted due to its heuristic nature, it is debatable whether this is a real issue as it provides identical results to the gradient methods, with simpler implementation and little added CPU time.

The final issue to be resolved is that of convergence towards local minima. Effectively, a TO problem can be reduced to finding the minimum of an objective function, for example the compliance of the structure (Altair University 2015). If the objective function is considered a curve, problems with only one optimum, called “convex problems”, are represented by only one minimum or “turning point” in the curve (Altair University 2015). However, typical problems possess more than one minimum on the curve (Figure 2.4). Of those minima, the lowest point represents the global optimum, while the others are local optima, and there is a possibility that the structure converges towards the latter.

Figure 2.4 : Function with several local minima (Altair University 2015)

This is an issue when searching for a global optimum, and there are several approaches to mitigate the problem. One method, as stated by (Sigmund 1994), consists of using the mesh-dependency filter. Effectively, by defining a low value for the filter zone (r_{min} in equation (2.5)), the intermediate density variation is limited. This has an undesired effect of allowing intermediate densities in the design; however, these can be eliminated by progressively increasing the filter zone value. This solution depends on the initial filter used, and the incremental increase applied.

Therefore, there is the possibility of using other algorithms to complement the VDM/SIMP method. Stochastic algorithms, which will be discussed further in a later section, can be useful in avoiding local minima, and one of these, Simulated Annealing (SA), has been

used in conjunction with the VDM/SIMP method (Garcia-Lopez et al. 2011). Using the description of an optimisation problem given by Figure 2.4, essentially SA helps the algorithm to search for the global optimum by allowing the structure to worsen, from an objective function point of view, if needed before converging towards the global optimum, subject to a certain probability.

It is important to state that these problems (checkerboard patterns, mesh dependency, local minima) are also inherent to other optimisation techniques. Therefore, the extra measures taken to counter these problems, and the possible extra CPU resources needed, do not contribute to any possible disadvantages of the VDM/SIMP method over other TO methods. For example, the original Evolutionary Structural Optimisation (ESO) method is also subject to checkerboard patterns and mesh dependency, and therefore the use of filters, similar to the *Mesh independent filtering* discussed above, is needed to avoid those issues.

As has been discussed, VDM/SIMP is essentially a parameterisation method for the structure. Usually it is used in conjunction with gradient based methods, such as the Method of Moving Asymptotes (Bendsøe and Sigmund 2003, Svanberg 1987), the Optimality Criteria (Bendsøe and Sigmund 2003, Venkayya 1989) or the Sequential Linear Programming (Dunning and Kim 2014) methods, which perform the optimum search via derivation of the objective function. In terms of software implementation, the VDM/SIMP method is used in a variety of programs, including Optistruct, where it is coupled with a more developed gradient based method, Multiple Starting Points Optimization (Altair University 2015, Altair Engineering 2009). Observing Figure 2.5, the benefit of having multiple starting points can be understood, namely increasing the chances of finding the global optimum (Altair University 2015). Whereas beginning the procedure from points A or B would result in a local optimum solution (P), beginning from point C would produce a global optimum (Q).

Figure 2.5 : Example of multiple starting points (Altair University 2015)

Application to vehicle structures

The VDM/SIMP method, through its ease of implementation and its use in existing FEA software, make it a viable solution for optimisation in linear static vehicle design. However, the implementation of relative density makes it a questionable solution for non-linear optimisation. Equation (2.3) demonstrates that the relative density, which dictates the distribution of material, is applied to the Young's modulus of the material. For the optimisation of linear static structures this is not an issue, however for non-linear material behaviour, this could be a problem, as the stiffness depends on different parameters, such as strain rate, material hardening during deformation, etc. Additionally, the equilibrium equation to solve is no longer linear as in equation (2.1), therefore the gradient based methods which are generally coupled with the VDM/SIMP method become extremely expensive to compute (Altair Engineering 2011). As a result, the VDM/SIMP method does not seem to be a viable solution for taking into account crashworthiness targets, for which the responses are non-linear. However, an extension of the VDM/SIMP method currently used is the Equivalent Static Load Method (ESLM) (Chuang and Yang 2012, Christensen et al. 2013) which adapts the non-linear loading scenario into several linear static load cases. Essentially, static loads are extracted at constant intervals during the analysis (e.g. at every defined timestep). However, several difficulties have arisen from such a procedure. Firstly, using the ESLM requires the use of linear material in the FE model. Therefore, the behaviour of such a material would differ greatly from the original non-linear crash model (Chuang and Yang 2012). Furthermore, one aspect that isn't taken into account in the linear static model is that during an impact, the crash structures become stiffer as they deform (Chuang and Yang 2012). Having been applied to a BIW roof optimisation example by Christensen et al.

(2013), the author states that parameter issues made the choice of the ESLM questionable, added to the fact that the resulting topology showed little change compared to a linear static optimisation procedure. It is also stated that the ESLM is best used for small non-linear displacements only (as the approximation of linear static behaviour is acceptable in this case), which of course differs greatly from the crashworthiness requirements of this PhD project.

VDM/SIMP however could be applied to areas of the vehicle that need to exhibit linear elastic behaviour throughout an impact, like for instance the “passenger cell”, as previously defined in Figure 1.1. Table 2.1 summarises the advantages and disadvantages of the VDM/SIMP method:

Table 2.1 : Advantages / disadvantages of the VDM/SIMP method

Advantages	Disadvantages
Well developed, and thoroughly tested in industrial and academic contexts	Unsuitable for non-linear optimisation (use of linear responses and material behaviour)
Mathematical, gradient based approach: verified method for linear optimisation	ESLM method only suited to low levels of non-linearity

The aim of this PhD is to find an optimisation algorithm or methodology that is able to cater for both linear and non-linear behaviour. Therefore, there is a need to find an inexpensive, efficient way of solving TO problems where non-linearity is present. The next section will explore another group of algorithms, namely heuristic/meta-heuristic methods.

2.2. Heuristic and Meta-Heuristic methods

The previous section focused on mathematical based optimisation methods. Whilst they are “robust” methods, in this case robustness relating to the stability of the methods as opposed to the branch of “Robust Optimisation,” and have been implemented into FEA software, they have been shown to have shortcomings in terms of non-linear optimisation. Therefore, the following section will focus on a different type of algorithm more generally used for non-linear behaviour: heuristic and meta-heuristic. Heuristic methods are based directly on experimental outputs, from FEA for example, rather than using gradient based methods. The most developed of these, Bi-Directional Evolutionary Structural Optimisation (BESO) and Hybrid Cellular Automata (HCA) will be discussed. Meta-heuristic methods extend beyond heuristic methods and are often based on natural

phenomena, such as ant colonies, swarms, or metal annealing. The validity and possible uses for these methods will also be discussed.

2.2.1. BESO method

Before discussing the current status of BESO, it is important to review the previous approach used. Evolutionary Structural Optimisation (ESO) is a relatively new procedure, developed by Xie and Steven (1993). Its basis is removing inefficient material based on FEA results. The main difference between this method and the VDM/SIMP procedure is the nature of the design variables. As mentioned, the VDM/SIMP method requires a continuous design variable (the relative density *ρ(x))* to avoid numerical instabilities due to the modification of the stiffness tensor. However, in ESO, the discretised element itself is considered as the design variable, and therefore can be removed from the model without creating any instabilities in the stiffness matrix (Huang and Xie 2010). In essence then, it is a discrete variable, as an element can either exist or not in the FE model. The main advantage of such a formulation is the absence of intermediate densities, which results of course in well-defined, easy to interpret structures.

The first version of ESO removed elements from the structure on the basis of low levels of stress to obtain the most even distribution of stress levels as possible (Xie and Steven 1993, Huang and Xie 2010). Essentially, in a loaded linear elastic structure, low levels of stress suggest the material is inefficient. Using FEA, the ESO algorithm compares the Von Mises stress in each element with the maximum Von Mises stress in the structure and the elements are deleted when the value is below a specified rejection ratio as shown in equation (2.6)(Xie and Steven 1993):

$$\frac{\sigma_e^{VM}}{\sigma_{max}^{VM}} < RR_i \tag{2.6}$$

where σ_e^{VM} is the element Von Mises stress, σ_{max}^{VM} the maximum Von Mises level in the structure and RR_i the rejection ratio for the current iteration i. The operation of deleting elements continues until the structure reaches a “steady state” where no more elements can be deleted with the current rejection ratio. Therefore, to continue the optimisation process, the rejection ratio is updated using an evolutionary ratio (equation (2.7)):

$$RR_{i+1} = RR_i + ER \tag{2.7}$$

where ER is the user-defined evolutionary ratio. Then the process continues as in equation (2.6) until an acceptable stress distribution is obtained (e.g. no stress levels below 25% of the maximum Von Mises stress (Xie and Steven 1993)).

This initial method was extended to other optimisation objectives, such as stiffness or displacement optimisation (Nha Chu et al. 1997). The stiffness constraint variation of the ESO method can be directly compared to the VDM/SIMP method, as it also seeks to minimize the compliance of the structure. The compliance is described as the total strain energy in the structure (equation (2.8)):

$$\mathrm{C} = \frac{1}{2}\boldsymbol{f}^T\boldsymbol{u} \tag{2.8}$$

where $\boldsymbol{f}$ is the load vector and $\boldsymbol{u}$ the displacement vector. In terms of sensitivity numbers, which as previously discussed represent the efficiency of an element, these are defined by equation (2.9):

$$\alpha_i^e = \frac{1}{2}\boldsymbol{u}_i^T\boldsymbol{K}_i\boldsymbol{u}_i \tag{2.9}$$

where α_i^e is the sensitivity number of the ith element, $\boldsymbol{u}_i$ its displacement tensor and $\boldsymbol{K}_i$ its stiffness tensor. Interestingly, this definition represents the element strain energy. Therefore, by combining equations (2.8) and (2.9), it is clear that to minimize the compliance when removing material from the structure, the elements with the lowest sensitivity numbers should be deleted. This procedure is followed with an element removal ratio (ERR) until a prescribed compliance limit is reached (Huang and Xie 2010).

Much like the VDM/SIMP method, this initial evolutionary algorithm allows efficient structures to be defined, and its design allows a simple implementation alongside FEA. However, it also suffers from problems such as checkerboard patterns, mesh dependency and the possibility of converging towards local optimum solution, and not a “global” optimum. Another problem with the ESO method is linked to the process of finding the optimum structure. The algorithm deletes elements from the FE model to find the optimal layout for given boundary conditions (BC), but it is possible that deleting an element could have an undesired effect such as stress concentrations. Retrieving this material cannot be achieved using ESO, therefore an updated procedure was developed to counter this problem and the others previously mentioned BESO.

BESO operates on the same basis as ESO, and for compliance minimisation optimisation, the problem can be summarised by equation (2.10):

$$\begin{gathered}\text{Minimize C} = \frac{1}{2}\boldsymbol{f}^T\boldsymbol{u} \\ \text{Subject to}: V^* - \sum_{i=1}^{N} V_i x_i = 0 \\ x_i = 0 \; or \; 1\end{gathered} \tag{2.10}$$

where V^* is the target volume, V_i the element volume and x_i the state of the element (solid = 1 and void = 0). The measures taken to avoid the problems exhibited by ESO consist of modifying the element sensitivities defined by equation (2.9) which are directly extracted from the FEA results before using them in the element deletion/addition process.

Firstly, it is good practice to define the element sensitivities not by their strain energy, but rather their strain energy density (Huang and Xie 2010). This means that in the event of different sized elements in the FE model, each element is compared equally in the optimisation process (equation (2.11)):

$$\alpha_i^e = \frac{\frac{1}{2}\boldsymbol{u}_i^T\boldsymbol{K}_i\boldsymbol{u}_i}{V_i} \tag{2.11}$$

Once these sensitivities are obtained, a filter scheme not dissimilar to the one employed in the VDM/SIMP method is used to mitigate checkerboard patterns and mesh dependency (Huang and Xie 2010). Firstly, element sensitivities are extrapolated to the nodes constructing that particular element (equation (2.12)):

$$\alpha_j^n = \sum_{i=1}^{M} w_i \alpha_i^e \tag{2.12}$$

where α_j^n is the sensitivity of the jth node, *M* the number of elements connected to the node, α_i^e the elemental sensitivity number and w_i a weighting factor defined by equation (2.13):

$$w_i = \frac{1}{M-1}\left(1 - \frac{r_{ij}}{\sum_{i=1}^{M} r_{ij}}\right) \tag{2.13}$$

where r_{ij} is the distance between the centre of the i[th] element and the j[th] node. By observing equation (2.13), we can conclude that the closer a node is to the centre of an element, the larger its sensitivity. It is important to state that these nodal sensitivities do not have a physical meaning as such, they are just a step in the process of obtaining checkerboard free, mesh independent topologies (Huang and Xie 2010).

With the nodal sensitivities obtained, a filter scheme almost identical to the one discussed for the VDM/SIMP method is used. Instead of using the element sensitivities, the nodal sensitivities inside the filter zone are taken into account, as depicted by Figure 2.6 and described by equation (2.14):

$$\alpha_i = \frac{\sum_{j=1}^{K} w(r_{ij}) a_j^n}{\sum_{j=1}^{K} w(r_{ij})} \tag{2.14}$$

where α_i is the revised element sensitivity, a_j^n the nodal sensitivity and $w(r_{ij})$ the weight factor characterised by equation (2.15):

$$w(r_{ij}) = r_{min} - r_{ij} \tag{2.15}$$

where r_{min} is the filter radius defined by the user (Figure 2.6)

Figure 2.6 : Filter scheme for BESO (Huang and Xie 2010)

These procedures make BESO a more robust and reliable method compared to the original ESO method, and parallels can be drawn between this algorithm and the VDM/SIMP method. One remaining problem that has been raised is the convergence issue, especially when the structure nears the volume constraint (Huang and Xie 2007).

As shown in the cantilever beam example in Figure 2.7, once the structure reaches the target volume, drastic changes occur in the topology of the structure, resulting in the peaks of compliance. Naturally, this phenomenon is unstable and undesired.

Figure 2.7 : Evolution history of single load cantilever beam optimisation with instabilities Adapted from (Huang and Xie 2007)

The process undertaken to avoid this problem consists of considering the element sensitivity history before the removal/addition process demonstrated by equation (2.16):

$$\alpha_i = \frac{\alpha_i^k + \alpha_i^{k-1}}{2} \tag{2.16}$$

By averaging the current element sensitivity with the sensitivities of past iterations, surges in compliance can be avoided as illustrated by Figure 2.8:

Figure 2.8 : Evolution history of single load cantilever beam with sensitivity averaging (Huang and Xie 2007)

In equation (2.16), k is the current iteration number. This whole process, from equations (2.11)-(2.16) allows accurate sensitivities to be calculated, before the process of elimination/addition of elements can begin. This process is articulated around the volume of the structure for each iteration, defined by equation (2.17):

$$V_{k+1} = V_k + ER \tag{2.17}$$

where V_{k+1} is the volume for the next iteration, V_k the current structural volume and ER the user defined evolutionary ratio. Knowing the required volume for the next iteration, and the volumes of each element, the number of elements to be removed to satisfy the volume can be determined. When the element sensitivities are ranked in descending order, a threshold is defined as the sensitivity α_n, where n is the number of elements to satisfy equation (2.17). Existing elements with sensitivities below that are deemed inefficient and can therefore be removed from the structure. Previously deleted elements, or “void elements”, can be reintroduced into the structure if their sensitivity is above the threshold (Huang and Xie 2007). The user can define a maximum volume addition ratio $ARmax$ to avoid too many elements being added in a single iteration, which would slow down the optimisation procedure and the convergence of the topology.

A convergence criterion, in this instance the objective function error calculated between succeeding optimisation iterations, is introduced in the algorithm to determine of the completion of the optimisation procedure and is defined by equation (2.18):

$$error = \frac{\left|\sum_{i=1}^{N} C_{k-i+1} - \sum_{i=1}^{N} C_{k-N-i+1}\right|}{\sum_{i=1}^{N} C_{k-i+1}} \leq \tau \quad (2.18)$$

where C is the objective function, k the current iteration, τ a user defined tolerance and N an integer which defines how many successive iterations are analysed to determine the convergence of the model (Huang and Xie 2007).

According to the authors, BESO produces clearly defined (absence of checkerboard due to the use of filtering), mesh independent structures, and when compared to the VDM/SIMP procedure results in more efficient structures, although the VDM/SIMP examples used in Huang and Xie (2007) still possessed intermediate densities, whose stiffness was estimated. It is possible to assume though that BESO is a viable method for TO of linear structures.

The BESO algorithm has however been shown to fail in certain circumstances (Zhou and Rozvany 2001). The example that shows the method's shortcomings is shown in Figure 2.9, as well as the problem faced:

Figure 2.9 : Test example (a) initial design (b) ESO error after 1 iteration (c) optimum design (Zhou and Rozvany 2001)

In Figure 2.9, "C" corresponds to the overall mean compliance of the structure, and "V_f" the volume fraction. It is evident from this example that the BESO procedure breaks down right from the start, as it removes a key element in the BCs. Having removed only

one element from the structure (Figure 2.9(b)), the mean compliance is almost four times higher than the theoretical optimum that should be obtained (Figure 2.9(c)). The solution suggested and verified was to decrease the size of the mesh to avoid the occurrence, or to block the elements adjacent to defined BCs so that they may not be removed (Huang and Xie 2008a). However, increasing the mesh size obviously comes at the cost of increased computational time, and as argued in Rozvany (2009), for a given mesh size a load can be defined which would cause the same problem as before. Furthermore, Huang and Xie (2008a) had argued that BESO is mesh independent. This problem highlights the fact that perhaps this is not the case. This is not surprising, as BESO directly uses FEA results in the element sensitivity calculations. FEA is inherently mesh-dependent; therefore, it seems logical that BESO shares this characteristic, despite the mesh-independence filter that alleviates much of the problem. In terms of freezing BC elements, this is also argued to be an unviable solution, as it may be that some BCs offer no support to the structure and may be deleted.

The solution discussed in Liu et al. (2008) and Rozvany (2009) consists of inserting an intermediate density (Rozvany 2009) or intermediate thicknesses (Liu et al. 2008) instead of deleting the element. The procedure in Liu et al. (2008) introduces a genetic algorithm into the evolutionary procedure, which will be discussed later. Both these solutions would result in a high strain value in that particular element, provided it had been wrongly removed. Therefore, the user, and indeed the algorithm, is informed that the element is required in the structure.

Similarly to the VDM/SIMP method, BESO is well adapted to be combined with other algorithms to solve the local minima issues. One such example is the combination between BESO and Genetic Algorithms (GA) to form a Genetic Evolutionary Structural Optimisation (GESO) algorithm (Liu et al. 2008). Genetic Algorithms function on the basis of survival of the fittest, and this is implemented into the FE model. Each element possesses an “n” sized, one-dimensional array, with each value initially equal to 1. This array essentially represents the fitness of an element, and through a combination of sensitivity numbers and genetic procedures such as mutation, crossover and selection, the “bits” in the array are gradually turned from “1” to “0” if the element is deemed inefficient (Liu et al. 2008). Only when all the bits in the array are turned to 0 is the element permanently deleted. A verification method is applied to avoid the problem demonstrated by Figure 2.9, in which the thickness of any element with a single “0” value in its fitness array is reduced. Hence, in the next FEA, if the element has wrongfully been

deemed “unfit”, its sensitivity value increases significantly, and therefore it’s probability of being deleted decreases (Liu et al. 2008). A potential drawback of using this particular technique is its unsuitability for 3D structures. Obviously, there is no thickness to reduce when using 3D elements in FE. However, the aim of the technique employed in Liu et al. (2008) is to weaken the elements through thickness reduction. This can also be achieved by introducing an intermediate density, much like discussed in Rozvany (2009). Therefore, to enable implementation for both 2D and 3D elements, this technique could be explored further. In terms of its overall effectiveness however, GESO has been shown to avoid the deletion problem exhibited by the original BESO as well as improving the search for a global optimum (Liu et al. 2008), in a similar fashion to SA with VDM/SIMP (Garcia-Lopez et al. 2011).

Another facet of BESO that has been explored is the implementation of multiple materials in the optimisation process (Huang and Xie 2009). In modern day structural design, using different materials is an increasing method of obtaining lighter structures. Therefore, it seems logical to incorporate this into the optimisation procedure. The way this is achieved in Huang and Xie (2009) is by introducing the Young’s modulus into the element sensitivity numbers as follows (equation (2.19)):

$$\alpha_{ij} = \begin{cases} \frac{1}{2}\left[1 - \frac{E_{j+1}}{E_j}\right] u_i^T K_i^j u_i & for\ materials\ 1, \dots, j \\ 0 & for\ materials\ j+1, \dots, n \end{cases} \tag{2.19}$$

where n is the total number of materials considered, α_{ij} is the sensitivity number for materials j and j+1, and E_j/E_{j+1} their respective Young’s modulus. Similarly to the standard BESO procedure, the element strain energy is used as a measure of the element’s efficiency, the only difference being the factor including the Young’s moduli. These sensitivity numbers are used to determine whether an element is switched from j to j+1, with E_j>E_{j+1}. Therefore, there are a total of (n-1) sensitivity numbers per element. These initial sensitivity numbers are then modified using the standard BESO filtering scheme. The additional calculations may increase the computational resources required, however this method does provide a way to introduce predefined multiple materials into the structure (no material is simply considered as a material with a Young’s modulus of 0).

Application to vehicle structures

As previously discussed, BESO differs from VDM/SIMP as it considers the elements themselves as the design variables, as opposed to modifying the material parameters. Additionally, no gradient based method is used in calculating the element sensitivities; therefore, BESO already seems to have a potential use in crashworthiness optimisation. Relating this statement back to the vehicle structure presented in Figure 1.1, the sections that constitute the "front end" of the vehicle could be determined via this TO method. While not extensive, some research on non-linear optimisation using BESO has been undertaken (Huang and Xie 2008b). One advantage with BESO for non-linear applications is the use of elemental strain energy as the basis for sensitivity calculations, much like for linear optimisation although in this case it is the strain energy of the final deformed structure. In an eventual extension for crashworthiness, the strain energy throughout the whole impact duration would need to be taken into account. Furthermore, the same filtering schemes used to obtain clear topologies can be applied. It should be noted that in Huang and Xie (2008b), the weighting factor $w(r_{ij})$ used to avoid checkerboard patterns and mesh dependency slightly differ from equation (2.15), as illustrated by equation (2.20):

$$w(r_{ij}) = \frac{\exp\left(-\left(\frac{r_{ij}^2}{2\left(\frac{r}{3}\right)^2}\right)\right)}{2\pi\left(\frac{r}{3}\right)} \tag{2.20}$$

where r is the filter radius defined by the user (r_{min} in equation (2.15)). While the calculation of the weight factor may be different, its purpose remains the same, namely allowing the closest neighbours having the most influence on the sensitivity of each element. The objective for non-linear optimisation given in Huang and Xie (2008b) is maximising the total strain energy, or external work, within a given volume constraint to obtain the stiffest structure. However, the optimisation convergence has been shown to be problematic, due to the elastic unloading of the material. The latter would create an oscillation phenomenon in the optimisation process between two "equivalent" solutions. In the case of non-linear optimisation described in Huang and Xie (2008b), two equivalent solutions would be structures with the same total strain energy, but different layouts. Therefore, there would be no way for the algorithm to differentiate between the two solutions with regards to the objective, obstructing the convergence of the procedure. In theory, the oscillation problem could also occur in a linear static scenario. Consider

the problem represented in Figure 2.10, namely a beam with a horizontal load of F = 10kN applied at the end.

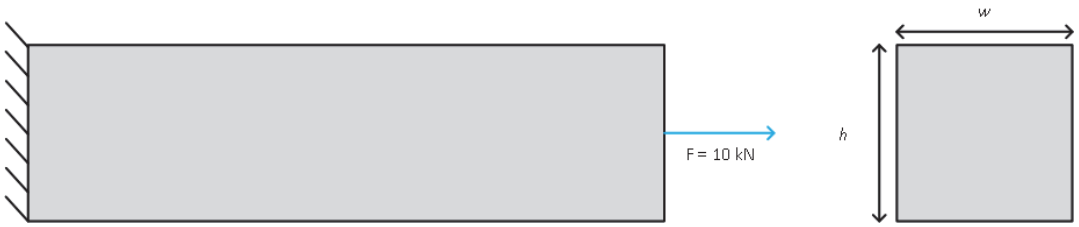

Figure 2.10 : Beam under tensile load optimisation example

The objective is to minimize the cross section subject to a maximum normal stress of σ = 50 MPa. In this instance, the design variables are the height of the cross section *h* and the width *w*. A further constraint is added to the problem, in that the maximum value for each design variable is 30 mm.

The minimum cross section capable of satisfying the stress constraint is equal to 200 mm^2. Assuming only integer dimensions are allowed, the problem yields the following four solutions:

- s1 : h = 8mm w = 25mm
- s2 : h = 10mm w = 20mm
- s3 : h = 20mm w = 10mm
- s4 : h = 25mm w = 8mm

This highlights the oscillation problem well. In terms of dimensions, these four solutions are all different, but in terms of the required performance, they are all identical. This simple example demonstrates the “uniqueness of global optimum” issue in optimisation problems, or in this case the lack thereof. Consequently, in the absence of termination criteria the optimisation procedure could potentially switch between these four solutions indefinitely, without converging. Obviously, convergence is an important aspect of any TO process, so this problem would need to be addressed. Much like the VDM/SIMP method, there may be an opportunity to use BESO in conjunction with a stochastic algorithm to improve the optimum search, and therefore the convergence of the structure. The extension of that to design energy absorbing structures for crashworthiness would be the addition of constraints such as the maximum crushing distance to protect the occupants from intrusion and the maximum crushing force to mitigate any injuries (Huang and Xie 2008b). The research done on BESO for energy absorption (Huang et al. 2007) focuses on maximising the energy per unit of volume (for

crash analysis where the FE model requires elements of the same size, this could easily be adapted as the maximum energy per element). The sensitivity numbers however differ from the original BESO method, as they take into account the volume as well as the energy as follows (equation (2.21)):

$$\alpha_n^j = \frac{V_j}{V} - \frac{E_n^j}{E} \tag{2.21}$$

where E_n^j is the total strain energy of the jth element, V_j its volume, V the total volume of the structure and E the total strain energy. Elements with a high positive sensitivity number should be eliminated from the structure (as it implies poor energy absorption per unit of volume) and the void elements with the lowest negative sensitivity number should be added (Huang et al. 2007). In order to reflect accurately the entire impact, and crushing distances, the overall sensitivity number for each element is calculated as the sum of equation (2.21) at each analysis iteration. While BESO does have its drawbacks when applied to non-linear optimisation, most notably the convergence issue, this algorithm as a whole does show potential in a possible use for non-linear optimisation. BESO can be summarised by the flowchart in Figure 2.11 (Christensen 2015):

Some materials have been removed due to 3rd party copyright. The unabridged version can be viewed in Lancester Library - Coventry University.

Figure 2.11 : BESO flowchart (Christensen 2015)

Finally, a method similar to BESO has been used for crashworthiness design (Forsberg and Nilsson 2006). Essentially, this method uses the distribution of the internal energy density as a measure to either remove elements from the structure, or reduce their thickness. The aim is to find a uniform distribution of energy throughout the structure,

and much like BESO the element strain energy determines the efficiency of that element. This procedure allows for multiple load cases, in which case the total internal energy density of an element is simply the sum for each load case. However, a problem raised

in Forsberg and Nilsson (2006) is that of the deletion of load paths caused by the premature deletion of elements from the structure. This is a reoccurrence of a BESO problem previously discussed (Zhou and Rozvany 2001).

The advantages and disadvantages of BESO are summarised in Table 2.2 below:

Table 2.2 : Advantages / Disadvantages of BESO

Advantages	Disadvantages
Directly uses FEA results: ease of implementation	Convergence issues (oscillations)
Uses information from previous optimisation iterations : smoother process	Unknown whether solution is local or global optimum
Suitable for non-linear optimisation	Issues with stability in certain load cases

2.2.2. BEETS Method

The previous section has analysed BESO, a well-developed heuristic TO algorithm. However, some drawbacks were also highlighted, the most important of which (concerning optimisation accuracy) are the convergence towards local optima and some issues with oscillations between solutions. An updated, BESO-based algorithm for non-linear TO has recently been developed: Bi-Directional Evolutionary Entropy Tabu search Simulated annealing, or BEETS (Christensen 2015). The name of the algorithm itself suggests a merge between several algorithms. The use of Tabu Search (TS), Simulated Annealing (SA) and Entropy are specifically used to avoid the shortcomings of BESO. These three additions will be detailed below, but overall statistical Entropy was used to estimate intermediate deformation levels, TS and SA were used to avoid oscillations between equal solutions and reduce the likelihood of converging towards a local optimum. These issues were identified as being the most critical to resolve to achieve a more valid non-linear optimisation algorithm. The actual element deletion/addition process will not need to be explained as it is based on BESO from Huang and Xie (2008b) explored in section 2.2.1.

The application of Entropy to take into account intermediate deformation levels is based on the Maximum Entropy Principle (MEP) (Penfield 2003). The overall principle, when applied to structural TO by Christensen (2015) is to use a probabilistic method to

determine which deformation state best represents the element in question for the sensitivity analysis. In essence, adding uncertainty to the calculation (by using probabilities) means the choice is unbiased.

Derived from (Penfield 2003), equations (2.22) and (2.23) are the main equations to understand the principles used (Christensen 2015):

$$ANSI_i = \frac{\sum_{t=\Delta tstart}^{\Delta tend}(E_i(t))}{N\Delta t} + \sum_{j=1}^{NNels}\left[\frac{\sum_{t=\Delta tstart}^{\Delta tend}(E_j(t))}{N\Delta t} * w_{ij}\right] \quad (2.22)$$

where $NNels$ is the number of neighbourhood elements, Δt the FEA timestep, $E_j(t)$the strain energy of element *j* at time *t* and $N\Delta t$ the total number of timesteps. w_{ij} is a similar weighting factor used in BESO in equation (2.20) (Christensen 2015). Therefore, one statement to make is that the BEETS method takes into account the neighbouring elements just like BESO, but in the same step as the MEP implementation. Also, the consideration of the timestep shows that the intermediate stages of deformation are taken into account. Following this average calculation, the probabilities are calculated using equations (2.23) - (2.25):

$$f(\beta) = \sum_{t=\Delta tstart}^{\Delta tend}\left[(ESE_i(t) - ANS_i * 2^{-\beta(ESE_i(t) - ANS_i}\right] \quad (2.23)$$

where $ESE_i(t)$ is the strain energy of element *i* at time *t* and β a Lagrange multiplier. Solving $f(\beta) = 0$ (where the entropy, or uncertainty level, is highest (Penfield 2003), β can be determined. From this, another Lagrange multiplier α can be calculated:

$$\alpha = log_2\left[\sum_{t=\Delta tstart}^{\Delta tend} 2^{-\beta E_i(t)}\right] \quad (2.24)$$

and the probability is calculated by using the two Lagrange multipliers as follows:

$$p\big(E_i(t)\big) = 2^{-\alpha}2^{-\beta E_i(t)} \quad (2.25)$$

The highest probability is then chosen as the state that best reflects the strain energy levels in the element. The implementation of TS and SA will now be analysed. As previously discussed, the two additional methods serve to widen the search area (avoiding convergence to a local optimum) and also avoid oscillations when the algorithm

attempts to converge. However, as mentioned by Christensen (2015), TS is better suited at avoiding the latter, while SA would help with the former.

TS is implemented in the “construct new design” section of BESO (step 5 in Figure 2.11), where equation (2.17) is applied (Christensen 2015). The TS principles originate from Bianchi et al. (2009). Three principles are used, and linked together to widen the search space. Firstly, for a given TO result, neighbouring solutions are created, and the neighbouring solution that best validates the objective function is chosen as the current solution, even if the original solution is deemed to be “better”. This clearly expands the search space, however if the next optimisation iteration is considered, the original solution (which is now a neighbouring solution) could again be chosen as a current solution. The previous statement is a further example of the oscillation problem highlighted in the previous section, and therein lies the second TS principle: tabu lists. Once a solution has been chosen, it is added to the "tabu list", and therefore cannot be chosen again further down the optimisation process. Finally, to avoid solutions that have not been explored from being ignored, an "aspiration criteria" is introduced, which requires a new solution to be better than the best solution found up until that point.

With regards to the implementation within BEETS, TS creates neighbouring solutions by changing non-void element statuses (Christensen 2015). The number of elements to be selected is decided as a fraction of the total number of non-void elements (the fraction is a user-input value), while the selection of which elements to change is merely decided by a random number generator. The ranking of each solution is conducted by comparing the ratio of volume to strain energy of the changed elements for each solution. In terms of storing the solutions chosen in the tabu lists previously discussed, only a certain amount of information can be stored per solution, and the elements are selected randomly. In theory, TS has the ability to avoid oscillation between solutions, improving on the convergence of the optimisation process.

However, to widen the search area, another principle must be employed. In the same optimisation step ("constructing a new design"), SA is employed, but only a certain aspect of it, namely the "cooling function" (Christensen 2015), which is as follows (equation (2.26)):

$$T(t) = \alpha^{j} T_o \qquad |0 < \alpha < 1| \tag{2.26}$$

where *j* is the number of "steps" (or iterations) since the start of the algorithm. This cooling function, in the context of BEETS, is applied to ER defined in equation (2.17).

The role of the function is to reduce the number of elements removed/added per iteration as the structure converges towards an optimum solution. However, as discussed in Christensen (2015), reducing the ER from the beginning of the optimisation process would have a detrimental effect on the TS implementation. Therefore, it is only applied in the process when the actual volume is within a certain interval of the target volume, as per equation (2.27):

$$TV_{j+1} \leq V_{end} * (1 \pm COOLIT) \leq TV_{j+1} \tag{2.27}$$

where $COOLIT$ is a user-defined fraction, TV_{j+1} the target volume for the next optimisation iteration and V_{end} the final volume target. When the conditions for equation (2.27) are verified, ER is gradually reduced by a user defined scale factor (Christensen 2015):

$$ER_{cool} = ER_{cool} - ER_{cool} * SF_{cool} \tag{2.28}$$

where SF_{cool} is the scale factor.

The implementation of the three methods discussed in this section leads to the overall BEETS flowchart in Figure 2.12, adapted from Christensen (2015) to include the equation numbers from this chapter.

Some materials have been removed due to 3rd party copyright. The unabridged version can be viewed in Lancester Library - Coventry University.

Figure 2.12 : BEETS method flowchart, adapted from (Christensen 2015)

A series of case studies comparing BEETS to BESO and VDM/SIMP were conducted to review how the attempts of avoiding BESO's drawbacks performed (Christensen 2015). On the three important issues previously discussed, the BEETS algorithm globally seemed to have considerably reduced them. The oscillation reduction between equal solutions and the widening of the search space were achieved, and avoiding convergence towards local optimum was verified as in some cases the BEETS method offered different solutions in structures. In terms of utilising intermediate deformation

states in the sensitivity calculation, implementation of MEP achieved that, however the feasibility of the solutions were questioned (Christensen 2015). Given the role of TO to offer design ideas, manufacturability is obviously a point that has to be addressed in the future. The algorithm is also still in its infancy, and therefore a wider number of case studies need to be implemented to correct several "teething issues". Furthermore, the version of the software studied only catered for 2D elements in a single (no out of plane 2D elements or 3D elements can currently be used), which has obvious effects on the algorithm's versatility at present (Christensen 2015). However, BEETS has shown good potential in avoiding several drawbacks from BESO, and can therefore be considered as a candidate in non-linear TO for the hybrid methodology developed throughout this thesis. A further advantage of the BEETS method is its modular nature to the user's needs: essentially, the user, stripping BEETS down to a BESO algorithm, can switch off the TS, SA and MEP “add-ons”. The advantages and disadvantages of the BEETS method are summarised in Table 2.3:

Table 2.3 : Advantages / disadvantages of the BEETS method

Advantages	Disadvantages
BESO-based for element deletion process: same advantages of implementation/usability with FEA results	Relatively untested method in its infancy compared to VDM/SIMP and BESO
Suitable for non-linear optimisation	Currently only caters for 2D elements
Implementation of TS and SA allowed for oscillation reduction and widening of search space	MEP implementation produced unfeasible results
MEP allowed to cater for intermediate deformation stages	

2.2.3. Hybrid Cellular Automata (HCA) method

HCA was first developed in 2004 (Tovar 2004), and is based on bone structures and the biology behind its growth. The overall procedure is to consider the layout of cells, which in FEA can easily be interpreted as elements. Each state of a cell is considered, but also that of its neighbours, where fixed rules determine their influence on the cell’s state. From this initial definition, a comparison can be drawn with BESO, which also uses the influence of neighbouring elements to determine the sensitivities of each element. The use of HCA for crashworthiness design has been studied (Patel 2007), and has also been implemented into LS-DYNA’s optimisation software, LS-TaSC (Roux 2011, Livermore Software Technology Corporation 2013). Similarly to BESO, energy FEA results are used in the optimisation procedure, although in this case the method seeks

to obtain a uniform strain energy distribution in the structure, subject to a mass constraint (Roux 2011). The optimisation problem can be summarised as follows (equation (2.29)):

$$\min_{x} \sum_{i=1}^{N} \sum_{j=1}^{L} \left(w_j U_j(x_i) - U_j^* \right)$$
$$subject\ to: \sum_{I=1}^{N} \rho(x_i)\, V_i \leq M^* \tag{2.29}$$

where N is the total number of cells or in this case finite elements, L the total number of load steps in the FE analysis, w_j a weighting factor, $U_j(x_i)$ the internal energy density of the ith element, V_i its volume, M^* the mass constraint, $\rho(x_i)$ the relative density of the element and U_j^* the internal energy density set point. What is interesting about this formulation is the use of a continuous relative density $\rho(x_i)$ much like VDM/SIMP. Therefore, power laws are used on the material properties in the same manner (Livermore Software Technology Corporation 2013). The change in the design variable is computed as follows (Roux 2011) (equation (2.30)):

$$\Delta x_i^t = \frac{K\left(U_i^t - U^*\right)}{U^*}$$
$$x_i^t = x_i^{t+1} + \Delta x_i^t \tag{2.30}$$

where K is a scaling factor. The implementation of this method into LS-TaSC has some advantages, most notably direct communication it has with FEA results through LS-DYNA. Furthermore, it is possible within LS-TaSC to define several constraints which are critical to obtain structures that can be easily reproduced or manufactured, such as extrusion and casting directions (Roux 2011). This is an obvious advantage in the automotive industry where parts must be easily manufacturable. However, from equations (2.22) and (2.23) and the definition of HCA (Tovar 2004), there is a notable deficiency, that of using sensitivity history in each optimisation iteration. Whereas BESO uses equation (2.16) to account for previous element statuses and sensitivities, this is absent in HCA. As equation (2.16) was used to aid the optimisation procedure convergence, it is possible that for complex loading scenarios (of which vehicle impacts are certainly part of) the HCA has issues with converging towards a global optimum. Table 2.4 below summarises the advantages and disadvantages of the HCA method employed by LS-TaSC:

Table 2.4 : Advantages / disadvantages of the HCA method

Advantages	Disadvantages
Implementation into LS-TaSC software (FEA)	Previous iterations not considered in optimisation process
Influence of neighbouring elements (should avoid checkerboard effect)	Issues with converging towards global optimum with complex load cases
Suitable for non-linear optimisation	Intermediate deformation stages are not taken into account (only final deformed state)

2.3. Conclusions and gaps

Several key findings can be drawn from the literature review. The existing methods in TO are clearly limited in their possible uses for non-linear TO. While the VDM/SIMP approach is a well-developed, and widely accepted, method for linear static optimisation, it has shortcomings when applied to highly non-linear FEA scenarios (the assumption of linear material behaviour is inaccurate in highly non-linear cases such as vehicle impacts).

The study into heuristic methods showed that BESO was a good basis for non-linear optimisation, due to its ease of implementation within FEA, filtering methods to reduce the checkerboard effects and mesh dependency, and its potential for use with multiple materials. However, several drawbacks called into question the validity of the solutions, such as the possibility of converging towards local optima and the oscillation issues when the solution is close to converging. An updated, BESO-based methodology was then presented, the BEETS method, which attempts to alleviate the aforementioned issues, using a combination of statistical entropy, SA and TS methods. This new methodology, while still in its infancy, was according to (Christensen 2015) globally successful in correcting issues displayed by BESO.

The comparison between the algorithms has highlighted an important aspect of this PhD: the choice of the algorithm(s). Each algorithm presented has underlined several issues, particularly when addressing non-linear optimisation. The complexity of the BIW structure also highlights that different sections must meet different criteria, and potentially behave in different ways to validate the latter. Currently, there is no algorithm available that simultaneously caters for the possible different behaviour (linear and non-linear) of each BIW section.

The overall aim of this PhD is therefore to develop a hybrid TO methodology which determines the optimum structure catering for both linear and non-linear component behaviour within a single system.

In order to achieve this aim, the following research objectives were identified:

- Explore the current commercially available TO algorithms and evaluate their capabilities of catering for coupled linear/non-linear component behaviour within the optimisation process.
- Assess the existing algorithms to make an informed decision on the selection of the best choices to make for the novel hybrid methodology.
- Define “hybrid optimisation parameters” which govern the novel optimisation process, and create a simple case study to determine their influence on the optimised structures obtained.
- Verify the validity of the hybrid optimisation tool developed using an industry relevant case study.

It should be highlighted at this stage that only isotropic material will be considered throughout this PhD. From a theoretical aspect, and the literature analysis undertaken on each algorithm, it emerges that perhaps by combining algorithms to cater for both linear and non-linear optimisation, a more efficient structure is created. However, the choice of algorithm is critical in this aspect. Therefore, a practical FEA study of current commercially available software is presented in the next chapter to further compare the algorithms, and also appreciate the processes from a feasibility point of view. Throughout this thesis, “feasibility” will relate to the manufacturability of the final topologies obtained.

3. Investigation into commercially available topology optimisation algorithms

The previous chapter established the need for an optimisation algorithm capable of simultaneously catering for coupled linear/non-linear behaviour exhibited by a vehicle structure in certain scenarios, for example vehicle impacts. It was also stated that current optimisation algorithms are well developed and in some cases implemented into finite element (FE) software. Therefore, this PhD focuses on combining these current algorithms to develop a methodology that caters for coupled linear/non-linear behaviour. The literature review has focused on the advantages and disadvantages of each main topology optimisation (TO) algorithm, and this chapter will extend these findings by using a simple but representative FE example to demonstrate further aspects of each algorithm, and use the data obtained to make a more informed decision on the appropriate algorithm(s) to use going forward. The basis for this study is a 2D plate impact scenario (Figure 3.1):

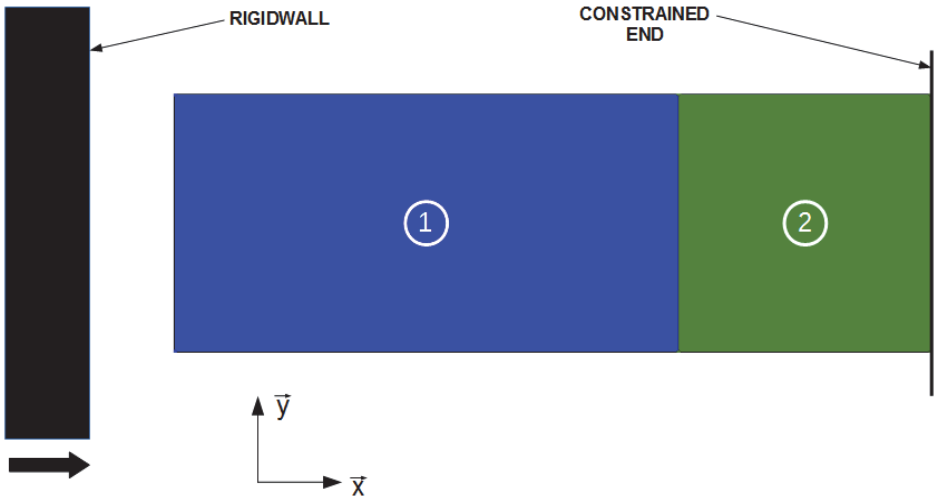

Figure 3.1 : 2D plate base model

The model contains 1200 quad elements 10mm in size, for a total model, and subsequently design volume size, of 600mm in the x-axis and 200mm in the y-axis, with a thickness of 1mm applied. The plate is split into two sections, section (1) being 400mm in length in the x-axis and section (2) 200mm in length in the x-axis (Figure 3.1). This allows the sections to be defined using different material behaviour, i.e. linear and non-linear. Essentially, this example is a simplified representation of a vehicle side view, and

the two sections previously defined in the literature review, the “front end” by section (1) and the “passenger cell” by section (2). The model is fully constrained along the right hand edge, and the loading in this case a rigid wall impact, is applied on the left hand edge. Depending on the optimisation algorithms used, the FEA modelling is conducted in either Altair Hypermesh or LS-DYNA. For the Hypermesh models, 1st order elements are used, as bending modes are not expected for the linear loadcases, reducing the need for 2nd order elements and the increase of CPU time. As for the LS-DYNA model, type 16 fully integrated elements are used. Essentially, these elements avoid the phenomenon of “hourglassing” modes of deformation, i.e. zero-energy deformation modes. These are especially common when point loads are applied in the FE model. Although hourglassing modes are avoided, using type 8 hourglassing control is recommended, as it adds warping stiffness to type 16 elements. A default value for the hourglass coefficient of 0.1 is used, as values of above 0.15 can lead to unstable simulations (Livermore Software Technology Corporation 2016a). These element types are used throughout this chapter, but also for case study 1 in Chapter 5, which is based off the present loading scenario and models. Throughout this study, several key parameters will be modified to monitor their influence as follows:

- *Algorithm*: The main aim of this study is to compare currently used, commercially available algorithms. The algorithms monitored during this study are LS-TaSC which is based on Hybrid Cellular Automata (HCA), Optistruct which uses the Variable Density Method / Solid Isotropic Material with Penalisation (VDM/SIMP), the Equivalent Static Load Method (ESLM) and two evolutionary based algorithms, Bi-directional Evolutionary Structural Optimisation (BESO) and Bi-directional Evolutionary Entropy Tabu search Simulated annealing (BEETS).
- *Material*: As mentioned in the previous chapter, only isotropic materials will be considered. However, the materials used within a vehicle body structure can vary not only in type (steel, aluminium, magnesium, etc.) but also in grade. For example, different grades of steel are used depending on their characteristics. Some sections of the vehicle, such as the B-pillar, which require high strength, will have different material characteristics to sections of the vehicle that require high energy absorption, such as the front end rails (Malen 2011). Crucially, the non-linear characteristics are impacted by the difference in material grade, and by extension could have an impact on the non-linear optimisation process. Two grades of steel will be applied to the model: Mild steel and High Strength steel

(HSS). The material properties are taken from Christensen (2015) and are summarised in Table 3.1 below:

Table 3.1 : Mild steel and High Strength steel material properties (Christensen 2015)

Material type	Young's Modulus (MPa)	Yield Strength (MPa)	Hardening parameter	Hardening exponent
Mild steel	210	276	0.017	0.51
High Strength steel	210	430	0.076	0.643

- *Loading*: Another parameter of interest is the magnitude of the loading, and by extension, the levels of non-linearity exhibited by the 2D plate in response. This is modelled differently depending on a dynamic or static scenario. Dynamic loading, as opposed to static loading, is time dependent and takes into account inertia/acceleration effects, which in the context of vehicle safety structures is important to consider. The dynamic impact scenario is represented by a rigidwall impact in LS-DYNA. The rigid wall is given a mass of 100 kg, an order of magnitude approximately 10 times less than a vehicle to reflect the relatively small size of the plate. Two impact scenarios are considered, a low velocity impact (velocity of 2.2 m/s) and a high velocity impact (velocity of 5.5 m/s). For the static scenarios, loads are applied to the plate's left hand edge nodes. These forces are representative of the impact force generated by the rigid wall by using the peak force output from the initial LS-DYNA analysis. The ESLM is however based on dynamic loading (which is converted to static load cases for optimisation) therefore a time dependent, load scale factor curve is applied to the point loads (Figure 3.2), the curve representing an estimation of the peak impact duration observed in LS-DYNA (Figure 3.3). The loading parameters are summarised in Table 3.2

Table 3.2 : Loading parameters

Load type	High Velocity	Low Velocity
Dynamic (m/s)	5.5	2.2
Static (kN)	90.1	76.7

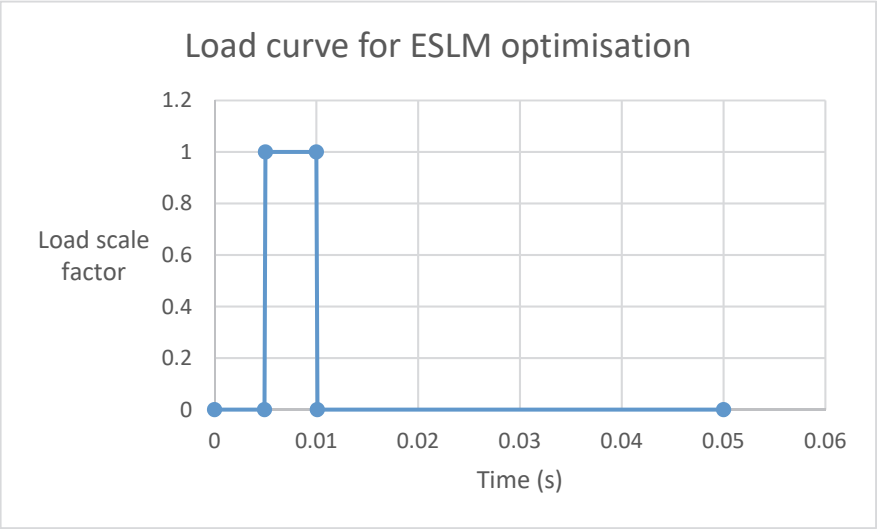

Figure 3.2 : Load curve for ESLM optimisation

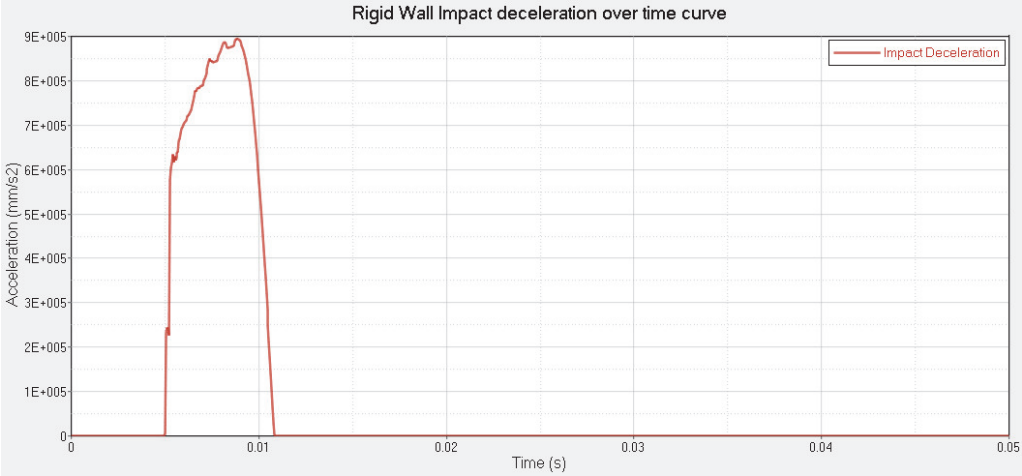

Figure 3.3 : Acceleration curve from dynamic impact scenario

- *2D plate sections*: As previously mentioned, the two sections (1) and (2) (Figure 3.1) represent the vehicle sections defined in the literature review, i.e. the “front end” and the “passenger cell”. The variable in this case is the material behaviour applied, either purely elastic behaviour, or elastic-plastic, therefore taking into account the non-linear behaviour of the material.

- *Constraints*: Figure 3.1 shows that the 2D plate is constrained along its right hand edge and there are two possible ways to define the constraint as discussed in the previous chapter, namely using the Inertia Relief (IR) method or Single Point Constraints (SPCs). IR effectively removes the constraints and uses internal accelerations to reach static equilibrium, thus representing inertia in scenarios where the latter is key, such as impacts. In order to represent the inertia of the 2D plate, if it were to represent a Body-in-White (BIW) impact scenario, point masses are added to the right hand edge nodes. Three different configurations will be studied: a single mass in the centre of the edge (Figure 3.4(a)), point masses along the whole edge (Figure 3.4(b)) and point masses that represent the remaining constraints in the SPC optimised model (Figure 3.4(c)).

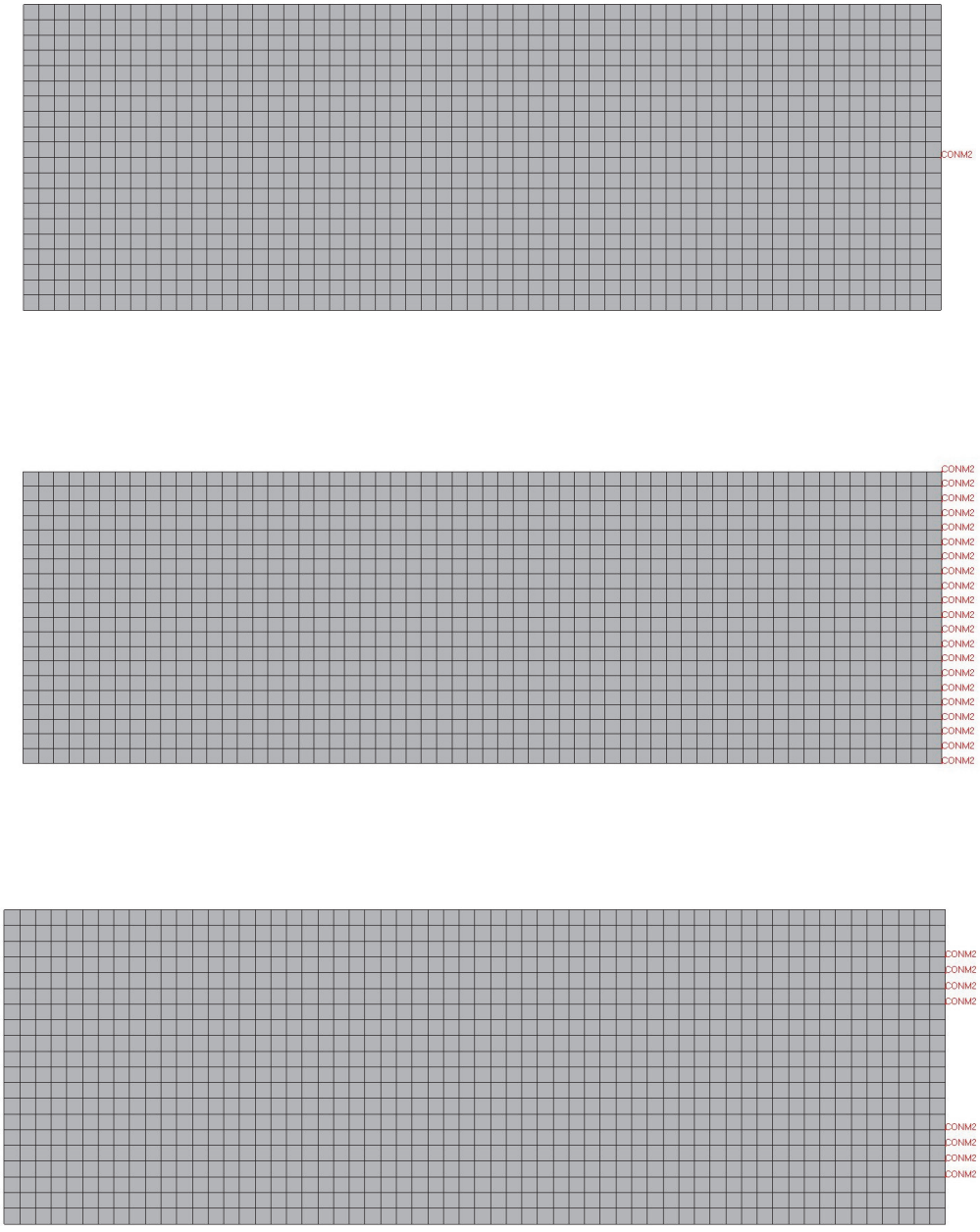

Figure 3.4 : IR models setup (a) Model 21 (b) Model 22 (c) Model 23

The following table summarises all the models for the subsequent studies, and the parameters discussed above (Table 3.3):

Table 3.3 : Case studies summary

Model Number	Optimisation Algorithm	Plate section definition		Static/Dynamic analysis (Table 3.2)	Plate material (Table 3.1)	Loading magnitude (High/Low)	Constraints
		Section 1	Section 2				
1	Optistruct	L	L	Static	Mild Steel	Low Velocity	SPC
2	Optistruct	L	L	Static	Mild Steel	High Velocity	SPC
3	LS-TaSC	L	L	Dynamic	Mild Steel	Low Velocity	SPC
4	LS-TaSC	L	L	Dynamic	Mild Steel	High Velocity	SPC
5	ESLM	NL	NL	Dynamic	HSS	High Velocity	SPC
6	ESLM	NL	NL	Dynamic	Mild Steel	High Velocity	SPC
7	ESLM	NL	NL	Dynamic	HSS	Low Velocity	SPC
8	ESLM	NL	NL	Dynamic	Mild Steel	Low Velocity	SPC
9	LS-TaSC	NL	NL	Dynamic	HSS	High Velocity	SPC
10	LS-TaSC	NL	NL	Dynamic	Mild Steel	High Velocity	SPC
11	LS-TaSC	NL	NL	Dynamic	HSS	Low Velocity	SPC
12	LS-TaSC	NL	NL	Dynamic	Mild Steel	Low Velocity	SPC
13	ESLM	NL	L	Dynamic	HSS	High Velocity	SPC
14	ESLM	NL	L	Dynamic	Mild Steel	High Velocity	SPC
15	ESLM	NL	L	Dynamic	HSS	Low Velocity	SPC
16	ESLM	NL	L	Dynamic	Mild Steel	Low Velocity	SPC
17	LS-TaSC	NL	L	Dynamic	HSS	High Velocity	SPC
18	LS-TaSC	NL	L	Dynamic	Mild Steel	High Velocity	SPC
19	LS-TaSC	NL	L	Dynamic	HSS	Low Velocity	SPC
20	LS-TaSC	NL	L	Dynamic	Mild Steel	Low Velocity	SPC
21	Optistruct	L	L	Static	Mild Steel	Low Velocity	IR
22	Optistruct	L	L	Static	Mild Steel	Low Velocity	IR
23	Optistruct	L	L	Static	Mild Steel	Low Velocity	IR
24	BESO	NL	NL	Dynamic	Mild Steel	Low Velocity	SPC
25	BESO	NL	NL	Dynamic	Mild Steel	Low Velocity	SPC
26	BESO	NL	NL	Dynamic	Mild Steel	Low Velocity	SPC
27	BESO	NL	NL	Dynamic	HSS	Low Velocity	SPC
28	BESO	NL	NL	Dynamic	Mild Steel	High Velocity	SPC
29	BESO	NL	NL	Dynamic	HSS	High Velocity	SPC
30	BEETS	NL	NL	Dynamic	Mild Steel	Low Velocity	SPC
31	BEETS	NL	NL	Dynamic	HSS	Low Velocity	SPC
32	BEETS	NL	NL	Dynamic	Mild Steel	High Velocity	SPC
33	BEETS	NL	NL	Dynamic	HSS	High Velocity	SPC
34	BESO	NL	L	Dynamic	Mild Steel	Low Velocity	SPC
35	BESO	NL	L	Dynamic	Mild Steel	Low Velocity	SPC
36	BESO	NL	L	Dynamic	Mild Steel	Low Velocity	SPC
37	BESO	NL	L	Dynamic	HSS	Low Velocity	SPC
38	BESO	NL	L	Dynamic	Mild Steel	High Velocity	SPC
39	BESO	NL	L	Dynamic	HSS	High Velocity	SPC
40	BEETS	NL	L	Dynamic	Mild Steel	Low Velocity	SPC
41	BEETS	NL	L	Dynamic	HSS	Low Velocity	SPC
42	BEETS	NL	L	Dynamic	Mild Steel	High Velocity	SPC
43	BEETS	NL	L	Dynamic	HSS	High Velocity	SPC

Table 3.4 summarises the differences between models 24-26 and models 34-36, which use the same FE model but with different filter radii for BESO. As discussed in the previous chapter, the filter radius captures the state of neighbouring element state when calculating a given element's sensitivity. The closer a neighbouring element, the more influence it will have in the element sensitivity calculation. The models from Table 3.4 will therefore give an overview of the filter radius's influence on BESO optimisation when a dynamic load is applied.

Table 3.4 : Filter radii used for models 24-26 and 34-36

Model Number	Optimisation Algorithm	Plate section definition		Radius
		Section 1	Section 2	
24	BESO	NL	NL	0
25	BESO	NL	NL	10.1
26	BESO	NL	NL	30.1
34	BESO	NL	L	0
35	BESO	NL	L	10.1
36	BESO	NL	L	30.1

The models will be analysed in three separate sections relating to how each section of the plate is defined (linear or non-linear behaviour). The results will be analysed and compared using the following criteria:

- ***Topology trends:*** Trends material distribution between each model will be compared from a global perspective but also at the interface between the two sections (1) and (2) defined in Figure 3.1.
- ***Feasibility of topology results:*** Throughout this PhD, the feasibility of a structure will refer to its manufacturability. Important aspects to look out for are for example the existence of intermediate densities or thicknesses, which from a manufacturing standpoint is not a satisfactory solution. This assessment criteria will also consider the existence of checkerboard patterns within the final "optimum" solution. Examples of viable manufacturing methods for the 2D plate example considered in this study include laser cutting and 3D printing, or indeed any manufacturing process where the material can be "cut out" of the original 2D plate design volume with no thin members (essentially solid/void designs as described in chapter 2).
- ***Linear/Non-linear compatibility:*** The algorithms will be judged where possible on their ability to cater for non-linearity in the model, and especially the high levels that can occur in impact scenarios such as this load case. This involves for example looking at the stress levels within the optimised structure and whether these are below the Yield stress if the plate section is defined using linear material behaviour.
- ***Other findings***

As stated in the previous chapter, the aim of this PhD is to develop a hybrid TO methodology which can cater for coupled linear and non-linear behaviour within the

structure. This chapter's study will therefore establish the suitability (or lack thereof) of each algorithm to achieve this aim, and allow the author to make a decision on which algorithm(s) to select for the subsequent methodology development.

3.1. Linear model

The first study will analyse the results from the optimisation procedure, when the 2D plate is defined as purely linear, i.e. linear material models are applied to both sections (1) and (2) from Figure 3.1. Table 3.5 recaps from Table 3.3 which models are part of the study:

Table 3.5 : Models for linear study

Model Number	Optimisation Algorithm	Plate section definition		Static/Dynamic analysis	Plate material	Loading magnitude (High/Low)	Constraints
		Section 1	Section 2				
1	Optistruct	L	L	Static	Mild Steel	Low Velocity	SPC
2	Optistruct	L	L	Static	Mild Steel	High Velocity	SPC
3	LS-TaSC	L	L	Dynamic	Mild Steel	Low Velocity	SPC
4	LS-TaSC	L	L	Dynamic	Mild Steel	High Velocity	SPC
21	Optistruct	L	L	Static	Mild Steel	Low Velocity	IR (Single)
22	Optistruct	L	L	Static	Mild Steel	Low Velocity	IR (Edge)
23	Optistruct	L	L	Static	Mild Steel	Low Velocity	IR (SPC)

For this study, Optistruct (VDM/SIMP) and LS-TaSC (HCA) are analysed. Table 3.5 shows that both section 1 and 2 (Figure 3.1) are defined as linear, i.e. linear material definition. Therefore, for these studies, the models use only a single design volume.

3.1.1. Optistruct - SPC

From the base model (Figure 3.1), the FE model in Figure 3.5 can be set up through Hypermesh with the appropriate parameters from Table 3.5:

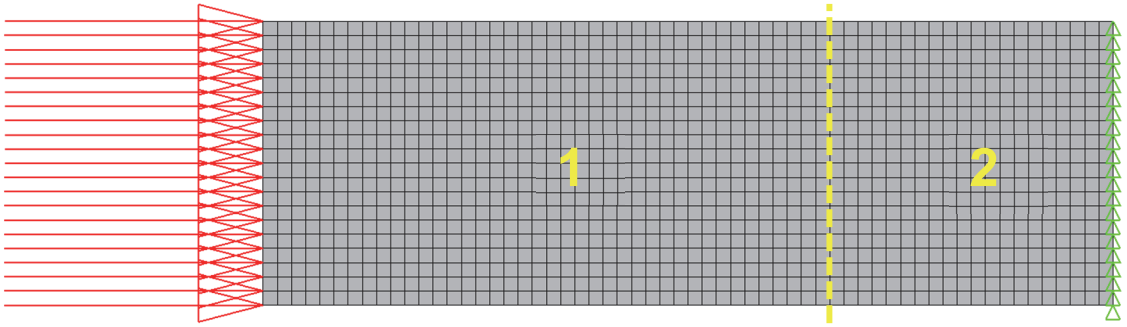

Figure 3.5 : Basic Optistruct setup

The static forces are representative of the impact loading as described in the introduction, one distributed load of 76.7 kN and 90.1 kN for the low velocity and high velocity scenarios respectively. The loads are applied to the left hand edge of the plate, for a force of 3.65 kN and 4.29 kN per node. Figure 3.5 also illustrates the "border" between sections (1) and (2) (Figure 3.1), but it should be reminded that only a single design volume is defined as both sections use the same material and geometry properties.

For this initial study, SPCs are applied to the right hand edge of the model and all degrees of freedom (DOFs) are constrained (translational and rotational DOFs in x, y and z direction). The objective of the optimisation procedure is to minimise the compliance subject to a volume fraction constraint of 50%. The penalisation factor described by equation (2.3) in the literature review was kept at the default value of 1, as the problem was deemed simple enough to obtain "clearly defined" topologies, i.e. absence of significant checkerboarding. The optimisation parameters are summarised in Table 3.6:

Table 3.6 : Optistruct optimisation parameters

Objective function	Constraint	Penalisation factor
Minimise compliance	Volume fraction = 50%	1

Results

Figure 3.6 and Figure 3.7 show the optimum topology obtained for model 1 and model 2 respectively, i.e. identical models but different loading magnitudes as per Table 3.2, specifically the element density distribution:

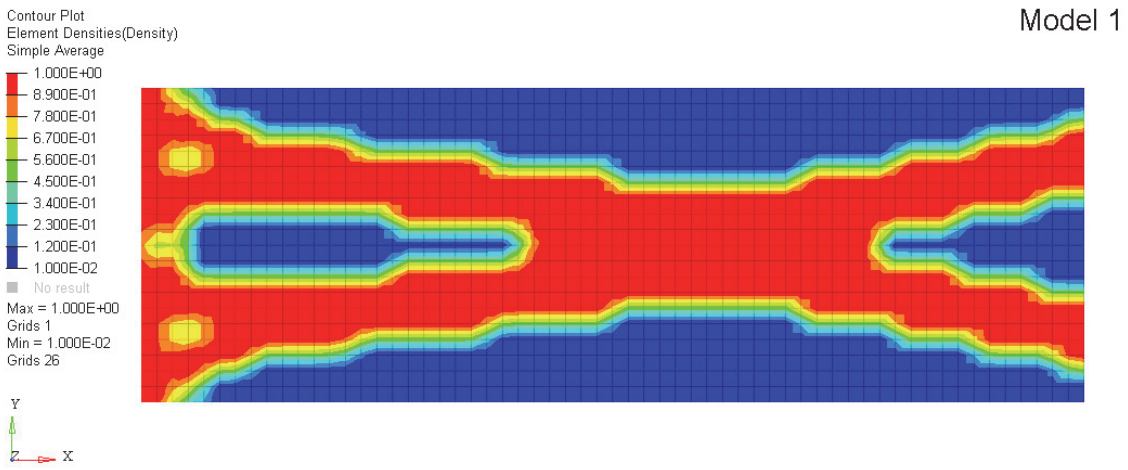

Figure 3.6 : Model 1 density distribution (with simple averaging filter applied)

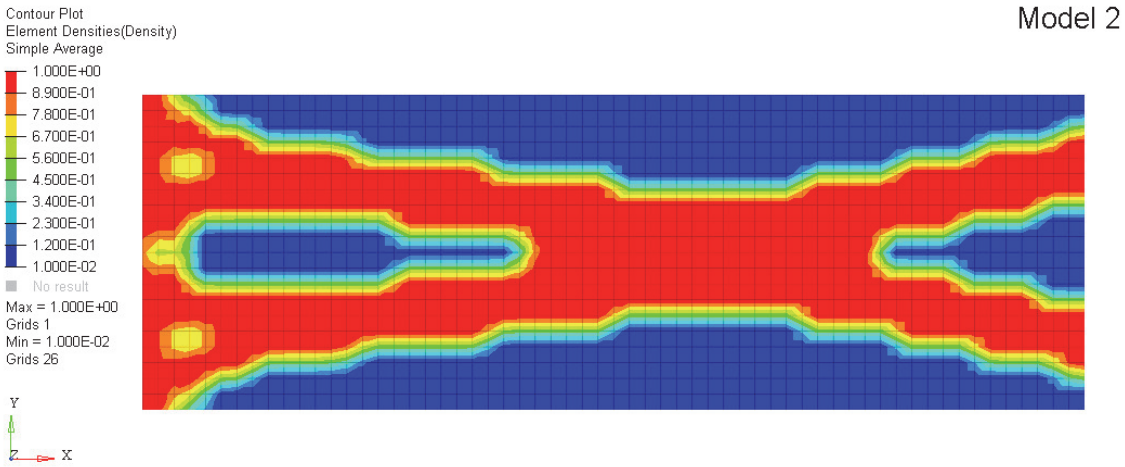

Figure 3.7 : Model 2 density distribution (with simple averaging filter applied)

Topology trends: The results show a clear load path through the model, and evidence of triangular patterns which is logical as they are the stiffest geometry in linear static load cases (Christensen and Bastien 2015).

Feasibility trends: Figure 3.8 shows the density distribution for model 2 without a post-processing averaging method applied, i.e. no “smoothing” of the density plot.

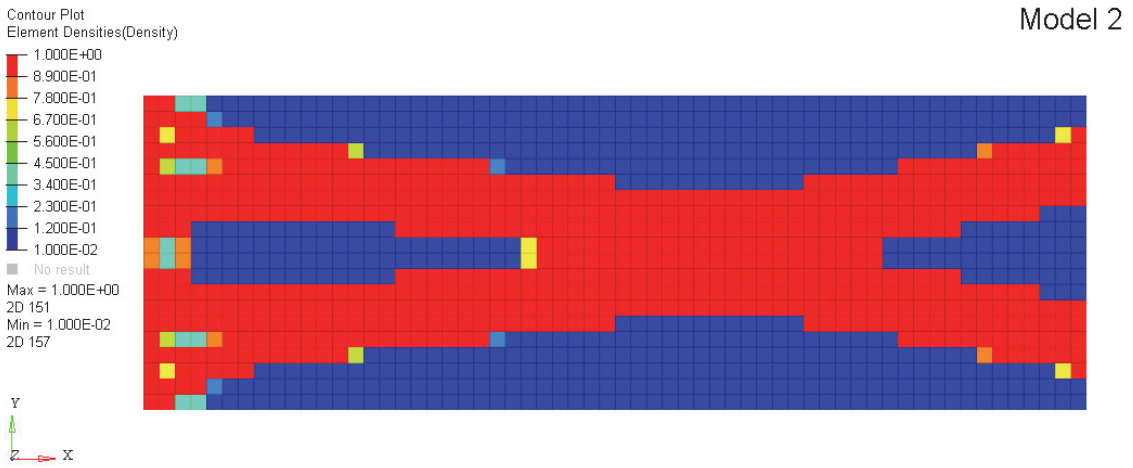

Figure 3.8 : Model 2 unfiltered density distribution

With no filter applied, the density of each individual element is displayed which in essence illustrates the efficiency of each element. Even without the averaging filter, there is no severe checkerboard effect as described in the literature review, only a small effect near the left hand edge of the plate where the loading is applied. However, it is of the author’s opinion that it does not affect the overall aspect of the optimum topology. From a manufacturing point of view, the optimum structure could relatively simply be

manufactured via laser cutting, as the load paths are clear, checkerboarding almost entirely absent and the members not too thin.

Linear/Non-linear compatibility: Model 1 and 2 being modelled as linear static coupled with the nature of the VDM/SIMP approach, i.e. modifying the stiffness matrix by scaling the Young's modulus, mean it would be irrational to conclude on VDM/SIMP's non-linear capabilities. Furthermore, Figure 3.9 shows the von Mises stress distribution for the optimum topology of model 2:

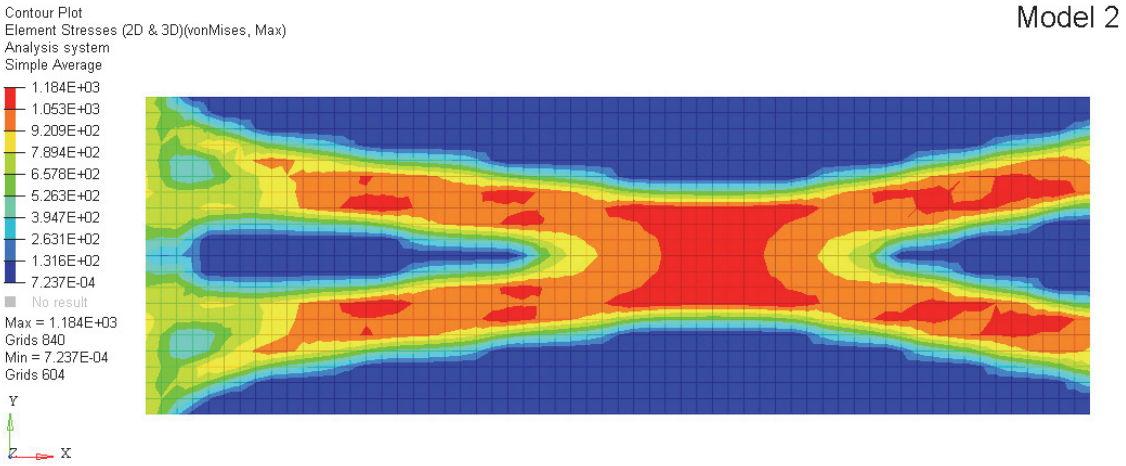

Figure 3.9 : Model 2 von Mises stress distribution (MPa)

Clearly, the stress values are above the Yield strength of both grades of steel defined in Table 3.1, therefore in this case defining sections (1) and (2) from Figure 3.1 as linear, and by extension using linear TO, does not seem to be an acceptable solution for the given loading scenarios in Table 3.2.

Other findings: An important aspect to mention with regards to these models is the similarities between the two optimum structures. This is due to the definition of linear static FEA and the VDM/SIMP method. Essentially, the displacement field is linear to the loading, and therefore a change only in loading magnitude (the only difference between model 1 and model 2), would not change the stress distribution or the loadpaths throughout the structure. In particular, with a target volume fraction defined, the final topologies obtained are identical. Even in the case of volume minimisation and a target compliance however, the global topology would still be the same for both models, with only member sizes changing to accommodate the larger loads in model 2. The implications of this statement are that for loadcases where linear static definition is acceptable, the optimisation process would only need to be performed once to obtain

the optimum geometry layout (for that particular loading direction). This could potentially be beneficial in the optimisation of vehicle structures, such as defined in Figure 3.1. For example, linear static optimisation could be used for the “passenger cell”. If the connection points are known between the “front end” and the “passenger cell” and remain the same, then there could be an argument that the optimum structure obtained be the same for all impact magnitudes in the same direction. This further validates the discussion above around the non-linear incompatibility of VDM/SMP. Regardless of the loading magnitude, even if those are beyond strength threshold of the material, the TO results would be the same.

3.1.2. Optistruct - IR

As mentioned in the literature review, an alternative method to constraining the model is using IR. The principle has been explained in the previous chapter, and three different configurations are illustrated in Figure 3.4 and summarised in Table 3.5. The third configuration, Figure 3.4(c), applies point masses on the right hand edge locations corresponding to the approximate locations of the SPCs for the final optimised topology of model 1 and model 2 (Figure 3.6 and Figure 3.7). This in essence should influence the optimisation process to distribute material around these points. An arbitrary mass of 2kg for each point mass was selected, superior to the approximate mass of 0.95kg for the whole 2D plate.

Results

Figure 3.10 - Figure 3.12 show the material distribution for each IR configuration discussed:

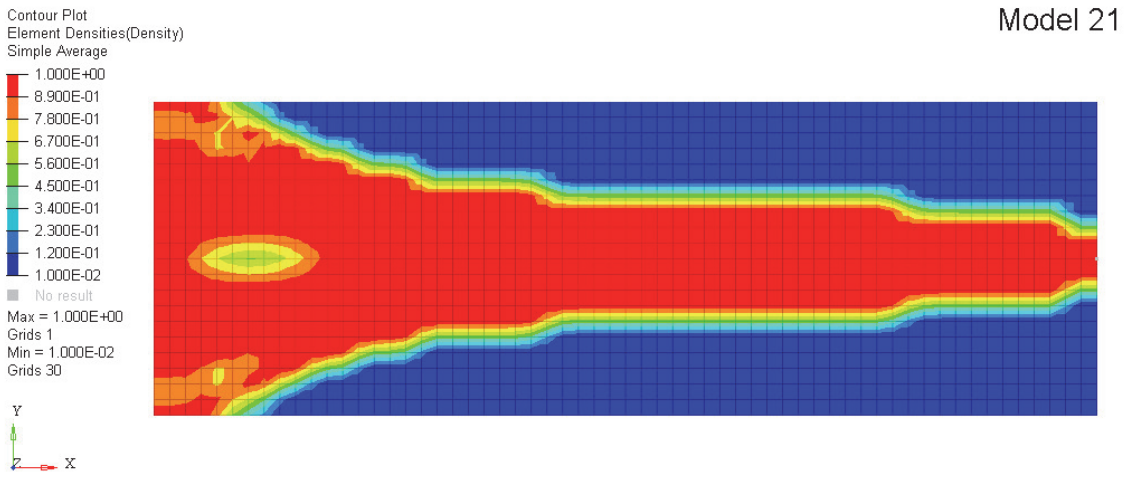

Figure 3.10 : Model 21 density distribution

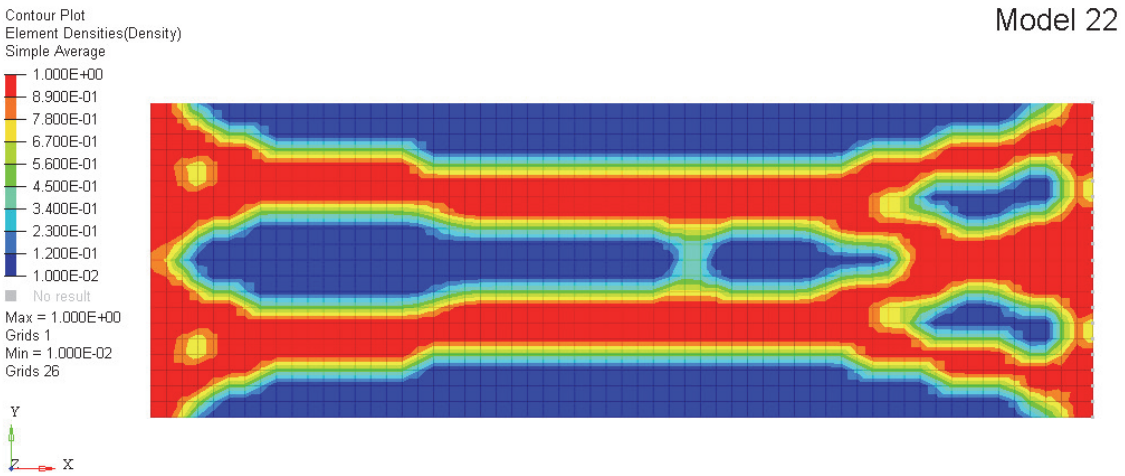

Figure 3.11 : Model 22 density distribution

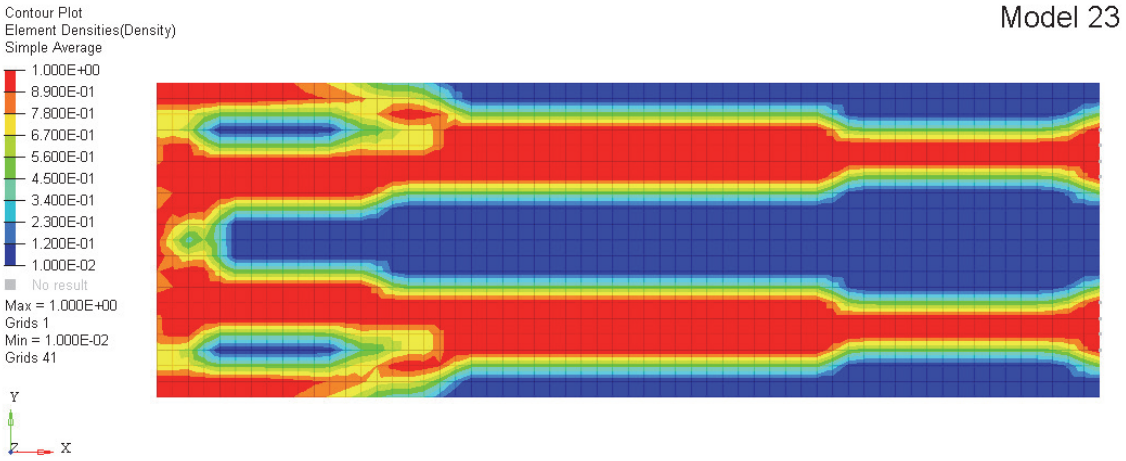

Figure 3.12 : Model 23 density distribution

Topology trends: In each of the models, the material distribution flows towards each mass point (Figure 3.4), creating different global optima. However there is a noticeable trend that column like structures are obtained as opposed to the triangulation obtained in the SPC models 1 and 2. Clearly, and unsurprisingly, the boundary condition (BC) definition has an influence on the optimum structure obtained. In this case, the magnitude of each mass point was arbitrary in order to create a large enough differential with the total mass of the plate. However, in reality these mass points would need to reflect accurately the inertia effects in the model, as well as their locations. It is also possible that each mass point would have a different value. These parameters are determined by the user's experience and therein lies a difficulty with this method. While not impossible, it could be difficult to reflect accurately a vehicle's inertia using these mass points for example.

Feasibility of topology results: Much like model 1 and model 2, IR produced relatively clear structures and an absence of severe checkerboard effects, as can be seen by the unfiltered density distribution for model 12 in Figure 3.13.

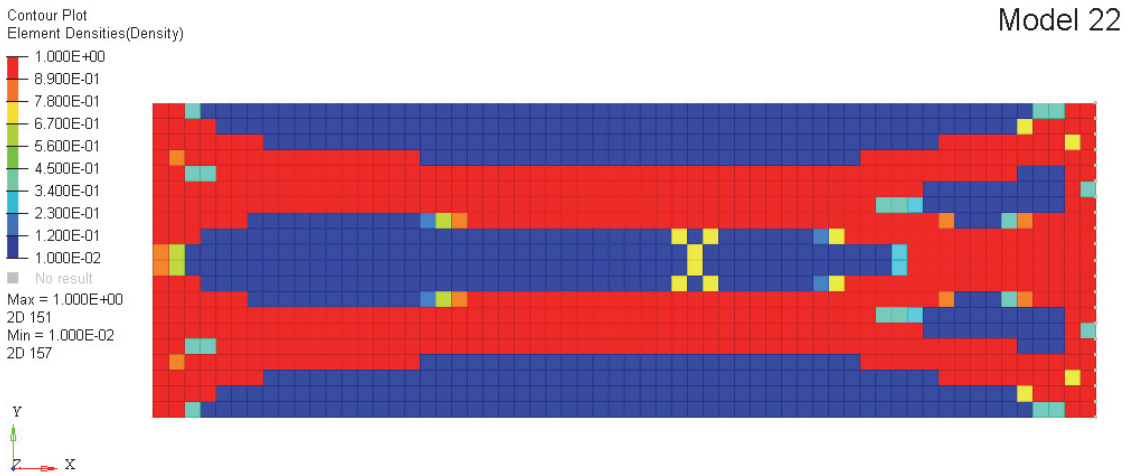

Figure 3.13 : Model 22 unfiltered density distribution

However, it should be noted that there is a tendency for an increase in checkerboarding when several point masses are used as opposed to a single point mass for example.

Linear/Non-linear compatibility: The conclusions are once again similar to the SPC models, in that IR is still linear static based, as the process creates internal accelerations and moments to find static equilibrium with the external forces. However, the fact that IR takes into account, as its name suggests, the inertia of the model makes it perhaps a better suited approximation of dynamic scenarios such as vehicle impacts where inertia is a key element of the overall behaviour.

Other findings: A further study was conducted on all the linear static Optistruct models to test their sensitivity to the loading direction. Three additional loading directions were tested: 15°, 30° and 45° anti-clockwise from the x axis, as illustrated by Figure 3.14 and summarised in Table 3.7:

Table 3.7 : Optistruct sensitivity analysis models

Model Number	Original model /Constraints	Loading angle (°)
44	Model 2 - SPC	15
45	Model 2 - SPC	30
46	Model 2 - SPC	45
47	Model 21 - IR (Point)	15
48	Model 21 - IR (Point)	30
49	Model 21 - IR (Point)	45
50	Model 22 - IR (Edge)	15
51	Model 22 - IR (Edge)	30
52	Model 22 - IR (Edge)	45
53	Model 23 - IR (SPC)	15
54	Model 23 - IR (SPC)	30
55	Model 23 - IR (SPC)	45

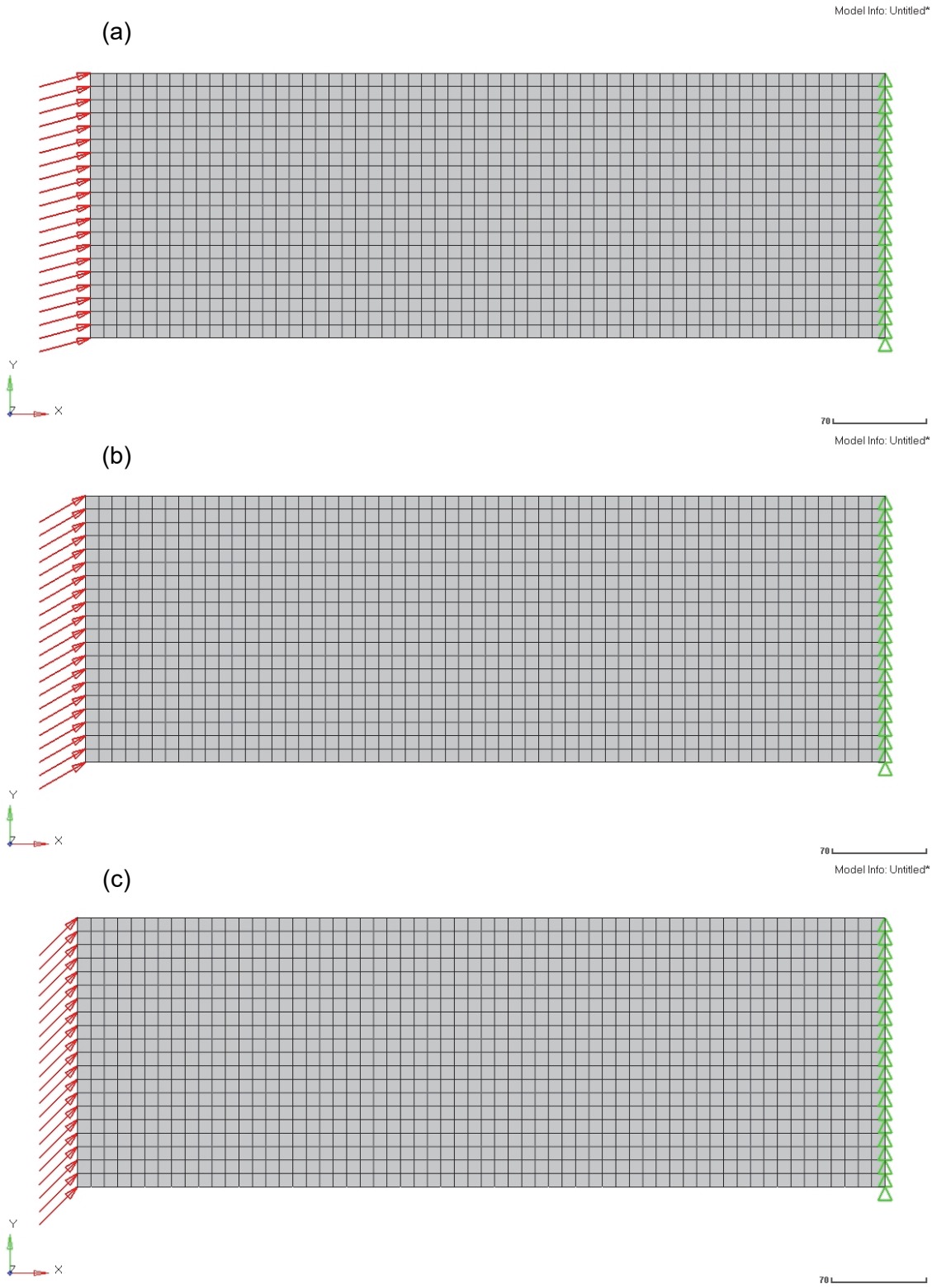

Figure 3.14 : Model 2 force sensitivity analysis setup (a) 15° (b) 30° (c) 45°

Figure 3.15 - Figure 3.18 show the results from the sensitivity analysis:

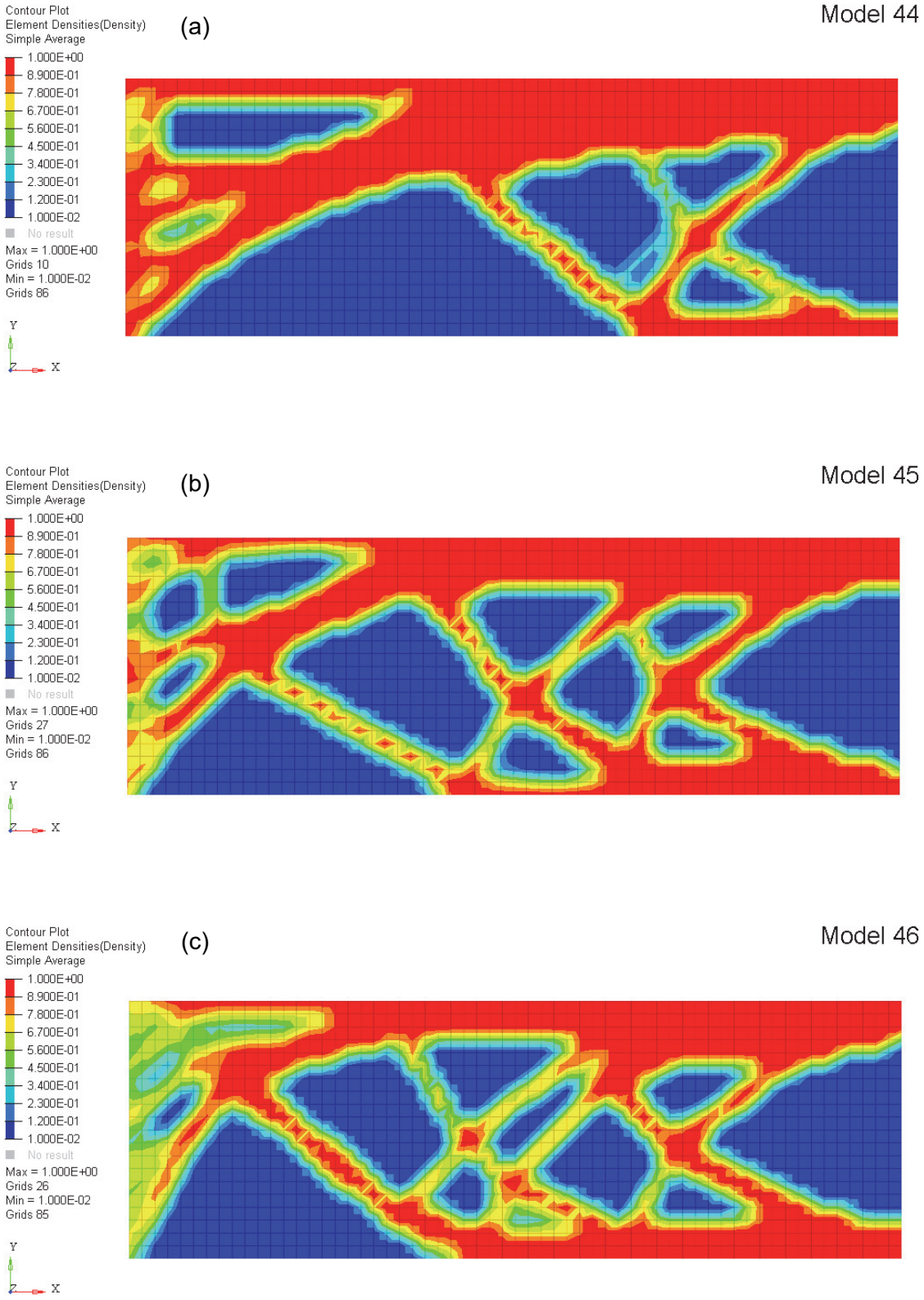

Figure 3.15 : Model 2 sensitivity analysis (a) model 44 (15°) (b) model 45 (30°) (c) model 46 (45°)

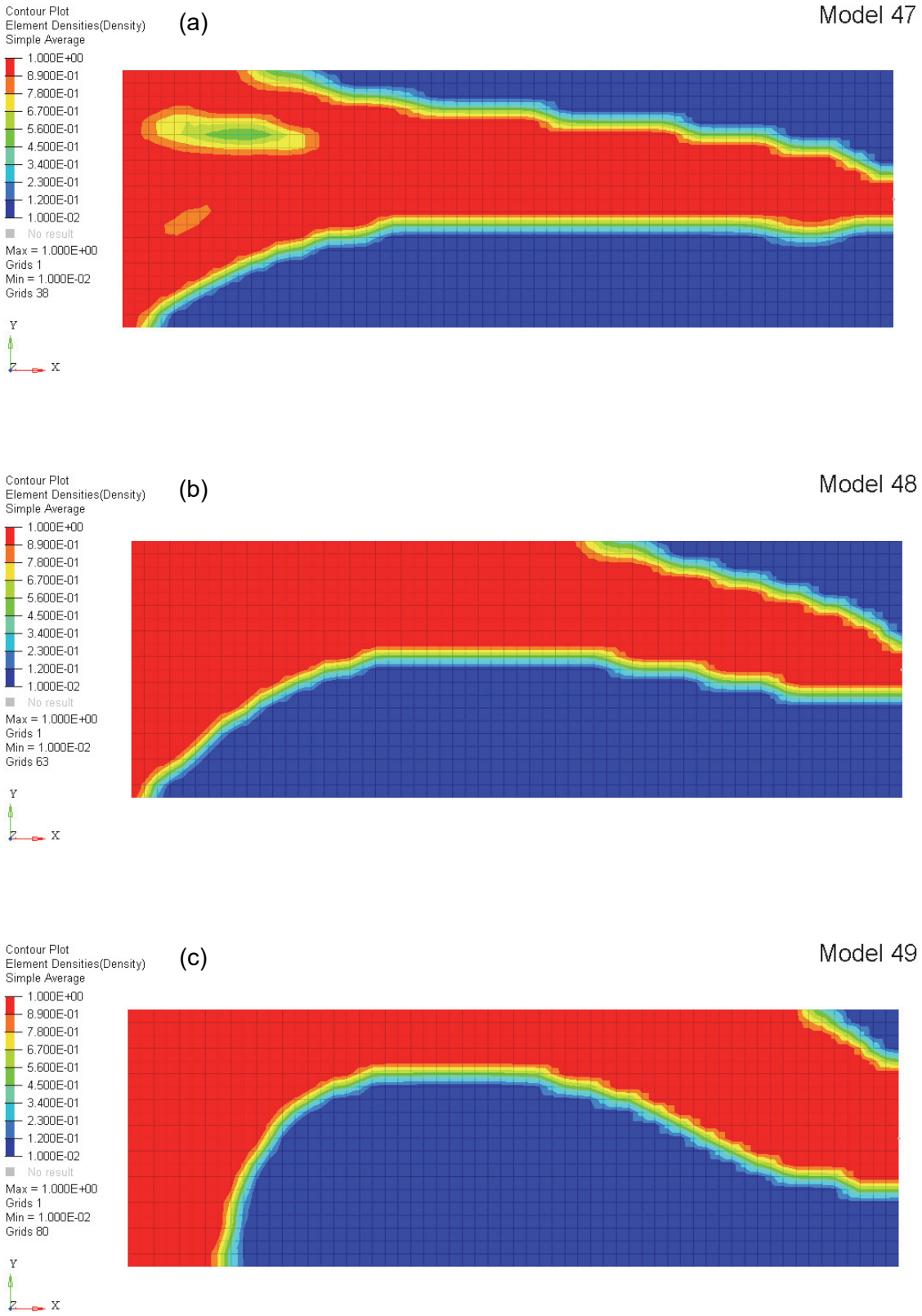

Figure 3.16 : Model 21 sensitivity analysis (a) model 47 (15°) (b) model 48 (30°) (c) model 49 (45°)

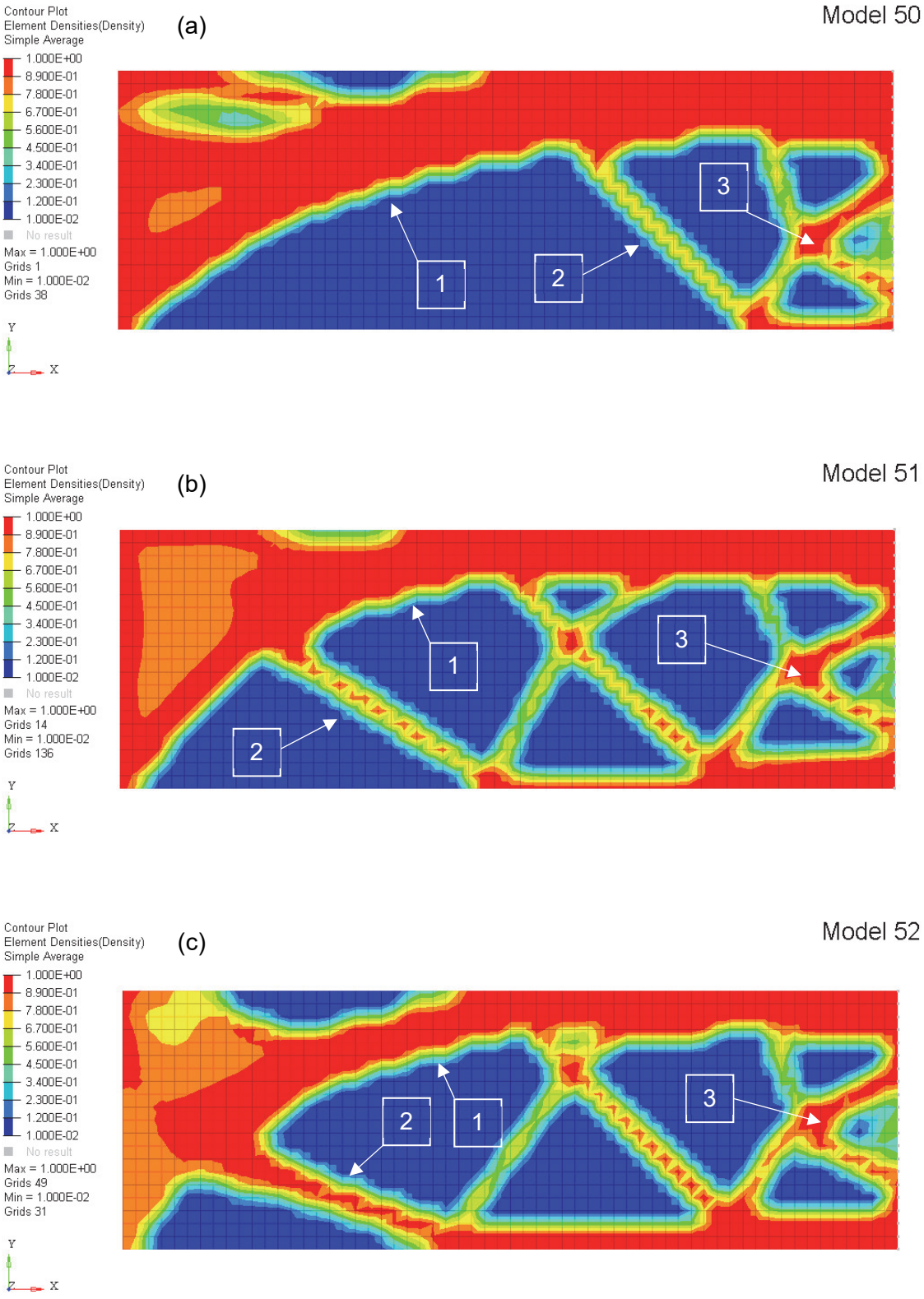

Figure 3.17 : Model 22 sensitivity analysis (a) model 50 (15°) (b) model 51 (30°) (c) model 52 (45°)

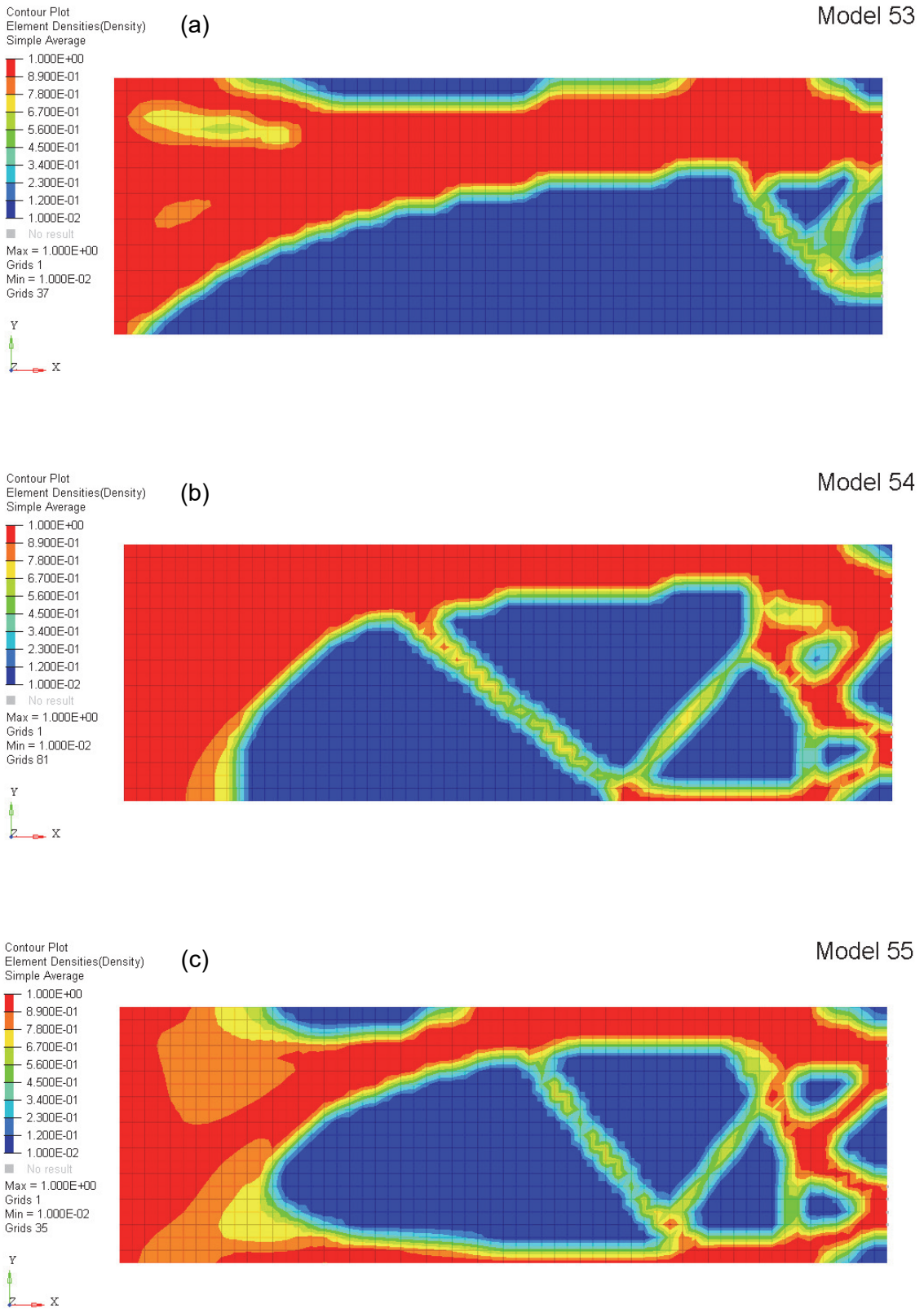

Figure 3.18 : Model 23 sensitivity analysis (a) model 53 (15°) (b) model 54 (30°) (c) model 55 (45°)

At first glance, for each model the optimum structures seem very different for each loading direction. A closer look reveals however that there are recurring trends between different directions. For example, for model 22 (i.e. model 50, 51 and 52), certain patterns are repeated such as those defined by sections (1), (2) and (3) in Figure 3.17. Similar pattern repetition can be seen in the other models. The consequence of this is when the loading direction rotates around the z-axis (Figure 3.14), certain patterns are repeated for each loadcase. Therefore as a time saving measure, it could be possible to perform only one asymmetrical loadcase optimisation instead of each loading direction. This is a similar conclusion to the previous statement on the difference in loading magnitude between model 1 and model 2 and the similarity in the optima obtained.

A further conclusion must be made on the change in "clarity" when the loading angle is increased. The figures above show that when the loading angle increases, there is also an increase in intermediate densities and therefore a more prominent checkerboard effect. This could however be reduced by increasing the penalisation factor in the optimisation parameters, as shown by model 56 in Figure 3.19 where the penalisation factor is increased to 3 for model 52.

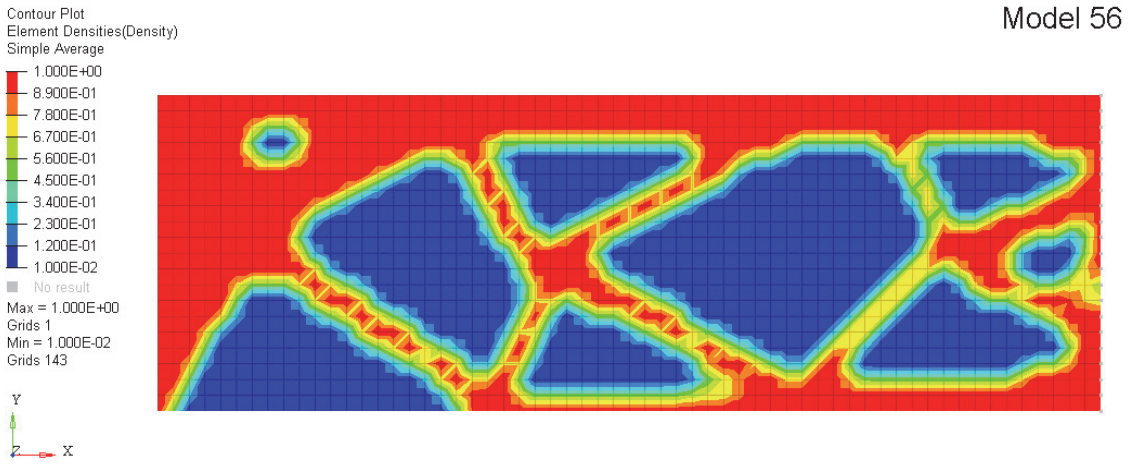

Figure 3.19 : Model 56 density distribution

Globally, Optistruct and by extension VDM/SIMP has shown it is capable of handling linear static loadcases, and the use of IR to take into account the model inertia could make it an interesting addition to satisfy the objective of catering for both linear and non-linear behaviour. The next section will analyse the capabilities of LS-TaSC software in linear static loadcases.

3.1.3. LS-TaSC

The model set up for LS-TaSC, using Oasys PRIMER software, is for the large part identical to the Optistruct models: the material properties are the same, as are the constraints i.e. SPCs along the right hand edge. However, a certain number of additional parameters need to be added, as the explicit solver (i.e. uses a small timestep to estimate accelerations) also caters for dynamic scenarios. Firstly, the loads applied to the left hand edge are time dependent. Figure 3.20 displays the load curve applied to the model:

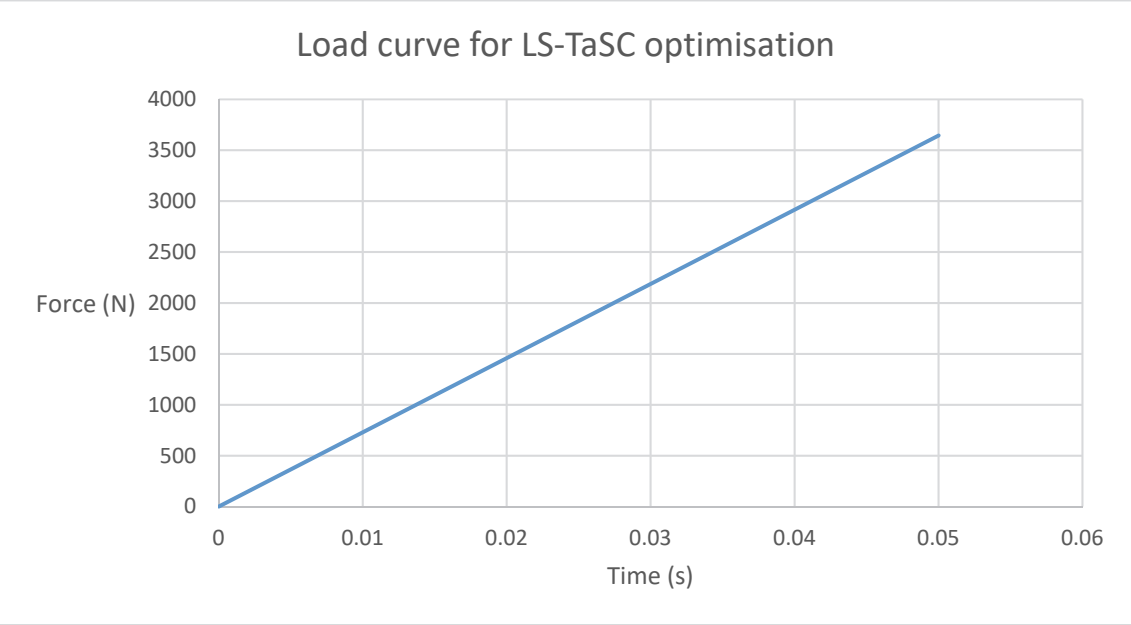

Figure 3.20 : Load curve for LS-TaSC optimisation

The timestep for the load case is t=1.66μs and an end time of 0.05s. The time step in explicit finite element analysis (FEA) is a function of the smallest elements size (in this case 10mm), the material Young's modulus and density (Macauly 1987). The end time was simply selected to reduce the run time of the simulation. Additionally, a control card was added to the model to avoid hourglassing behaviour, an undesirable effect of using single point load. Figure 3.21 represents the completed FE model for both LS-TaSC cases:

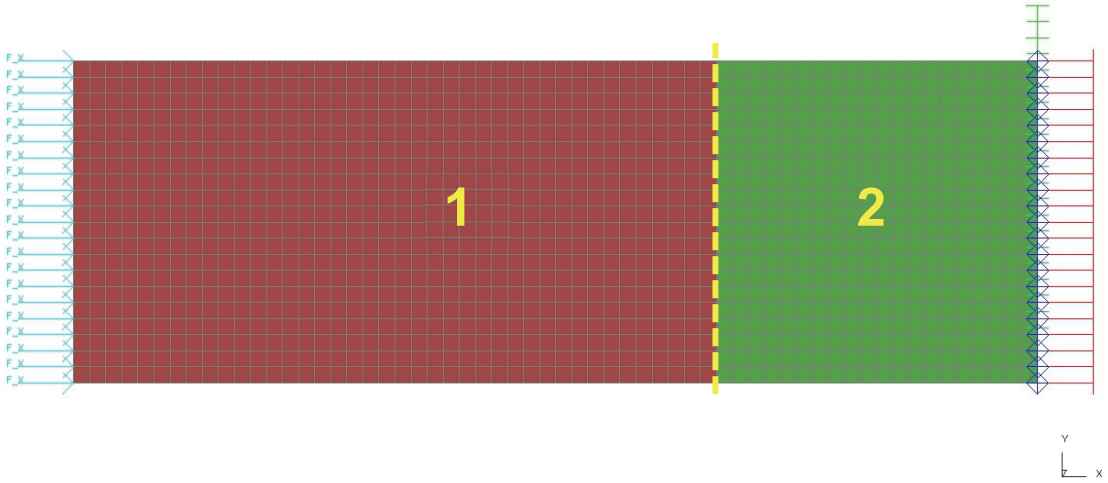

Figure 3.21 : Basic LS-TaSC FE model setup

The setup illustrates the two different sections defined in Figure 3.1. However, in this section, both sections are modelled using the same material and geometry properties, therefore act as a "single" section, similar to Figure 3.5. The optimisation set up using LS-TaSC is slightly different to Optistruct. Firstly, a volume fraction has to be supplied by the user for each section (1) and (2) (Figure 3.21). A volume fraction of $v_f = 0.5$ was chosen to mirror the Optistruct models. Effectively, the volume fraction is the constraint, and by default in LS-TaSC the objective is to obtain an even distribution of strain energy in the structure. Before the optimisation process can be performed, the convergence criteria need to be specified. These are provided by both a maximum number of iterations (set at the maximum of 100 for both models) and the convergence tolerance, which in LS-TaSC corresponds to the minimum mass redistribution ratio (essentially how much is the model being modified per iteration). The parameters are summarised in Table 3.8:

Table 3.8 : LS-TaSC optimisation parameters

Objective function	Constraint	Maximum number of iterations	Convergence tolerance
Uniform strain energy	Volume fraction = 50%	100	Material distribution ratio = 0.001

As discussed in the literature review, the objective in LS-TaSC is to produce a structure with uniform strain energy distribution, based on work by (Patel 2007). This process ensures each element in the structure contributes equally towards energy absorption,

which in the context of crashworthiness is important to obtain controlled plastic deformation.

Furthermore, for shell elements, LS-TaSC uses element thickness distribution to optimise the structure, as opposed to Optistruct, which uses element density distribution. In this regard, LS-TaSC is more comparable to topometry optimisation (Livermore Software Technology Corporation 2013).

Results

Figure 3.22 and Figure 3.23 show the optimum thickness distribution obtained for model 3 and model 4 respectively:

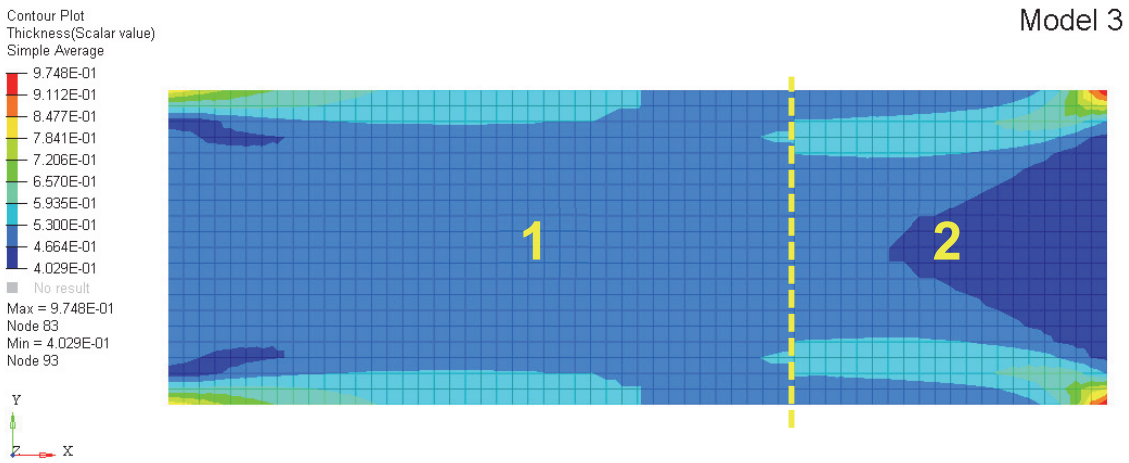

Figure 3.22 : Model 3 thickness distribution (mm)

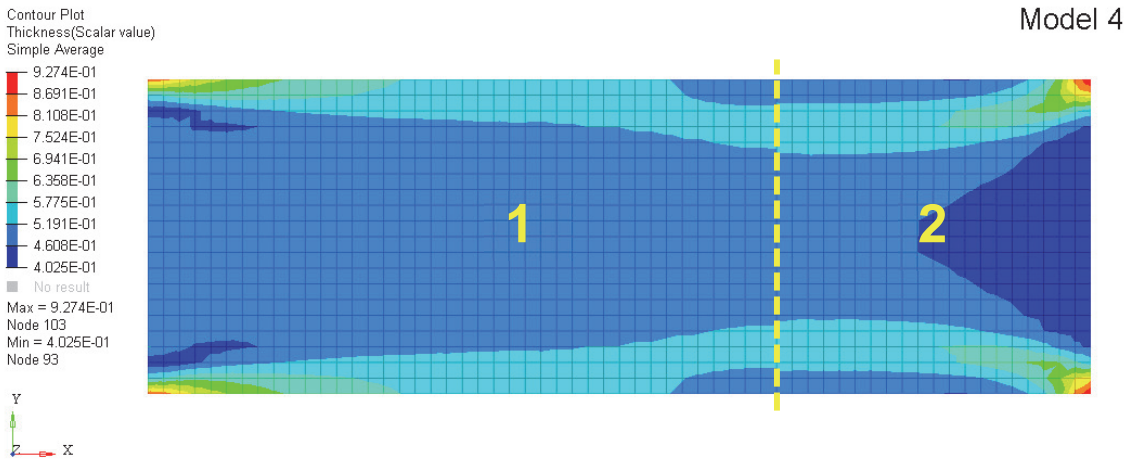

Figure 3.23 : Model 4 thickness distribution (mm)

Topology trends: Both models show a vastly different topology as opposed to the Optistruct models 1 and 2. The models show mostly full thickness in small sections of

the right hand corners of the plate. From there, the material is mostly distributed on the upper and lower edges of the plate. Interestingly, the material distribution does not run entirely along the edges of section (1), and a difference between model 3 and 4 has been highlighted in Figure 3.22 and Figure 3.23. Compared to Optistruct, there are more differences between model 3 and 4, however these are not by any means considerable. Similarly to Optistruct therefore, LS-TaSC seems to obtain similar results despite a difference in loading magnitude. However, it must be reminded in this instance that, with elastic material defined in both sections (1) and (2), the responses are linear.

Feasibility of topology results: There are considerable differences between the feasibility of models 3 and 4 and the Optistruct models. This is for the large part due to the nature of LS-TaSC. The topology obtained is a thickness distribution, and LS-TaSC deletes low-thickness elements, but in this instance, the thicknesses are not low enough to consider the elements for complete removal. A closer look at Figure 3.22 and Figure 3.23 reveals that the lowest thickness is around 0.4mm, just under half the original thickness. From a manufacturing point of view, the structures obtained would be more difficult to produce than the Optistruct models, which are “solid/void” definitions. Therein lies the first issue of LS-TaSC: the literature review presented TO as being a “tool” to aid the user in designing efficient structures by essentially revealing the loadpaths through the structure.

Linear/Non-linear compatibility: Much like the Optistruct models, no conclusions can be made from this load case on the non-linear capabilities of LS-TaSC. However, some comments can be made on its linear capabilities. The results show the software is able to perform linear optimisation, however the model set up shows that perhaps it is not the best suited, namely the necessity to define additional control cards for hourglassing. Figure 3.24 illustrates the convergence of the optimisation procedure for model 3:

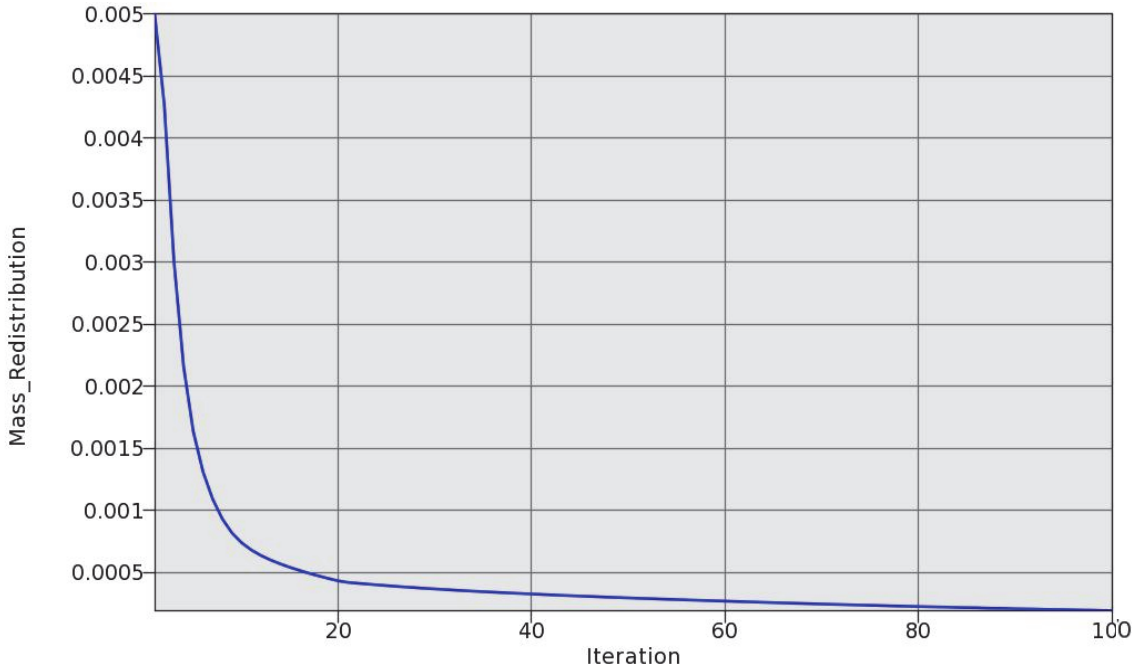

Figure 3.24 : Model 3 optimisation convergence criteria graph

Even though the LS-TaSC procedure did not terminate due to a satisfied convergence criteria, Figure 3.24 shows a converging pattern. Therefore, the absence of "convergence termination" could be down to a too strict convergence tolerance. Figure 3.25 below illustrates the von Mises stress distribution for the reanalysis of model 4, taken from the final iteration TO results (Figure 3.23):

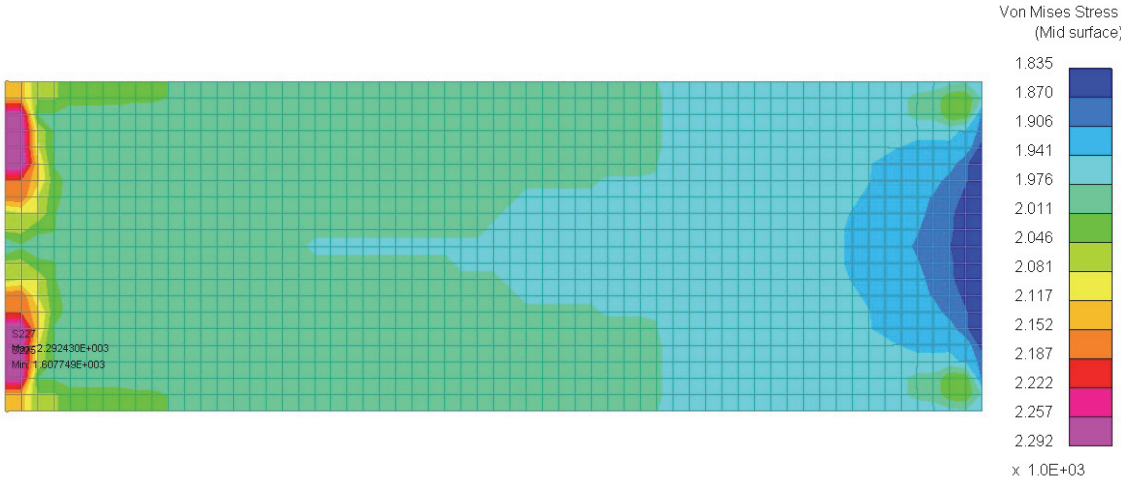

Figure 3.25 : Model 4 von Mises stress distribution (MPa)

Similarly to the Optistruct results, the Figure 3.25 reveals that the stress results are beyond the yield strength of the material, and therefore the use of linear TO would not

be suggested. However, directly comparing the results to the Optistruct results (Figure 3.9), the maximum von Mises stress is approximately double the value obtained for the LS-TaSC model. Therefore, this could indicate that the TO method used for LS-TaSC, i.e. homogeneous internal energy density within the structure by redistributing element thicknesses, is not as adapted to linear responses as Optistruct.

Other findings: Several key points have been highlighted and discussed regarding the LS-TaSC process. Firstly, a closer look at the interface between sections (1) and (2) for both models reveal an interesting phenomenon, especially for model 3: there seems to be a small discontinuity in the thickness distribution despite both sections having the same definition. It is likely that the LS-TaSC algorithm, when taking neighbourhood FEA information into account for the sensitivity calculation, only includes elements in the same section i.e. *PART card in the keyword file. In order to verify this, model 57 was created where all the elements were put into a single section from model 3, and the optimisation process was re-run (Figure 3.26):

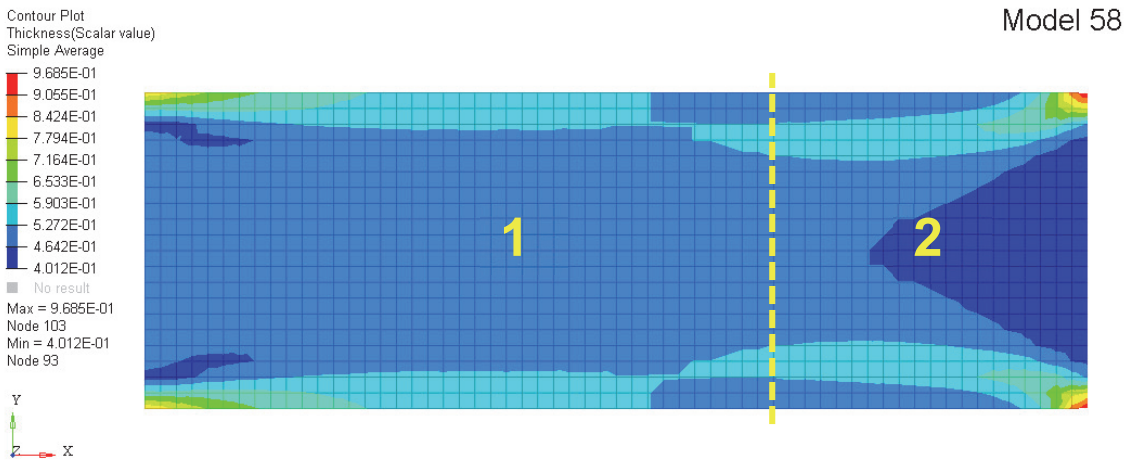

Figure 3.26 : Model 57 thickness distribution (mm)

The discontinuity previously observed has disappeared, the material distribution has a more “flowing” pattern to it. Globally, the topology has not drastically changed, however this effect is important to underline in the event of having two linear sections that share an interface. One aspect that was highlighted was the material distribution process of LS-TaSC by which the thickness is modified throughout the structure for each element. The version utilised for this study (version 2.1) also implemented an approach that, similarly to SIMP, can “force” the material thicknesses towards 0, i.e. the element is deleted, or the original element thickness. By default, this option is not used for shell elements, however it is possible to activate this option. Therefore, in an attempt to visualise this phenomenon, model 58 was created where the target volume fraction was reduced to a value of v_f = 0.2, and the optimisation process re-run with the SIMP activated for shell elements. However, this process terminated after iteration 16 due to instabilities in the FE model (Figure 3.27):

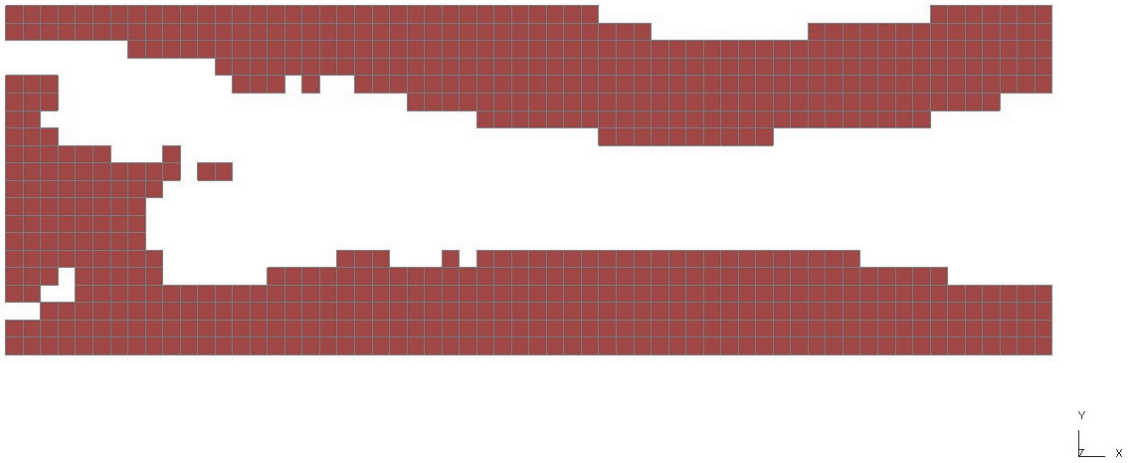

Figure 3.27 : Model 58 with activated SIMP structure at iteration 16

The instability that caused the premature termination of the optimisation process is due to a force applied to a massless node. As shown by Figure 3.27, two adjacent elements are deleted on the left hand edge of the structure where the point forces are applied (Figure 3.21). However, LS-TaSC does not remove the nodes from the model, which results in a force applied on a non-structural node. Therefore, from a stability point of view, activating SIMP for shell elements can cause instabilities. This is the case when point loads are applied to elements included in the design volume. A pressure load, contact force or rigidwall impact could avoid this issue, as the forces are not applied directly onto the structural nodes. Nevertheless, this represents a significant drawback

to using LS-TaSC for linear optimisation. Furthermore, Figure 3.28 below illustrates the convergence graph of the optimisation process before termination at iteration 16

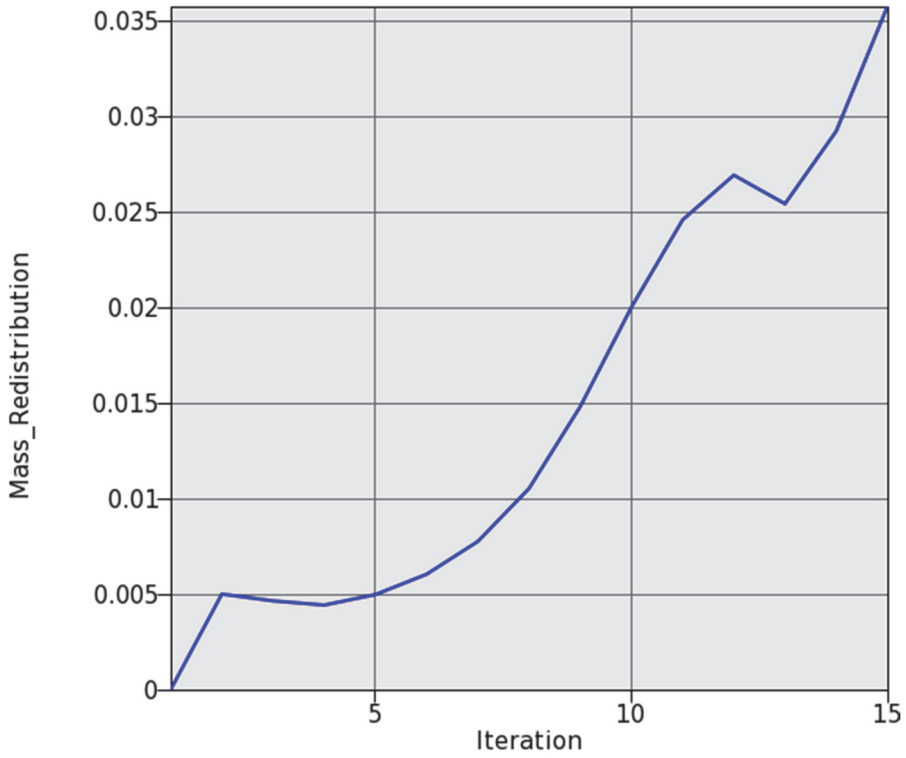

Figure 3.28 : Model 58 with SIMP activation optimisation convergence criteria graph

The graph above demonstrates that, before the error termination, the convergence criteria, i.e. the mass redistribution, was increasing and therefore not close to termination. This is very different from the phenomenon observed when SIMP was not activated (Figure 3.24). This could indicate that the optimisation process is less stable for shell elements when SIMP is activated. At this point it should be reminded that, by default, this option is deactivated in LS-TaSC for shell elements.

3.1.4. Conclusion

In essence, this section has shown that TO results are highly dependent on the BCs, particularly where the loads are applied. This in itself is not surprising as the TO results are based on FEA results, themselves a function of how the BCs are defined. Due to the relatively simply design volume, the loadpaths obtained are also relatively simple, i.e. “straight” members joining the forces and SPCs. Although the structures obtained are 50% lighter due to the volume target constraint, they have also shown to be unsuitable

as the von Mises stress results illustrate stresses well beyond the elastic limit. This first section has established both algorithm's capabilities when encountering purely linear behaviour. From these results, it seems that Optistruct is more developed, stable (fully integrated elements needed for LS-TaSC) and suitable for linear static behaviour. However, the importance of non-linear behaviour in vehicle design has been mentioned in the literature review. It has also been discussed that VDM/SIMP cannot directly cater for non-linear responses in its algorithm. However, ESLM can adapt a dynamic load into a series of linear static loadcases, after which linear optimisation via VDM/SIMP is performed. ESLM and LS-TaSC will therefore be analysed in the following section on "purely" non-linear behaviour, along with the BEETS and BESO evolutionary methods.

3.2. Non-linear model

Similarly to the linear static study, this study will analyse the optimisation results when both sections of the plate (1) and (2) are defined using a non-linear material model. Table 3.9 recaps the models implicated in the study:

Table 3.9 : Models for non-linear study

Model Number	Optimisation Algorithm	Plate section definition		Static/Dynamic analysis	Plate material	Loading magnitude (High/Low)	Constraints
		Section 1	Section 2				
5	ESLM	NL	NL	Dynamic	HSS	High Velocity	SPC
6	ESLM	NL	NL	Dynamic	Mild Steel	High Velocity	SPC
7	ESLM	NL	NL	Dynamic	HSS	Low Velocity	SPC
8	ESLM	NL	NL	Dynamic	Mild Steel	Low Velocity	SPC
9	LS-TaSC	NL	NL	Dynamic	HSS	High Velocity	SPC
10	LS-TaSC	NL	NL	Dynamic	Mild Steel	High Velocity	SPC
11	LS-TaSC	NL	NL	Dynamic	HSS	Low Velocity	SPC
12	LS-TaSC	NL	NL	Dynamic	Mild Steel	Low Velocity	SPC
24	BESO	NL	NL	Dynamic	Mild Steel	Low Velocity	SPC
25	BESO	NL	NL	Dynamic	Mild Steel	Low Velocity	SPC
26	BESO	NL	NL	Dynamic	Mild Steel	Low Velocity	SPC
27	BESO	NL	NL	Dynamic	HSS	Low Velocity	SPC
28	BESO	NL	NL	Dynamic	Mild Steel	High Velocity	SPC
29	BESO	NL	NL	Dynamic	HSS	High Velocity	SPC
30	BEETS	NL	NL	Dynamic	Mild Steel	Low Velocity	SPC
31	BEETS	NL	NL	Dynamic	HSS	Low Velocity	SPC
32	BEETS	NL	NL	Dynamic	Mild Steel	High Velocity	SPC
33	BEETS	NL	NL	Dynamic	HSS	High Velocity	SPC

Models 24 – 26 differ only by their sensitivity filtering radii, as stated in Table 3.4. First, ESLM will be analysed followed by LS-TaSC, and finally the BESO/BEETS evolutionary algorithms.

3.2.1. ESLM

From the Optistruct models 1 and 2, only two changes need to be made to the model to accurately set it up for ESLM optimisation:

- ***Loading:*** As the name suggests, the ESLM takes a dynamic load and transforms it into a series of linear static load cases for optimisation. Therefore, dynamic loads need to be defined for the analysis. This is done by applying the load curve in Figure 3.2 to the static loads from the Optistruct models, thus approximating the rigidwall impact response.
- ***Material:*** In order to allow for non-linear material behaviour, a simplified Johnson-Cook material model (MAT_098) was employed using the parameters listed in Table 3.1. This model enables strain rate effects to be considered. This feature will however not be utilised initially; consequently, a simpler material model such as MAT_03, plastic-kinematic, may also have been used. Nevertheless, strain rate effects are generally highly influential on crash performance, an aspect that may be investigated at a later point. In order to ease this transition, the MAT_098 material model was selected from the onset. At this stage, no strain rate dependency parameters were defined, consequently the MAT_098 model will in essence behave as a MAT_03 model. As this is a comparative study, the selection of a specific material model is not critical in this context, provided it enables comparison between linear and non-linear material behaviour.

The end time provided is the same as the LS-TaSC procedures, i.e. 0.05s. Furthermore, the explicit solver is chosen for the analysis. These steps ensure that the model is correctly set up for ESLM. The four different models are a combination of different loading magnitudes, i.e. different impact velocities, and different grades of steel with the same optimisation parameters as Table 3.6.

Results

The results from the initial ESLM runs were clear: none of the models would perform the analysis to completion. An investigation into this revealed an interesting phenomenon. When the energy levels became too high, i.e. high deformation levels, the analysis timestep reduces by increments and reaches levels of an order of magnitude of 10^{-12}. Clearly, this is insufficient to perform the optimisation procedure. It however shows a shortcoming highlighted in the literature review (Christensen et al. 2013): ESLM is poor at handling high levels of non-linearity in the model. In order to verify this statement, the magnitude is dropped considerably to 200N/node. With this magnitude, and the same force/time curve from Figure 3.2, the optimisation procedure performed successfully and Figure 3.29 shows the density distribution for the optimum structure obtained.

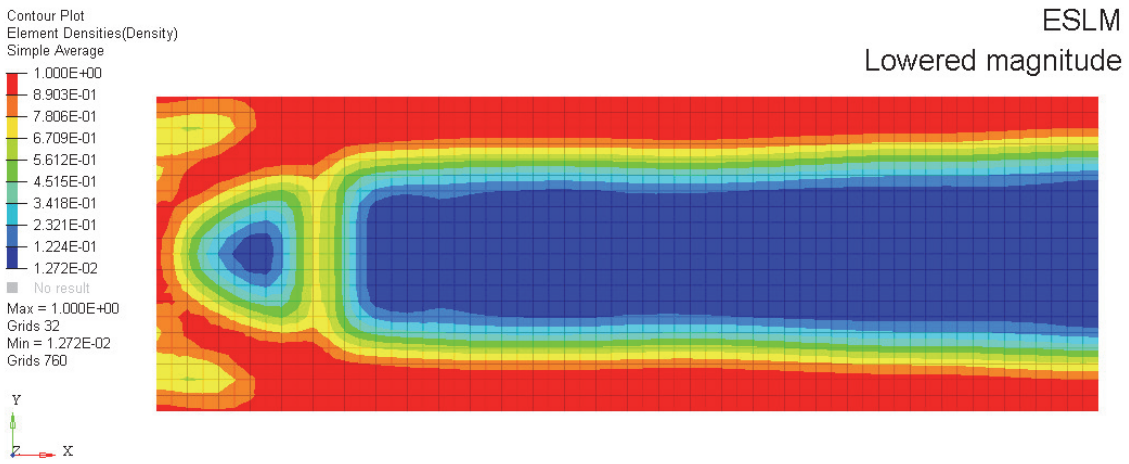

Figure 3.29 : ESLM lowered magnitude density distribution

Observing the trends, it is interesting to notice that the material distribution is closer to that observed in model 3 and model 4 from LS-TaSC, i.e. the majority of the material is located on the upper and lower edges of the plate, apart from the curved pattern observed near the loaded edge. The strain plots showed however that no plastic strain was present, backed up by the maximum von Mises stress value of 34 MPa, well below both material Yield strength values. As the loads were lowered, this is not a surprise. What it does demonstrate however, is that no material non-linearities were present, and by extension the structural responses were linear. Therefore, the suitability of ESLM for non-linear applications such as vehicle impacts could be called into question. This could stem from the non-linear explicit solver instabilities of RADIOSS/OPTISTRUCT more than the optimisation process itself.

3.2.2. LS-TaSC

The model set up for the four LS-TaSC models is essentially the same as the previous LS-TaSC models, and similarly to the previous ESLM models, non-linear behaviour is added to both sections of the plate using the Johnson-Cook information provided (Table 3.1). The one key difference here however is the use of a rigidwall as the loading, defined by the velocity and mass information provided in the first section of this chapter. The same LS-TaSC optimisation parameters are used as previous procedures (Table 3.8).

Results

Topology trends: Figure 3.30 - Figure 3.33 display the optimum thickness distribution obtained for models 9-12 respectively:

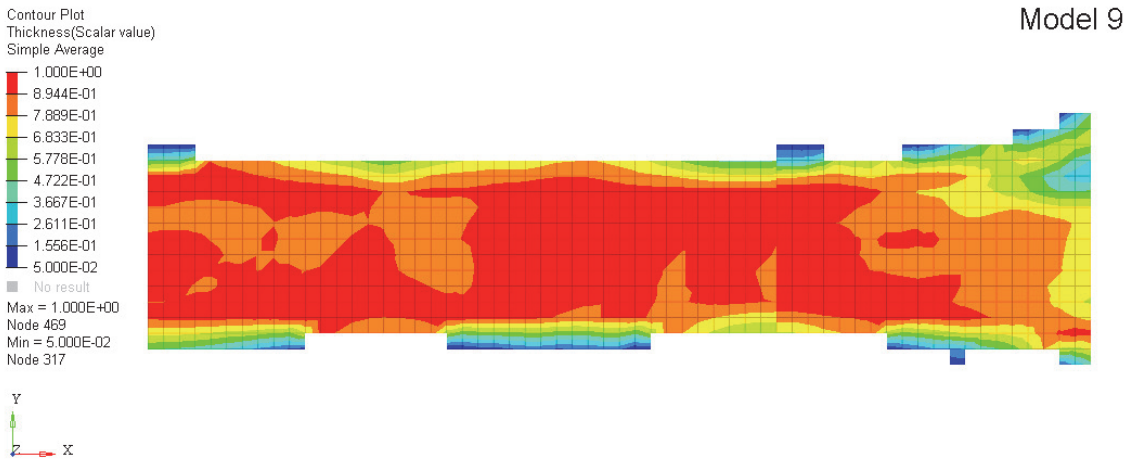

Figure 3.30 : Model 9 thickness distribution (mm)

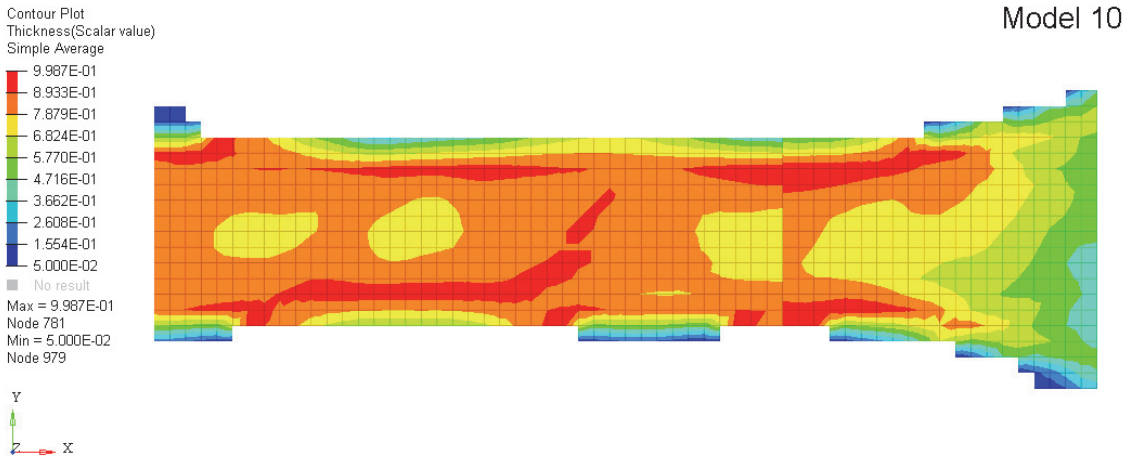

Figure 3.31 : Model 10 thickness distribution (mm)

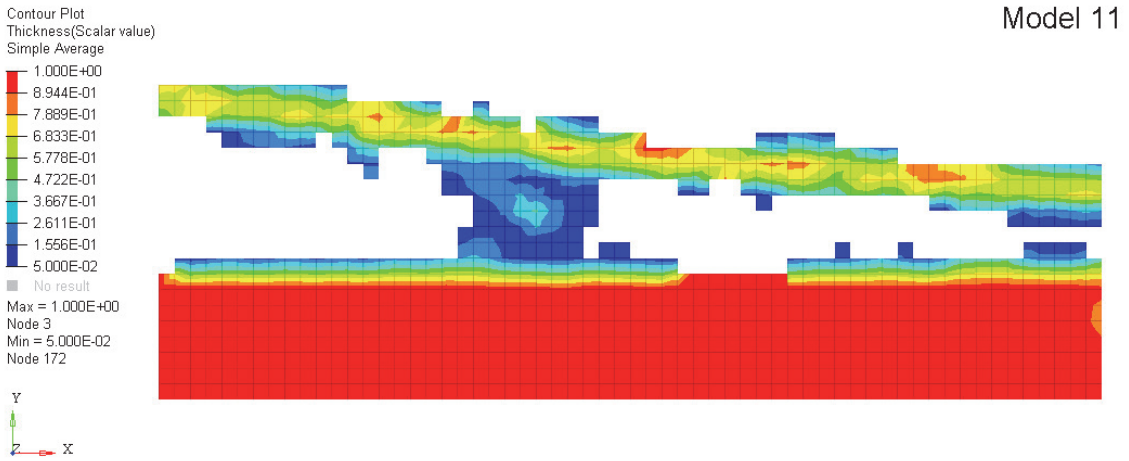

Figure 3.32 : Model 11 thickness distribution (mm)

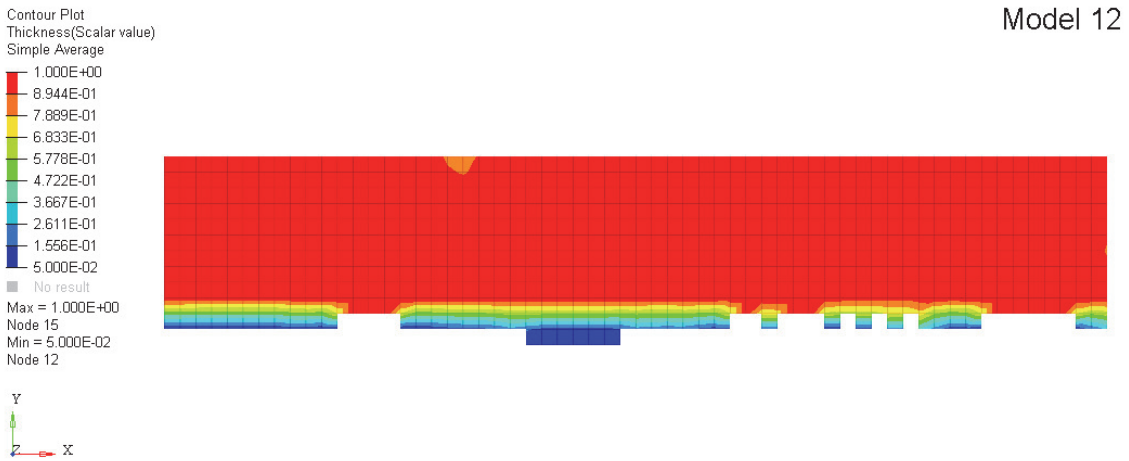

Figure 3.33 : Model 12 thickness distribution (mm)

As a general observation on topology trends, there seems to be a pattern between models whereby the overall geometry is that of a column. Even for model 11 (Figure 3.32), where there is an extra member (1), it could be argued that this member is of little importance due to the low thickness in the “connecting” member (2). This could perhaps showcase that for “purely” non-linear structures, the topology is independent of loading magnitude or indeed the material’s non-linear behaviour.

Feasibility of topology results: Interestingly, compared with model 3 and model 4, there is evidence here in all models that the same elements have been removed. This results in globally “clearer” optimum structures. However this is relative, as in all but model 12, there are also multiple intermediate thickness levels, which as previously mentioned could hamper manufacturability. Furthermore, these intermediate

thicknesses are more prominent near the SPC locations on the right hand edge. The results would also indicate that the final topologies obtained are clearer when the loading is higher

Linear/Non-linear compatibility: LS-TaSC is capable of catering for non-linearities in the structural behaviour, as showcased by Figure 3.34, which plots the effective plastic strain in the optimised structure for model 9:

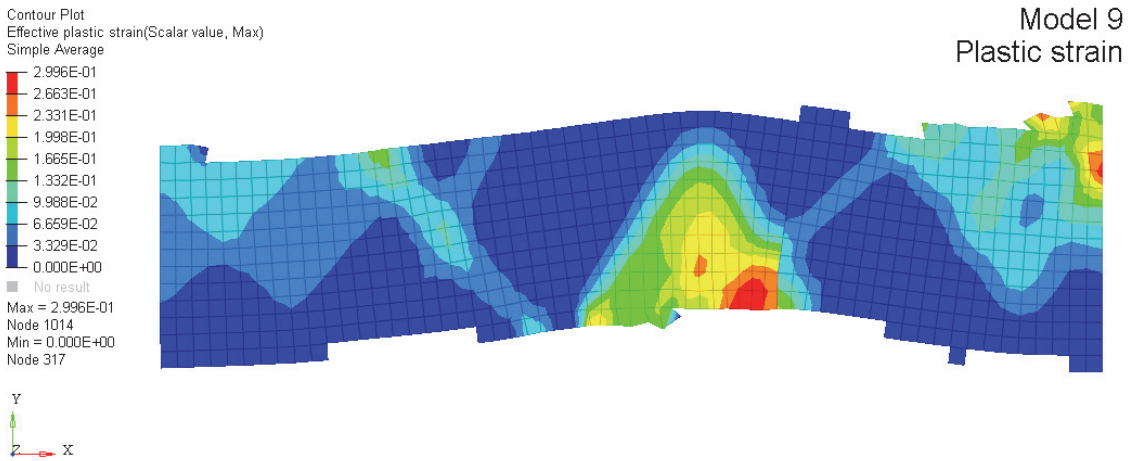

Figure 3.34 : Model 9 plastic strain plot

From the evaluated algorithms, LS-TaSC is the 1st to show a potential in catering for non-linear behaviour, especially the high levels present in the impact loadcase.

Other findings: Similarly to the previous LS-TaSC models, a recurring trend was the discontinuity at the interface. Both the thickness plot (Figure 3.30) and the plastic strain plot (Figure 3.34) for model 9 show this interface well. Mirroring the solution for the linear static models, a new optimisation procedure based on model 9 is performed with all the elements part of a single, non-linear section (model 59). As evidenced by the thickness distribution (Figure 3.35) and the plastic strain distribution (Figure 3.36) below, the phenomenon is eliminated.

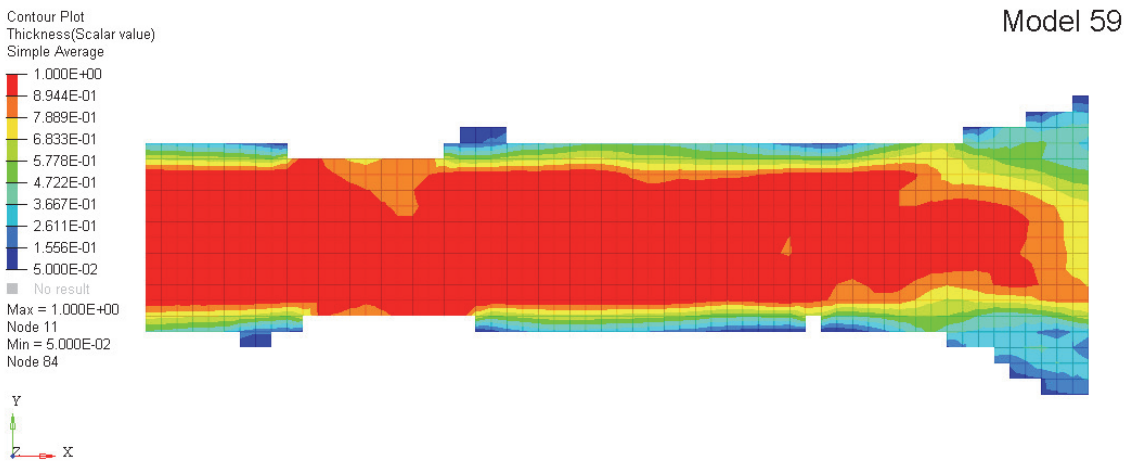

Figure 3.35 : Model 59 single section thickness distribution

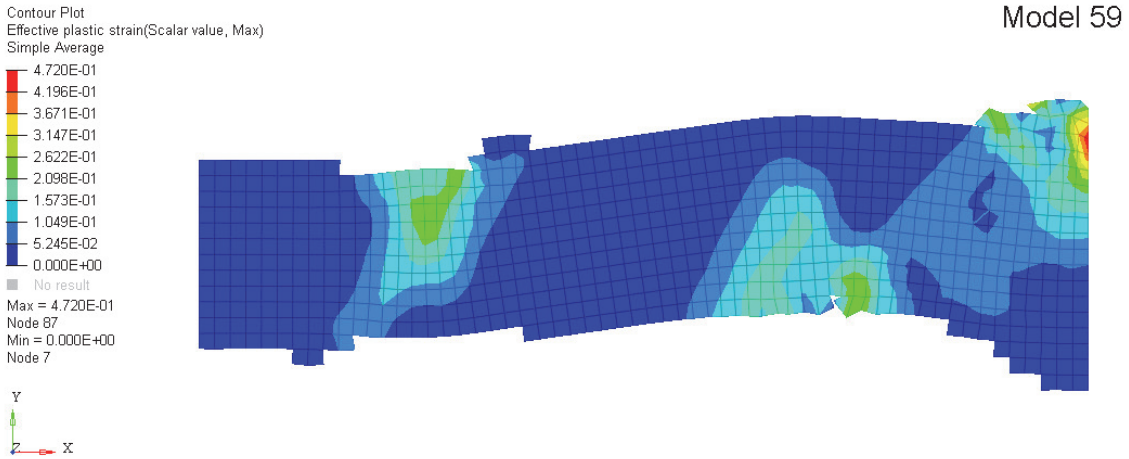

Figure 3.36 : Model 59 single section plastic strain plot

Interestingly, the maximum plastic strain value has (a) changed location and (b) increased by approximately 50%. This would suggest that the definition of sections in the plate has a large influence on the optimisation procedure. Generally, for all LS-TaSC models in the current and previous sections, it would seem that the interface between sections has a large influence on the optimum structures obtained. For these simple loadcases, that may limit the influence somewhat on the overall outcome. However, in the context of vehicle structural optimisation, with more complex geometries and the definitions/requirements defined in the literature review, the interface could play a key role in the hybrid TO procedure.

Similarly to section 3.1.3, model 60 is set up based on model 12 with the SIMP option activated, to determine its influence for non-linear behaviour. Figure 3.37 below illustrates the structure obtained after 100 iterations, i.e. the maximum number selected:

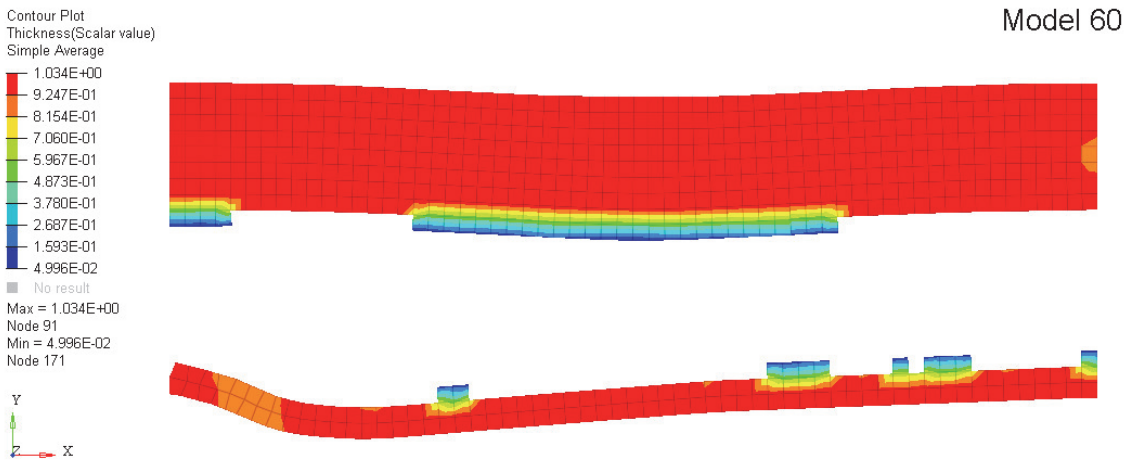

Figure 3.37 : Model 60 thickness distribution (mm)

Compared to model 12 (Figure 3.33), activating SIMP has had the effect of creating an extra, lower member in the structure. Overall however, it has retained the column-like structure. Furthermore, much like the other LS-TaSC models, there was no termination due to convergence of the objective function, in this instance material redistribution ratio. Figure 3.38 below illustrates the convergence graph for model 60:

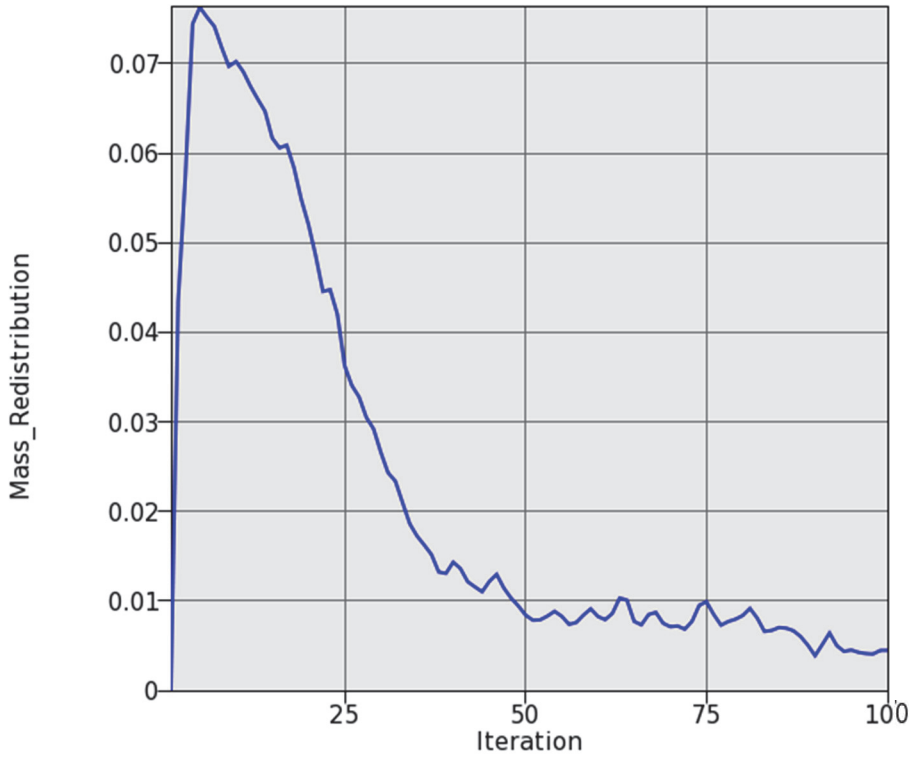

Figure 3.38 : Model 60 optimisation convergence criteria graph

In this case, there appears to be more oscillation in mass redistribution towards the end of the optimisation process compared to Figure 3.24. This could be due a more "hard-kill" method in optimisation, i.e. deleting elements as opposed to redistributing thickness. The convergence tolerance automatically selected by LS-TaSC in this case was 0.002 (as opposed to 0.001 selected in section 3.1.3.

3.2.3. BESO / BEETS

This final section in the non-linear study will analyse both evolutionary procedures highlighted in the literature review, namely BESO and BEETS. The FE model set up for these procedures is identical to the previous LS-TaSC model, as they work off LS-DYNA element results. Therefore, for the forthcoming, and indeed all BESO/BEETS studies, the same material properties (Table 3.1), rigidwall parameters and constraint information are used. Both procedure will be run using the BEETS Powershell software developed by J. Christensen, where for BESO all BEETS additions such as Entropy and Tabu Search (TS) are deactivated (Christensen 2015). As for the BEETS procedures, entropy will be activated as a means of comparing both algorithms. In order to function with the software, an element set needs to be created that accommodates all design elements, named "Design". Furthermore, all elements connected to an SPC must not be included in the design elements in the current version of the software. Finally, an extra column of elements adjacent to the SPC elements is removed from the design elements set to add stability to the FE model. Aside from the filter radius comparison models (Table 3.4), all models will be given a filter radius of 30.1mm, equivalent to 3 times the element size. The optimisation parameters are given in Table 3.10 below:

Table 3.10 : BESO/BEETS optimisation parameters

ER	ARmax	Objective function tolerance	Target volume fraction
0.05	0.05	0.025	50%

Similarly to LS-TaSC the aim is to reduce the structural volume by 50%. A difference here can already be distinguished between BESO/BEETS and LS-TaSC. In the former's case, the aggressiveness of the procedure can be controlled via the Evolutionary Ratio (ER) parameter, in this case 5% of the structural volume is removed per iteration. A maximum Addition Ratio (ARmax) equal to ER is selected.

Results – BESO

Topology trends: Figure 3.39 – Figure 3.42 show the structures obtained from the BESO method, and Figure 3.43 illustrates a summary of the topology trends:

(a)

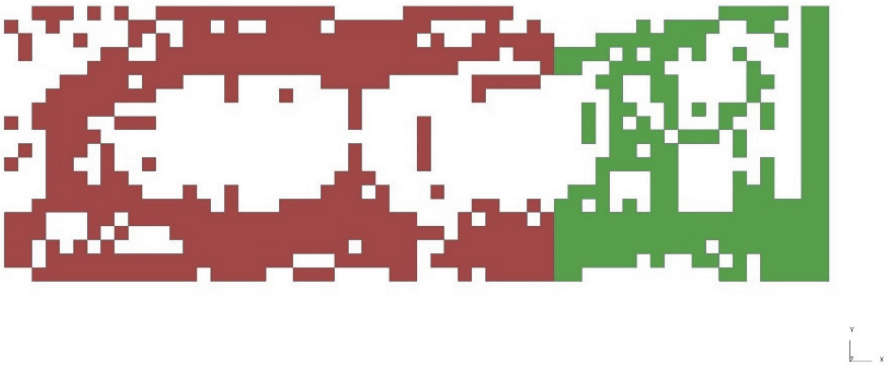

(b)

(c)

Figure 3.39 : Final topology (a) Model 24 (b) Model 25 (c) Model 26

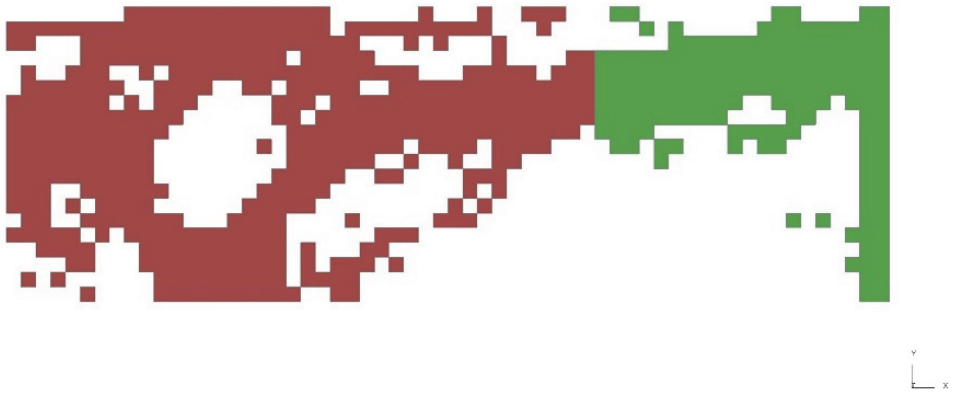

Figure 3.40 : Final topology model 27

Figure 3.41 : Final topology model 28

Figure 3.42 : Final topology model 29

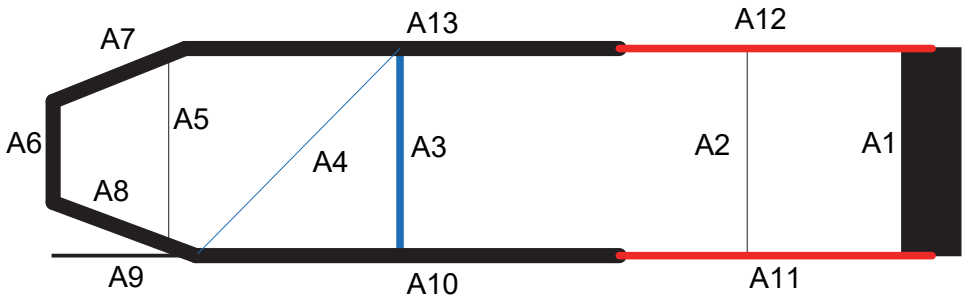

Figure 3.43 : Topology trends for models 24 - 29

The topology trends in Figure 3.43 are labelled A1 – A13, and the "thickness" of the loadpaths represent the frequency with which they appear in models 24 – 29. The colourised trends are loadpaths that do not appear simultaneously in the models. For example, loadpaths A12 and A11 do not seem to appear together in the linear section of the topologies obtained, as is the case for A4 and A3. Figure 3.43 indicated that A1 is the most common trend in all models, which is not a surprise as the linear SPCs are placed in that location. For the most part, the trends indicate horizontal members in the structure (A13 and A10) that connect to each other near the impacted edge (A6, A7, A8), although A13 and A10 do not always appear in the same model, as illustrated by Figure 3.40 and Figure 3.41.

Globally, while the loadpaths are quite clear, the topologies are quite unstable with disconnected elements and visible checkerboard patterns. Furthermore, and interestingly, the filter radius has no visible effect on the topology. One explanation could be that the radius is only applied to void elements, and therefore perhaps has less effect than the filter radius scheme described in Huang and Xie (2010). Another explanation could be the highly dynamic scenario creates large differences between element strains.

Feasibility of topology results: Compared to the low velocity LS-TaSC models when SIMP is not activated, it could be argued that the feasibility is greater in that the information provided on loadpaths is clearer than the thickness distribution method of LS-TaSC when the velocity is lower. As previously mentioned however, the amount of checkerboard patterns and disconnected elements somewhat reduces this advantage. Activating the SIMP option in LS-TaSC didn't show less "variable" thickness in the optimised solution (Figure 3.37), although this is most likely due to an already clear topology in model 12 (Figure 3.33). However, it should be reiterated that the LS-TaSC method, with the SIMP option activated, failed to converge with an automatic convergence tolerance parameter.

Linear/Non-linear compatibility: Much like the LS-TaSC method, the advantage of BESO/ BEETS resides with its use of LS-DYNA as an FE solver, and therefore is capable of catering for non-linearities, as shown by the plastic strain distribution plot for model 27 (Figure 3.44):

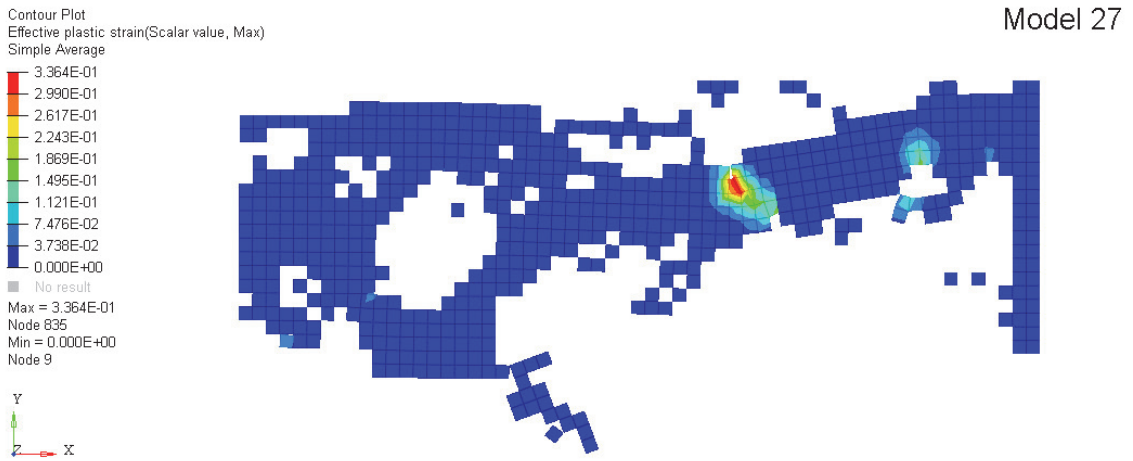

Figure 3.44 : Model 27 plastic strain plot

Other findings: Compared to LS-TaSC, it was observed that the BESO/BEETS method converged and terminated much quicker than LS-TaSC for the same models, precisely after 16 iterations for most cases. This is compared to LS-TaSC, which failed to converge after 100 iterations. This is obviously a big advantage for BESO based algorithms. Overall however, it has been demonstrated that BESO can be improved if it is set to be a candidate for hybrid TO.

Results – BEETS

As mentioned in the literature review, the aim of the BEETS method was to avoid or reduce the disadvantages presented by BESO.

Topology trends: Figure 3.45 – Figure 3.48 show the structures obtained from the BEETS study for models 30-33 and Figure 3.49 illustrates a summary of the topology trends:

Figure 3.45 : Final topology model 30

Figure 3.46 : Final topology model 31

Figure 3.47 : Final topology model 32

Figure 3.48 : Final topology model 33

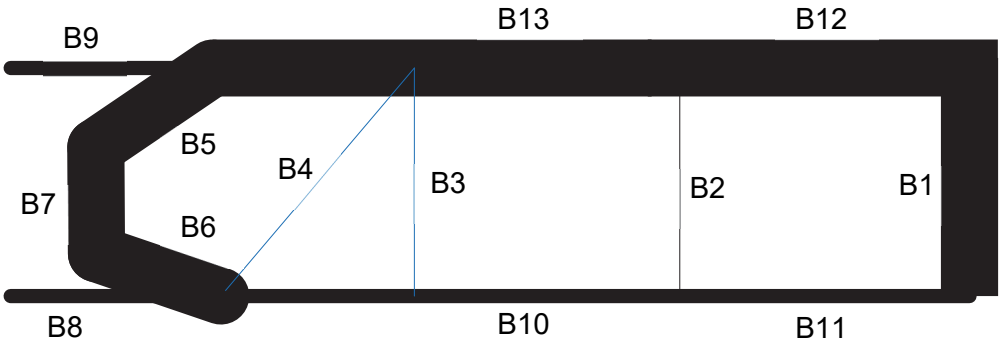

Figure 3.49 : Topology trends for models 30-33

Compared with the trends from the BESO models Figure 3.43, Figure 3.49 indicates that several loadpaths appear more often, specifically the impacted loadpaths (B5, B6 and B7) and the upper horizontal loadpaths (B12 and B13). The trends are very similar for the “internal” load paths, with B3 and B4 not appearing in the simultaneously. B8 and B9 indicate that compared to the BESO models, there is a greater tendency to generate a horizontal loadpath that extends entirely to the impacted edge of the structure.

While not globally eliminated, it is clear from these examples that the checkerboard effect and disconnected elements observed for BESO are greatly reduced. As a result, the loadpaths are much clearer. It can be observed that the BEETS optimised structures greatly resemble their BESO counterparts (except for model 28, however the topology for the latter is relatively uninformative). This reinforces the statement that BEETS is an improvement on BESO’s shortcomings, without however changing the overall results (as BEETS is BESO-based).

Feasibility of topology results: Clearly, compared to BESO, the final topologies are an improvement and provide much clearer information to the user. By observing two analogous models (model 26 and model 30 for example), there is a clear reduction in disconnected elements and checkerboard patterns (Figure 3.39(c) and Figure 3.45 respectively). This is not the case when comparing the BEETS results with those of LS-TaSC. While it can be argued that from a feasibility point of view, some of the LS-TaSC models are relatively poor, i.e. many intermediate thicknesses, the same could be said with BEETS with its detached elements. Furthermore, the intermediate thicknesses can be suppressed by activating the SIMP option.

Linear/Non-linear compatibility: In terms of non-linear compatibility, there are no differences between BESO and BEETS as both feed off LS-DYNA results. An extra advantage of BEETS is the improved simulation stability due to the reduced checkerboard patterns and disconnected elements.

3.2.4. Conclusion

Overall, for purely non-linear behaviour, both the BEETS and LS-TaSC solvers have shown benefits and drawbacks. BEETS is a quicker optimisation process compared to LS-TaSC (Table 3.11):

Table 3.11 : BEETS vs LS-TaSC run time comparison

	BEETS	**LS-TaSC**
Number of iterations	16	100
Total run time (estimated in minutes)	30 (model 30)	200 (model 10)
Convergence achieved	Yes	No

However, LS-TaSC produced final topologies with no detached elements which BEETS was unable to remove completely, despite the improvement compared to BESO. The aim of this PhD is to be able to cater for both linear and non-linear behaviour within the same structure. The next section will therefore analyse a case where the two sections of the plate are defined similarly to what would be expected from a vehicle BIW structure: section (1) using non-linear material definition and section (2) using linear material definition. ESLM is discounted from this study as this section has shown that its shortcomings when dealing with high levels of non-linearity, a pattern repeated during the following study. Therefore only LS-TaSC and BESO/BEETS models will be discussed.

3.3. Combined linear / non-linear model

Each model used in this section has exactly the same definition (loading, SPC, etc.) as the ones studied in the previous section, the only difference being the material definition of section (2) (Figure 3.1) changing from non-linear to linear. The same optimisation parameters as in Table 3.8 for LS-TaSC and Table 3.10 for the BESO/BEETS algorithms are used. Table 3.12 summarises the models for this study:

Table 3.12 : Models for combined linear/non-linear behaviour study

Model Number	Optimisation Algorithm	Plate section definition		Static/Dynamic analysis	Plate material	Loading magnitude (High/Low)	Constraints
		Section 1	Section 2				
17	LS-TaSC	NL	L	Dynamic	HSS	High Velocity	SPC
18	LS-TaSC	NL	L	Dynamic	Mild Steel	High Velocity	SPC
19	LS-TaSC	NL	L	Dynamic	HSS	Low Velocity	SPC
20	LS-TaSC	NL	L	Dynamic	Mild Steel	Low Velocity	SPC
34	BESO	NL	L	Dynamic	Mild Steel	Low Velocity	SPC
35	BESO	NL	L	Dynamic	Mild Steel	Low Velocity	SPC
36	BESO	NL	L	Dynamic	Mild Steel	Low Velocity	SPC
37	BESO	NL	L	Dynamic	HSS	Low Velocity	SPC
38	BESO	NL	L	Dynamic	Mild Steel	High Velocity	SPC
39	BESO	NL	L	Dynamic	HSS	High Velocity	SPC
40	BEETS	NL	L	Dynamic	Mild Steel	Low Velocity	SPC
41	BEETS	NL	L	Dynamic	HSS	Low Velocity	SPC
42	BEETS	NL	L	Dynamic	Mild Steel	High Velocity	SPC
43	BEETS	NL	L	Dynamic	HSS	High Velocity	SPC

Firstly, the LS-TaSC models will be studied followed by the BESO/BEETS examples.

3.3.1. LS-TaSC

Results

Topology trends: Figure 3.50 – Figure 3.53 show the thickness distribution obtained for models 17-20 respectively.

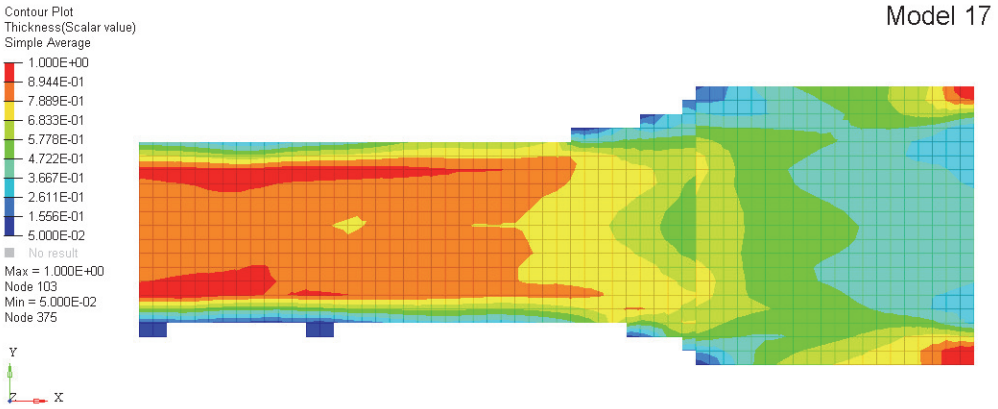

Figure 3.50 : Model 17 thickness distribution

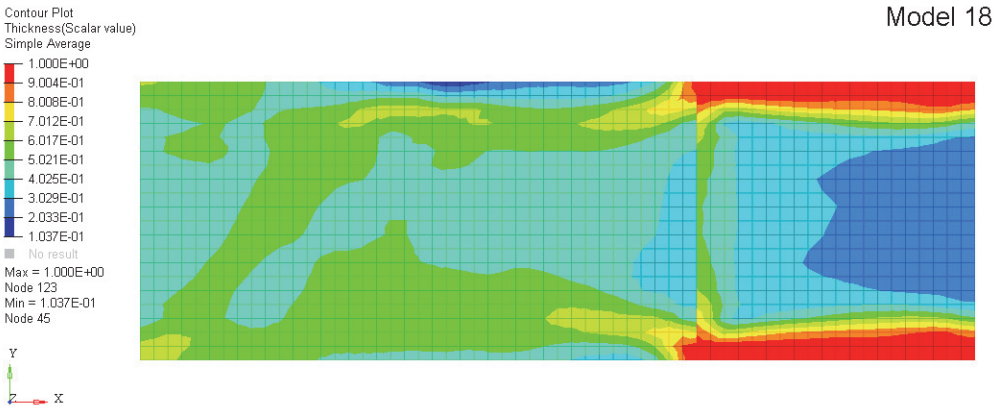

Figure 3.51 : Model 18 thickness distribution

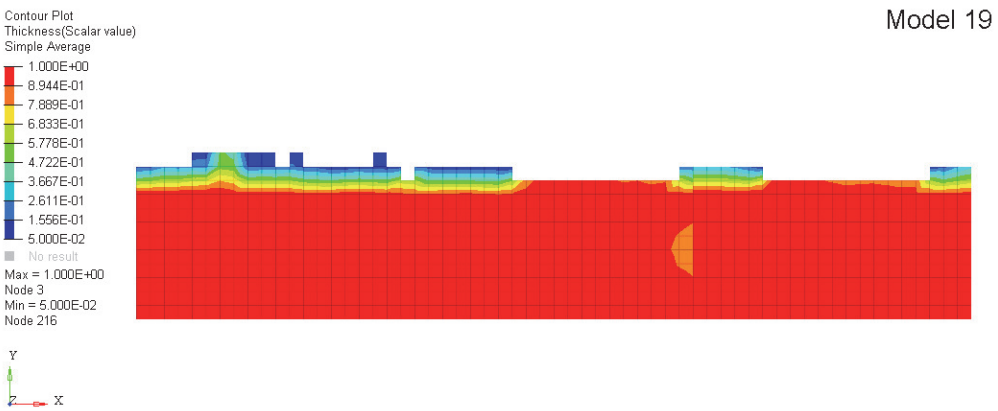

Figure 3.52 : Model 19 thickness distribution

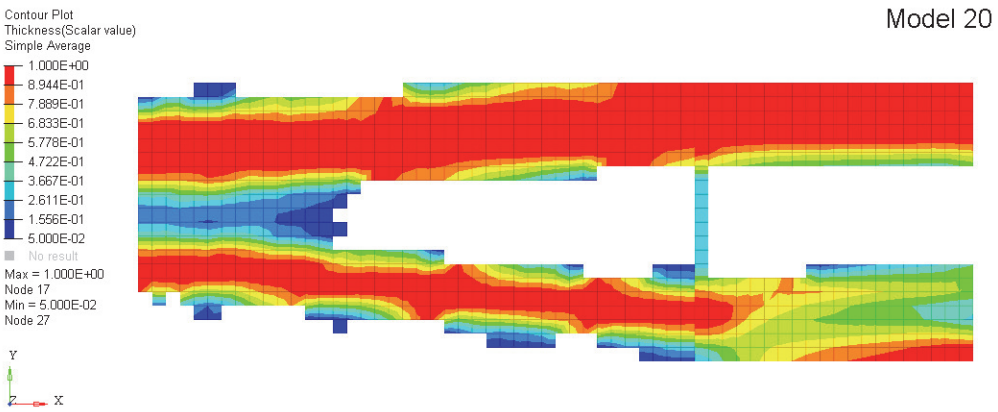

Figure 3.53 : Model 20 thickness distribution

At a glance, there are no real trends between the models. A closer look however reveals that there are some similarities, particularly for the linear section (2). Excluding model 19, which from the result does not seem to follow any logical pattern for the applied loadcase, most of the material in the linear section is located on the upper and lower edges of the plate. The distribution shows there are two influences on the linear section: firstly, the material distribution at the interface between both sections, essentially the load inputs into the linear section. Secondly, the constraints on the right hand edge also have an influence, which leads back onto the discussion of constraints for linear behaviour and the possible use of IR. This would in all likelihood need a combination of Optistruct and a non-linear capable algorithm to cater for both linear and non-linear behaviour. Essentially this is a first indication of a potential solution for hybrid TO.

Feasibility of topology results: Much like the other LS-TaSC models, once again the feasibility is reduced due the various thicknesses present in the model. It is difficult to obtain conclusive design ideas from these solutions. For example, a rough FE model based on the solution for model 17 was set up and a simple analysis performed with the same loadcase/parameters as model 17 (Figure 3.54). In this instance, being a re-analysis model, both sections of the structure are assigned the non-linear material card.

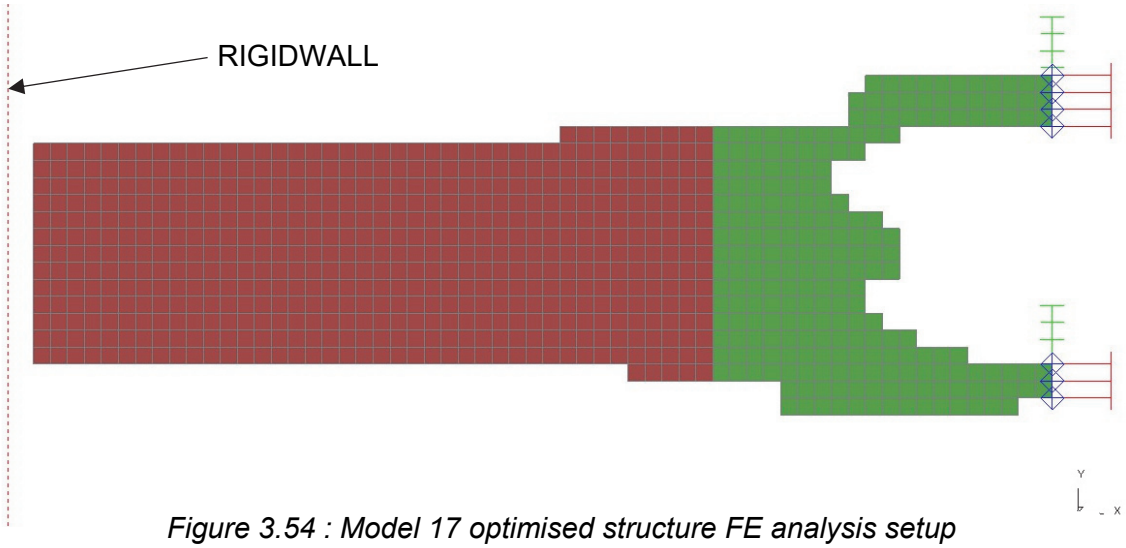

Figure 3.54 : Model 17 optimised structure FE analysis setup

Figure 3.55 displays the behaviour at t=0.008s and Figure 3.56 at t = 0.014s

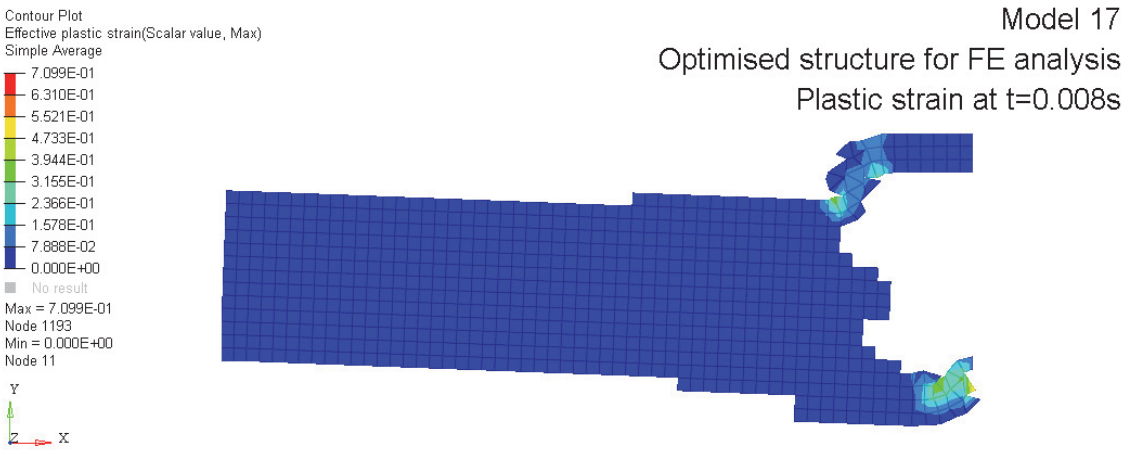

Figure 3.55 : Model 17 optimised for FE analysis plastic strain at t=0.008s

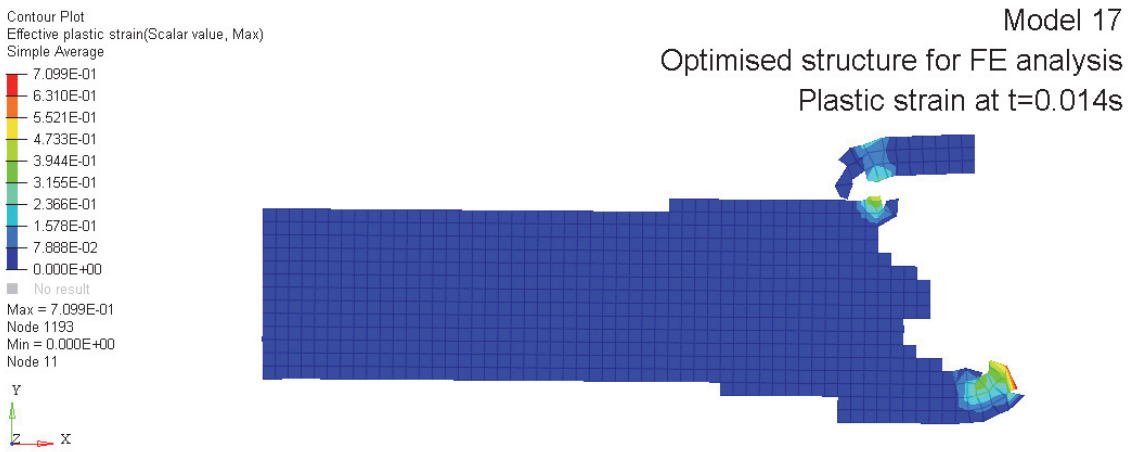

Figure 3.56 : Model 17 optimised for FE analysis plastic strain at t = 0.014s

Figure 3.56 shows that the structure fails in section (2) of the structure at t = 0.014s. This clearly calls into question the validity of the solution, and by extension could indicate that LS-TaSC is not well adapted for coupled linear/non-linear behaviour.

Other findings: Visualising the deformation trends for models 17-20, the primary deformation mode for the non-linear section (1) seems to be buckling. In order to avoid this phenomenon, model 61 was set up with a shorter non-linear section (2) of 130mm instead of the original 400 mm (Figure 3.57).

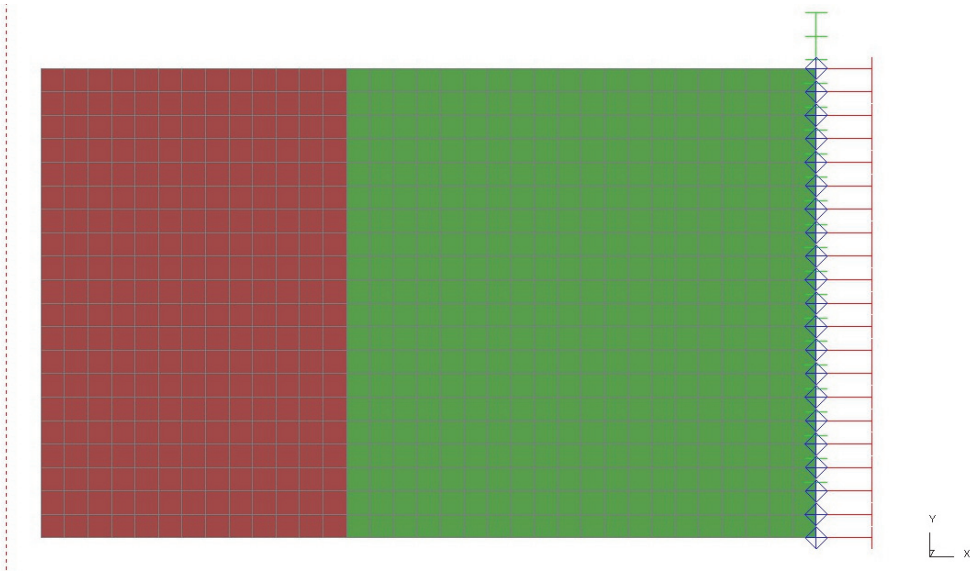

Figure 3.57 : Model 61 setup

Figure 3.58 shows the thickness distribution obtained and Figure 3.59 the von Mises stress plot obtained:

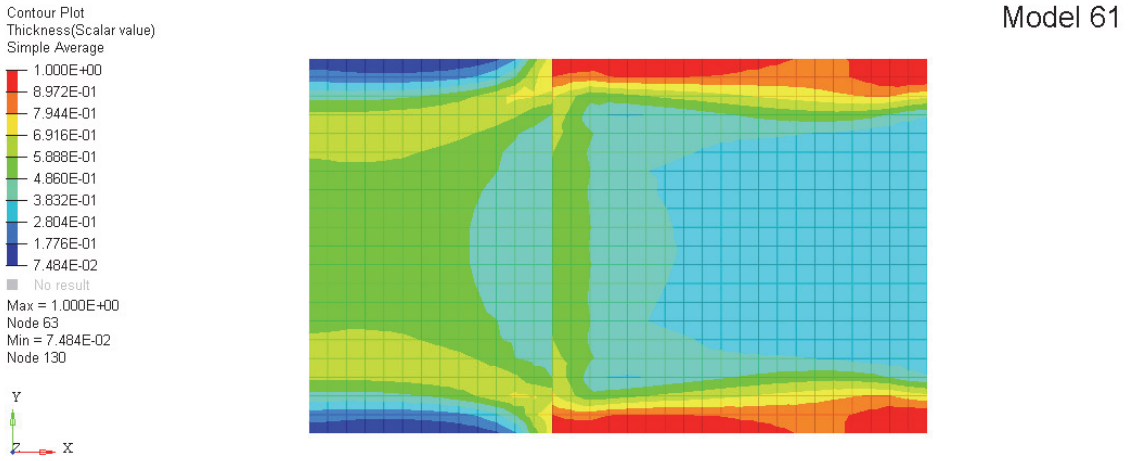

Figure 3.58 : Model 61 thickness distribution

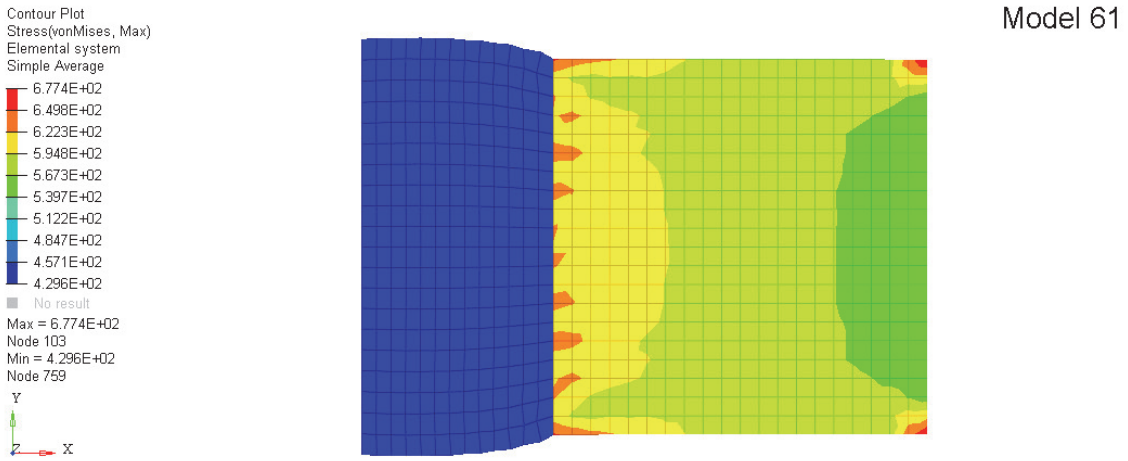

Figure 3.59 : Model 61 von Mises stress plot (MPa)

The deformation is more stable than model 17, in that it avoids buckling modes, and the result is a more symmetrical topology. However, from a feasibility point of view, there is no improvement compared to the previous models, i.e. thickness distribution.

Finally, similarly to the two previous studies into LS-TaSC, model 62 is created based on model 20 with the SIMP option activated to determine whether this improves LS-TaSC's ability to handle coupled linear/non-linear behaviour. Figure 3.60 below illustrates the structure obtained after 100 iterations, i.e. the maximum number selected:

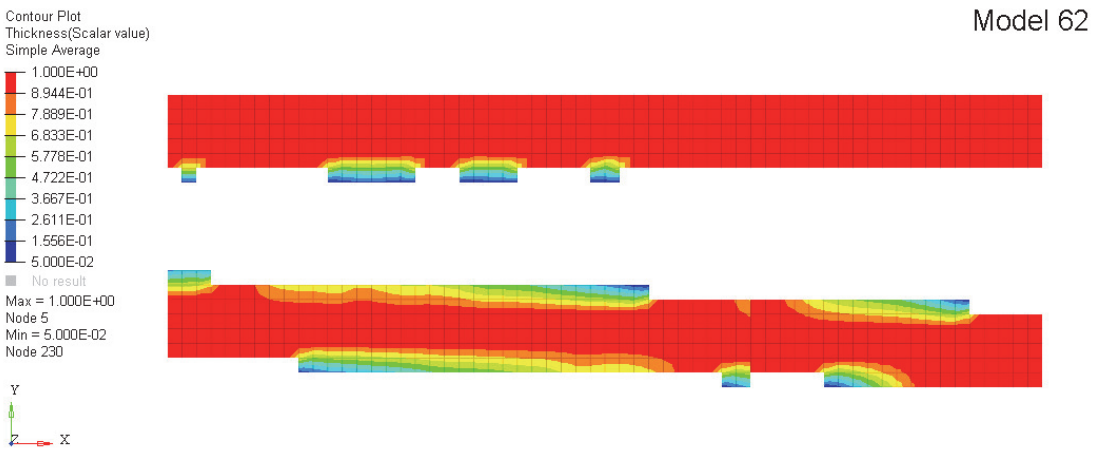

Figure 3.60 : Model 62 thickness distribution

This result is in essence very similar to the original model 20 (Figure 3.53), where the low thickness areas have been removed. The re-analysis is set up in the same fashion as model 17, i.e. both sections (1) and (2) assigned non-linear material. Figure 3.61 below illustrates the plastic strain after re-analysis:

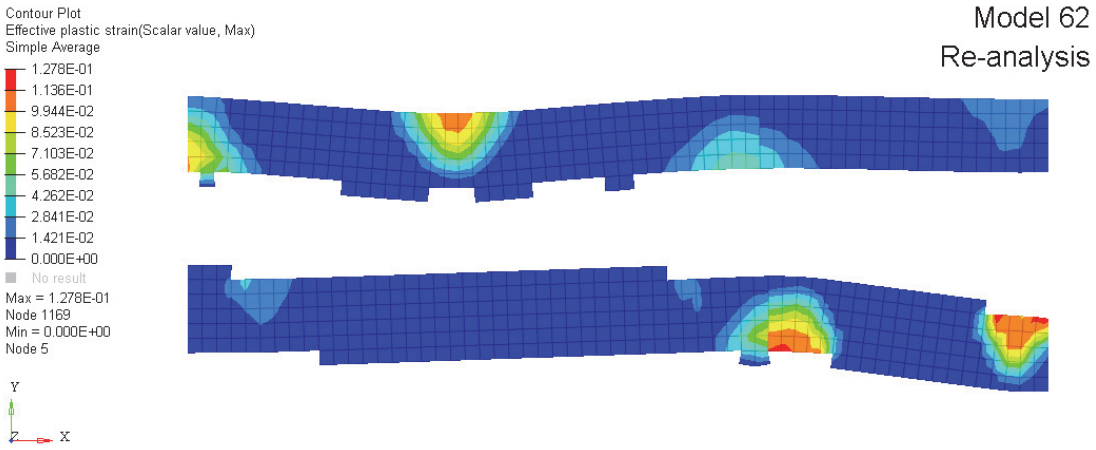

Figure 3.61 : Model 62 re-analysis plastic strain plot

Although not as severe as for the re-analysis of model 17, there is still a large amount of plastic strain in section (2) of the structure (a value of around 13% in the lower member). In order to verify the influence of activating SIMP, model 63 was set up this time based on model 18 as the thickness distribution contained more intermediate thicknesses. Figure 3.62 below illustrates the thickness distribution result and Figure 3.63 the behaviour of the structure when re-analysed:

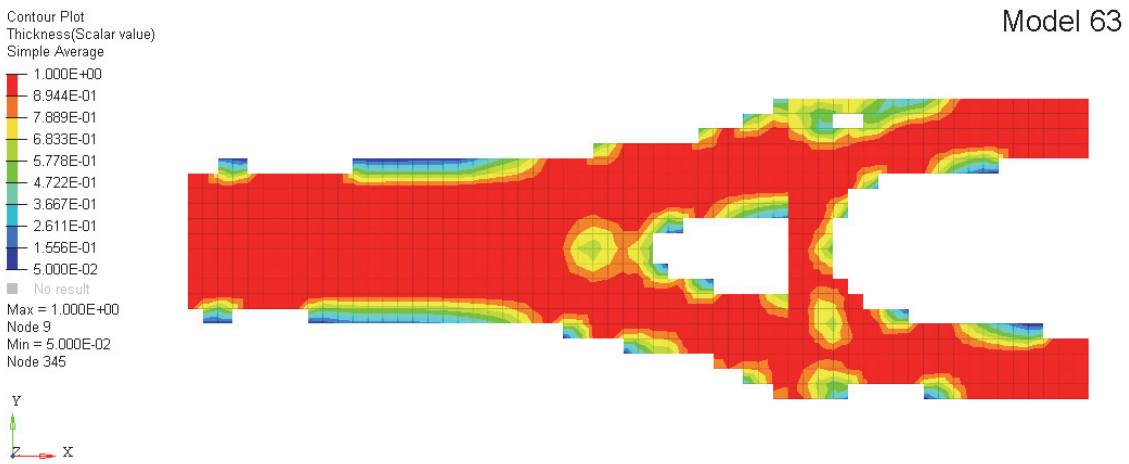

Figure 3.62 : Model 63 thickness distribution

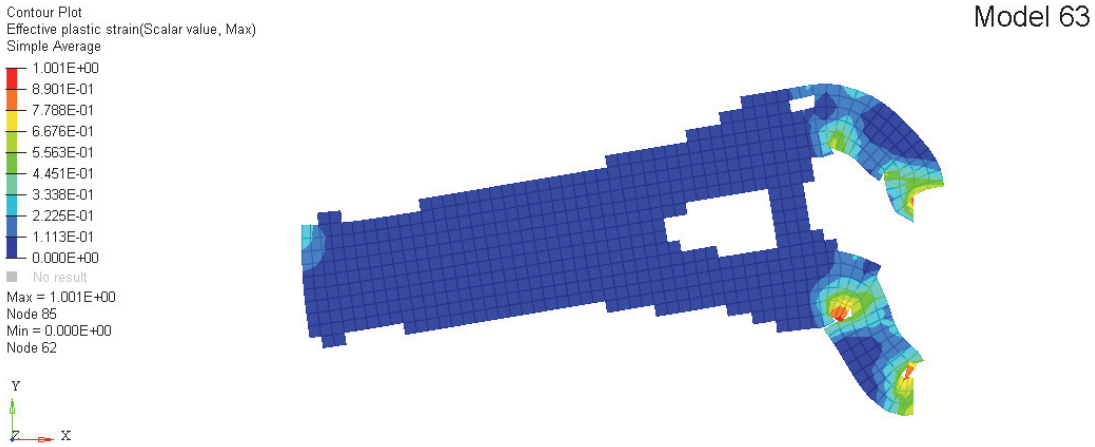

Figure 3.63 : Model 63 re-analysis plastic strain plot

This behaviour is captured at t=0.014s before a disconnection similar to Figure 3.56 occurs. Overall, activating SIMP has not enabled LS-TaSC to cater for coupled linear/non-linear behaviour

This section has highlighted a couple of important points. Firstly, the difference between purely non-linear and combined linear/non-linear means the definition of each section before optimisation is critical to the process. Secondly, the interface between the two sections is also key the process, and how the loadpaths are defined between the two.

3.3.2. BESO / BEETS

The previous BESO/BEETS study for purely non-linear structures highlighted the improvements of BEETS relative to the original BESO process for non-linear

optimisation. This section will look into the validity of the BESO/BEETS procedure when subjected to a mixture of linear and non-linear behaviour.

Results – BESO

Topology trends: Figure 3.64 – Figure 3.67 show the optimised structures obtained for models 34-39:

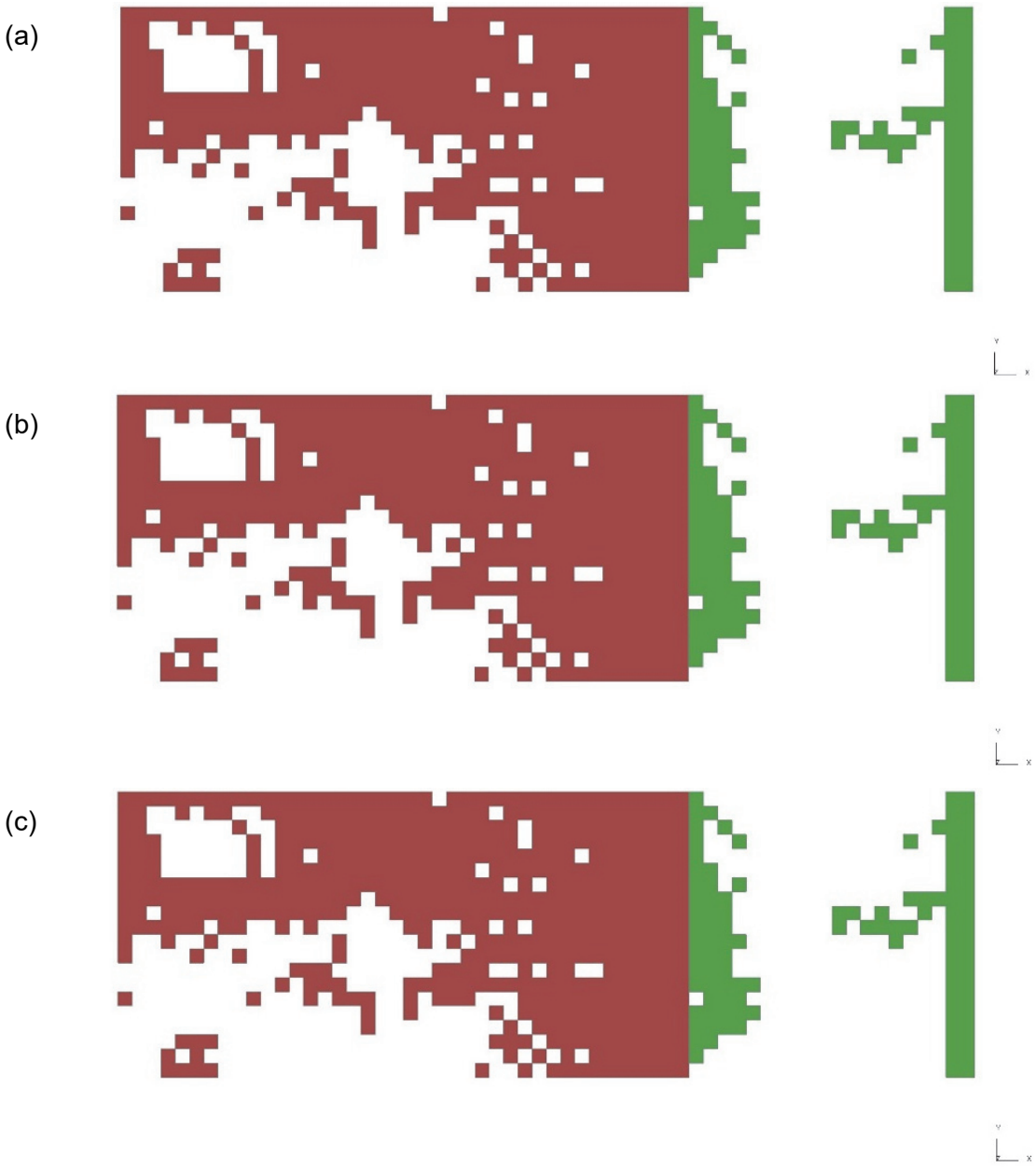

Figure 3.64 : Final topology (a) model 34 (b) model 35 (c) model 36

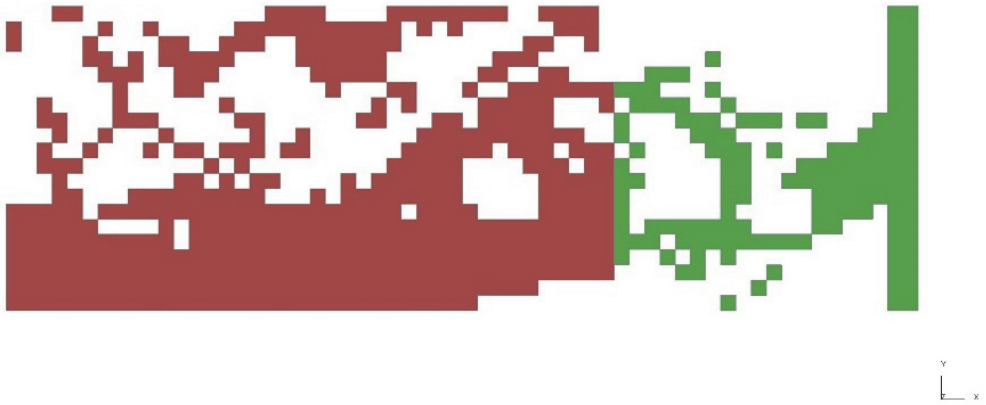

Figure 3.65 : Final topology model 37

Figure 3.66 : Final topology model 38

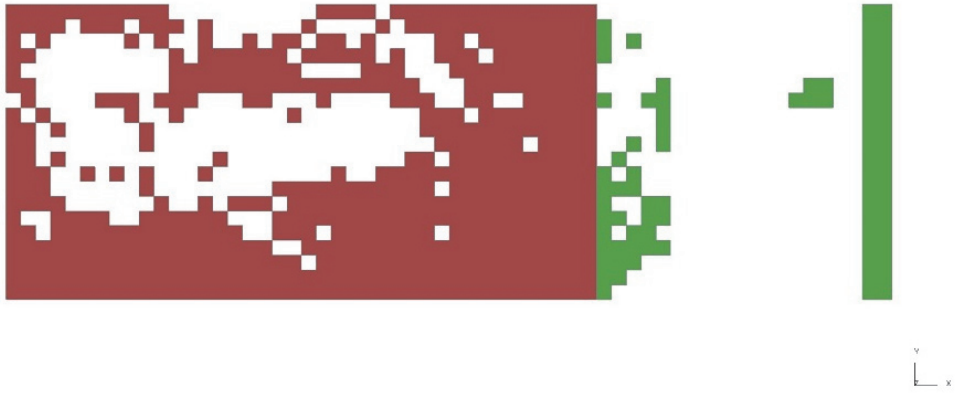

Figure 3.67 : Final topology model 39

The first noticeable trend in all these models (save for model 37) is the complete breakdown of the structure in section (2), which in these studies uses linear material definition. This result is somewhat expected, as relative to the non-linear section, the strain levels in section 2 are much lower, as shown by Figure 3.68:

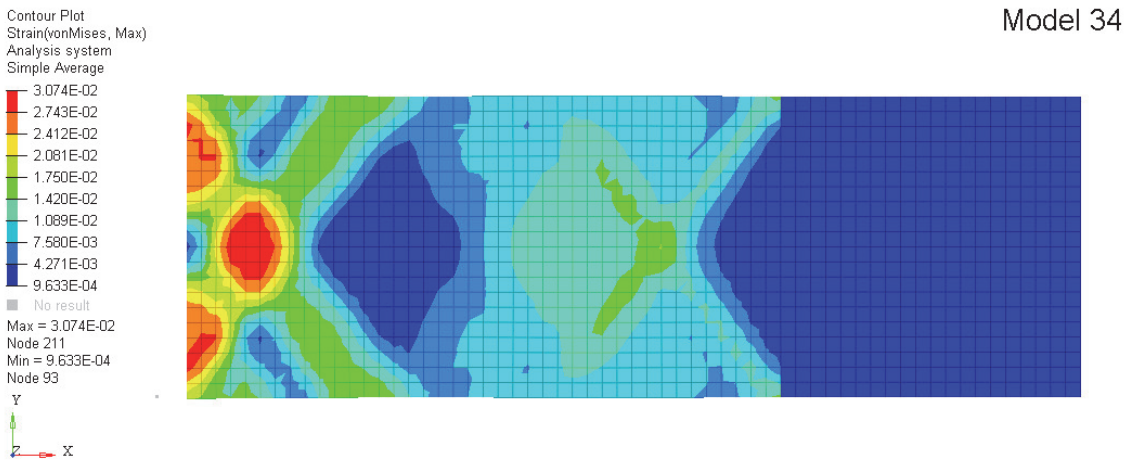

Figure 3.68 : Model 34 initial von Mises strain distribution

Therefore, the algorithm recognises the low levels of strain and removes elements from section 2. Therefore, it is the author's belief that BESO has very limited indeed almost no capabilities when handling both linear and non-linear behaviour. Another trend, parallel to the purely non-linear case studies is the lack of effect of the filter radius, as shown by the three models in Figure 3.64. Again, this effect will warrant further study.

Feasibility of topology results: In terms of feasibility, these structures offer very little information on optimal load paths. Furthermore, the disconnection between the non-linear and linear section is an obvious flaw in the design and cannot be considered manufacturable. In this regard, it could be argued that LS-TaSC is a better option than BESO.

Linear/Non-linear compatibility: The results clearly show that in terms of catering for both linear and non-linear behaviour simultaneously, BESO on its own falls short of being a viable option. Figure 3.65 does display a less severe breakdown of the structure compared to the other BESO models. This is due to a combination of low velocity impact and HSS material definition, meaning the relative difference in strain values between sections (1) and (2) is lower. However, while not completely broken it is clear that the connections between section (1) and section (2) in model 37 are still very limited. The next section will analyse whether BEETS provides a better option than BESO for this particular scenario.

Results – BEETS

Topology trends: Figure 3.69 – Figure 3.72 show the optimised structures for models 40 – 43

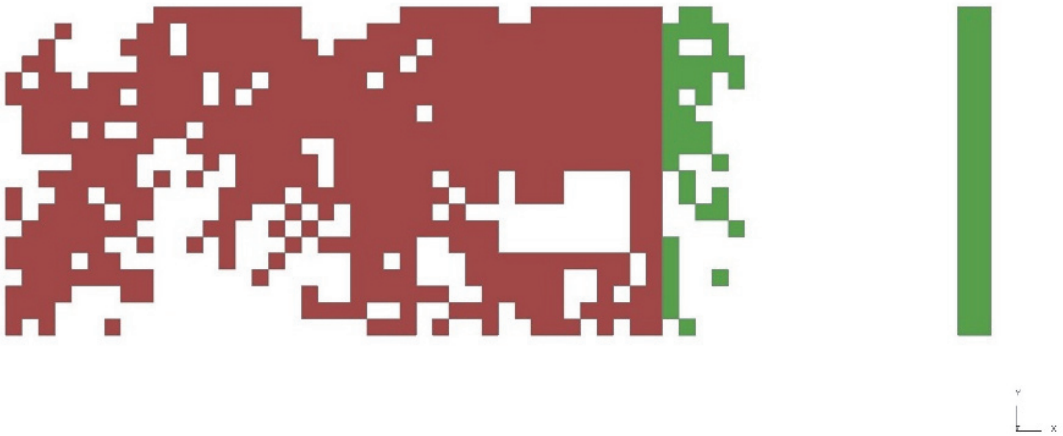

Figure 3.69 : Final topology model 40

Figure 3.70 : Final topology model 41

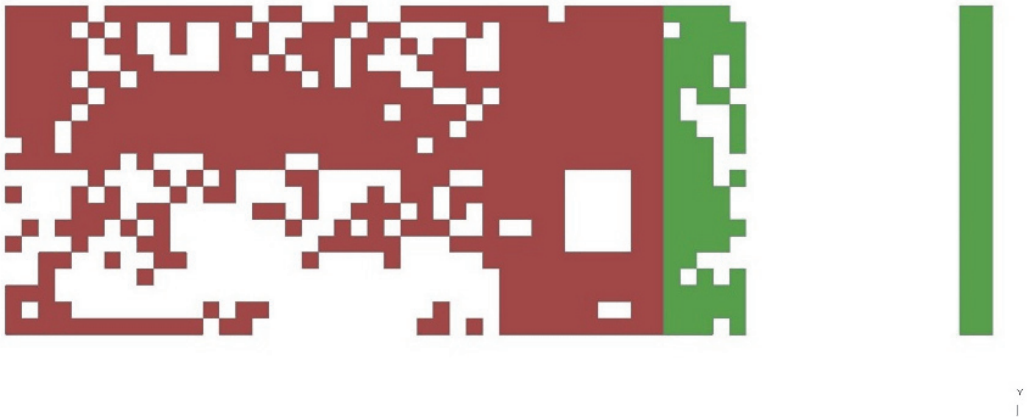

Figure 3.71 : Final topology model 42

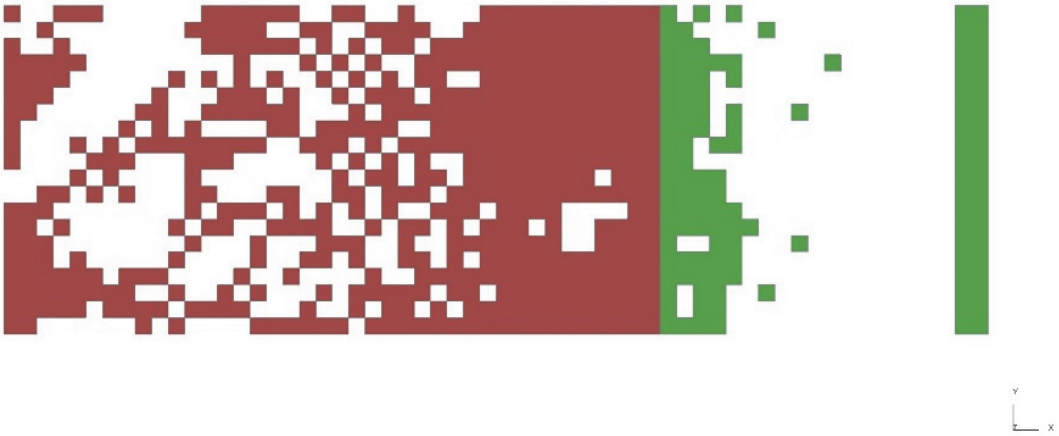

Figure 3.72 : Final topology model 43

Once again, in all examples there is a breakdown in the structure in section 2, for the same reasons indicated for BESO. This is not a surprise, as BEETS works off the same LS-DYNA FEA results as BESO, and of course BEETS is primarily a BESO-based algorithm, therefore the breakdown was likely.

Feasibility of topology trends: The same conclusions can be made for BEETS as was made for BESO. There is a clear lack of connection between section (1) and section (2) which results in an unfeasible structure.

Linear/Non-linear compatibility: Similarly to BESO, the BEETS method shows many limitations with regards to catering for both linear and non-linear behaviour. In this case none of the models maintain any connections in section 2, therefore their validity as load path indicators is questionable.

3.4. Conclusion

This study has highlighted a crucial aspect of current TO methods: there is no single algorithm currently available that produces coherent, feasible and informative results for structures that display both linear and non-linear behaviour. The results show that LS-TaSC produces clearer solutions than BESO or BEETS when a structure exhibits both behaviours. However it has been shown that the credibility of the results are limited, and that the thickness distribution nature means the loadpaths are sometimes difficult to determine (when the SIMP option is not activated for shell elements in LS-TaSC). It is also clear that the alternatives, BESO and BEETS, are not suited to catering for coupled linear/non-linear behaviour. Therefore the idea of a hybrid method is put forward, where the most suitable algorithms are used and combined for linear behaviour and non-linear behaviour. From the linear studies, it is clear that the VDM/SIMP method used by Optistruct is a quicker, more reliable method when compared to LS-TaSC. Consequently, for linear sections, Optistruct will be used as the optimisation software.

The choice for the non-linear optimisation solver is a more complex one, as both LS-TaSC and BEETS have shown potential to be used in the hybrid methodology. As concluded in section 3.2, BEETS is a faster process compared to LS-TaSC which after 100 iterations failed to converge. This is despite an automatic convergence tolerance being selected when SIMP was activated. However, BEETS also suffers from detached elements, and so the loadpaths could be deemed less meaningful than LS-TaSC, specifically when SIMP is activated for the latter. In essence, both of the solvers could be implemented within the hybrid optimisation methodology, and as a future direction for the methodology, the user could potentially select either. For the purposes of this PhD, BEETS is selected due to access to the source code (and by extension the possibility for refinement) and its quicker run time. However, it should be reiterated that BEETS could potentially be swapped for LS-TaSC. The essence of this PhD lies in the combination of existing optimisation algorithms into the hybrid methodology, not the creation of an entirely new one algorithm.

From these conclusions, a hybrid method is therefore suggested combining Optistruct for linear behaviour and BEETS for non-linear behaviour to cater for both in the same structure. The next chapter will present the combined method and the articulation of both algorithms at the interface between linear and non-linear sections.

4. Methodology

The previous chapter investigated the various structural topology optimisation (TO) solvers and their suitability for combined linear/non-linear behaviour. The results from this study demonstrated the need for a hybrid methodology whereby two algorithms are combined in order to cater simultaneously for linear and non-linear behaviour. Bi-directional Evolutionary Entropy Tabu search Simulated Annealing (BEETS) and Optistruct were selected as the algorithms to combine, and this following chapter will describe the process of creating and programming the hybrid algorithm, with a particular focus on the interface that will provide both a physical, i.e. the structure / Finite Element (FE) model, and computational, i.e. scripting, link between the two.

4.1. Hybrid optimisation: Interface parameters

Figure 4.1 is an extension of Figure 3.1, which displays the starting point for the hybrid optimisation process. In essence there are two FE models, one modelled in LS-DYNA for non-linear optimisation using BEETS (section 1) and the other modelled for linear optimisation via Optistruct (section 2). The interface previously mentioned is therefore key for exchanging data (e.g. interface forces) between the two models.

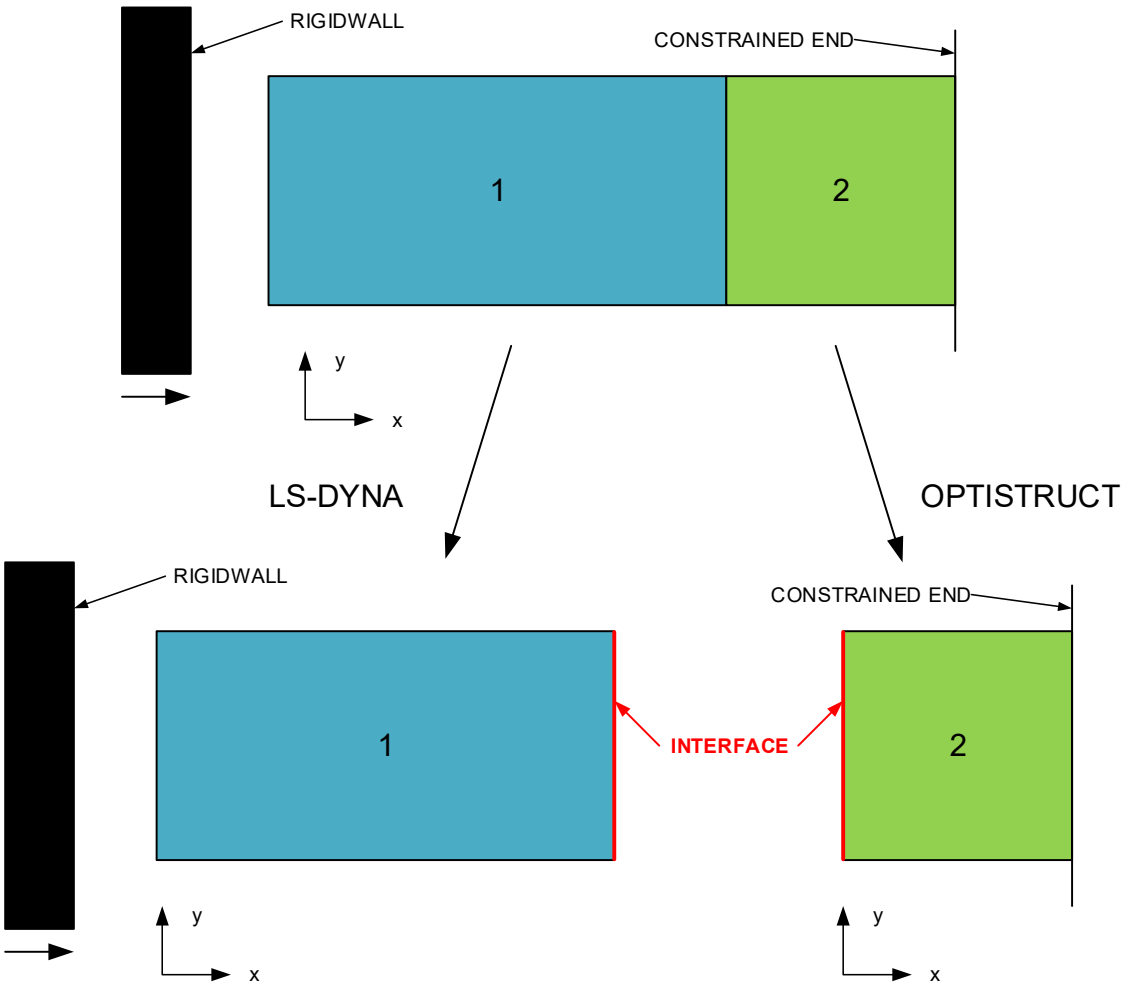

Figure 4.1 : Hybrid optimisation basic FE setup

The first step in developing the hybrid algorithm is to identify any parameters linking the non-linear and linear sections as in essence changes to parameters at the structural interface may modify the model boundary conditions (BCs), which will filter down to the optimisation process.

- **Interface size (Number of elements):** This parameter will essentially determine how many non-design elements are present within the non-linear model, which provides a “buffer zone” that guarantees a connection between the two sections. The presence or not (and size for the former) will be studied to evaluate the effects on the optimised structures.
- **Rate of exchange:** The interface’s role in transferring forces from the non-linear model to the linear model has been mentioned. The rate of exchange in this instance is similar to the external/internal loop process for the Equivalent Static Load Method (ESLM). This parameter determines how many BEETS iterations (non-linear optimisation) are performed before the interface force data is

transferred over to the linear optimisation process. The second part of the rate of exchange determines how many maximum iterations can be performed within the Optistruct run by modifying the DESMAX value (Altair 2017). In theory, an increase in data exchange frequency should provide a more efficient final optimised structure, as the force data input used in the linear optimisation solver is updated. However, the gains in accuracy and performance could be marginal against an extended run time. Different combinations of the two facets of this parameter will be analysed.

- **Linear model optimisation objective / constraint*:*** The linear model, i.e. Optistruct, optimisation criteria are set originally to match the BEETS process, specifically minimising the compliance (objective) subject to a target volume per external iteration (constraint). The latter is modified dynamically to match the BEETS evolutionary ratio (ER) and the rate of exchange discussed previously. This set up ensures a final combined structural volume close to the target volume specified by the user in the BEETS process. However, another common approach to linear optimisation is to minimise mass (or volume), subjected to specific constraints on displacement or stress (Altair University 2015). Therefore, the difference in overall structural performance will be analysed with the two optimisation constraint settings.
- **Interface boundary conditions (BC):** The parameters identified so far have focused on the exchange of forces from the non-linear optimisation process to the linear process. A second crucial aspect is the constraints applied at the interface in the non-linear model. Commonly, Single Point Constraints (SPCs) or another form of rigid tied connections (nodal rigid bodies / constrained extra nodes in LS-DYNA) would be applied. However, in the case of hybrid optimisation, the non-linear model only represents part of the whole structure and applying SPCs at the interface could be simplistic when considering the interface links with a compliant structure, i.e. the linear model. Therefore, a BC method using zero length beams on the interface reflecting the linear model (via the beam stiffness) will form part of the algorithm. The latter is detailed in section 4.2.4.
- **Linear model BCs:** The previous chapter introduced and analysed Inertia Relief (IR) included in the linear model, and concluded on the need for further analysis regarding its influence on the linear optimisation process, specifically regarding the mass elements applied. Therefore, IR capabilities will be integrated within the hybrid optimisation process.

These are the main parameters that need to be considered when designing and programming the hybrid optimisation algorithm, as they will correspond either to a change in the FE model or variables defined specifically for the hybrid process. Having identified these parameters, the next section will describe the main programming aspects surrounding the interface.

4.2. Hybrid optimisation: Software development

The overall flowchart for the hybrid optimisation algorithm is defined in Figure 4.2.

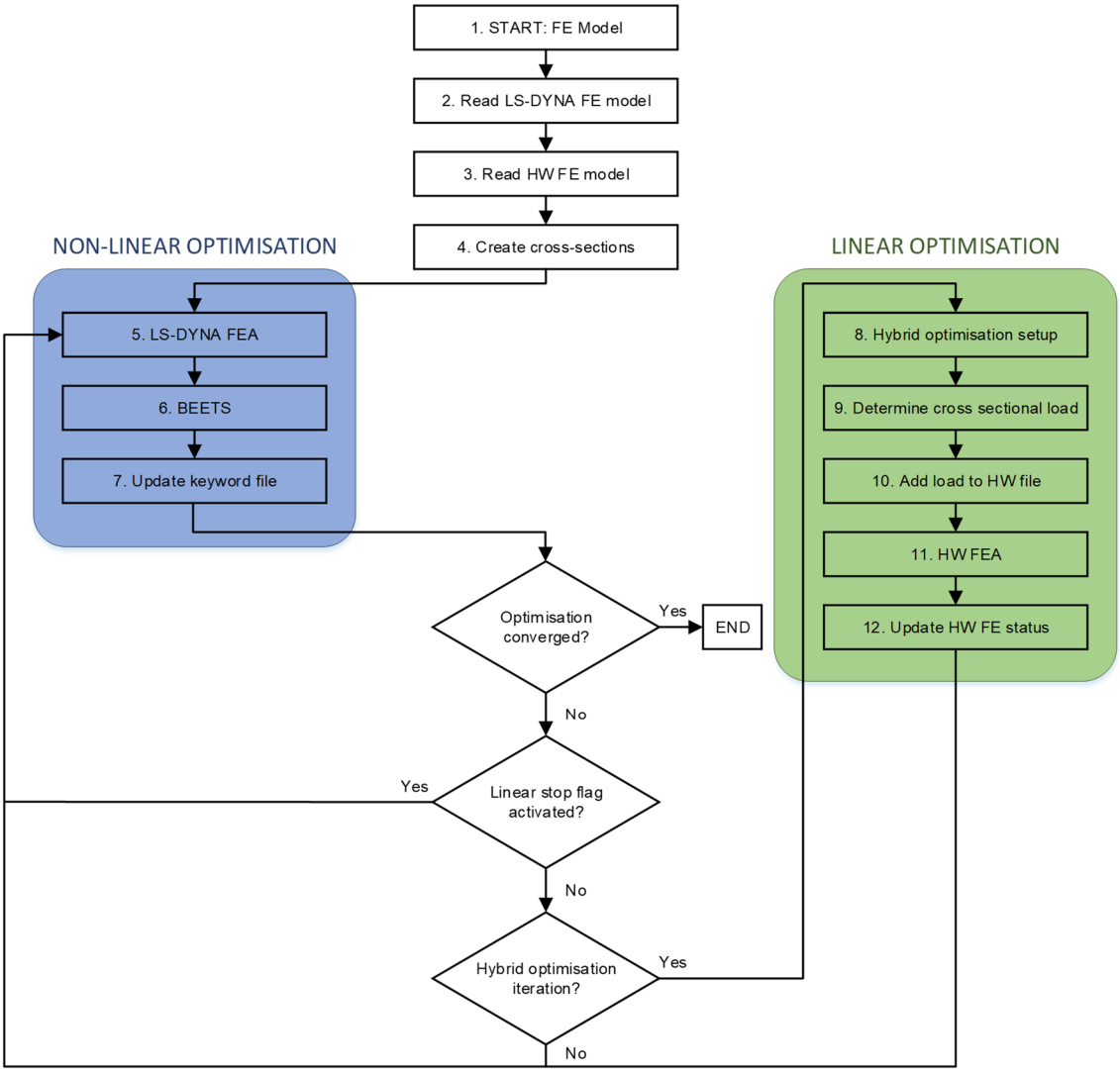

Figure 4.2 : Overall hybrid optimisation algorithm flowchart

It should be noted that the BEETS section of the flowchart is not expanded, as it is taken from Figure 2.12. As mentioned in the previous chapters, the BEETS algorithm in this case corresponds to the BESO algorithm with the statistical entropy module activated, i.e. Tabu Search (TS) and Simulated Annealing (SA) are not used.

During the BEETS development stage described by Christensen (2015), Windows Powershell was chosen as the basis for scripting the algorithm. It allows for modifications of the FE models (which can be considered as text files in their structure (Christensen 2015)) and can execute external software, in this case useful for running both Optistruct and LS-DYNA solvers. Furthermore, High Performance Computing (HPC) capabilities have been added to BEETS, and Windows Powershell allows for access, upload and download of data from Secure Shell (SSH) networks. Therefore, and in order to create a versatile and complete optimisation suite with an eye also on any future developments, integrating hybrid optimisation aspects into the existing BEETS software via Windows Powershell is chosen. Table 4.1 lists the main functions added to BEETS and their purpose within the hybrid optimisation algorithm:

Table 4.1 : Summary of hybrid optimisation functions

File	Description	Algorithm steps (Figure 4.2)	Notes/equations used
A	Read and extract from the Optistruct .fem file the element / node information (coordinates, connectivity) and creates .fem template files for adding updated element / node information	3	
B	Determines the presence of non-design elements and updates the elements hashtable ($Delements) accordingly	3	
C	Calculates the total structural volume depending on the status of elements in the FE model (retained or removed)	3	
D	Creates cross sections at the interface nodes/elements in the non-linear model. Interface elements/nodes are determined by specifying in LS-DYNA a node set named "Interface_Nodes_xx" where "xx" denotes the number of the interface	4	Process detailed in section 4.2.1 and Figure 4.5
E	From the extracted force data of the non-linear optimisation run, determines the individual nodal forces applied at the interface in the linear model	9	Process detailed in section 4.2.1
F	Similar to the function applied for the BEETS optimisation process, determines neighbouring elements for each element in the linear model within a user defined radius	3	
G	Sets up the hybrid optimisation by determining: - Equivalence between LS-DYNA and Optistruct interface nodes (using user defined radius) ➔ 1st iteration only - Add optimisation parameters to the template files depending on objective / constraints selected by user at beginning of hybrid process ➔ 1st iteration only - Add element, node and boundary condition data depending on status determined from optimisation process (retained or removed) ➔ each iteration	8	Process detailed in section 4.2.2
H	Main function for hybrid optimisation functions, plus adds forces to the template file	Main function for 8-12	
I	Uses the relative element density data for each element extracted from Optistruct (.sh file) to determine the status of each element (1 = retained, 0 = removed), depending on the optimisation objectives / constraints used	12	Process detailed in section 4.2.3

Table 4.2 lists the names of each powershell function associated with the files from Table 4.1:

Table 4.2 : Hybrid optimisation functions names

File	Algorithm file name
A	Read_Hyperworks_FE_data.ps1
B	Determine_HW_design_elements.ps1
C	Calculate_HW_shell_element_volume.ps1 / Calculate_HW_solid_element_volume.ps1
D	Create_multiple_LSD_cross_sections.ps1
E	Determine_cross_sectional_load.ps1
F	Determine_HM_shell_elements_neighbouring_elements.ps1
G	Hybrid_optimisation_setup.ps1
H	Hybrid_non_linear_linear.ps1
I	Update_HW_FE_data_status.ps1

The functions described in Table 4.1, added to BEETS (Christensen 2015), form the basis of the hybrid optimisation method. Many of these functions are analogous to the functions used in the BEETS method, specifically regarding reading FE files, sorting node/element data. The following sections will describe in detail the more crucial aspects created for the hybrid optimisation process.

4.2.1. Force exchange

The hybrid optimisation method revolves around an exchange of data between the non-linear and linear solvers. In the case of automotive crashworthiness (Figure 1.1) and the basic 2D plate setup in Figure 4.1, the load input in the linear optimisation model is dependent on the force data at the interface of the non-linear model (assuming the impact from the rigid wall is as shown and the stress wave travels along the non-linear section first). This section will describe the process of extracting and transferring the forces.

FE model setup (step 4 in Figure 4.2): The first aspect of force extraction is to set up the interfaces and parameters within the FE model that will allow the script to extract, read and sort the force data. The interface nodes are simply defined as a node set within the FE model, and must be named as “Interface_Nodes_xx”, where “xx” corresponds to an integer as the algorithm allows for several interfaces in the model. This allows for the interface node set to be differentiated from any node sets with other functions in the model (e.g. constraints in other areas of the model). Following a personal communication

with Arup UK (who provide pre and post-processing software for LS-DYNA), it was clear that currently there is no capability within the software to directly obtain the nodal forces from the Finite Element Analysis (FEA). Therefore, another method is needed to determine the forces at the nodes.

- ***Method 1:*** The first method consisted simply of defining a cross section ("*DATABASE_CROSS_SECTION_PLANE" LS-DYNA keyword) in the FE model at or close to the interface, and from the LS-DYNA run the cross section forces can be extracted from the "secforc" file (Figure 4.3a). The section forces are then simply divided by the number of interface nodes present to determine the nodal forces at the interface (in the non-linear model (Figure 4.3b). The main issue with this method however is the assumption that the forces at the interface are constant through the cross section. In the 2D plate example (Figure 4.3), this could be the case for the given load case at the first iteration as the plate is perfectly rectangular, the material isotropic and the impact direction perpendicular to the plate. However, it is clear that once elements are removed from the plate throughout the optimisation process, this is no longer the case, as the forces will differ depending on the load paths that begin to appear (Figure 4.3c).

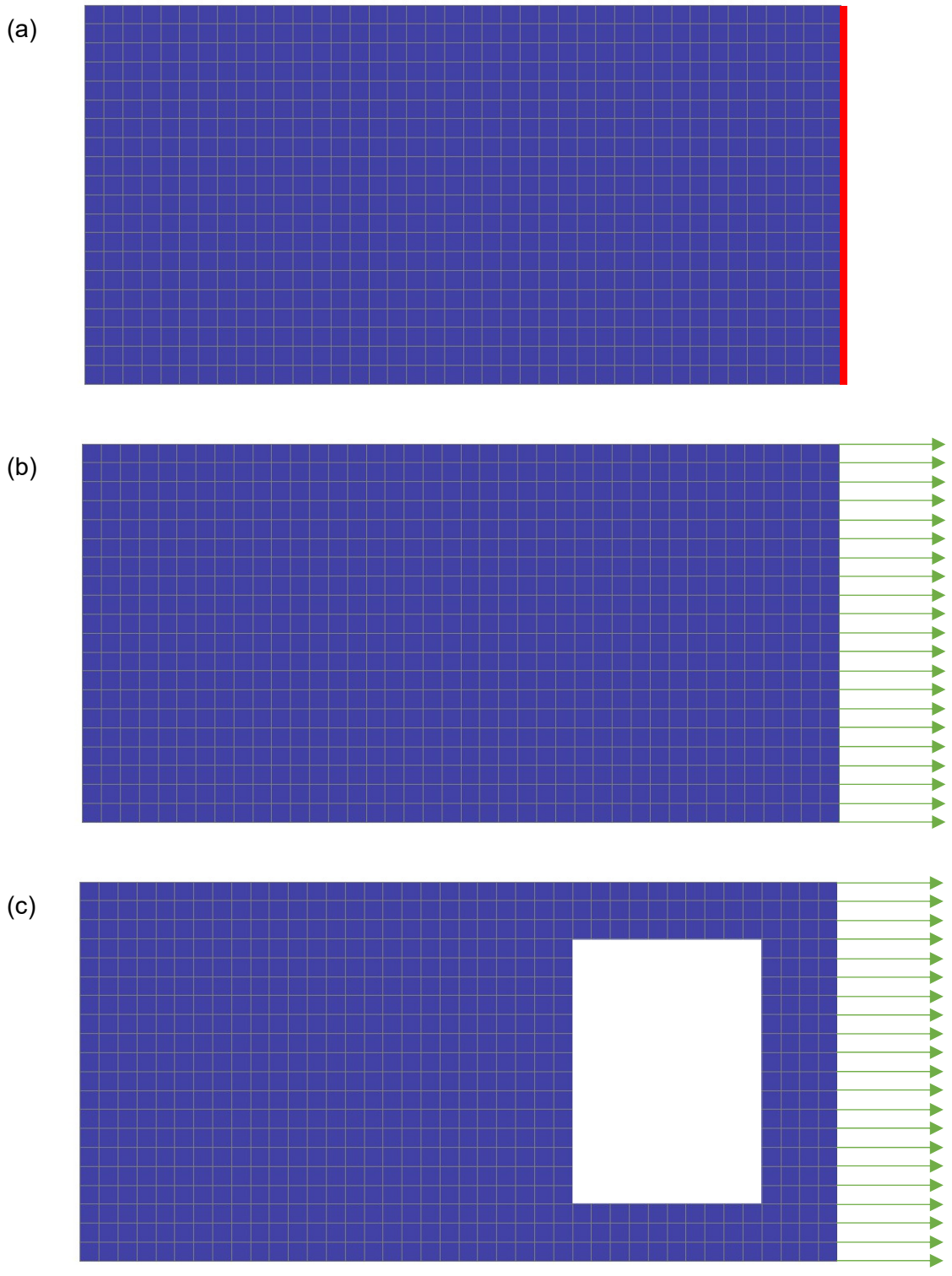

Figure 4.3 : Force transfer method 1 (a) Non-linear model with main cross section (b) Initial non-linear nodal forces determined from main cross section force (c) Incorrect nodal forces during optimisation process

Ideally, there needs to be a better method to represent the current forces in each element, and by extension each node at the interface.

- ***Method 2:*** The second, more complex method consists of creating cross sections, similar to the main cross section defined for Method 1, for each element at the interface (Figure 4.4a). This can be done via the *DATABASE_CROSS_SECTION_SET keyword in LS-DYNA. The complexity here is in the fact that an individual element set needs to be created for each element at the interface, and then an individual cross section that references the individual element set. It is clear that this method, if done manually via an FEA pre-processor, can quickly become cumbersome should the number of nodes/elements at the interface increase. Therefore, a function in the hybrid algorithm was created in order to automatically create each element set and individual element cross section using the “Interface_Nodes_xx” sets created by the user in the pre-processor (File “D” in Table 4.1 and Table 4.2). The forces would then be extracted from the “secforc” file similarly to the first method, and the forces divided by the number of interface nodes attached to each element (for shell element a maximum of two, for solid elements a maximum of four (Figure 4.4c)). Initially, the “exterior” nodes highlighted in Figure 4.4b would have half the force magnitude of the other nodes, as they are only attached to a single cross section as opposed to two. This differs from Method 1, where the forces are evenly distributed along the nodes at the interface. Due to discretisation, Method 1 is an inaccurate representation of a uniform force across the interface as the stress values in the corner interface elements would be higher than the remaining interface elements. Therefore Method 2, which initially automatically reduces the forces at the interface edge nodes, is an overall more accurate method of distributing the forces at the interface. This comes at a cost of added computational time, mainly associated with the additional sorting of the cross section data, which for very large interfaces (i.e. number of interface elements) would be substantial. Both methods are implemented within the tool developed in this thesis, and the effect of the incorrect (Method 1) and correct (Method 2) force extraction methods are discussed in Chapter 5.

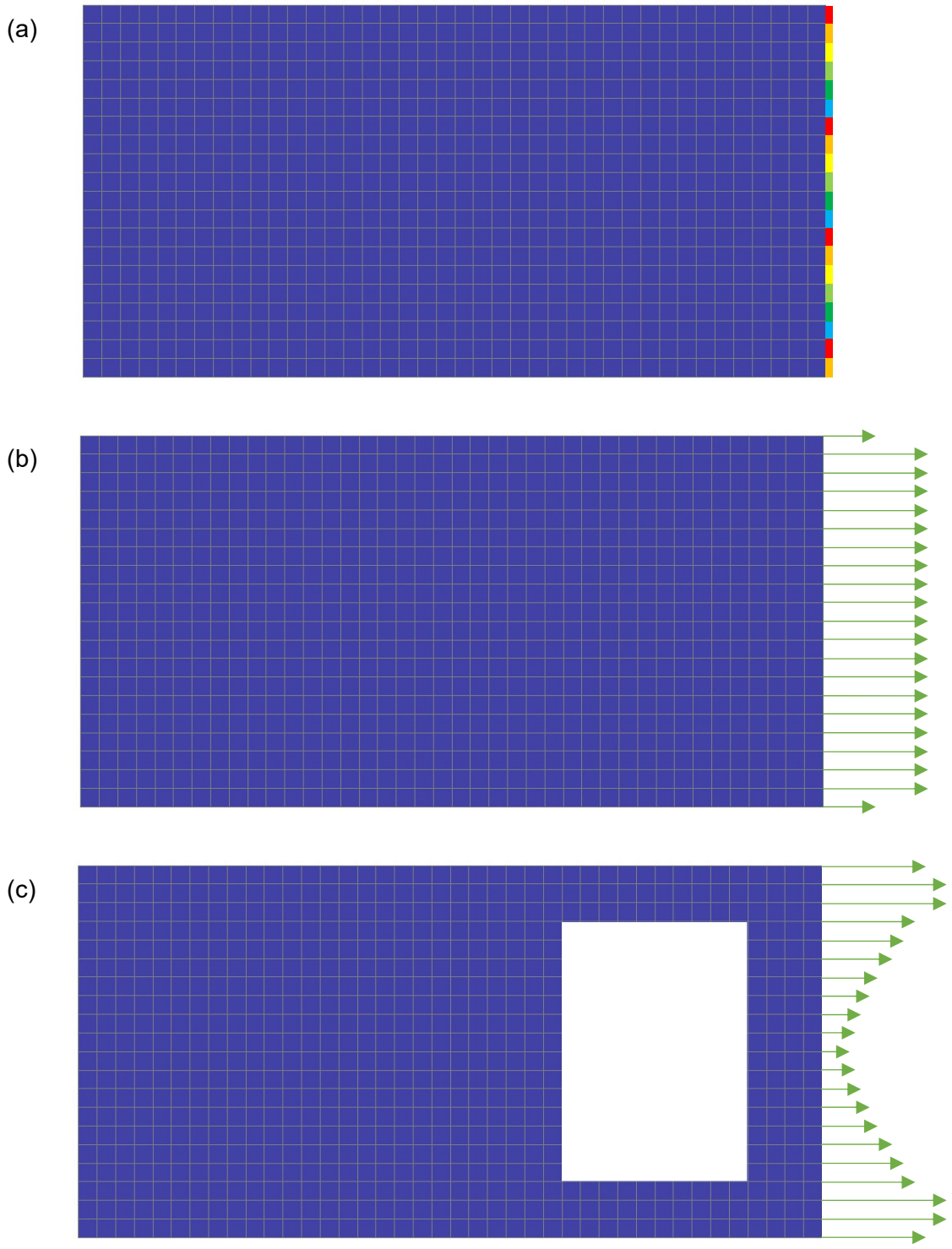

Figure 4.4 : Force transfer method 2 (a) Non-linear model with individual cross sections (b) Incorrect initial non-linear nodal forces determined from individual cross section forces (c) Nodal forces during optimisation process

The flowchart below (Figure 4.5) summarises the cross section creation process described above, and implemented in the “Create_multiple_LSD_cross_sections.ps1” function (Table 4.1 and Table 4.2):

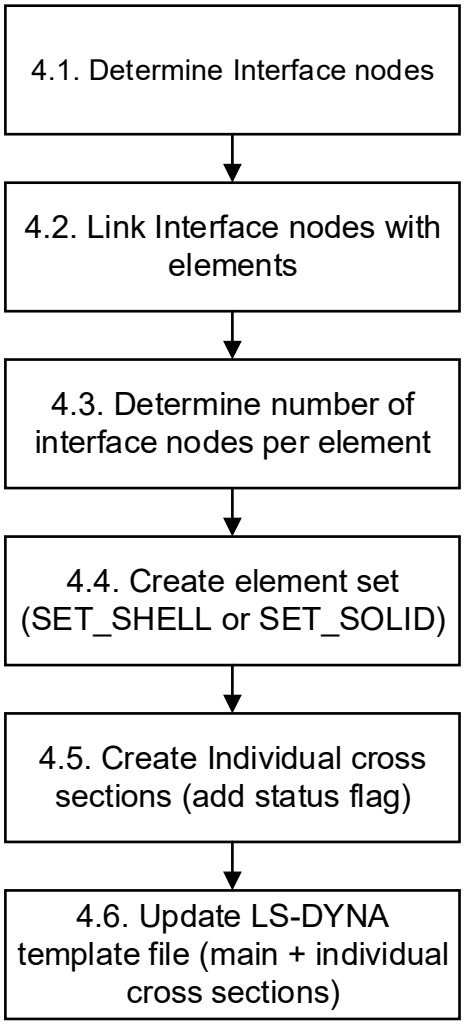

Figure 4.5 : Step 4 "Create cross sections" function flowchart

The creation of the cross sections described above (step 4.5 in Figure 4.5) is complemented in step 4.3, where the number of interface nodes per element, i.e. individual cross section, is calculated so that forces can be accurately divided per individual cross section. In essence, a link is created between the individual cross section and the corresponding interface nodes, via the connected element. Step 4.5 and 4.6 also relate to the formatting of the cross sections as variables within the algorithm, i.e. the cross sections are stored in a table. This format is important, as much like the nodes and elements, the cross sections possess a status flag (0 = deleted, 1 = retained) which

determines whether the cross section is added to the keyword file. Essentially, the status flag will depend on the status of the element referenced by the SET_SHELL or SET_SOLID, in turn referenced by the cross section (steps 4.4 and 4.5). A cross section that references a set containing a deleted element would result in an error termination of the FEA process. Therefore, in step 4.6, only the main cross section (which is defined via an arbitrary plane in the pre-processor and therefore does not directly reference any elements or nodes) and any individual cross sections referencing non-design elements are added into the template file. The remaining cross sections referencing design elements are therefore added to the keyword file in step 7 (Figure 4.2) along with other FE entities such as nodes and elements.

Force extraction and manipulation (step 9 in Figure 4.2): The FE model is setup to output both the main cross section force data and the individual element cross section force data as described by Figure 4.3 and Figure 4.4 respectively. The first approach to analysing the forces is to determine the peak force. The force data output from LS-DYNA, i.e. “secforc” file, is obviously time dependent, specifically dependent on the user-defined sampling rate in the pre-processor. As an initial analysis of the sampling rate effect on cross sectional force accuracy and force extraction duration, a simple study was carried out based on the 2D plate example from chapter 3. The plate was separated as illustrated in Figure 4.1 and cross sections placed at the interface as per Figure 4.3(a) and Figure 4.4(a). The model was then run in LS-DYNA, and a simplified version of the hybrid optimisation force extraction function was run. The simplified function performed the following tasks:

- Open/extract data from “secforc” file into an array
- Sort data so only numerical values remain, i.e. removing blank spaces and text
- Place data into a hashtable containing cross section ID, force data (x, y and z directions) with corresponding timestamp
- Determine maximum force in “x” direction for each individual cross section (Figure 4.4(a)) based on maximum force timestamp in “main” cross section (Figure 4.3(a))

Three different sampling rates for the “secforc” data were selected and the results are summarised in Table 4.3 below:

Table 4.3 : Cross-sectional force data sampling rate effect

Run time (s)	Sampling rate (s)	Number of sampling points	Maximum force time (s)	Maximum force value (N)	Function run time (s)
0.05	5.00E-03	10	5.00E-03	55680	0.7
0.05	5.00E-04	100	6.00E-03	55730	2.6
0.05	5.00E-05	1000	2.55E-03	56197	277.4

The main observation from the results in Table 4.3 relates to the run time of the function. The difference in run time is considerable when the sampling rate is increased to 1000 points across the analysis run time. Furthermore, there is not a considerable change between the different maximum force values extracted between the three sampling rates. However, there is a difference regarding when the maximum force occurs. Figure 4.6 and Figure 4.7 below illustrate the “main” cross-sectional force curves for the three sampling rates:

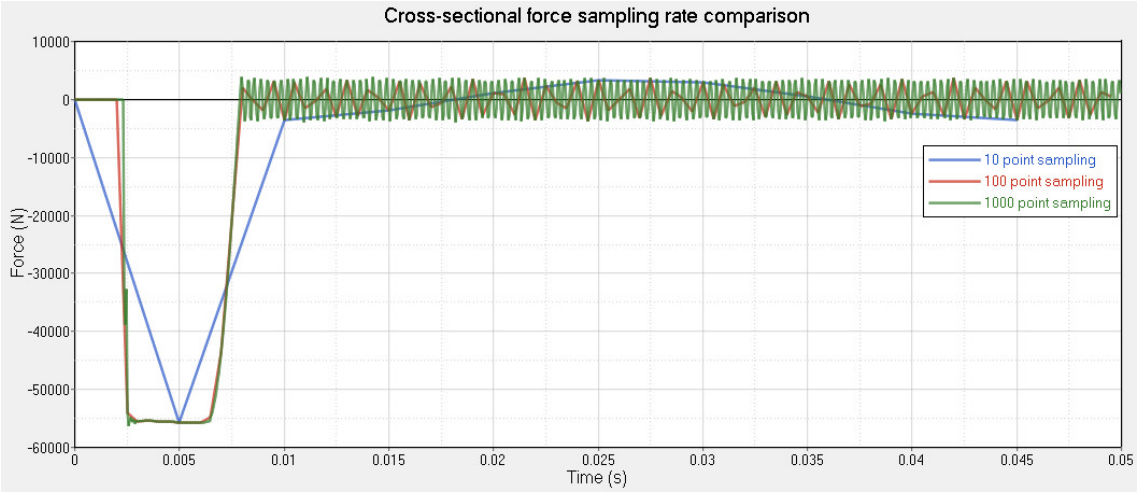

Figure 4.6 : Cross-sectional force sampling rate effect comparison

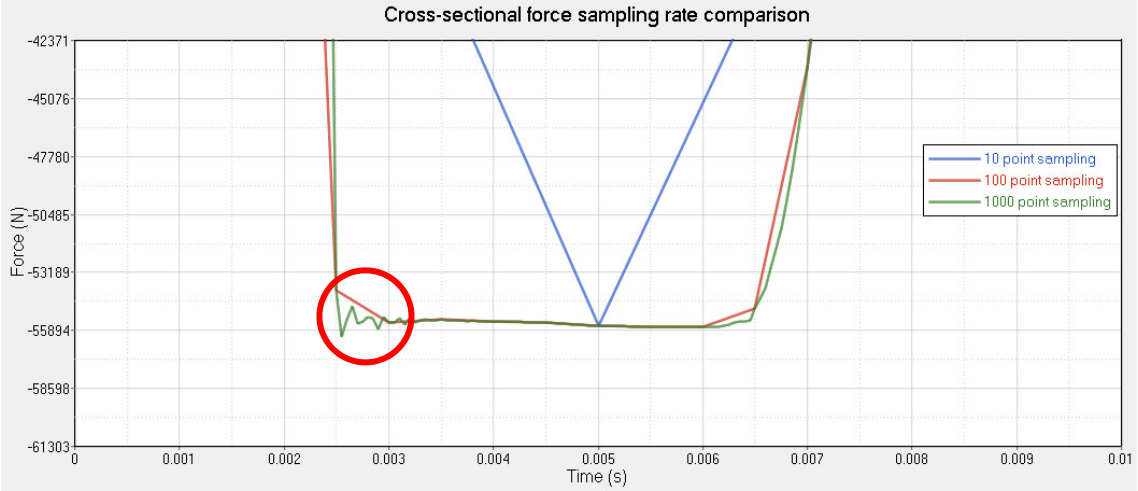

Figure 4.7 : Cross-sectional force sampling rate effect maximum force

Figure 4.7 illustrates why there is a difference between the maximum force value timestamps extracted from the “secforc” data. Where only 10 points exist in the analysis run time, only a single point represents the peak force behaviour, very different to the behaviour depicted by the 100 and 1000 point sampling curves. The difference between the 100 and 1000 point maximum force timestamp can be explained by the behaviour circled in Figure 4.7. The maximum force occurs in this instance for the 1000 point curve, whereas a lower sampling rate does not replicate the behaviour, and the maximum force occurs at 6ms for the 100 point sampling rate. Overall however, the difference in maximum force is minimal, and the 100 point sampling rate is an acceptable representation of the impact behaviour considering the difference in CPU time to extract the force data. Therefore, a sampling rate of 100 points, i.e. 0.5ms for a 50ms run time, is selected. Given the sampling rate could be highly model/load case dependent, a recommendation to the user would be to conduct several analyses before the optimisation process to determine an acceptable value.

For both force extraction methods illustrated in Figure 4.3 and Figure 4.4, the forces are selected at the peak force timestamp for the “main cross section” as it represents the global force travelling through the structure. From this timestamp, using the methods described above, the forces are determined for each non-linear interface node. The remaining operation is to transfer the forces from each non-linear node to their linear counterpart(s), determined in the “Hybrid_optimisation_setup.ps1” function at the first iteration. This process allows for different mesh sizes between the non-linear and linear models, as the user-defined radius determines the equivalent Optistruct interface nodes.

4.2.2. Hybrid optimisation setup

The next aspect to examine is the hybrid optimisation setup, the first step in the linear optimisation process (step 8 in Figure 4.2). This step serves two main purposes, as demonstrated by the flowchart below (Figure 4.8):

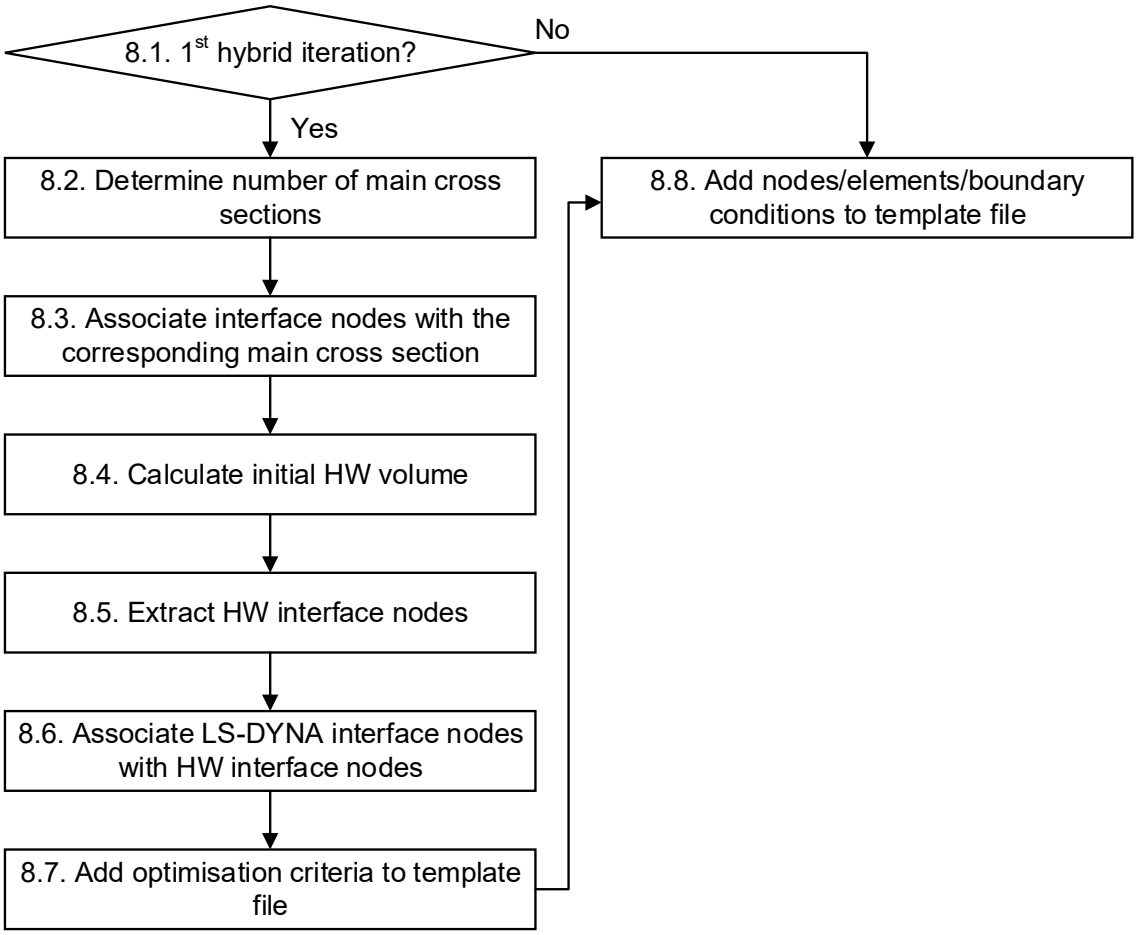

Figure 4.8 : Step 8 "Hybrid optimisation setup" function flowchart

The first purpose is to set up all the key aspects of the hybrid method at the first linear iteration. Essentially these are elements that will remain unchanged during the process and therefore only need to be performed once (steps 8.2 – 8.6 in Figure 4.8). Step 8.2 is especially important in the case of multiple interfaces existing in the structure. The main cross sections are set up by defining a plane in the pre-processer (with x,y and z coordinates) for each interface. Therefore, in the LS-DYNA keyword file, there is no indication as to which interface nodes belong to which cross section. This is an issue when determining the peak force and corresponding timestamp for the interface force calculation. However, once the LS-DYNA solver has terminated the analysis, the .otf file

created contains analysis data including the nodes taken into account for each cross section in the structure. Therefore, if the main cross sections are correctly defined in the pre-processor, i.e. the normal to the plane points towards the interface nodes and not in the opposite direction, the .otf file will list the correct interface nodes for each main cross section, and step 8.2 reads the .otf file to extract this information.

The other key aspect of the function is to link the non-linear (LS-DYNA) and linear (HW) interface nodes together (step 8.6 in Figure 4.8). Once the HW interface nodes are extracted from the linear FE model file in step 8.5, a user-defined radius is used for each LS-DYNA interface node to match them to one or several HW interface nodes. Whether a HW node is linked is decided in a very similar fashion to the element neighbourhood calculation in the BEETS process (Figure 2.6 and equation 2.15 in Chapter 2).

The second purpose of this function is to insert all the “variable” entities into the linear FE model file, and this action is performed before each linear optimisation iteration. Essentially this step is an update of the FE file which depends on the entity (e.g. nodes) status determined at step 12 (Figure 4.2) of the previous iteration.

4.2.3. Update HW FE status

The next step that warrants further explanation is step 12 (Figure 4.2), which essentially extracts the linear optimisation information in order to update element/node status. This process is illustrated in Figure 4.9 below:

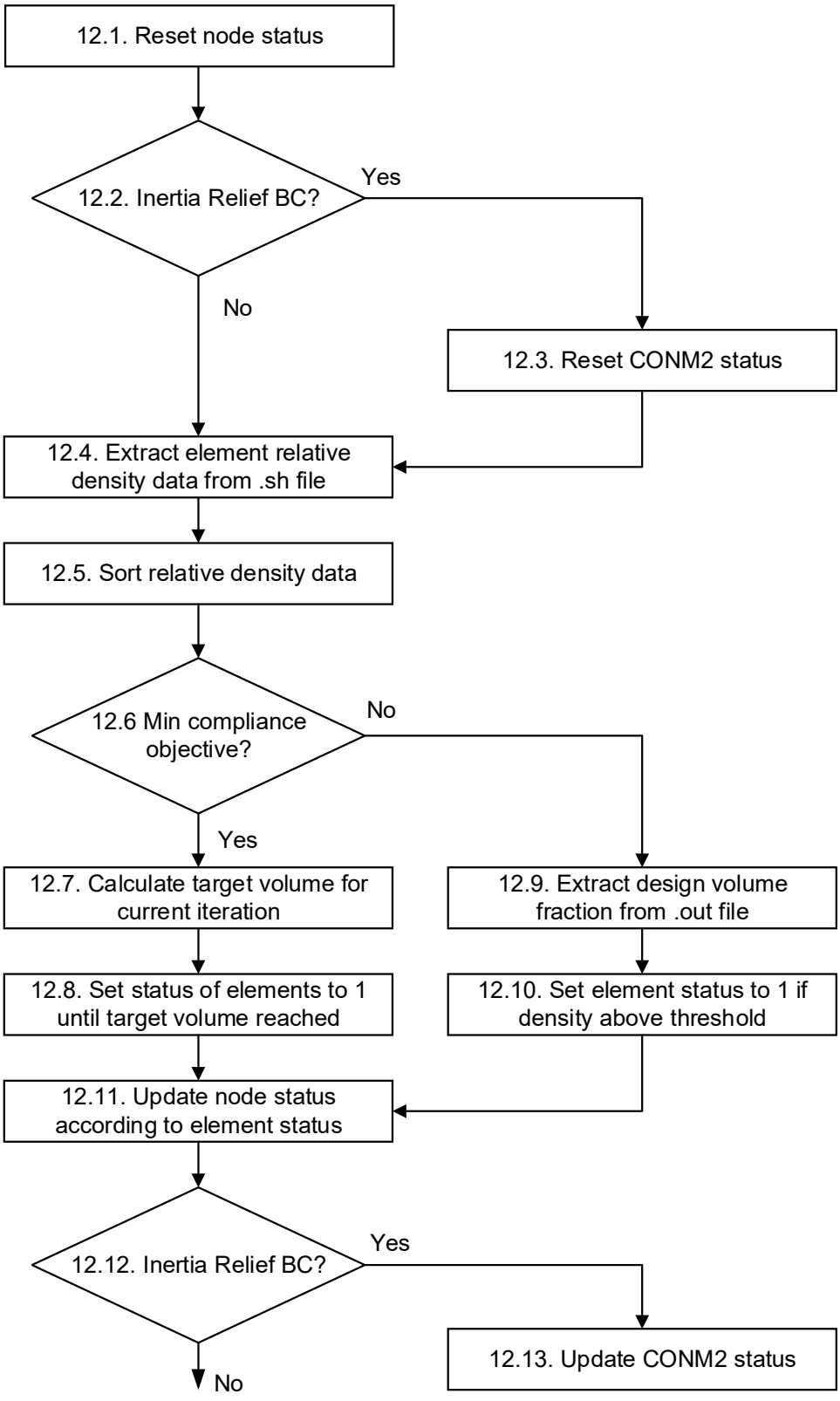

Figure 4.9 : Step 12 "Update HW FE status" function flowchart

The main aspects of step 12 revolve around the difference in element status modification depending on the objective function selected by the user. In essence, the information provided in the .sh file in step 12.4 (Figure 4.9) is the same for both objectives (minimise mass or minimise compliance). However, the way the data is interpreted differs as follows:

- ***Minimise compliance:*** In the case where "minimise compliance" is selected as the objective function, the key here is the constraint, which is a target volume per iteration. The target volume is calculated in step 12.7 using equation (4.1) below:

$$V_{k+1} = V_k * HW_{volfrac} \quad (4.1)$$

where V_k corresponds the current volume, V_{k+1} the target volume and $HW_{volfrac}$ the volume fraction for the current linear iteration, calculated by equation (4.2)

$$HW_{volfrac} = ER * Rate\ of\ exchange \quad (4.2)$$

The equation demonstrates that the linear volume target closely follows the non-linear volume. For example, if five iterations of BEETS are performed before a linear optimisation loop, then ER is multiplied by five for the linear volume target in order to reflect the rate of exchange. In the following step (12.8), the element statuses are set to 1 until the target volume is reached. Seeing as step 12.5 has sorted the element density by descending value, the elements with the highest relative density are retained within the structure.

- ***Minimise mass:*** In the case where "minimise mass" is selected as the objective function, the ".out" file created during the linear optimisation process contains information relative to each iteration. Included in this information is a "Design Volume Fraction" value, which acts as a threshold value for retaining or deleting an element in order to meet the constraints. Therefore, step 12.9 extracts this value for the final iteration of the linear optimisation process, and step 12.10 retains elements that possess a relative density higher or equal to the value.

4.2.4. Zero-length beam stiffness update

One of the parameters determined to be of interest (section 4.1) in the hybrid optimisation process was the BCs used at the interface for the non-linear model. As stated, one possibility that could differ to using SPC type constraints would be to apply zero length beams at the interface. One end of the beam would be tied to constraints such as SPCs,

and the other tied to an interface node. The beam would then be able to deform (slightly), acting as a representation of the linear model. Using the beam method there are two possibilities:

- **Method A:** The first method consists simply of applying a stiffness equal to the Young's Modulus to each beam, and not applying any modifications during the optimisation process.
- **Methods B:** The second method would extend Method A by using displacement data from the linear model to modify the zero length beam stiffness in the non-linear model. The formula used would simply be (equation (4.3)):

$$k = \frac{F}{\Delta l} \tag{4.3}$$

where *F* is the force applied at the node and *Δl* the displacement generated. This operation is carried out for the three translational degrees of freedom (DOFs) in the global x, y and z directions. The stiffness is updated in the material card attached to each zero-length beam (material card *MAT_066 LINEAR ELASTIC DISCRETE BEAM is used for this operation). *MAT_066 is specifically designed for zero length beams, as it transforms the stiffness values defined into six springs representing the six DOFs (Livermore Software Technology Corporation 2016b). Therefore, using zero length beams has no negative impact on the timestep used for explicit LS-DYNA FEA. The process uses the same LS-DYNA / Optistruct node equivalence process as the force extraction procedure.

This chapter has presented the core aspects of the hybrid TO algorithm developed and the main exchanges of data that exist between the non-linear solver (BEETS/LS-DYNA) and the linear solver (Optistruct). The parameters that govern the interaction between the solvers have also been introduced. The next chapter will present the first case study, which applies the hybrid optimisation algorithm to the model presented in chapter 3.

5. Case study 1: Investigation into hybrid topology optimisation parameters

This first case study will explore the parameters inherent to the hybrid topology optimisation (TO) process, i.e. relative to the interface between linear / non-linear structures. At this stage, it is important to mention that the inherent parameters for both optimisation solvers (for example the evolutionary ratio (ER) for Bi-directional Evolutionary Entropy Tabu search Simulated annealing (BEETS)) will not be modified during the case study to obtain an overview of the hybrid TO parameters' influence only. A study to determine the appropriate parameters can be found in Appendix A, and the parameters are summarised in Table 5.1 and Table 5.2 below:

Table 5.1 : Summary of Optistruct parameters for case study 1

Parameter	Description	Value
DISCRETE	SIMP Penalisation factor as explained in the literature review	3
MINDIM (mm)	Determines a target "minimum size" for the member created during optimsation	30
CHECKER	Similar "empirical" parameters that attempt to suppress the checkerboarding effect	No
MMCHECK		No

Table 5.2 : Summary of BEETS parameters for case study 1

Parameter	Description	Value
ER	Evolutionary Ratio, determines the rate of element removal for each BEETS iteration (see literature review, section 2.2.1)	0.05
COOLIT	Determines at which point in the BEETS optimisation process the reduction of ER is activated (see literature review, section 2.2.2)	No
SF	Scale factor that determines by how much ER is reduced (see literature review, section 2.2.2)	No

5.1. Hybrid optimisation parameters study

The internal BEETS and Optistruct parameters having been established, case study 1 will focus on the hybrid TO parameters identified in chapter 4. Initially, the parameters will be studied on an individual basis, i.e. one parameter is modified at a time, followed by combinations of the most influential parameters. The finite element (FE) setup for the study mirrors the 2D plate structure used in chapter 3, the difference being that sections 1 and 2 are separated for non-linear and linear optimisation respectively (as demonstrated by Figure 4.1 in chapter 4). The model parameters are as summarised in Table 5.3:

Table 5.3 : Case study 1 FE model parameters

Section		**Non-linear (1)**	**Linear (2)**
Dimensions	**x (mm)**	400	200
	y (mm)	400	200
Material model		Mild steel Johnson cook linear elastic plastic (Table 3.1)	Mild steel linear elastic (E = 210 GPa)
Rigidwall	**mass (kg)**	100	
	velocity ($m.s^{-1}$)	2.2	

Firstly, it is essential to establish the behaviour of the overall structure, i.e. the non-linear (1) and linear (2) sections from Figure 4.1 are attached, to evaluate the starting point of the optimisation process. The setup of the model is illustrated in Figure 5.1:

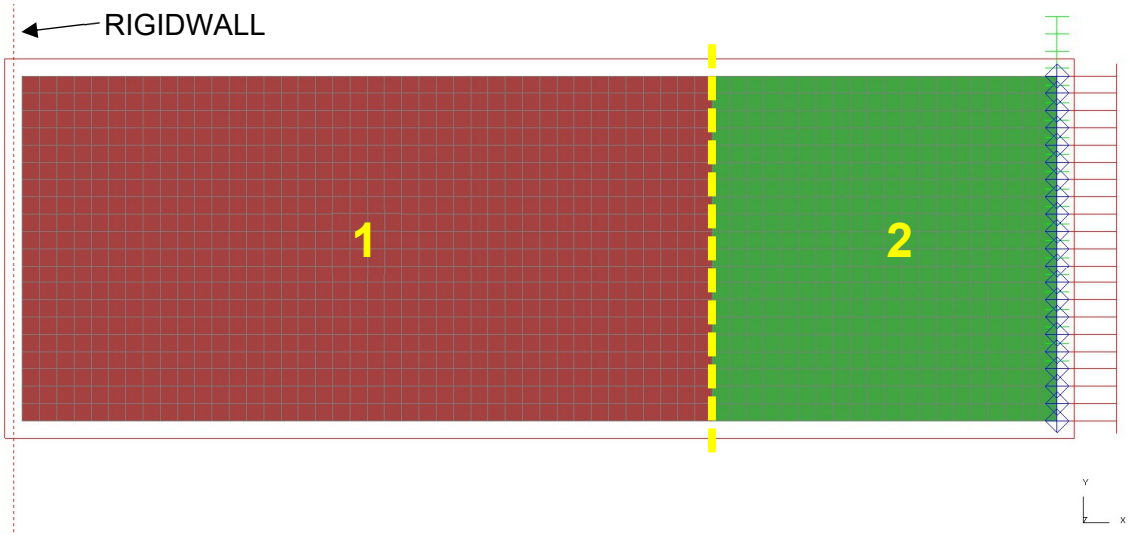

Figure 5.1 : Initial structure behaviour test FE setup

In this case, both section 1 and section 2 are defined using the Johnson-Cook non-linear material defined in Table 3.1, as these sections both constitute a “single” component in this case. Figure 5.2 displays the plastic strain distribution through the model.

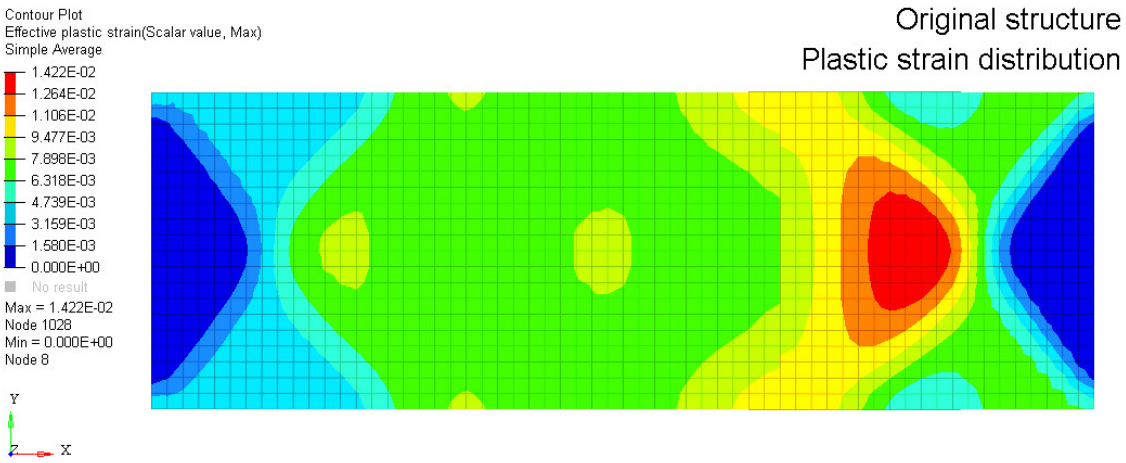

Figure 5.2 : Initial structure plastic strain distribution

The first key observation is the presence of plastic strain throughout the structure, included in the section intended for linear optimisation (and therefore required linear behaviour). This however is logical given the rigidwall impacting the structure perpendicular to the plate. Given the ideal geometry of the plate, i.e. a rectangle, there is no reason for the non-linear section to deform more than the linear section from an initial standpoint. This is something that should be addressed during the optimisation process as elements are removed from the structures by the respective linear and non-linear methods. From a performance point of view, the final structures will be assessed on two criteria. Firstly, the presence of plastic strain in section 2 of the structure (“linear”) will be monitored. Secondly, the total internal energy will be calculated for the structure as the sum of the internal energy of both sections. LSTC define the internal energy as the sum of the elastic energy and work done in plastic deformation (Livermore Software Technology Corporation 2018a). Furthermore, the internal energy is calculated by using stress, strain and volume data for each element (Livermore Software Technology Corporation 2018b). Therefore, the internal energy of the system is a good indication of the energy absorbed by the structure through deformation. Because it is not possible to separate elastic and plastic strain energy from the internal energy value, the total internal energy value is used, with the plastic strain in section (2) indicating whether this section has deformed too much, i.e. has deformed beyond the “linear” requirement.

The parameters that are varied during case study 1 are briefly described below:

- **Interface size (Number of elements):** The interface size, as mentioned in chapter 4, relates to the number of non-design nodes included at the interface of the non-linear structure. Figure 5.3 illustrates the four values tested.

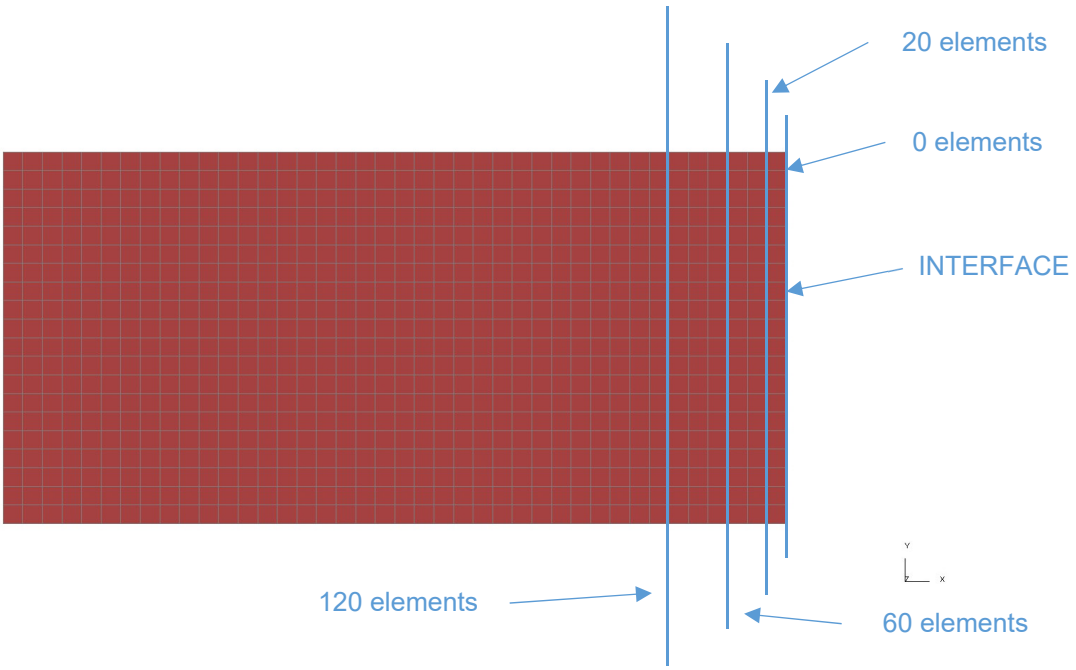

Figure 5.3 : Interface size study non-linear section

Based on Figure 5.3, for each individual study all elements to the right of the "interface size line" are considered non-design.

- **Rate of exchange**: As discussed in chapter 4, the "rate of exchange" is made up of two parameters. The first part of this parameter directly influences the switch between a non-linear and a linear optimisation process, while the latter (the Optistruct "DESMAX" parameter) dictates how many maximum linear optimisation iterations are performed (the process may converge before the DESMAX value is reached). Figure 5.4 illustrates the rate of exchange process:

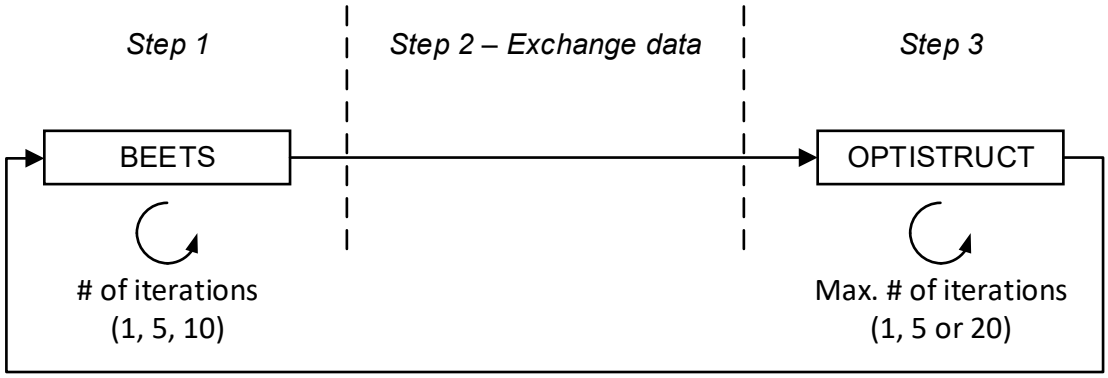

Figure 5.4 : Rate of exchange flowchart

- **Linear model optimisation objective / constraint:** This study will analyse the effects of modifying the optimisation criteria study for the linear (Optistruct) process. Two different configurations are considered. The first is the minimisation of compliance (min. comp.), subject to a volume target constraint. Effectively what this means is that at the end of the process, the structural volume will always reach the target volume, and the structure will be the stiffest possible for that given volume. However, there is no constraint on the "linearity" of the structure, therefore a second configuration is considered, namely the minimisation of mass (min. mass) subject to a global von Mises stress constraint on the linear structure. Effectively what this means is that during the optimisation process, as much material as possible is removed from the linear structure if the stress levels remain under a given stress value. A constraint value of 276 MPa, the Yield strength indicated in the LS-DYNA material card, is selected.
- **Interface boundary conditions (BC):** As discussed in chapter 4, the BCs at the interface could be influential in the hybrid TO process. By default, Single Point Constraint (SPC) type BCs are used. However there may be a different way to represent the linear structure using zero length beams. The two methods introduced in chapter 4.2.2 are analysed in this section. Method A considers zero length beams with constant stiffness at the interface, and Method B considers zero length beams with variable stiffnesses dependent on the linear model displacement data.
- **Linear model BCs:** The final parameter of interest in this initial hybrid TO study is the BCs applied in the linear structure. The models previously analysed used SPCs as the BCs, however in the case of optimisation vehicle structures as mentioned in the literature review, Inertia Relief (IR) is sometimes preferred to

account for the structural mass in the linear equilibrium. Therefore, this study is to analyse the effects of using such a BC on the hybrid TO process. Three different mass point configurations are analysed, identical to the configurations used in chapter 3, as follows:

- ***Config 1*** : A single point mass
- ***Config 2*** : A mass along the edge of the structure
- ***Config 3*** : Mass points added at the equivalent SPC locations for the initial linear static optimisation performed in chapter 3 (Figure 3.6)

These configurations are illustrated in Figure 5.5 - Figure 5.7

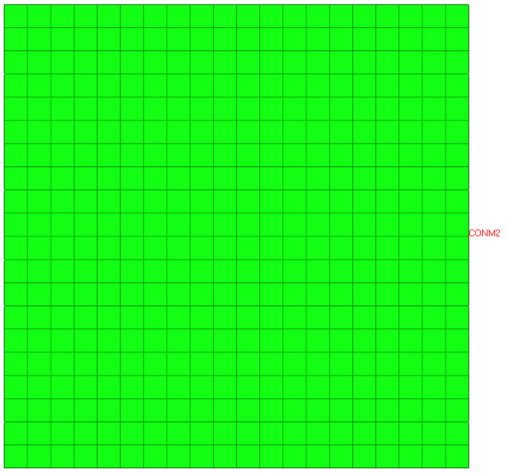

Figure 5.5 : Config 1 FE setup

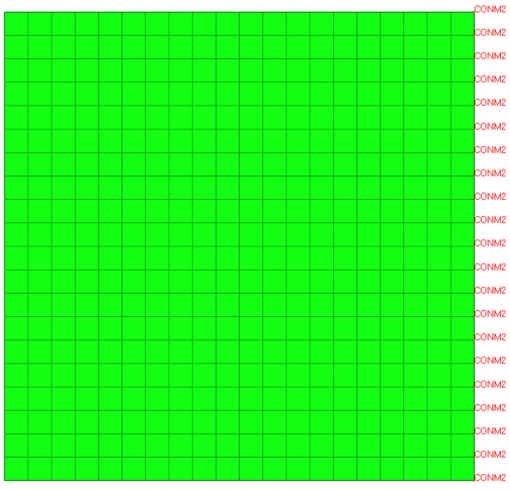

Figure 5.6 : Config 2 FE setup

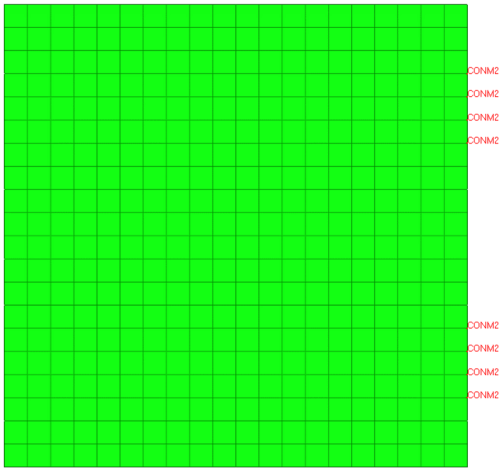

Figure 5.7 : Config 3 FE setup

Table 5.4 displays the different case study models and their respective parameters:

Table 5.4 : Hybrid optimisation plate study models

Study	Model Number	Interface size (Number of elements)	Rate of exchange		Interface BC	Linear BC	Linear model objective	Linear model constraint *Volume fraction = 50% von Mises stress = 276 MPa*
			BEETS	Optistruct				
A	PS_M01	0	1	1	SPC	SPC	Min. comp	Volume fraction
	PS_M02	20	1	1	SPC	SPC	Min. comp	Volume fraction
	PS_M03	60	1	1	SPC	SPC	Min. comp	Volume fraction
	PS_M04	120	1	1	SPC	SPC	Min. comp	Volume fraction
B	PS_M05	20	5	1	SPC	SPC	Min. comp	Volume fraction
	PS_M06	20	10	1	SPC	SPC	Min. comp	Volume fraction
	PS_M07	20	1	5	SPC	SPC	Min. comp	Volume fraction
	PS_M08	20	5	5	SPC	SPC	Min. comp	Volume fraction
	PS_M09	20	10	5	SPC	SPC	Min. comp	Volume fraction
	PS_M10	20	1	20	SPC	SPC	Min. comp	Volume fraction
	PS_M11	20	5	20	SPC	SPC	Min. comp	Volume fraction
	PS_M12	20	10	20	SPC	SPC	Min. comp	Volume fraction
C	PS_M13	20	1	1	SPC	SPC	Min. mass	von Mises stress
D	PS_M14	20	1	1	Beams (A)	SPC	Min. comp	Volume fraction
	PS_M15	20	1	1	Beams (B)	SPC	Min. comp	Volume fraction
E	PS_M16	20	1	1	SPC	IR (config 1)	Min. comp	Volume fraction
	PS_M17	20	1	1	SPC	IR (config 2)	Min. comp	Volume fraction
	PS_M18	20	1	1	SPC	IR (config 3)	Min. comp	Volume fraction
F	PS_M19	0	5	1	SPC	SPC	Min. comp	Volume fraction
	PS_M20	60	5	1	SPC	SPC	Min. comp	Volume fraction
	PS_M21	120	5	1	SPC	SPC	Min. comp	Volume fraction
	PS_M22	0	10	1	SPC	SPC	Min. comp	Volume fraction
	PS_M23	60	10	1	SPC	SPC	Min. comp	Volume fraction
	PS_M24	120	10	1	SPC	SPC	Min. comp	Volume fraction
	PS_M25	0	1	5	SPC	SPC	Min. comp	Volume fraction
	PS_M26	60	1	5	SPC	SPC	Min. comp	Volume fraction
	PS_M27	120	1	5	SPC	SPC	Min. comp	Volume fraction
	PS_M28	0	5	5	SPC	SPC	Min. comp	Volume fraction
	PS_M29	60	5	5	SPC	SPC	Min. comp	Volume fraction
	PS_M30	120	5	5	SPC	SPC	Min. comp	Volume fraction
	PS_M31	0	10	5	SPC	SPC	Min. comp	Volume fraction
	PS_M32	60	10	5	SPC	SPC	Min. comp	Volume fraction
	PS_M33	120	10	5	SPC	SPC	Min. comp	Volume fraction
	PS_M34	0	1	20	SPC	SPC	Min. comp	Volume fraction
	PS_M35	60	1	20	SPC	SPC	Min. comp	Volume fraction
	PS_M36	120	1	20	SPC	SPC	Min. comp	Volume fraction
	PS_M37	0	5	20	SPC	SPC	Min. comp	Volume fraction

Study	Model Number	Interface size (Number of elements)	Rate of exchange		Interface BC	Linear BC	Linear model objective	Linear model constraint *Volume fraction = 50% von Mises stress = 276 MPa*
			BEETS	Optistruct				
F	PS_M38	60	5	20	SPC	SPC	Min. comp	Volume fraction
	PS_M39	120	5	20	SPC	SPC	Min. comp	Volume fraction
	PS_M40	0	10	20	SPC	SPC	Min. comp	Volume fraction
	PS_M41	60	10	20	SPC	SPC	Min. comp	Volume fraction
	PS_M42	120	10	20	SPC	SPC	Min. comp	Volume fraction
G	PS_M43	0	1	1	Beams (A)	SPC	Min. comp	Volume fraction
	PS_M44	60	1	1	Beams (A)	SPC	Min. comp	Volume fraction
	PS_M45	120	1	1	Beams (A)	SPC	Min. comp	Volume fraction
	PS_M46	0	1	1	Beams (B)	SPC	Min. comp	Volume fraction
	PS_M47	60	1	1	Beams (B)	SPC	Min. comp	Volume fraction
	PS_M48	120	1	1	Beams (B)	SPC	Min. comp	Volume fraction
H	PS_M49	0	1	1	SPC	IR (config 1)	Min. comp	Volume fraction
	PS_M50	60	1	1	SPC	IR (config 1)	Min. comp	Volume fraction
	PS_M51	120	1	1	SPC	IR (config 1)	Min. comp	Volume fraction
	PS_M52	0	1	1	SPC	IR (config 2)	Min. comp	Volume fraction
	PS_M53	60	1	1	SPC	IR (config 2)	Min. comp	Volume fraction
	PS_M54	120	1	1	SPC	IR (config 2)	Min. comp	Volume fraction
	PS_M55	0	1	1	SPC	IR (config 3)	Min. comp	Volume fraction
	PS_M56	60	1	1	SPC	IR (config 3)	Min. comp	Volume fraction
	PS_M57	120	1	1	SPC	IR (config 3)	Min. comp	Volume fraction
I	PS_M58	0	1	1	SPC	SPC	Min. mass	von Mises stress
	PS_M59	60	1	1	SPC	SPC	Min. mass	von Mises stress
	PS_M60	120	1	1	SPC	SPC	Min. mass	von Mises stress
J	PS_M61	20	5	1	Beams (A)	SPC	Min. comp	Volume fraction
	PS_M62	20	10	1	Beams (A)	SPC	Min. comp	Volume fraction
	PS_M63	20	1	5	Beams (A)	SPC	Min. comp	Volume fraction
	PS_M64	20	5	5	Beams (A)	SPC	Min. comp	Volume fraction
	PS_M65	20	10	5	Beams (A)	SPC	Min. comp	Volume fraction
	PS_M66	20	1	20	Beams (A)	SPC	Min. comp	Volume fraction
	PS_M67	20	5	20	Beams (A)	SPC	Min. comp	Volume fraction
	PS_M68	20	10	20	Beams (A)	SPC	Min. comp	Volume fraction
	PS_M69	20	5	1	Beams (B)	SPC	Min. comp	Volume fraction
	PS_M70	20	10	1	Beams (B)	SPC	Min. comp	Volume fraction
	PS_M71	20	1	5	Beams (B)	SPC	Min. comp	Volume fraction
	PS_M72	20	5	5	Beams (B)	SPC	Min. comp	Volume fraction
	PS_M73	20	10	5	Beams (B)	SPC	Min. comp	Volume fraction
	PS_M74	20	1	20	Beams (B)	SPC	Min. comp	Volume fraction
	PS_M75	20	5	20	Beams (B)	SPC	Min. comp	Volume fraction
	PS_M76	20	10	20	Beams (B)	SPC	Min. comp	Volume fraction
K	PS_M77	20	5	1	SPC	IR (config 1)	Min. comp	Volume fraction
	PS_M78	20	10	1	SPC	IR (config 1)	Min. comp	Volume fraction

Study	Model Number	Interface size (Number of elements)	Rate of exchange		Interface BC	Linear BC	Linear model objective	Linear model constraint *Volume fraction = 50% von Mises stress = 276 MPa*
			BEETS	Optistruct				
K	PS_M79	20	1	5	SPC	IR (config 1)	Min. comp	Volume fraction
	PS_M80	20	5	5	SPC	IR (config 1)	Min. comp	Volume fraction
	PS_M81	20	10	5	SPC	IR (config 1)	Min. comp	Volume fraction
	PS_M82	20	1	20	SPC	IR (config 1)	Min. comp	Volume fraction
	PS_M83	20	5	20	SPC	IR (config 1)	Min. comp	Volume fraction
	PS_M84	20	10	20	SPC	IR (config 1)	Min. comp	Volume fraction
	PS_M85	20	5	1	SPC	IR (config 2)	Min. comp	Volume fraction
	PS_M86	20	10	1	SPC	IR (config 2)	Min. comp	Volume fraction
	PS_M87	20	1	5	SPC	IR (config 2)	Min. comp	Volume fraction
	PS_M88	20	5	5	SPC	IR (config 2)	Min. comp	Volume fraction
	PS_M89	20	10	5	SPC	IR (config 2)	Min. comp	Volume fraction
	PS_M90	20	1	20	SPC	IR (config 2)	Min. comp	Volume fraction
	PS_M91	20	5	20	SPC	IR (config 2)	Min. comp	Volume fraction
	PS_M92	20	10	20	SPC	IR (config 2)	Min. comp	Volume fraction
	PS_M93	20	5	1	SPC	IR (config 3)	Min. comp	Volume fraction
	PS_M94	20	10	1	SPC	IR (config 3)	Min. comp	Volume fraction
	PS_M95	20	1	5	SPC	IR (config 3)	Min. comp	Volume fraction
	PS_M96	20	5	5	SPC	IR (config 3)	Min. comp	Volume fraction
	PS_M97	20	10	5	SPC	IR (config 3)	Min. comp	Volume fraction
	PS_M98	20	1	20	SPC	IR (config 3)	Min. comp	Volume fraction
	PS_M99	20	5	20	SPC	IR (config 3)	Min. comp	Volume fraction
	PS_M100	20	10	20	SPC	IR (config 3)	Min. comp	Volume fraction
L	PS_M101	20	5	1	SPC	SPC	Min. mass	von Mises stress
	PS_M102	20	10	1	SPC	SPC	Min. mass	von Mises stress
	PS_M103	20	1	5	SPC	SPC	Min. mass	von Mises stress
	PS_M104	20	5	5	SPC	SPC	Min. mass	von Mises stress
	PS_M105	20	10	5	SPC	SPC	Min. mass	von Mises stress
	PS_M106	20	1	20	SPC	SPC	Min. mass	von Mises stress
	PS_M107	20	5	20	SPC	SPC	Min. mass	von Mises stress
	PS_M108	20	10	20	SPC	SPC	Min. mass	von Mises stress

Throughout this chapter, the model numbering scheme (PS_Mxx) will be used, “PS” specifying the plate study and “Mxx” the model number where “xx” is replaced by and integer. As mentioned in the first part of this section, the influence of individual parameters will be studied initially, followed by a combination of the most influential. For future reference, section (1) refers to the section of the structure optimised via BEETS (non-linear) and section (2) refers to the section optimised via Optistruct (linear), analogous to Figure 4.1 in chapter 4.

5.1.1. Study A - Interface size

Models PS_M01 – PS_M04 are considered for study A. Figure 5.8 – Figure 5.11 display the final structure deformation (both non-linear and linear sections attached) obtained and re-analysed after the optimisation process, with Figure 5.12 and Figure 5.13 summarising the loadpath trends in the “non-linear” and “linear” sections respectively:

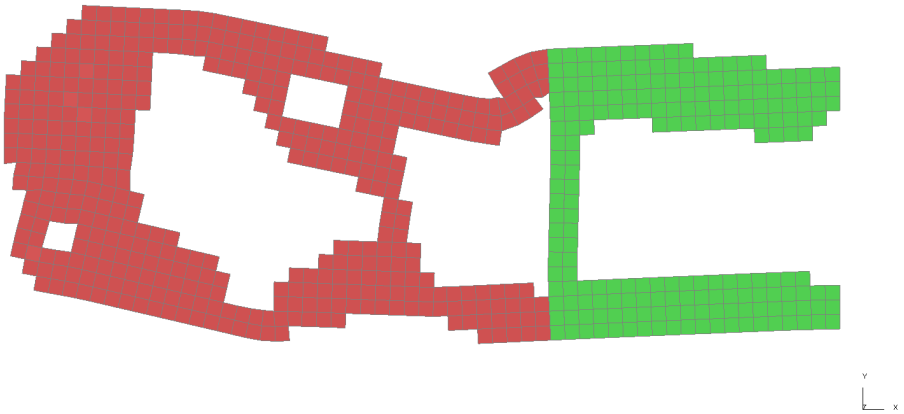

Figure 5.8 : PS_M01 final topology deformed state

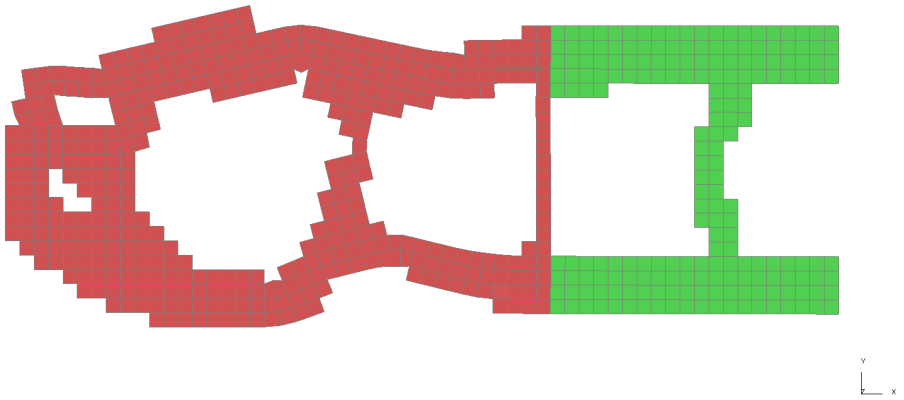

Figure 5.9 : PS_M02 final topology deformed state

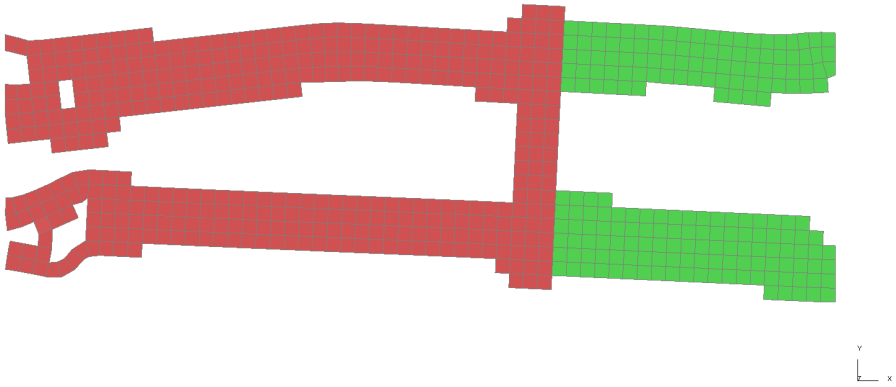

Figure 5.10 : PS_M03 final topology deformed state

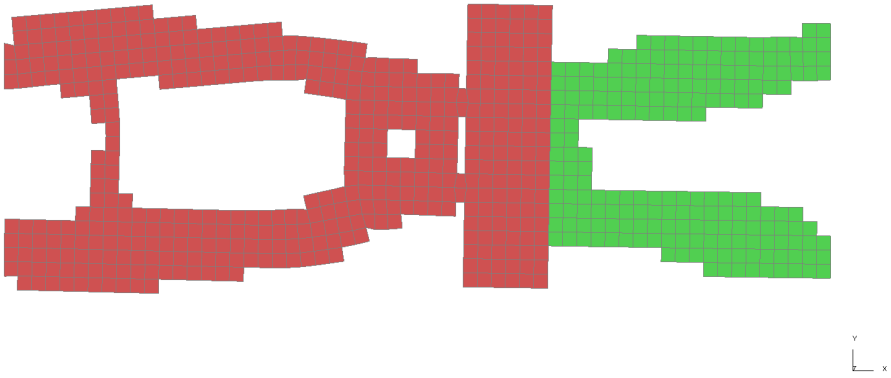

Figure 5.11 : PS_M04 final topology deformed state

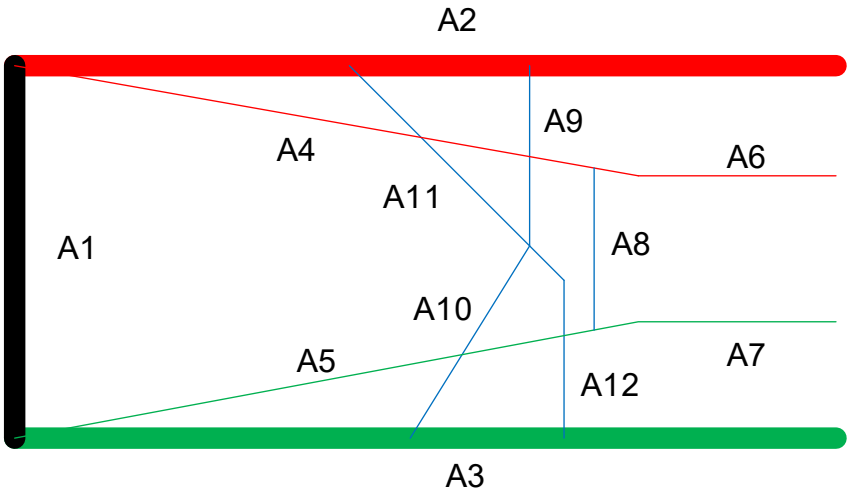

Figure 5.12 : Topology trends non-linear section models PS_M01 - PS_M04

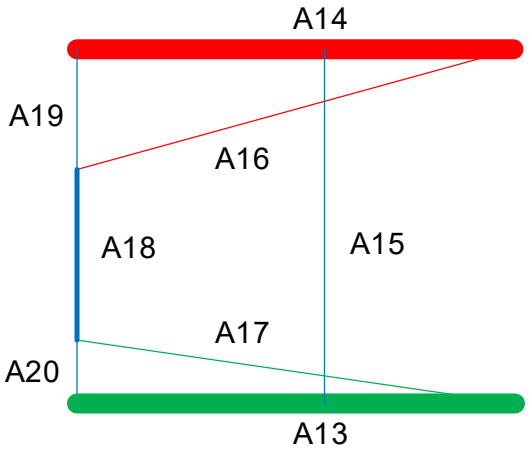

Figure 5.13 : Topology trends linear section models PS_M01 - PS_M04

In Figure 5.12 and Figure 5.13 and indeed in all subsequent final topology loadpath summaries, the colourised loadpaths represent trends that do not appear simultaneously in the same model. For example, A14 is “replaced” by loadpath A16 in model PS_M04 (Figure 5.13).

As these figures illustrate, there are differences between the different structures, in both the non-linear and linear sections. This is anticipated as essentially the interface size parameter, in its implementation, modifies the design volume of the non-linear structure, increasingly limiting the possibilities of removing elements.

Furthermore, the change in load paths in the non-linear sections also modifies the force distribution along the interface, and by extension, the loading conditions of the linear section. However, it is interesting that despite the differences in the non-linear sections (there are three vastly different structures), globally the linear structures are quite similar in that the majority of the elements are removed from the inside, while the load bearing structures tend to remain on the upper and lower edges of the structure.

A re-analysis run is performed on each of the four models (and will be run for all subsequent models). The optimised structures are effectively attached together and run in LS-DYNA, similarly to Figure 5.1. The same FE parameters are used, and both sections are defined using a Johnson-Cook material card as defined in Table 3.1.

The re-analysis of the models further illustrated the differences in the structures, this time from a performance point of view. The plastic strain plots are extracted from the “linear” section, i.e. section 2 (Figure 5.1), to verify that the intended global non-linear / linear coupled behaviour is achieved. Furthermore, the internal energy curves for both sections are extracted, as an indication of the overall contribution of each section of the structure in the overall energy absorption. Figure 5.14 displays the plastic strain plot for the linear section (section (2)) of PS_M01, and Figure 5.15 the corresponding internal energy graph. Table 5.5 summarises the values for the four models considered in this study:

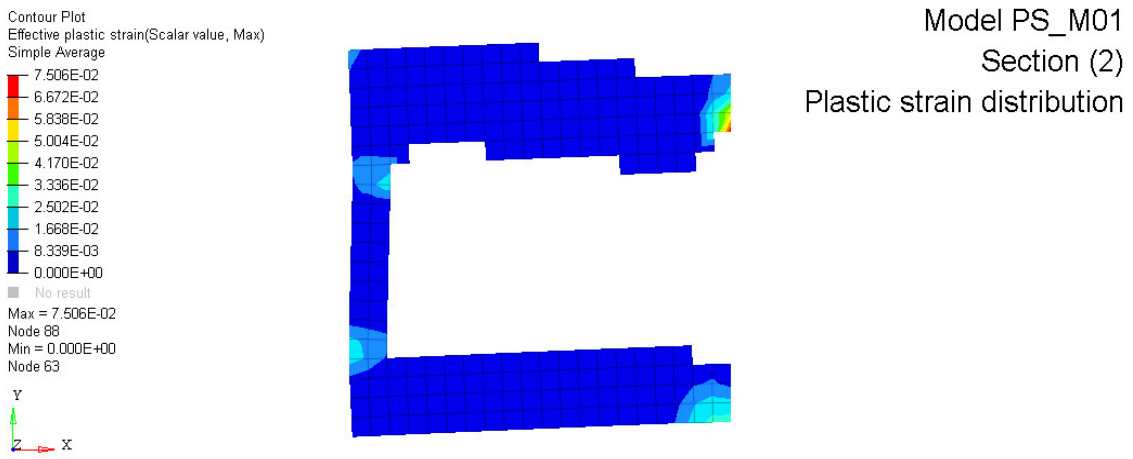

Figure 5.14 : Model PS_M01 section (2) plastic strain distribution

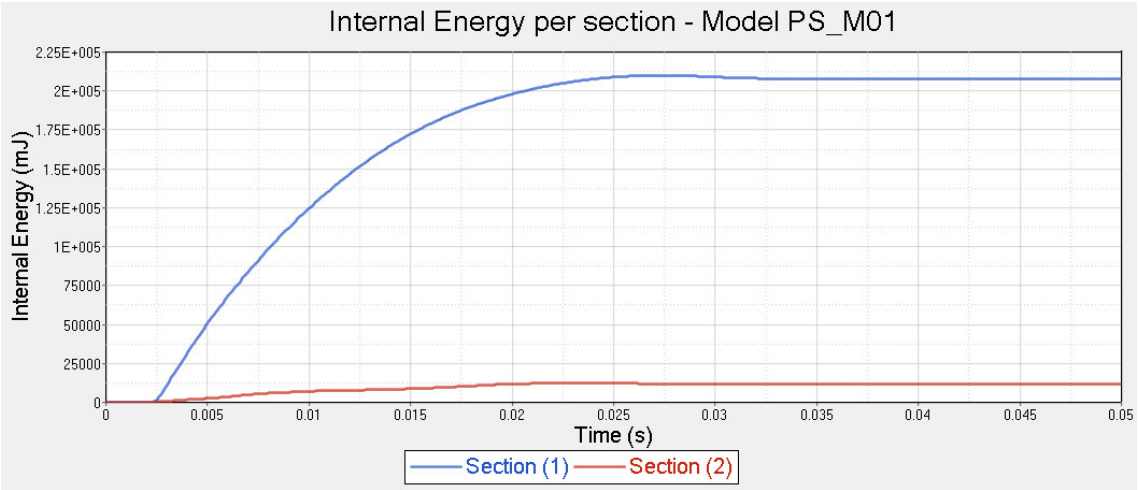

Figure 5.15 : Component internal energy (mJ) of PS_M01 vs time (s)

Table 5.5 : Study A re-analysis data

Model Number	Plastic strain section (2) (%)	Total Internal Energy (mJ)
PS_M01	7.5	222327.51
PS_M02	0.085	238716.14
PS_M03	34.2	236938.10
PS_M04	14.6	239388.87

Overall, PS_M01 and PS_M02 in particular show relatively low levels of plastic strain compared to PS_M03 and PS_M04. This could be explained by the previously discussed interface size implementation. If the non-linear section design volume is restricted too much, it could be possible that the final design obtained is sub-optimal from a performance point of view. For PS_M01 and PS_M02, where the interface sizes are small, the first optimisation iterations demonstrated that the elements are mostly removed near the interface. This of course is not possible for the larger interface sizes, hence the relatively poor performance. Furthermore, PS_M03 displays essentially two large longitudinal members through both the non-linear and linear sections. In essence, there is no difference between the two sections, and therefore much like the original plate (Figure 5.2), there is no reason that the non-linear section should deform substantially more than the linear section. Interestingly, it would appear that the energy absorbed by the optimised topologies is higher for the models with an interface, as the total internal energy is very similar for PS_M02 – PS_M04, and the energy absorbed is around 6% higher than PS_M01.

It is clear therefore that the interface size has considerable effect on the hybrid TO process, and by extension the structural performance. Overall, these initial results indicate that the larger interface sizes could be too restrictive. While the results also indicate that PS_M02 performs better than PS_M01, it is too early to assume that having a small number of non-design elements (i.e. PS_M02) is consistently better than no non-design volume.

Finally, it should also be considered that the four were cases studied with a rate of exchange 1 BEETS iteration per linear iteration, with a DESMAX value of 1. What this means is that only a single linear iteration is performed, and therefore convergence of the results could be influential. The next section will therefore focus on modifying the rate of exchange.

5.1.2. Study B - Rate of exchange

Models PS_M05 – PS_M12 are considered for Study B. It should be noted that the interface size used is the “20” option, therefore these results should be compared to PS_M02. PS_M05 and PS_M06 possess a DESMAX value of 1, PS_M07 – PS_M09 a value of 5 and PS_M10 – PS_M12 a value of 20. Figure 5.16 – Figure 5.23 display the final structure deformation (both non-linear and linear sections attached) obtained and re-analysed after the optimisation process, with Figure 5.24 summarising the loadpaths trends for the “linear” sections:

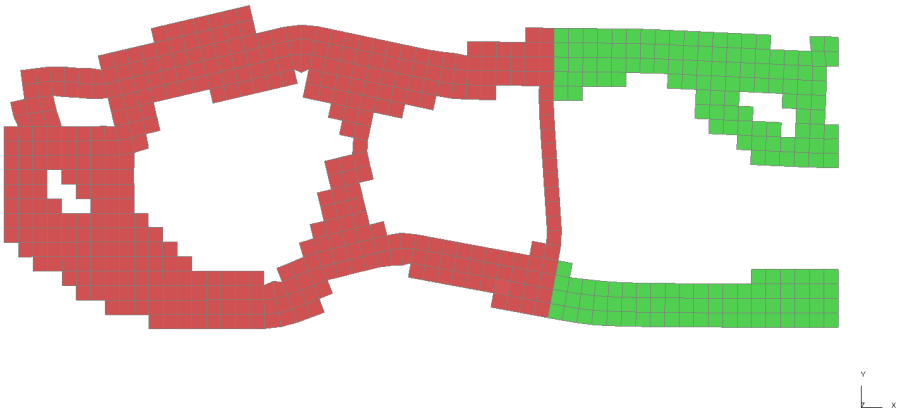

Figure 5.16 : PS_M05 final topology deformed state

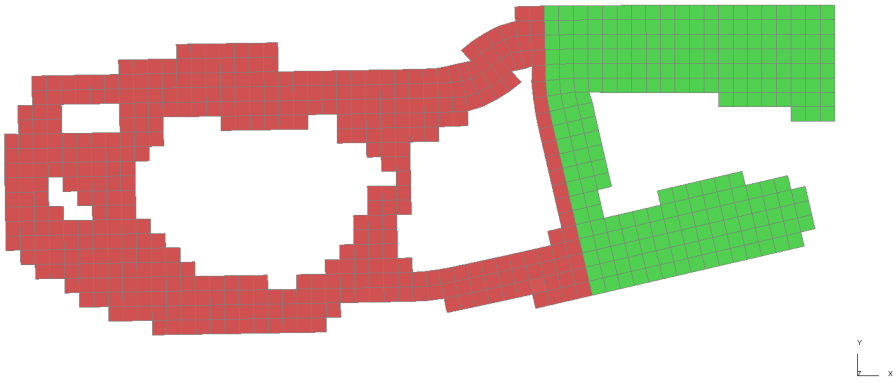

Figure 5.17 : PS_M06 final topology deformed state

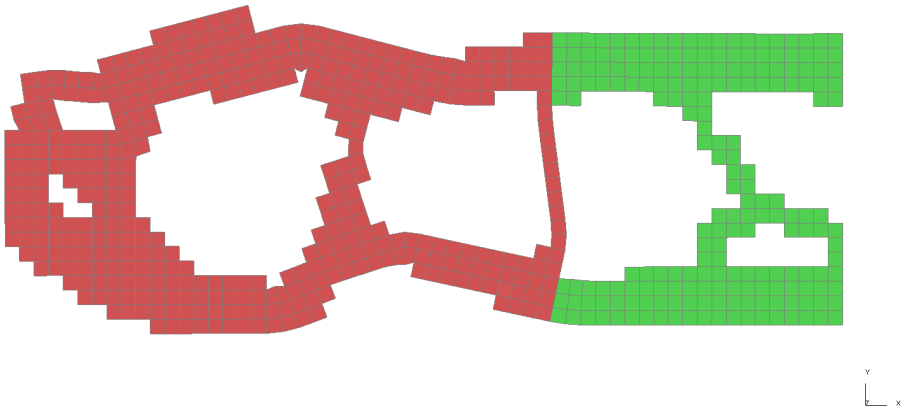

Figure 5.18 : PS_M07 final topology deformed state

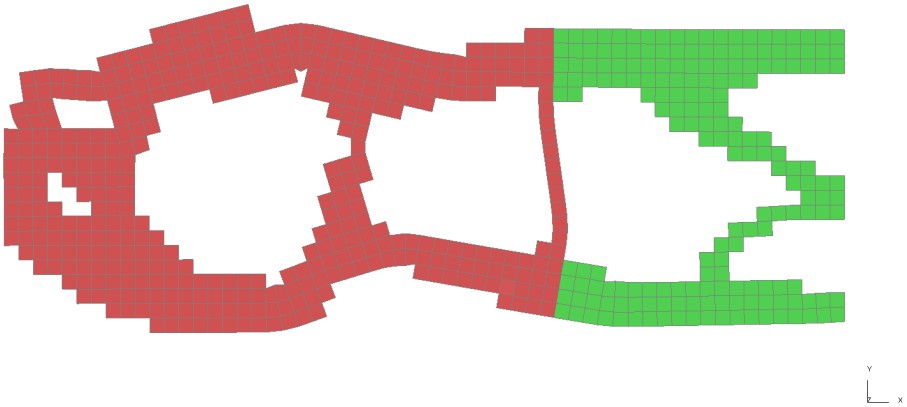

Figure 5.19 : PS_M08 final topology deformed state

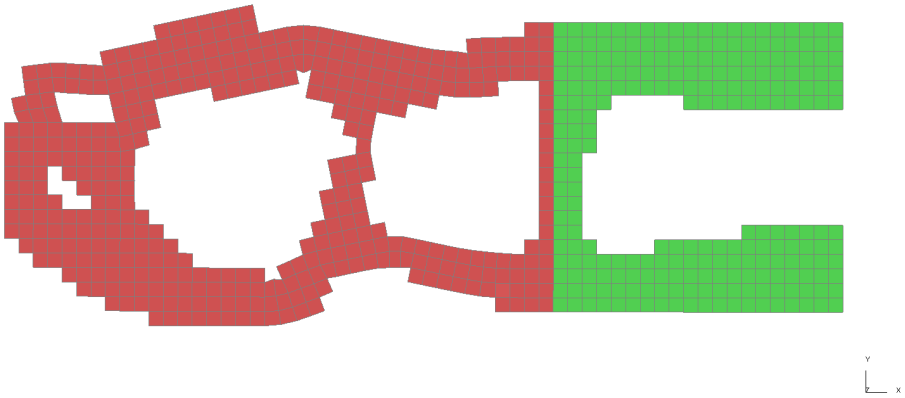

Figure 5.20 : PS_M09 final topology deformed state

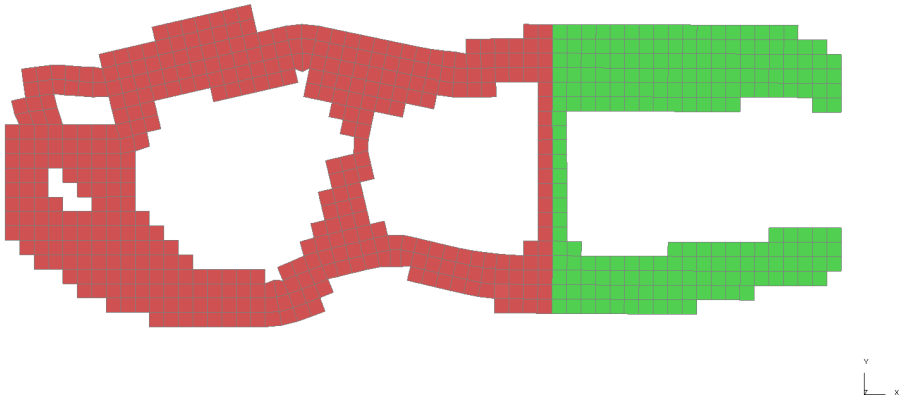

Figure 5.21 : PS_M10 final topology deformed state

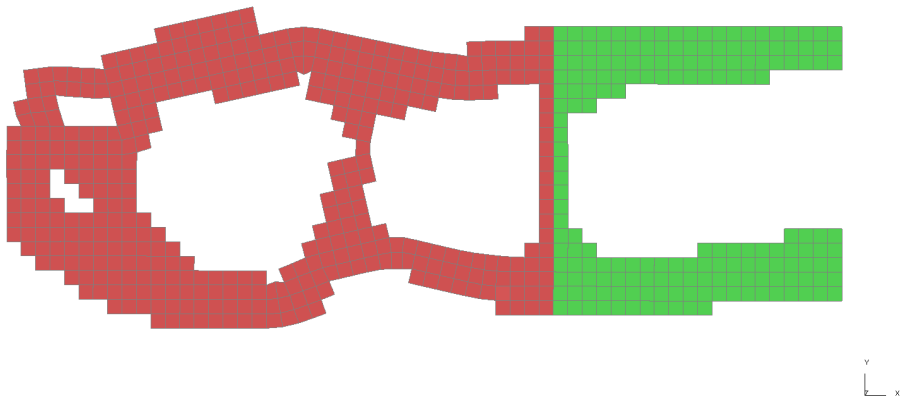

Figure 5.22 : PS_M11 final topology deformed state

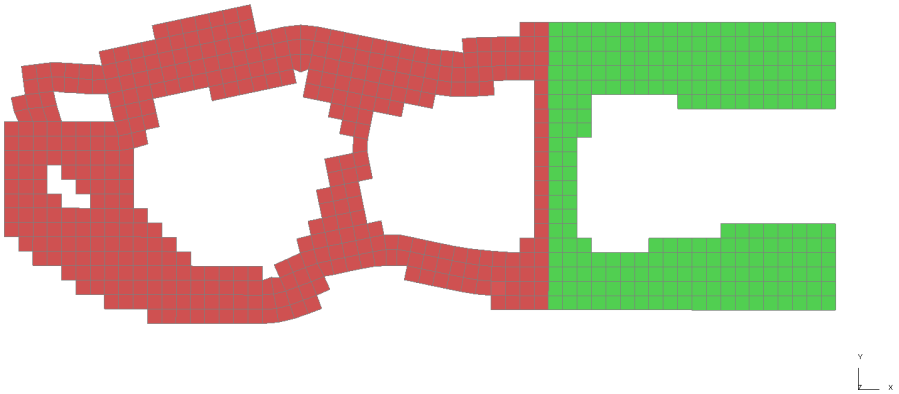

Figure 5.23 : PS_M12 final topology deformed state

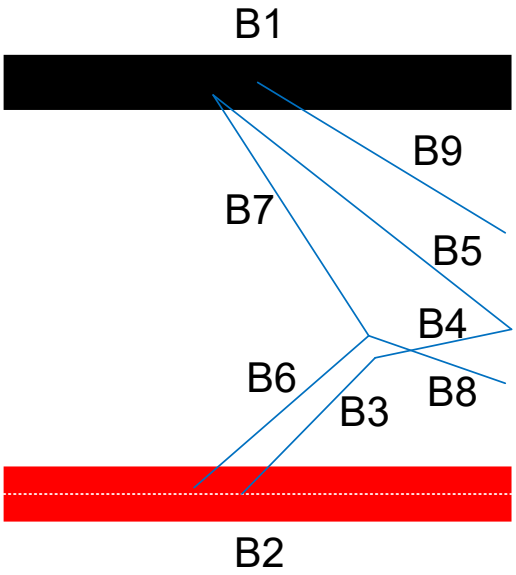

Figure 5.24 : Topology trends linear section models PS_M05 - PSM12

The first observation refers to the non-linear section, which for all models remains unchanged. This however is unsurprising, as the BCs haven't changed between models (SPCs are used), the loading conditions are the same as are the interface sizes, i.e. the design volume. This means that the cross section forces for each non-linear iteration are the same, and therefore any change in the linear section topology will be purely as a result of the rate of exchange parameters.

Observing the deformation of PS_M06 (Figure 5.17), it is apparent that during the optimisation process, a disconnection has been created in the lower member of the linear

section (the dotted line in loadpath A2 in Figure 5.24). This has significantly weakened the structure, as the large displacement illustrates.

It also appears that, regardless of the exchange between the non-linear and linear optimisation processes (the first rate of exchange parameter), the increase of the DESMAX value results in more similar linear sections. This backs up the claim in Study A that the convergence of the linear optimisation process could be one of the most influential parameters. This is illustrated in Figure 5.24, where the inner loadpath combinations (A3-A4-A5, A6-A7-A8 and A9) occur infrequently, and for lower DESMAX values.

Figure 5.25 displays the plastic strain plot for the linear section (section (2)) of PS_M06 to illustrate the disconnection problem, and Figure 5.26 the corresponding internal energy graph. Table 5.6 summarises the values for the models considered in this study:

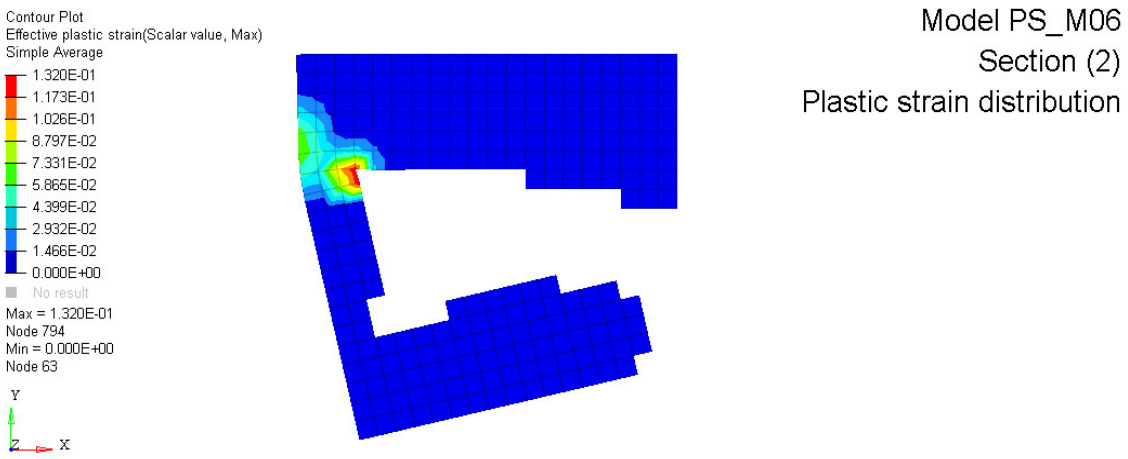

Figure 5.25 : PS_M06 section (2) plastic strain distribution

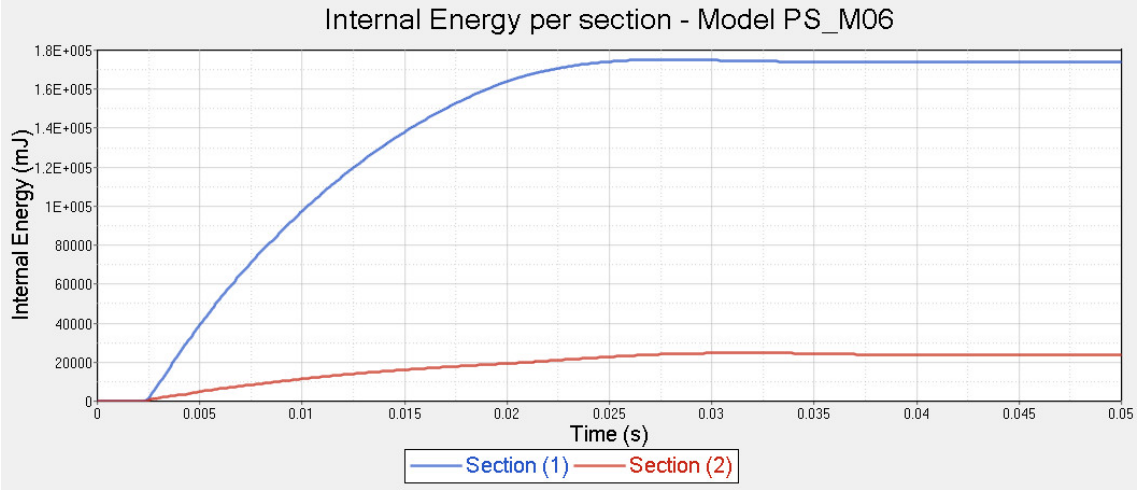

Figure 5.26 : Component internal energy (mJ) of PS_M06 vs time (s)

Table 5.6 : Study B re-analysis data

Model Number	Plastic strain section (2) (%)	Total Internal Energy (mJ)
PS_M05	16	241228.58
PS_M06	24.2	199843.10
PS_M07	17.7	240239.30
PS_M08	19.8	239523.21
PS_M09	0.0177	237686.03
PS_M10	1.39	238605.26
PS_M11	0.34	238036.44
PS_M12	0.0124	237707.31

Figure 5.25 and Table 5.6 illustrate the disconnection in the linear structure, but also the nature of the behaviour. The plastic strain that occurs in the linear section is very localised, and this is reflected in the total energy absorbed which is substantially lower than the other models in Study B. This result is unsurprising as the disconnection allows the lower member to rotate around the point of plastic strain, and therefore the displacement is very high. This disconnection is undesirable, and the DESMAX value has corrected the disconnection as can be observed in Figure 5.20 and Figure 5.23.

Table 5.6 also demonstrates the influence that DESMAX has had performance-wise. PS_M10, PS_M11 and PS_M12 all have a DESMAX value of 20, and their respective maximum plastic strain values are all acceptable concerning the intended linear behaviour. The extension of this observation is that the convergence of the linear section is crucial in obtaining non-linear and linear behaviour in the respective sections, and is even more crucial when the force data exchange is less frequent. The only “anomaly” is

PS_M02 (Table 5.5), where the maximum plastic strain of the linear section is low, despite a DESMAX value of 1. This could be explained by the formation of a vertical member which could stiffen the structure. The overall trend however remains that an increase in DESMAX contributes towards more efficient structures, which in this instance relates to the levels of plastic strain in the “linear” section. This effect in combination with the interface size will be analysed in this chapter. It should also be noted that because of the calculation of the target volume at each iteration (equation (4.1) and (4.2)), the rate of exchange changes will modify the final volume of the linear structure depending on when the convergence of the BEETS process is achieved, which terminates the hybrid TO process. Therefore there are slight differences in the volume, which explains why for example the plastic strain in PS_M12 is lower than PS_M11 or PS_M10.

The following section will focus on the “linear model optimisation objective/constraint” parameter.

5.1.3. Study C – Linear model optimisation objective/constraint

Model PS_M13 is considered for study C. The maximum stress value selected as the linear optimisation constraint is 276 MPa (the Yield strength of the non-linear material card in LS-DYNA). Figure 5.27 displays the final structure deformation (both non-linear and linear sections attached) obtained and re-analysed after the optimisation process:

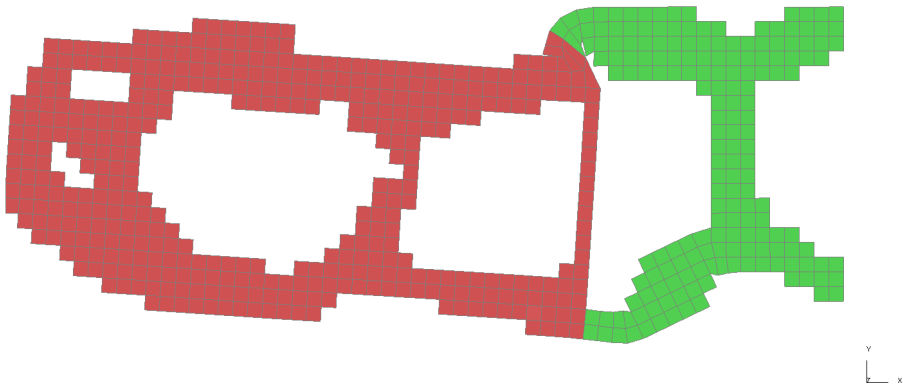

Figure 5.27 : PS_M13 final topology deformed state

The results display large amounts of deformation at the interface, which at first glance cold be surprising as this model should be compared to PS_M02 (Figure 5.9) which has identical hybrid TO parameters except for the linear model optimisation objective and constraint (minimise compliance / volume target). Both structures are very similar in that they have two very clear load paths in the upper and lower edges of the linear structure,

and also have a vertical member. However the behaviours are very different. A closer look however reveals that at the interface, the upper and lower members are thinner than PS_M02. It could be therefore that the more crucial areas of the structure are the sizes of the upper and lower members, and more crucially the sizes near the interface.

Figure 5.28 displays the plastic strain plot for the linear section of PS_M13, and Figure 5.29 the corresponding internal energy graph. Table 5.7 summarises the values for the models considered in this study:

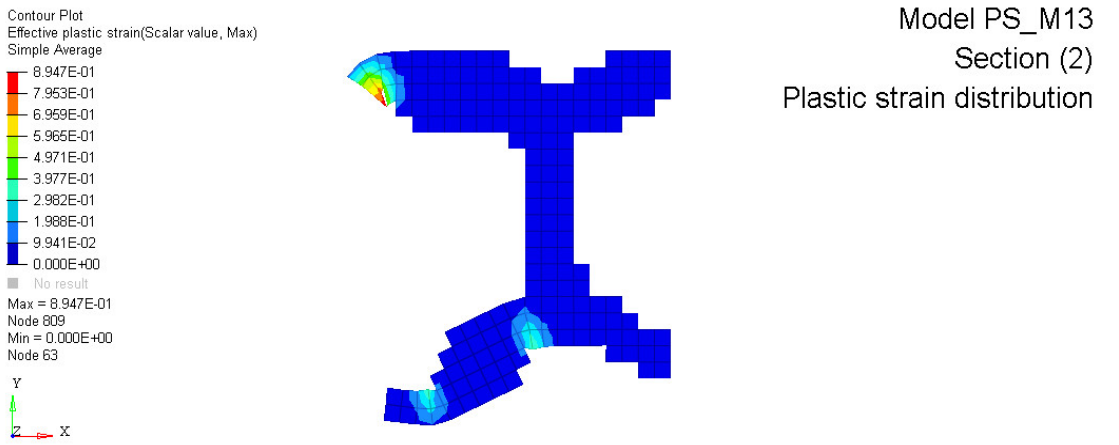

Figure 5.28 : Model PS_M13 section (2) plastic strain distribution

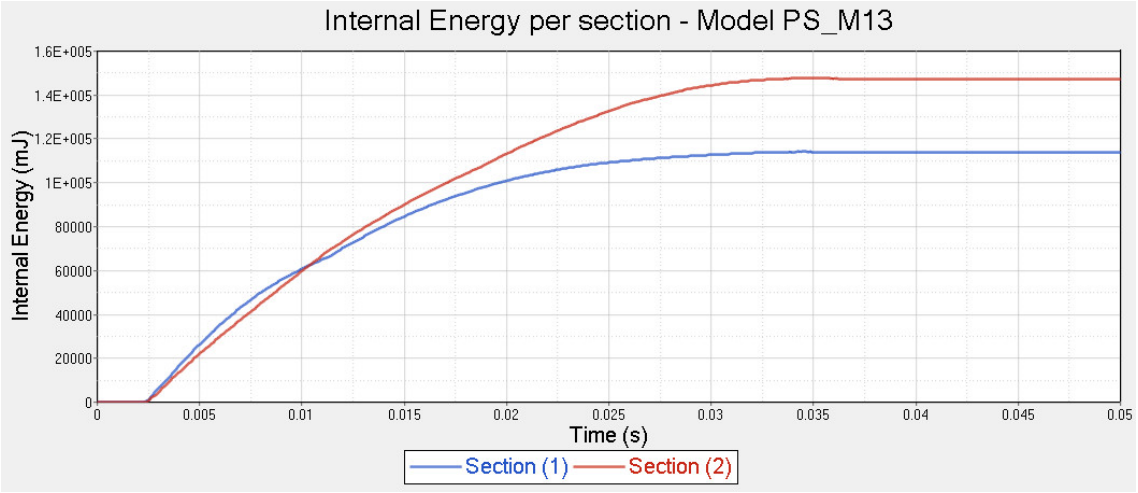

Figure 5.29 : Component internal energy (mJ) of PS_M13 vs time (s)

Table 5.7 : Study C re-analysis data

Model Number	Plastic strain section (2) (%)	Total Internal Energy (mJ)
PS_M13	89	261735.60

The plastic strain results back up the observations made from the structural deformation. Furthermore, the internal energy graphs in Figure 5.29 illustrate that the internal energy absorbed by the linear section (section (2)) is higher than that of the non-linear section (section (1)). This of course is undesirable in the context of vehicle crashworthiness, and can perhaps be explained by the DESMAX value. The deletion of the elements in the linear section occurs at iteration 1 of the hybrid process, and in the following iterations no more volume is removed from the structure. Figure 5.30 illustrates the density distribution for iteration 1 of the process and Figure 5.31 the von Mises stress distribution for the same iteration:

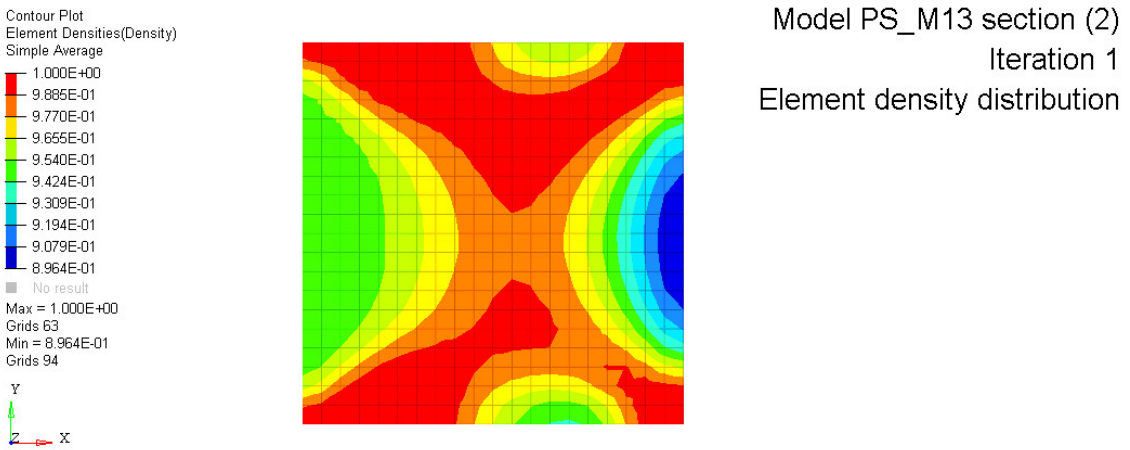

Figure 5.30 : PS_M13 section (2) iteration 1 element density distribution

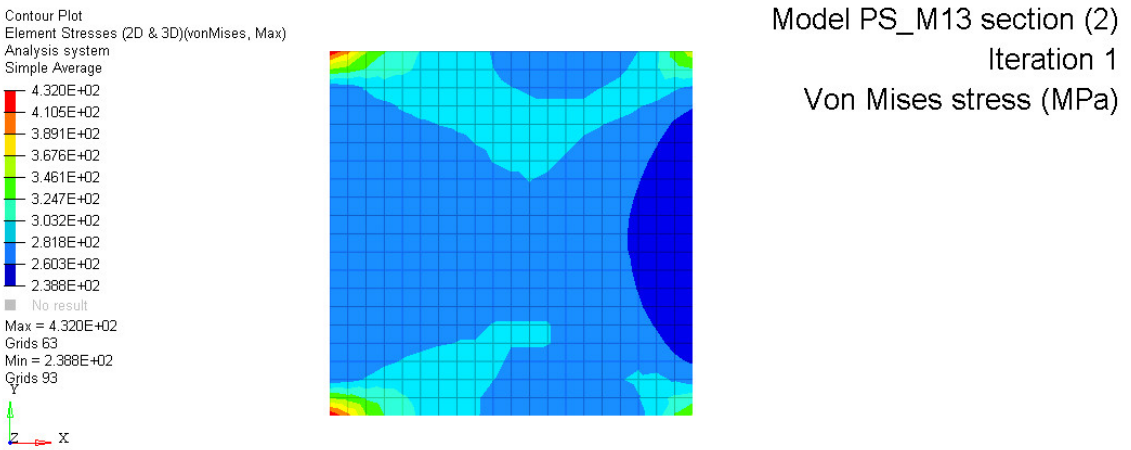

Figure 5.31 : PS_M13 section (2) iteration 1 von Mises stress (MPa)

The relative density plot unsurprisingly reveals the load path obtained at the end of the optimisation process. However, a closer look at the values reveals that even the lowest relative density values are still high at 0.89. In most cases, elements with a relative density value of 0.89 would not be candidates for deletion. However, the von Mises

distribution plot also reveals elements with stress levels below the set constraint. Therefore at the first hybrid iteration, many elements are removed from the structure. Effectively, this is logical with the element removal process. The inefficient structure created as a consequence of this method is more to do with the maximum iteration parameter DESMAX, which is set to 1. It would appear that, for the “minimise mass” case, and in particular with respect to the stress constraint, the convergence of the linear structure, and therefore a higher DESMAX value is more crucial. This will be tested later in the chapter.

The following section will focus on the “interface BCs” parameter identified in chapter 4.

5.1.4. Study D - Interface BC

Models PS_M14 and PS_M15 are considered for study D. Figure 5.32 - Figure 5.33 displays the final structure deformation (both non-linear and linear sections attached) obtained and re-analysed after the optimisation process:

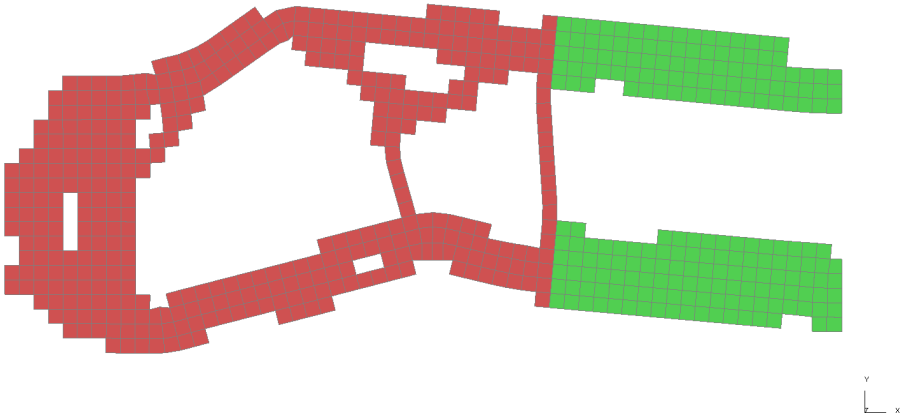

Figure 5.32 : PS_M14 final topology deformed state

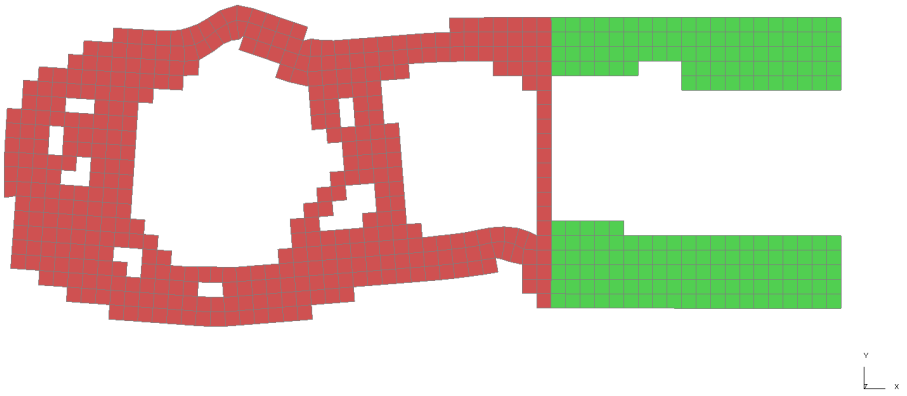

Figure 5.33 : PS_M15 final topology deformed state

Figure 5.34 re-illustrates PS_M02 (which can be compared to the two models in this study), with Figure 5.35 and Figure 5.36 summarising the loadpath trends for the three models:

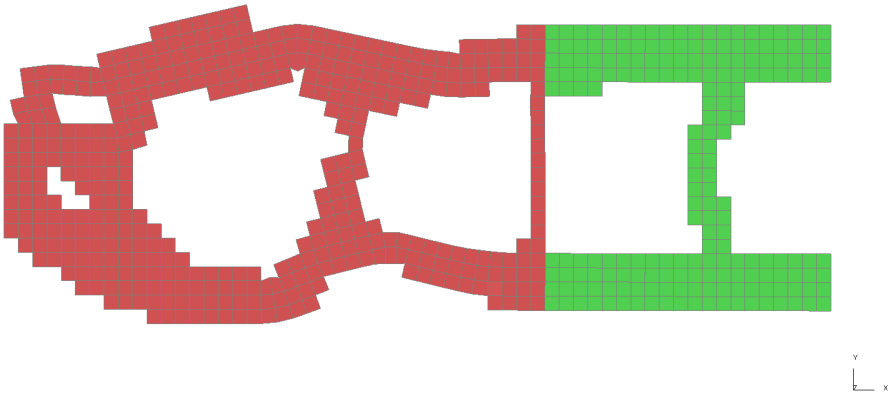

Figure 5.34 : PS_M02 final topology deformed state

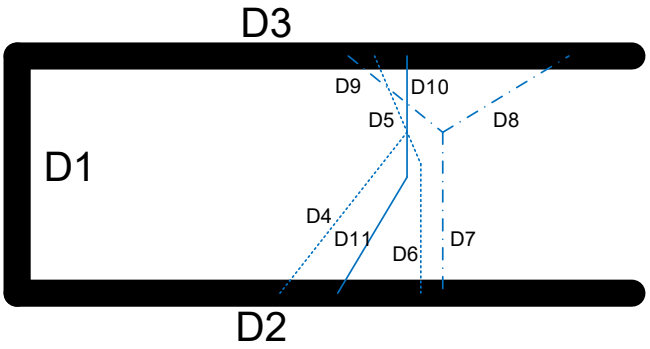

Figure 5.35 : Topology trends non-linear section for models PS_M02, PS_M14 and PS_M15

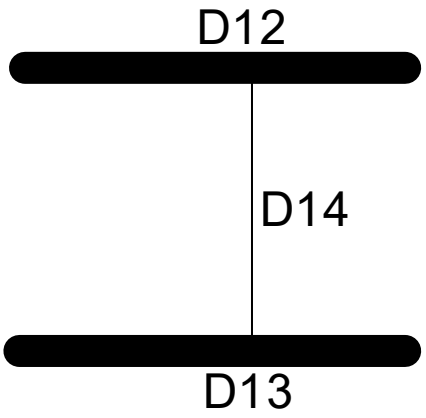

Figure 5.36 : Topology trends linear section for models PS_M02, PS_M14 and PS_M15

Globally, there are no major changes in the structures compared to PS_M02, but some small modifications in the non-linear structure seem to have had an effect on the overall behaviour. The changes mostly seem to be in the central member of the non-linear structure as illustrated in Figure 5.35 where the different trend combinations are represented by the solid line (D10-D11 for PS_M02), the dashed lines (D4-D5-D6 for PS_M14) and the dashed-dotted lines (D7-D8-D9 for PS_M15). The behaviour would suggest that method B, i.e. updating the zero length beam stiffness, has produced a more efficient structure than a constant stiffness (method A).

Table 5.8 summarises the maximum linear section plastic strain and total internal energy values for the models considered in this study:

Table 5.8 : Study D re-analysis data

Model Number	Plastic strain section (2) (%)	Total Internal Energy (mJ)
PS_M14	19.3	237842.67
PS_M15	0.1	241693.85

The observations from Figure 5.32 and Figure 5.33 are clearly illustrated in the re-analysis results. PS_M14 is exposed to relatively high levels of deformation in the linear section (in comparison to the more acceptable levels in PS_M02 and PS_M15). PS_M15 demonstrates very similar results to PS_M02, therefore it is too early at this stage to fully establish the effects of the modifying the BCs at the interface. It would appear that not modifying the stiffness of the beams throughout the optimisation process has a negative effect on the efficiency of the structure. This parameter will be analysed in combination with the rate of exchange and interface size parameters, where essentially it will be

possibly to determine the difference in consistency of results compared to using SPCs at the interface.

The next section will focus on the BCs applied in the linear section (section (2)) of the structure, in this case applying IR.

5.1.5. Study E - Linear BC

Models PS_M16 – PS_M18 are considered for study E. Of the three models considered, PS_M17 resulted in an error termination in the linear FE analysis during the optimisation process due to detached elements in the model. This issue most likely results from the combination of two factors. Firstly, the mass points are located along the entire edge of the structure (Figure 5.6), meaning that there is no clear load path through the structure (as opposed for example with PS_M16 and a single mass point used). Secondly, for this study DESMAX had a value of 1, which clearly means that the linear optimisation process could not converge. Coupled with the mass points, this results in intermediate densities and elements wrongfully removed from the structure, hence the appearance of detached elements. Figure 5.37 displays the density distribution at hybrid iteration 4, and Figure 5.38 the structure used at iteration 5 with the disconnected element:

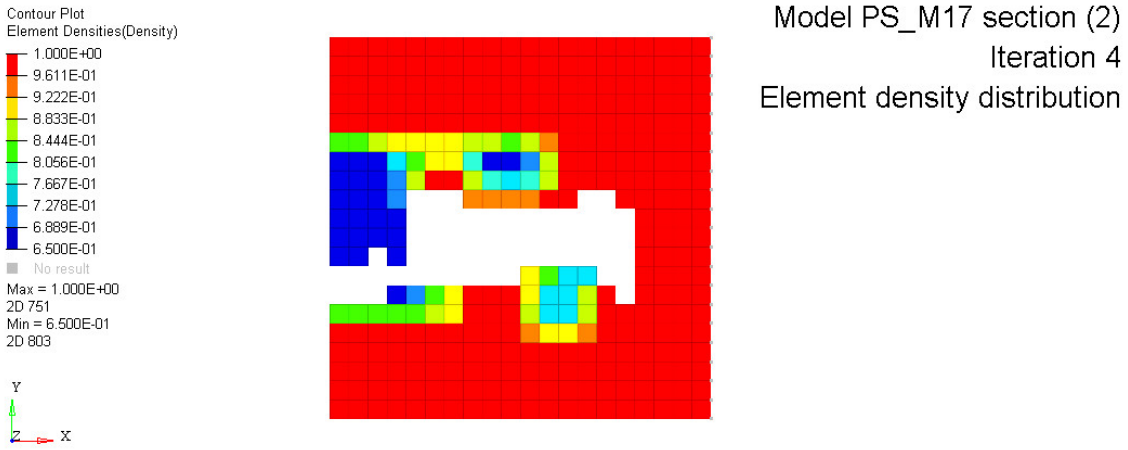

Figure 5.37 : PS_M17 section (2) iteration 4 element density distribution

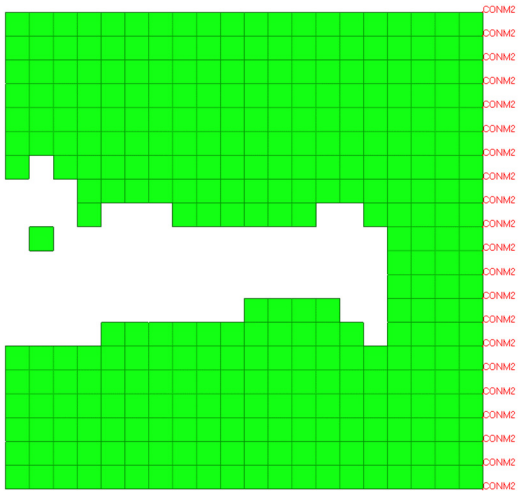

Figure 5.38 : PS_M17 section (2) iteration 5 FE setup

Although there are clearly low density elements in the structure, the "minimise compliance/volume target" case dictates the number of elements removed from the structure. Therefore there is a risk of detached elements appearing in the structure. For the re-analysis, the structure at iteration 4 was used for PS_M17, and Table 5.9 summarises the results:

Table 5.9 : Study E re-analysis data

Model Number	Plastic strain section (2) (%)	Total Internal Energy (mJ)
PS_M16	8.95	241942.05
PS_M17	0.083	241916.82
PS_M18	25.5	241748.46

Table 5.9 illustrates the issues with IR at this stage. Even though the total internal energy values are somewhat higher than the equivalent SPC model PS_M02 (238716.14 mJ), this is due to either too much deformation in the "linear" section (PS_M16 and PS_M18) or the substantially higher volume in PS_M17 due to the linear section being taken from iteration 4. Overall, it is clear from these results that the structures are inefficient when compared to previous models using SPCs. However, as previously mentioned, the rate of exchange has a large part to play in the overall optimisation process, and these initial results show that its influence could be greater when IR is used in the linear structure. Therefore IR warrants further analysis to establish a better understanding of its influence compared to SPCs.

So far, this study has focused on modifying and analysing the effects of a single optimisation parameter at a time. However, to fully establish an overview of the effects of each parameter, it is necessary to study combinations of the most influential parameters thus far to determine whether they can reduce or even eliminate each other's drawbacks. From these initial analyses, the rate of exchange and the interface size have been shown to be the most influential parameters on the optimised structures. Therefore the subsequent studies will evaluate the effects of combining these two parameters with each other and the remaining hybrid TO parameters. The following section will analyse the combined effects of the rate of exchange and the interface size.

5.1.6. Study F - Interface size / Rate of exchange

The initial studies into both these parameters (5.1.1 and 5.1.2) revealed that a relatively large interface size created unfeasible designs, whereas in terms of the rate of exchange, an insufficient number of linear iterations (controlled by the DESMAX parameter) could create disconnections in the final structure. This section will study the effects of combining these two parameters. Models PS_M19 – PS_M42 are considered. Three groupings are analysed, depending on the interface sizes as in this instance the non-linear structures are identical to the initial interface size study, i.e. SPCs are used at the interface as BCs, therefore no variation of interface BCs during the optimisation process. It should be noted that, although this study doesn't include the models with a "20" interface size, this is because in essence these have been analysed during the initial rate of exchange study in section 5.1.2 as this interface size is the "default setting". The groupings are summarised in Table 5.10 below:

Table 5.10 : Combined interface size / rate of exchange study groupings

Grouping 1 – 0" interface size	**Grouping 2 – "60" interface size**	**Grouping 3 – "120" interface size**
PS_M19	PS_M20	PS_M21
PS_M22	PS_M23	PS_M24
PS_M25	PS_M26	PS_M27
PS_M28	PS_M29	PS_M30
PS_M31	PS_M32	PS_M33
PS_M34	PS_M35	PS_M36
PS_M37	PS_M38	PS_M39
PS_M40	PS_M41	PS_M42

Grouping 1

Table 5.11 summarises the plastic strain and total internal energy after re-analysis:

Table 5.11 : Study F – Grouping 1 re-analysis data

Model Number	Plastic strain section (2) (%)	Total Internal Energy (mJ)
PS_M19	22.1	239672.06
PS_M22	22.9	162511.34
PS_M25	1.1	216510.05
PS_M28	30.4	238518.98
PS_M31	3.1	216167.37
PS_M34	1.1	216712.55
PS_M37	35.5	236182.47
PS_M40	3	216233.26

These results demonstrate an emerging pattern. Firstly, PS_M22 (i.e. the first linear optimisation process takes place after 10 non-linear iterations, and a DESMAX value of 1) displays a disconnection in the structure, very similar to the effect in model PS_M06 (Figure 5.17). The only difference between the two is an interface size of 0 (PS_M06) and 1 (PS_M22). Therefore this illustrates the problem stated in section 5.1.2 that a combination of a low DESMAX value and low frequency of force data exchange can result in these disconnections. Figure 5.39 illustrates the problem in PS_M22:

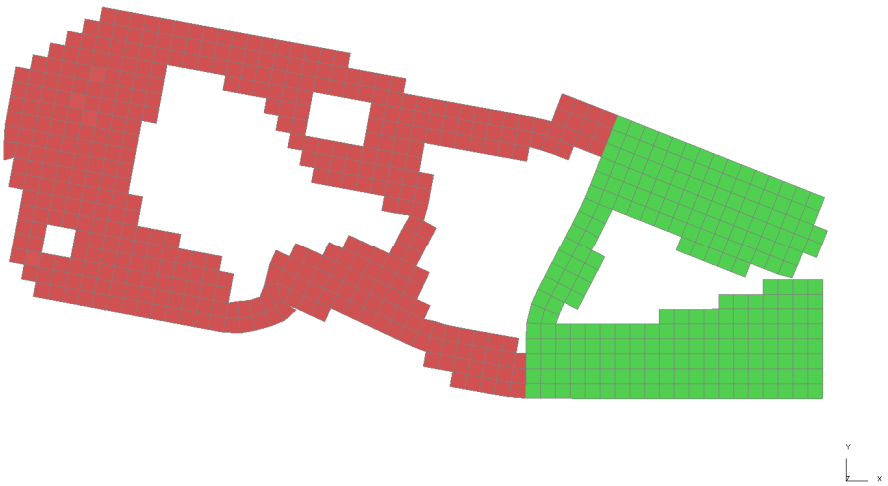

Figure 5.39 : PS_M22 final topology deformed state

The results show similar trends compared to the individual parameter studies. The disconnection in PS_M22 is avoided when the DESMAX value is increased, and PS_M19, PS_M28, and PS_M27 suffer from the same “issue” regarding the target volume calculation as discussed in section 5.1.2. Furthermore, the plastic strain results

would suggest that exchanging the force data at every iteration (PS_M25 and PS_M34) produce the best structures. However, the results on the other end of the scale, i.e. every 10 iterations for PS_M31 and PS_M40, also produce acceptable results in terms of maximum plastic strain in the linear structure. Therefore, relating back to the issue in PS_M22, it is allowable for the data exchange to be less frequent provided there is an increase in iterations within the linear optimisation process.

Observing the geometry obtained in this grouping compared to the results in section 5.1.2, there is a noticeable similarity between the models. The non-linear structures are very similar, therefore the load paths through the structures are also likely to be comparable. Therefore, there is no reason for vastly different structures. Figure 5.40 illustrates an example of the similarities between PS_M10 and PS_M34:

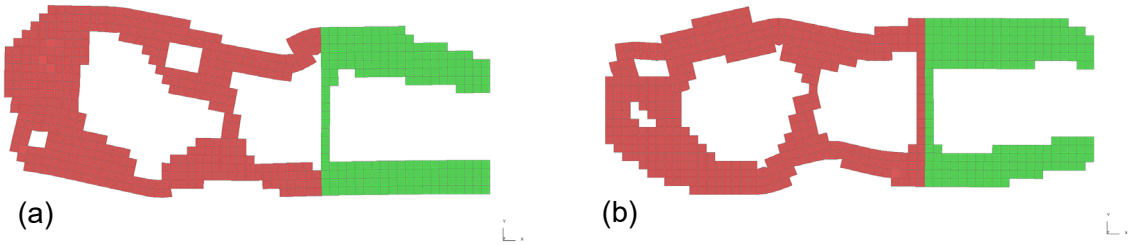

Figure 5.40 : Final topologies for (a) PS_M10 and (b) PS_M34

Overall, the same geometry in the linear section, i.e. the upper and lower “horizontal” members, are repeated in many of the models, and increasingly so with a higher DESMAX value (more convergence in the linear optimisation process). This is illustrated in Figure 5.41 where the white-dashed line represents the disconnection present in PS_M22:

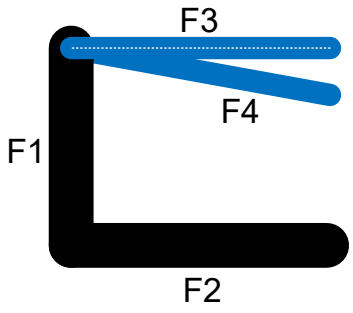

Figure 5.41 : Topology trends linear section for Study F Grouping 1

Grouping 2

Table 5.12 summarises the plastic strain and total internal energy after re-analysis:

Table 5.12 : Study F - Grouping 2 re-analysis data

Model Number	Plastic strain section (2) (%)	Total Internal Energy (mJ)
PS_M20	43.3	238073.88
PS_M23	2.8	234124.84
PS_M26	77.3	235666.41
PS_M29	25.3	238340.43
PS_M32	0.12	240374.25
PS_M35	46.9	237047.72
PS_M38	33	239830.99
PS_M41	0.12	240305.61

Firstly, similarly to the first grouping (PS_M22), a disconnection appears in the final structure of PS_M23. Again this is due to the combination of the low DESMAX value and the low frequency of force data exchange (after 10 non-linear iterations). Figure 5.42 illustrates the issue:

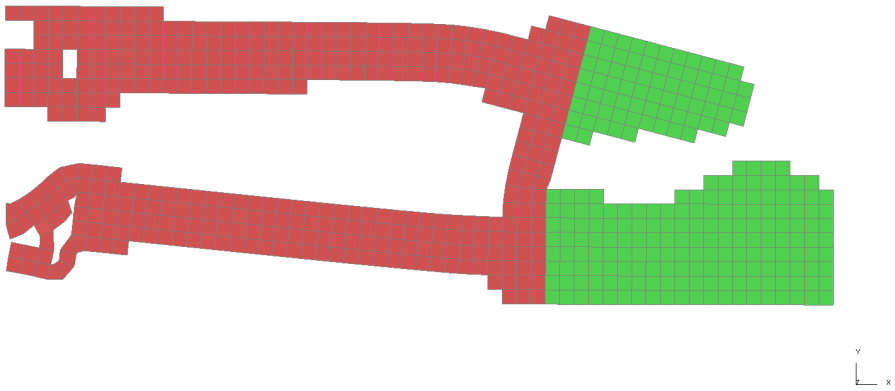

Figure 5.42 : PS_M23 final topology deformed state

Again, this phenomenon disappears when the DESMAX value is increased in the other models (PS_M32 and PS_M41). Furthermore, as mentioned in previous examples, the models with force exchange every 10 iterations generally perform better due to the volume calculation.

Secondly, it is evident from the results that the structures generally perform quite poorly in terms of combined linear / non-linear behaviour. In section 5.1.1 , the problems with the final non-linear structure for this particular interface size have been discussed. Essentially, the assembled linear and non-linear geometries form two single upper and

lower horizontal members, therefore there is a mechanism that allows the linear structure to deform more than the non-linear section. This is reflected in some of the internal energy results in Table 5.12 and in Figure 5.43 below:

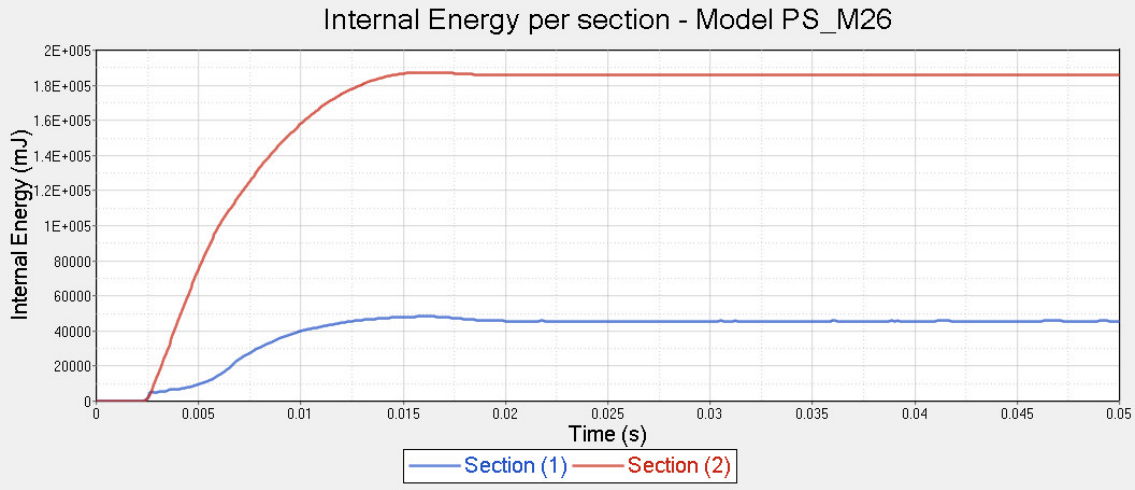

Figure 5.43 : Component internal energy (mJ) of PS_M26 vs time (s)

The graph above illustrates the overall issue with the majority of models in this grouping, i.e. the internal energy in the linear section is in many cases similar to or higher than in the non-linear section. What these results demonstrate is that modifying the rate of exchange hasn't improved on the issues highlighted in section 5.1.1. The main loadpaths from grouping 2 are summarised in Figure 5.44 below, where the white-dashed line represents the disconnection in loadpath F6 visible in model PS_M23:

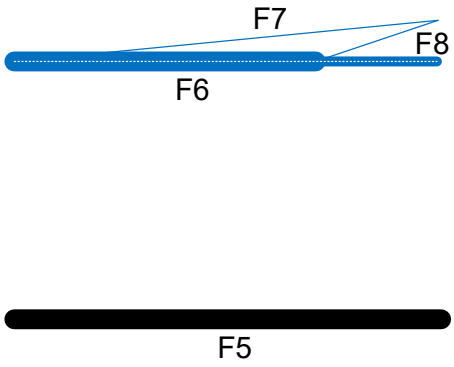

Figure 5.44 : Topology trends linear section for Study F Grouping 2

Grouping 3

Table 5.13 summarises the plastic strain and total internal energy after re-analysis:

Table 5.13 : Study F - Grouping 3 re-analysis data

Model Number	Plastic strain section (2) (%)	Total Internal Energy (mJ)
PS_M21	59.9	239549.18
PS_M24	39.7	237828.80
PS_M27	34.2	240650.42
PS_M30	49.1	234568.54
PS_M33	26.3	241193.47
PS_M36	18	240997.58
PS_M39	34.6	240137.87
PS_M42	17.7	240615.58

These results show that overall, the final iteration topologies in grouping 3 are relatively poor, due to the excessive plastic strain in the “linear” section of the structure. This is despite quite different structures being obtained with the variation of the DESMAX value as displayed in Figure 5.45. The trends for the linear section are summarised in Figure 5.46:

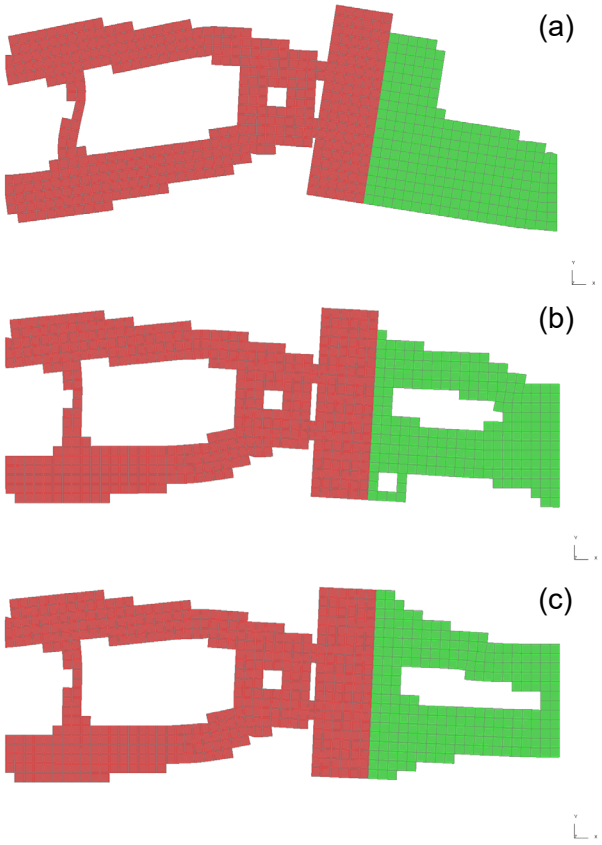

Figure 5.45 : Grouping 3 final topologies deformed state (a) PS_M24 (b) PS_M33 (c) PS_M42

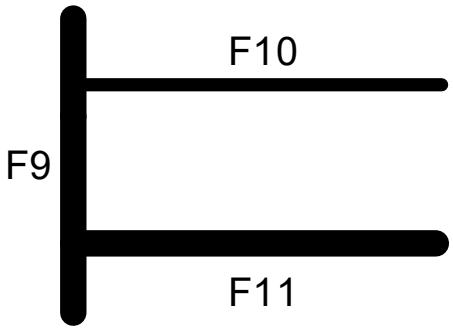

Figure 5.46 : Topology trends linear section for Study F Grouping 3

Overall, the three groupings have demonstrated that the combined rate of exchange and interface size modifications have a limited effect on the structures. In essence, for the cases where the interface size over-restricted the non-linear design volume and by extension unfeasible designs were obtained ("60" and "120" element size interfaces), the modifications of the rate of exchange had little effect in trying to obtain an efficient linear section, i.e. small plastic strain. Similarly to section 5.1.2, the DESMAX value had the most influence on the linear optimisation results, however this was the case only for structures that had feasible non-linear designs. This could demonstrate that the frequency of force data exchange from the non-linear optimisation process to the linear optimisation process, i.e. the second aspect of the rate of exchange, has little effect on the linear topology results, but it also could stem from a relatively small and simple linear design volume. Therefore this aspect will need to be considered and evaluated for more complex structures and future case studies.

The next section will focus on the combined effects of the interface size and the interface BCs.

5.1.7. Study G - Interface size / interface BC definition

The interface BC study in section 5.1.4 analysed the effects of replacing the default BCs at the interface (SPCs) by zero length beams. The initial results suggested that not modifying the stiffness of those beams (method A) according to the linear section displacement results had a negative impact on the overall performance results. By modifying the beam stiffness values (method B), the final iteration topologies were very similar to the equivalent SPC model, however this observation is based on only one model and also on a model that had good performance results. Therefore the study in this section will generally focus on trying to improve on unfeasible non-linear structures, and seeing if that extends to a good performing overall structure. Models PS_M43 – PS_M48 are considered for this study. Table 5.14 summarises the plastic strain and total internal energy after re-analysis:

Table 5.14 : Study G re-analysis data

Model Number	Plastic strain section (2) (%)	Total Internal Energy (mJ)
PS_M43	7.55	247544.34
PS_M44	0.28	241767.79
PS_M45	7.72	253276.87
PS_M46	21	239846.29
PS_M47	11	235707.93
PS_M48	0.61	240955.61

These results are compared to the initial interface study models in section 5.1.1 (PS_M01, PS_M03 and PS_M04). Firstly, comparing PS_M43 and PS_M46 to PS_M01, the results indicate that no improvement was obtained from a plastic strain point of view, and in the case of modifying the beam stiffness values (PS_M46), the plastic strain in the "linear" section was considerably higher. This is interesting as the initial studies into the interface BCs indicated that the worsening of the structure occurred with constant beam stiffness values, and the performance was similar when these were modified. In this case however, the opposite has transpired, and in fact the total internal energy in PS_M43 is higher than PS_M01, though the presence of plastic strain in the linear section remains. Initially, this observation could indicate that there is no real pattern to the structural performance when modifying the interface BCs for the optimisation process.

Observing the other two interface size configurations (PS_M44/ PS_M47 and PS_M45/ PS_M48), interestingly both interface BC modifications have improved the performance of the optimised structure compared to their respective initial results (Table 5.5 in section 5.1.1). Firstly, this indicates that, from a performance point of view at least, using zero length beams provides an improvement on structures that were deemed unfeasible or inefficient in the initial study. Once again, there is a noticeable difference between the results with the updated and constant beam stiffness values, and much like discussed earlier in this section, both have provided different levels of improvement depending on the model with no real pattern. Figure 5.47 displays an example of the improved structures for PS_M45 and PS_M48 compared to PS_M04.

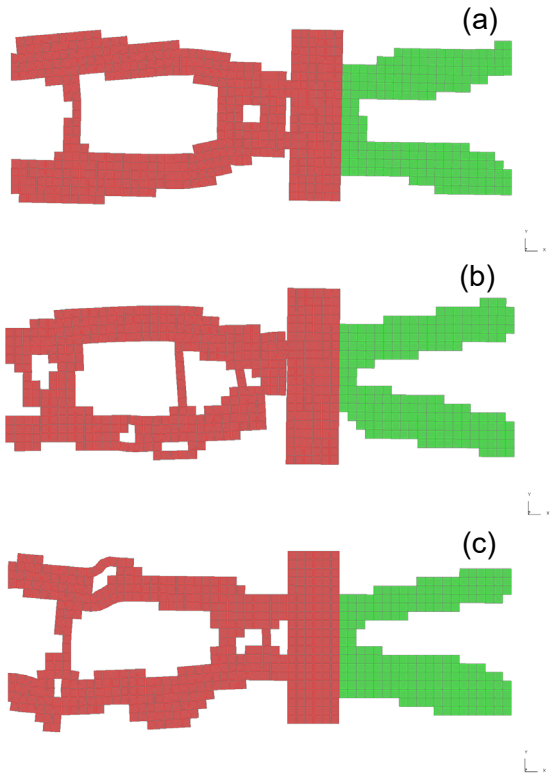

Figure 5.47 : Final topologies (a) PS_M04 (b) PS_M45 (c) PS_M48

The first element of interest concerns the linear final iteration topologies. Interestingly, these have not changed significantly for each interface BC configuration. However, small details have changed in the non-linear structures, even though the overall geometry is very similar. Interestingly, the best performing structure, when regarding the plastic strain values in Table 5.14 PS_M48 is perhaps more similar to the worst performing structure PS_M04. The key differences lie in added holes in the load bearing members that act as crush initiators and more strength in the connection to the non-design area in the non-linear section. Figure 5.48 and Figure 5.49 below summarise the loadpaths in the non-linear and linear sections respectively for study G. It illustrates that, similar to Figure 5.35 in section 5.1.4, the main loadpaths that appear the most frequently are the upper and lower horizontal members (G3 and G2), but are sometimes replaced by a slightly different configuration (G4-G6 replace G2 in PS_M48).

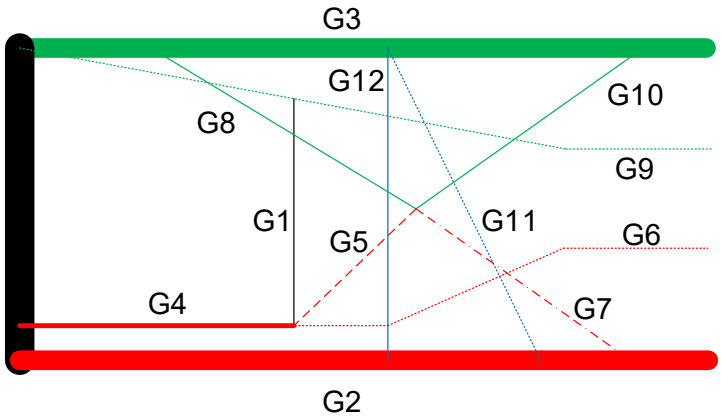

Figure 5.48 : Topology trends non-linear section for Study G

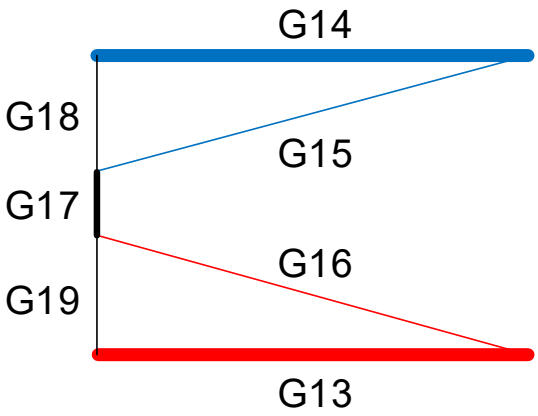

Figure 5.49 : Topology trends linear section for Study G

Overall, the results are quite mixed and no particular trend has emerged in terms of which BC configuration could be considered better. However, the initial results indicate that, performance wise, the zero-length beams could provide an improvement for the initials cases where the interface size is too restrictive. Observing Figure 5.47, it could be debated that these structures remain unfeasible but this is something that is dependent for example on the manufacturing process used which is not considered in this instance. Further analysis will be conducted on these parameters in subsequent section in combination with other parameter.

The next section will focus on the combined effects of the interface size and the linear structure BCs.

5.1.8. Study H - Interface size / linear BC

This section will focus on the interface size parameter in combination with the linear section BCs, and more specifically the difference between SPCs and using IR. Models PS_M49 – PS_M57 are considered for this study. Table 5.15 summarises the plastic strain and total internal energy after re-analysis:

Table 5.15 : Study H re-analysis data

Model Number	Plastic strain section (2) (%)	Total Internal Energy (mJ)
PS_M49	19.2	241818.74
PS_M50	25.6	239122.98
PS_M51	11.3	241186.32
PS_M52	16.6	241833.74
PS_M53	36	241579.71
PS_M54	61.8	241905.01
PS_M55	22	241597.90
PS_M56	53.8	239529.67
PS_M57	11.3	241254.89

Firstly, the results demonstrate none of the models considered can be considered acceptable in terms of combined linear / non-linear behaviour, with the plastic strain too high in each case. This is very similar to the initial observations made in section 5.1.5. A further comparable aspect to the initial investigation is the problem of disconnected elements appearing in the cases of mass point used along the whole edge of the initial linear structure, as depicted by Figure 5.6. PS_M52 and PS_M53 appear have disconnected elements early on in the optimisation process, however that element is deleted immediately in the case of PS_M53 allowing the hybrid TO process to continue (with the linear analysis error termination, elements are deleted according to element numbering as depicted by Figure 5.50).

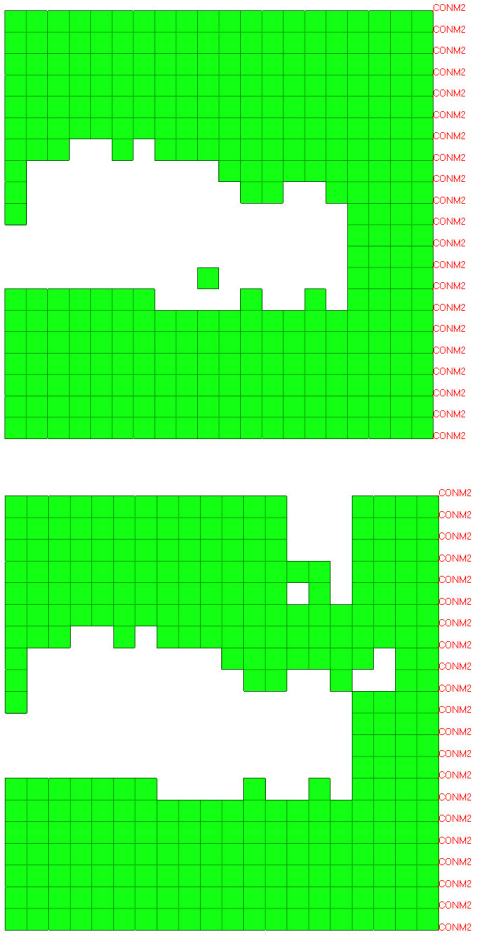

Figure 5.50 : PS_M53 (a) iteration 5 result with detached element (b) iteration 6 with detached element deleted

Overall, the modification of the interface size has not impacted on the feasibility of the structures with IR, as it has much less influence on the linear optimisation process than the mass point location and the rate of exchange (including the DESMAX value), which further underlines the conclusions made in the initial investigation into this parameter in section 5.1.5.

The next section will focus on the final parameter to be coupled with the interface size, the linear model optimisation objective/constraint.

5.1.9. Study I - Interface size / linear model optimisation objective/ constraint

The initial study in section 5.1.3 evaluated the possibility of using other linear optimisation criteria besides minimising compliance with a target volume, i.e. minimising mass subject to a stress constraint on the linear section. The study, with the initial interface size of "20" revealed that the linear optimisation process was perhaps more dependent on the DESMAX value controlled in the "rate of exchange" than the "minimise compliance" option. Before the combined study of these two options at a later stage, this section will focus on verifying whether this phenomenon is repeated with the other interface sizes. Models PS_M58 – PS_M60 are considered for this study. For all three models considered, the results illustrated disconnected elements in section (2), and by extension an error termination during the linear optimisation process. As an example, Figure 5.51 illustrates the element density distribution of section (2) for PS_M58 at iteration 8, and Figure 5.52 shows the subsequent FE setup for iteration 9 with the disconnected elements:

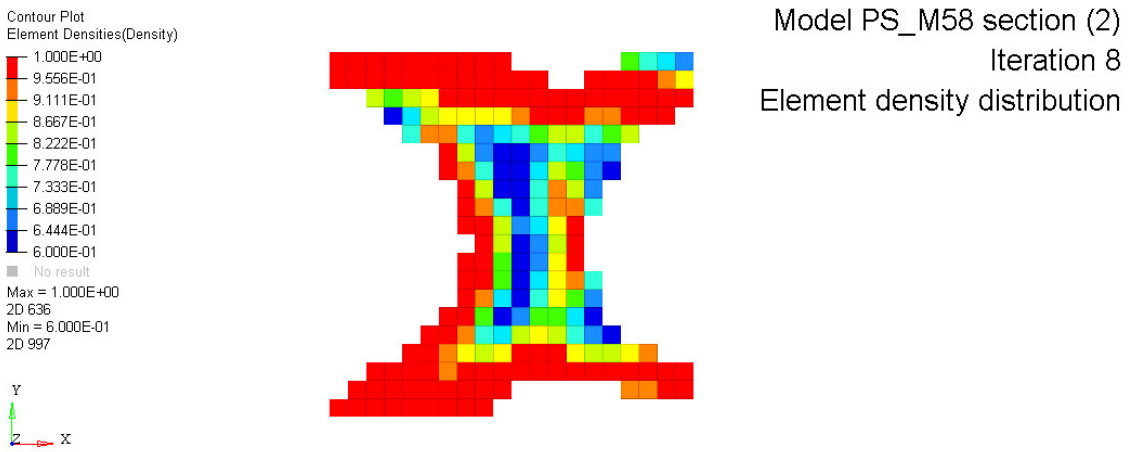

Figure 5.51 : PS_M58 section (2) iteration 8 element density distribution

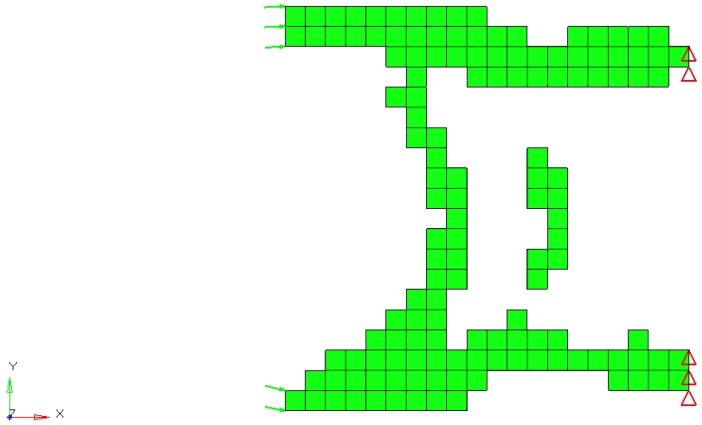

Figure 5.52 : PS_M58 section (2) iteration 9 FE setup

While the structures, and the detached elements that arise in this case differ from the initial study in section 5.1.3, the mechanism conclusions are in fact the same. Effectively, the lack of convergence due to the low DESMAX value means that elements are erroneously deleted from the structure, and they are deleted according to incorrect density and stress data. Whereas this only occurred in the first iteration for PS_M13 in section 5.1.3 (hence the poor performance results after reanalysis), this issue occurred several times for the models in this study, eventually creating detached elements.

Overall, a study into the combination of the rate of exchange and the linear optimisation objective/constraint will provide more substantial information on the validity of using a “minimise mass” linear optimisation objective.

The next section will focus on the combination of the rate of exchange with the interface BC definition.

5.1.10. Study J - Rate of exchange / Interface BC

The initial investigation into the rate of exchange parameter (section 5.1.2) and the subsequent study in combination with the interface size parameter (section 5.1.6) revealed mainly that the DESMAX property within Optistruct had considerably more influence on the optimised structure than the frequency of force data exchange. In some cases, disconnections appeared in the linear section of the structure, and overall the performance of the final iteration topologies was relatively poor if the non-linear structure was unfeasible (in the cases of the higher interface sizes).

However, when modifying the interface BCs, some of the issues with the high interface size cases were reduced and produced better performing structures. Therefore this section will analyse whether the modified interface BCs can also reduce the problems encountered in the rate of exchange studies. Models PS_M61 – PS_M76 are considered for this study. The models are separated into two groupings to represent the two different BC configurations, with and without modification of the zero length beam stiffness values. Table 5.16 summarises the two grouping evaluated:

Table 5.16 : Combined rate of exchange / interface BCs groupings

Grouping 1 – constant beam stiffness	Grouping 2 – modified beam stiffness
PS_M61	PS_M69
PS_M62	PS_M70
PS_M63	PS_M71
PS_M64	PS_M72
PS_M65	PS_M73
PS_M66	PS_M74
PS_M67	PS_M75
PS_M68	PS_M76

Grouping 1

Table 5.17 summarises the plastic strain and total internal energy after re-analysis:

Table 5.17 : Study J - Grouping 1 re-analysis data

Model Number	Plastic strain section (2) (%)	Total Internal Energy (mJ)
PS_M61	7.41	242008.50
PS_M62	1.26	242302.69
PS_M63	0.15	242430.97
PS_M64	25	241913.07
PS_M65	0	242281.44
PS_M66	0.14	242394.95
PS_M67	14.6	241950.99
PS_M68	0	242274.27

Except PS_M61, PS_M64 and PS_M67, which have the same target volume issues due to the rate of exchange, i.e. both structures have a linear section below the volume target, the optimised structures globally perform similarly or better than the cases with SPCs (section 5.1.2). However, it should be taken into account that with the rate of exchange parameters used, PS_M62, PS_M65 and PS_M68 have a slightly higher volume for the linear section than the set volume target. Figure 5.53 illustrates an example of an

optimised structure. The non-linear section remains the same for all models in this grouping (as there is no modification of the beam stiffness values throughout the hybrid TO process).

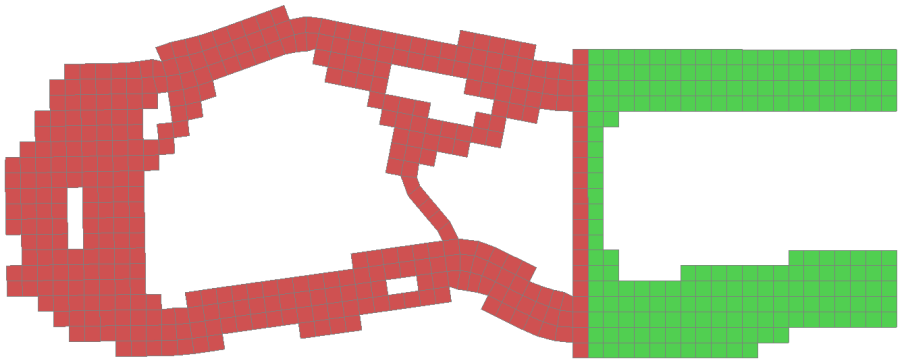

Figure 5.53 : Model PS_M63 final topology deformed state

Where there were issues with the initial interface BC model with constant beam stiffness (Figure 5.32 in section 5.1.4), increasing the DESMAX value (which is the case of both PS_M63 and PS_M66) has slightly altered the linear section of the structure to obtain combined linear / non-linear behaviour in the overall structure. Furthermore, the results for PS_M63 (data exchange every iteration and a DESMAX value of 5 cf. Table 5.17) are better than the equivalent SPC model in section 5.1.2, PS_M07. This difference is less significant when DESMAX is again increased (difference between PS_M66 and PS_M10). However, PS_M67 is significantly worse in terms of plastic strain compared to its SPC equivalent model PS_M11 in section 5.1.2. This could indicate a similar pattern to the combined interface size / interface BC study of section 5.1.7 that the improvements provided by the zero length beams are not consistent. Figure 5.54 below summarises the main loadpath trends through the linear section. Overall, there is very little change in the main loadpaths, with a slight change for models PS_M63 and PS_M66 where J3 is replaced by J4.

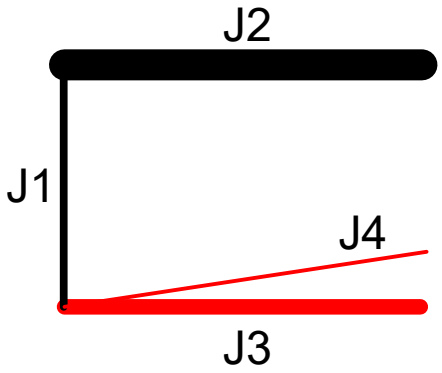

Figure 5.54 : Topology trends linear section for Study J Grouping 1

Grouping 2

Table 5.18 summarises the plastic strain and total internal energy after re-analysis:

Table 5.18 : Study J - Grouping 2 re-analysis data

Model Number	Plastic strain section (2) (%)	Total Internal Energy (mJ)
PS_M69	0.053	242158.11
PS_M70	19.2	242142.00
PS_M71	7.78	241907.19
PS_M72	0.06	242240.70
PS_M73	0	244855.90
PS_M74	5.9	241909.78
PS_M75	0.23	241346.72
PS_M76	0.052	245061.22

Interestingly, the results indicate similar trends to grouping 1, in that there is no consistent improvement in the structure. For example, model PS_M71 has increased the plastic strain in the linear section compared to its SPC equivalent model PS_M07 whereas model PS_M74 has reduced it compared to model PS_M10. Figure 5.55 displays the final structure obtained for model PS_M71 and model PS_M74, with Figure 5.56 and Figure 5.57 summarising the loadpath trends in the non-linear and linear section respectively:

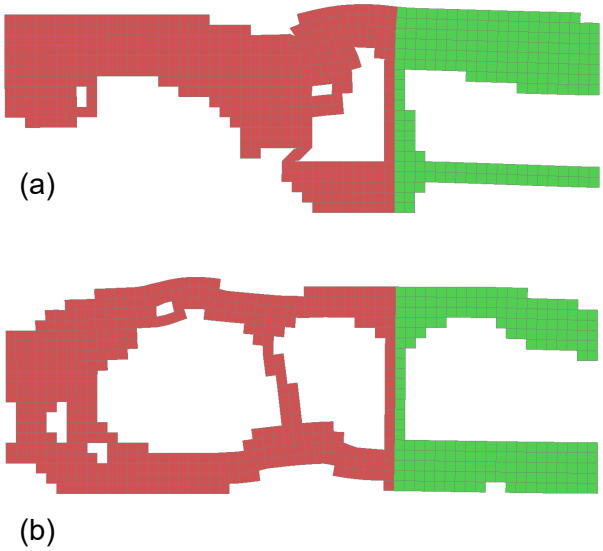

Figure 5.55 : Grouping 2 final topology deformed state (a) model PS_M71 (b) model PS_M74

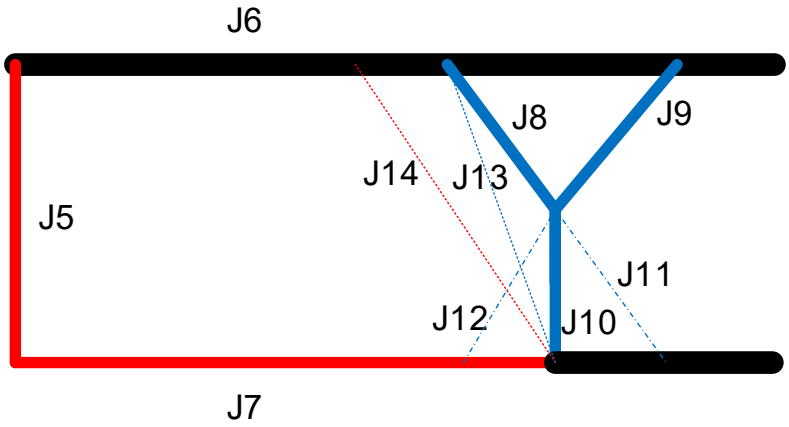

Figure 5.56 : Topology trends non-linear section for Study J Grouping 2

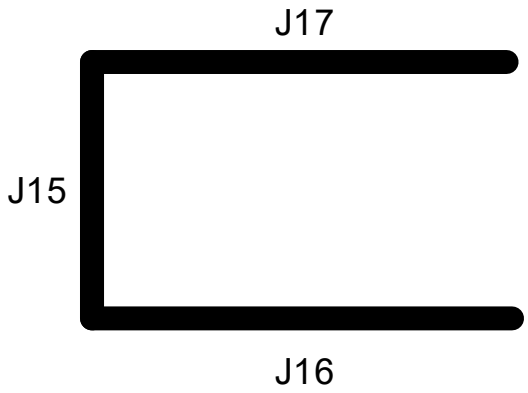

Figure 5.57 : Topology trends linear section for Study J Grouping 2

The first point of interest is the vastly different structure obtained in PS_M71. The weakness near the lower area of the non-linear structure is most likely the reason behind the poor performance of the overall structure. This is represented by loadpath J14 in Figure 5.56

However, a positive from this method seems to be when observing PS_M69, PS_M72 and PS_M75. These three models exchange the data every 5 iterations, and as mentioned before these configurations create linear structures with less volume than the intended volume target. However, the plastic strain reanalysis results in Table 5.18 would indicate that these structures perform in the required manner, i.e. combined linear and non-linear behaviour.

Once again, as with Figure 5.35 in section 5.1.4 and Figure 5.48 in section 5.1.7, the main changes incurred by modifying the zero length beam stiffnesses are in the “inner” reinforcements at a “detail” level, but the overall loadpaths remain very similar (J5-J6-J7). Overall, these additional models have shown that using zero length beams as interface BCs can be beneficial. However as highlighted in this and previous sections, no trend emerges as to which option (constant or modified stiffness) is preferable or which hybrid TO parameters work best in combination with the zero length beams.

The next section will analyse the rate of exchange combined with the use of different IR BC configurations.

5.1.11. Study K - Rate of exchange / linear BC

The previous investigations into the use of IR as the linear BC definition (section 5.1.5 and section 5.1.8) demonstrated that the rate of exchange, and more specifically the DESMAX parameter could potentially be even more influential on obtaining efficient structures than it was when SPCs were used in Optistruct (section (2)). This section will attempt to clarify this statement. Models PS_M77 – PS_M100 are considered for this study. The models are separated into three separate groupings according to the different IR configurations described in study E (section 5.1.5) and summarised in Table 5.19:

Table 5.19 : Combined rate of exchange / linear BC groupings

Grouping 1 – Config 1	Grouping 2 – Config 2	Grouping 3 – Config 3
PS_M77	PS_M85	PS_M93
PS_M78	PS_M86	PS_M94
PS_M79	PS_M87	PS_M95
PS_M80	PS_M88	PS_M96
PS_M81	PS_M89	PS_M97
PS_M82	PS_M90	PS_M98
PS_M83	PS_M91	PS_M99
PS_M84	PS_M92	PS_M100

Grouping 1

Table 5.20 summarises the plastic strain and total internal energy after re-analysis:

Table 5.20 : Study K - Grouping 1 re-analysis results

Model Number	Plastic strain section (2) (%)	Total Internal Energy (mJ)
PS_M77	71.2	241741.43
PS_M78	15.5	241945.28
PS_M79	28.9	244043.16
PS_M80	28.5	244501.49
PS_M81	9.78	241923.64
PS_M82	30	244403.69
PS_M83	16.5	244076.58
PS_M84	28.6	244627.21

The results demonstrate that for this particular mass point configuration, the different combinations of rate of exchange parameters do not create better performing structures, i.e. high levels of plastic strain in the “linear” section. This however is most likely due to the mass point configuration, in this case a single point mass as in Figure 5.5. The single

mass point location determines a well-defined “triangular” load path from the interface edge to the boundary edge of the linear section, and the rate of exchange does not affect the load path. This was also the case for the combined interface size / linear BC study.

Grouping 2

Table 5.21 summarises the plastic strain and total internal energy after re-analysis:

Table 5.21 : Study K - Grouping 2 re-analysis data

Model Number	Plastic strain section (2) (%)	Total Internal Energy (mJ)
PS_M85	81.4	248121.48
PS_M86	51.9	241672.43
PS_M87	0	241971.64
PS_M88	13.2	241764.21
PS_M89	1.3	242063.21
PS_M90	21.8	241791.63
PS_M91	66.4	241915.58
PS_M92	0.5	241964.72

The table demonstrates that overall, the issues mentioned in previous studies regarding the linear BC (section 5.1.5 and section 5.1.8) remain. PS_M87 was reanalysed after extracting the linear section from the 4th iteration, as in subsequent iterations disconnected elements appeared resulting in error terminations for the linear solver. This is illustrated in Figure 5.58 below:

(a)

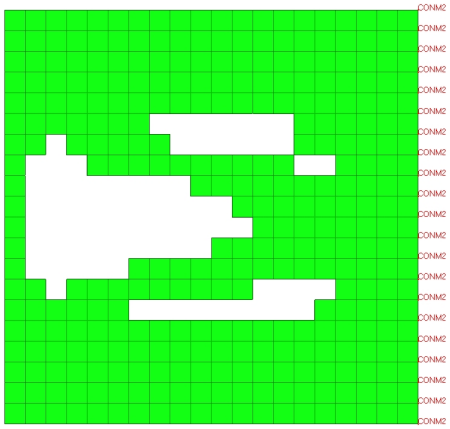

(b)

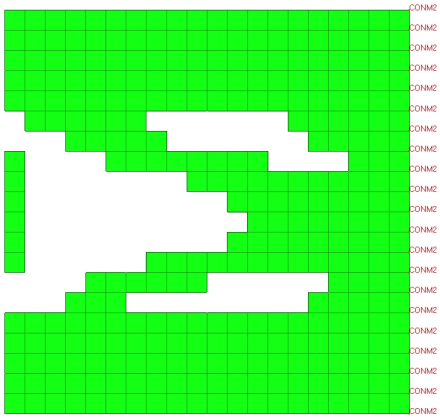

Figure 5.58 : PS_M87 linear section (a) after iteration 4 (b) after iteration 5

Figure 5.58 shows that the detached elements appear quite early on in the process, hence the good performance, i.e. low plastic strain in section 2, of the final structure (only 20% of the initial linear model was removed).

Furthermore, the results show the models where the force exchange is performed every 10 iterations, i.e. the final volume is above the volume target in the linear section, the results are acceptable when DESMAX is increased (PS_M89 and PS_M92). For example, the final volume in the linear section is 60% as opposed to the target volume of 50%. The results in Table 5.21 would therefore indicate that the volume removal of between 40% and 50% is the critical value before weaknesses are created in the structure.

Grouping 3

Table 5.22 summarises the plastic strain and total internal energy after re-analysis:

Table 5.22 : Study K - Grouping 3 re-analysis data

Model Number	Plastic strain section (2) (%)	Total Internal Energy (mJ)
PS_M93	67.5	233444.46
PS_M94	0.27	241906.04
PS_M95	18.7	241895.28
PS_M96	11.3	241935.73
PS_M97	0.49	241939.12
PS_M98	8.9	241934.53
PS_M99	22.9	241814.96
PS_M100	0.11	242022.18

The results indicate similar trends to those in grouping 2. The models with the slightly higher volume (PS_M94, PS_M97 and PS_M100) perform better than the other rate of exchange configurations. However, in this case the initial load paths through the structure are better defined due the mass point definition (Figure 5.7). Therefore there are no cases where disconnections appear in the linear section of the structure.

The studies with the use of IR, and by extension the use of mass points have shown that the latter have much more influence over the final structure obtained. The variation of the hybrid TO parameters such as the rate of exchange and interface size had little influence on the overall geometry of the optimised linear section, although the rate of exchange did appear to have an influence over the stability of the optimisation process when detached elements appeared. Overall, the validity of IR is dependent on the load case, initial structure and the correct location of mass points (and by extension the magnitude).

The next section will focus on the rate of exchange combined with a different linear optimisation objective/constraint.

5.1.12. Study L - Rate of exchange / linear model optimisation objective / constraint

The previous investigations into the use of a “minimise mass” objective / stress constraint for the linear section of the plate structure as opposed to a “minimise compliance” objective / volume fraction constraint have shown that the former could be more sensitive to the change in the number of linear iterations, i.e. the convergence of the Optistruct process. Initially, in section 5.1.3, the structure obtained was poor, as the energy absorbed by the “linear” section of the plate absorbed more energy than the “non-linear” section, i.e. the intended coupled linear / non-linear behaviour was not achieved. In section 5.1.9, with the variation of the interface size, during the linear optimisation process disconnected elements appeared, as can be seen in the example in Figure 5.52. This section will verify whether the rate of exchange, and in particular the DESMAX value, can improve the structures for this particular optimisation objective. Models PS_M101 – PS_M108 are considered for this study. Table 5.23 summarises the plastic strain and total internal energy after re-analysis:

Table 5.23 : Study L re-analysis data

Model Number	Plastic strain section (2) (%)	Total Internal Energy (mJ)
PS_M101	0.67	246114.79
PS_M102	35.8	241805.44
PS_M103	33.2	241919.83
PS_M104	1.15	242099.47
PS_M105	0	241959.22
PS_M106	1.56	241907.77
PS_M107	0	241950.28
PS_M108	0	241950.28

The results demonstrate some interesting trends. Firstly, in similar fashion to the previous studies, the models with a DESMAX value of one (only one linear optimisation iteration) produced geometries with disconnections. Figure 5.59 displays an example of this with PS_M101 and the disconnection in the upper “horizontal” member of the linear section:

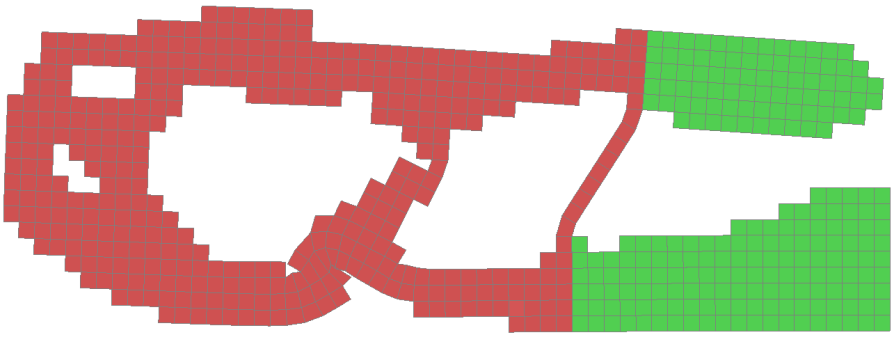

Figure 5.59 : PS_M101 final topology deformed state

Secondly, the performances of the structures seem to improve when the DESMAX value is increased. This is especially true when the DESMAX value is increased to 20, when all three models PS_M106, PS_M107 and PS_M108 have very little plastic strain in the linear section of the structure. Figure 5.60 displays the final topologies for the latter three models:

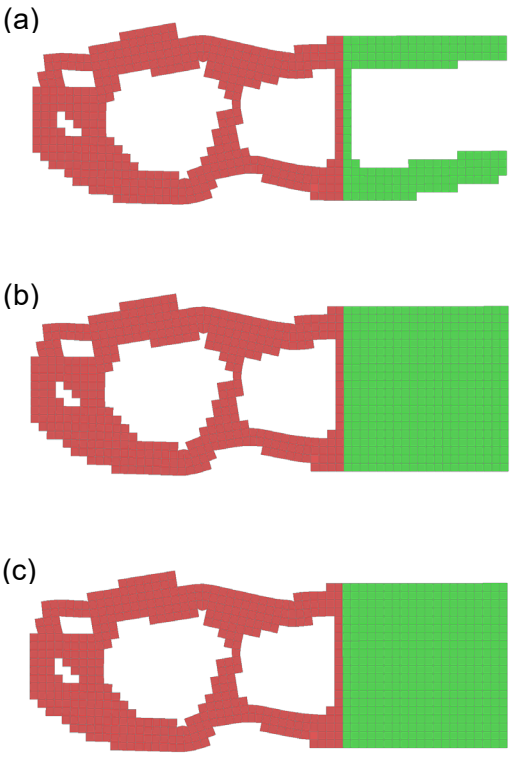

Figure 5.60 : Rate of exchange / linear optimisation objective/constraint final topology deformed state (a) PS_M106 (b) PS_M107 (c) PS_M108

Interestingly, the only model to have removed any material from the linear section is PS_M106. Firstly, no element removal from PS_M107 or PS_M108 is not necessarily an error from the software. Essentially, because PS_M107 and PS_M108 only perform linear optimisation every 5 and every 10 iteration respectively, it could be that the forces transferred across the interface at those iterations create stresses that are considered too high in the linear model, and therefore no material is removed as per the minimise mass / stress constraint optimisation criteria. The way to verify this is to view the element removal per iteration for PS_M106, where the linear optimisation process is performed after each non-linear optimisation. Figure 5.61 illustrates the element removal per linear optimisation process:

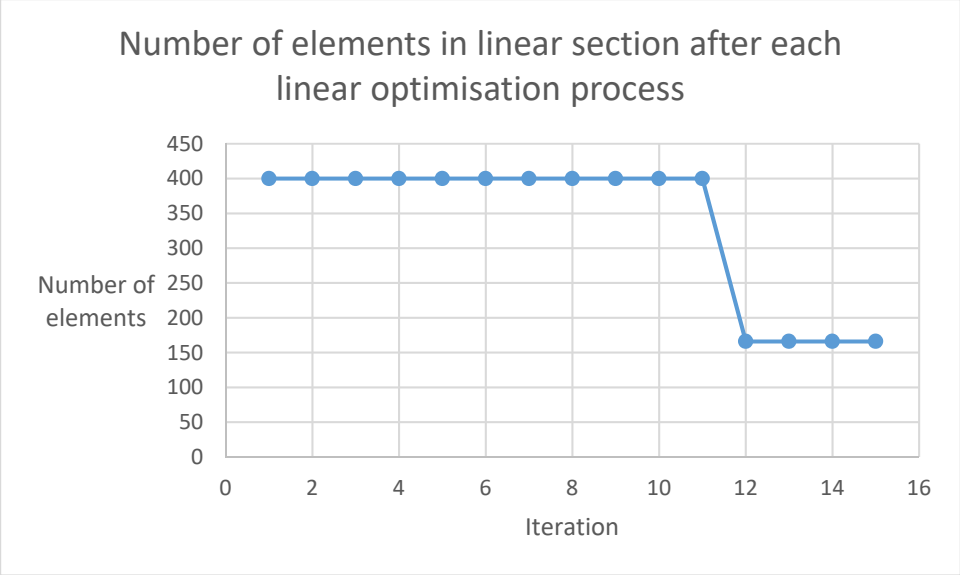

Figure 5.61 : Graph depicting number of elements in linear section of structure after each hybrid TO iteration

As the graph above depicts, in the case of PS_M106, elements are removed from the linear section of the plate only at the 12th iteration of the hybrid TO process. Evidently, for PS_M107 and PS_M108 and their respective rates of exchange, no linear optimisation is performed at iteration 12, therefore no elements are removed from the structure. This could mean that depending on the linear optimisation objectives selected by the user, a lower frequency of force exchange, i.e. less linear optimisation processes, results in important information not being taken into account.

Overall, the conclusions from the previous studies on the linear optimisation objective/constraint have been validated. The increase in the DESMAX value has

avoided any disconnections appearing in the structure, and this study has also revealed that a “minimise mass” objective is also sensitive to the frequency of force exchange between the non-linear and linear solvers. This is not necessarily the case for the “minimise compliance” case as it works off a volume target that is adapted according to the frequency of force exchange (equation (4.1) and equation (4.2)), whereas Figure 5.61 illustrates, important information can be overlooked if the data exchange doesn’t occur at every iteration, and by extension a sub-optimal structure could be obtained.

5.2. Conclusions

This initial study on the hybrid TO method has provided a general overview of the validity of the method and also has established the key parameters in the process. From the previous studies, the following initial conclusions are made for each parameter:

- ***Interface size:*** These initial investigations have demonstrated that an interface size that is too large, i.e. a higher number of non-design elements in the non-linear model, is too restrictive on the design volume for non-linear optimisation. This results in geometries that are inefficient in terms of the evaluated performance criteria and can be unfeasible in terms of their design (e.g. models with an interface size of 6 times the element size created structures with very small contact patches between the design and non-design volumes). The performance issue was reduced for these restrictive interface sizes with the modification of the interface BCs to zero length beams, but because the geometries were globally very similar, it could be argued that in terms of feasibility there was no improvement.
- ***Rate of exchange:*** The studies showed that the two parameters that make up the rate of exchange have varying influences on the optimisation process and by extension the final iteration topologies. While the frequency of force exchange between the non-linear and linear solver did have an influence on the structural performance for lower DESMAX values, when the latter was increased this influence was reduced and overall the final iteration topologies were very similar. This however could be due to the relatively simple load case and geometry used in this case study, therefore more analysis will be performed on this particular aspect of the rate of exchange. By comparison, the DESMAX Optistruct parameter had a lot more influence on the performance of the final structures. When set to the initial value of 1, i.e. only 1 Optistruct iteration, inefficient linear

structures, i.e. high levels of plastic strain, were obtained and increasing the value created more efficient, and usually better defined structures. This is essentially understandable and predictable behaviour as in most cases for TO, several iterations are needed before obtaining an acceptable solution. As Optistruct uses the Variable Density Method/Solid Isotropic Material with Penalisation method (VDM/SIMP), after only 1 linear optimisation iteration there could be many intermediate density elements located in the model, reducing the clarity of the optimum load path through the structure. This could also be amplified by the use of other Optistruct optimisation control parameters such as the DISCRETE parameter of 3 and the MINDIM value of 30 mm (as defined in Appendix A). These values (as opposed to the default settings DISCRETE = 1 and no MINDIM defined) generally require more iterations to obtain a solid/void structure. Therefore, it is clear that enough iterations to reach convergence of the linear optimisation process are needed to obtain efficient structures. This should be determined before the hybrid TO process is run, as the objective function convergence is model-dependent.

- ***Linear model optimisation objective / constraints:*** The modification of the linear optimisation criteria had a significant influence on the final iteration topologies. Compared to the original linear optimisation objective of minimising compliance, the “minimise mass” cases were more sensitive to modifications of the rate of exchange. For lower values of DESMAX, disconnected elements were more frequent in the linear section than for the “minimise compliance” cases. Therefore, a higher number of linear iterations in order for the optimisation process to converge is even more crucial for this particular objective. Furthermore, the structures were also more sensitive to the frequency of force exchange between the linear and non-linear optimisation solvers, i.e. how many non-linear optimisation “loops” are performed per linear optimisation process. Essentially, as shown by PS_M106, PS_M107 and PS_M108 in section 5.1.12, if the forces are not exchange after every non-linear optimisation loop, the linear optimisation solver could be missing an iteration where element removal is possible, i.e. the stress constraint is not violated. This is not the case for the “minimise compliance” case as the element removal is structured around the volume target, the ER selected by the user for the non-linear optimisation process and the frequency of force exchange between the two solvers (as per equations (4.1) and (4.2)).

- ***Interface BC:*** Replacing the SPCs used at the interface, i.e. the BCs used in the non-linear FE model, with zero length beams had a varying influence on the structures, depending on the other hybrid TO parameters used. Table 5.24 below compares the models with identical hybrid TO parameters other than the interface BCs. For each group, the model that produces the most "efficient" structure(s) as measured by the plastic strain in the linear section are highlighted in green. If the results are very similar between two or more configurations, then both are highlighted in the table.

Table 5.24 : Comparison between interface BC models with identical hybrid TO parameters

	SPC	Zero length beams (constant stiffness)	Zero length beams (updated stiffness)
	PS_M01	PS_M43	PS_M46
	PS_M02	PS_M14	PS_M15
	PS_M03	PS_M44	PS_M47
	PS_M04	PS_M45	PS_M48
	PS_M05	PS_M61	PS_M69
	PS_M06	PS_M62	PS_M70
	PS_M07	PS_M63	PS_M71
	PS_M08	PS_M64	PS_M72
	PS_M09	PS_M65	PS_M73
	PS_M10	PS_M66	PS_M74
	PS_M11	PS_M67	PS_M75
	PS_M12	PS_M68	PS_M76
TOTAL	5	7	7

The results demonstrate that introducing the zero length beams has not provided a significant and consistent improvement in all scenarios, although in some cases there has been a slight increase in the total internal energy, i.e. energy absorption. Furthermore, there is no particular trend as to which configuration of zero length beams (with and without stiffness updates) is better. A significant drawback to the zero length beam configuration resides in its FE setup. For each interface node, a beam must be created therefore a second set of interface nodes at the same location must also be created (hence "zero-length"). For larger structures, this is can be a very laborious procedure. Furthermore, in the case of updating the beam stiffness values, each beam requires its own unique material card, and by extension PART_ID. Again, these tasks can be very time consuming and given the varying results as illustrated in Table 5.24, combined with the added CPU time due to monitoring/modifying the beam stiffnesses, the use of the

zero length beams is doubtful. Therefore, in the following case study this parameter will not be analysed further. However, if the process of setting up the zero length beams in the FE model could be automated, then further studies could be carried out on more complex structures.

- ***Linear BC:*** The IR study has mainly shown that the majority of other hybrid TO parameters have very little influence compared to the placement of the mass points in the linear model. The most influential parameter was the rate of exchange, and more specifically the DESMAX value, but this mostly affected the stability of the element removal process, i.e. avoiding detached elements, for configuration 2 (Figure 5.6). Overall, the use of IR is possible, but is essentially case study dependent. This parameter will be analysed in the next case study, where the mass point locations and magnitude can more accurately reflect the real-world scenarios.

At this stage, a mention should be made about the force distribution applied to linear models in the hybrid methodology. It was stated in chapter 4 that two force exchange procedures were employed, which are summarised below:

- Method 1: When the force at the interface can be assumed constant through the cross section, an interface force is calculated for the entire cross section and divided evenly between the nodes at the interface
- Method 2: When the force at the interface cannot be assumed constant through the cross section, interface cross sections are created for each interface elements and the forces at each cross section are divided equally between the interface nodes that make up the cross section.

However as mentioned in Chapter 4, Method 1 is in fact inaccurate in this instance, as the edge nodes are only connected to a single element whereas the interior nodes are connected to two elements, based on the plate models from chapter 3 and 5. Therefore, in order to keep a constant pressure load across the interface and avoid high stresses in the corners, the edge nodes should only perceive half the force of the interior nodes. This could potentially influence the linear optimisation results, and by extension the hybrid optimisation process.

In order to evaluate the consequences, Model 2 from Chapter 3 (i.e. linear static optimisation) is re-run, but this time the forces are distributed according to the changes discussed above, as displayed by Figure 5.62 below:

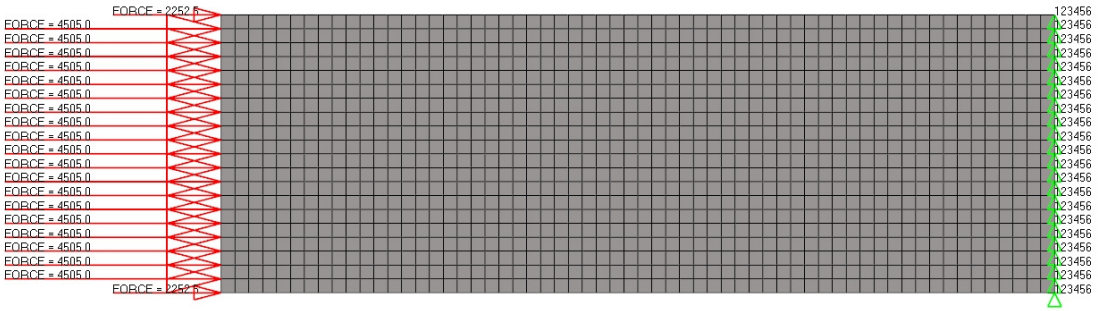

Figure 5.62 : Model 2 updated forces FE setup

The density distribution result is illustrated below in Figure 5.63 and compared to the initial results from this chapter in Figure 5.64:

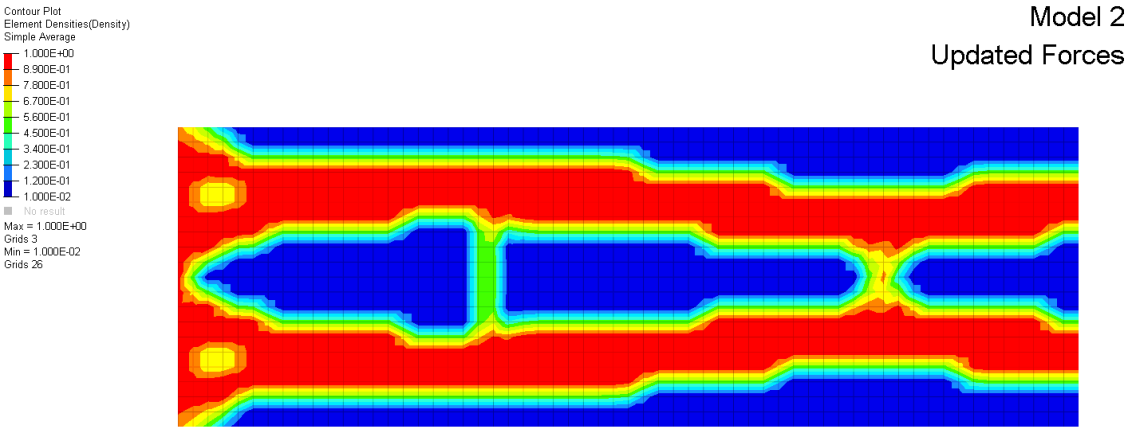

Figure 5.63 : Model 2 updated forces density distribution (with simple averaging filter applied)

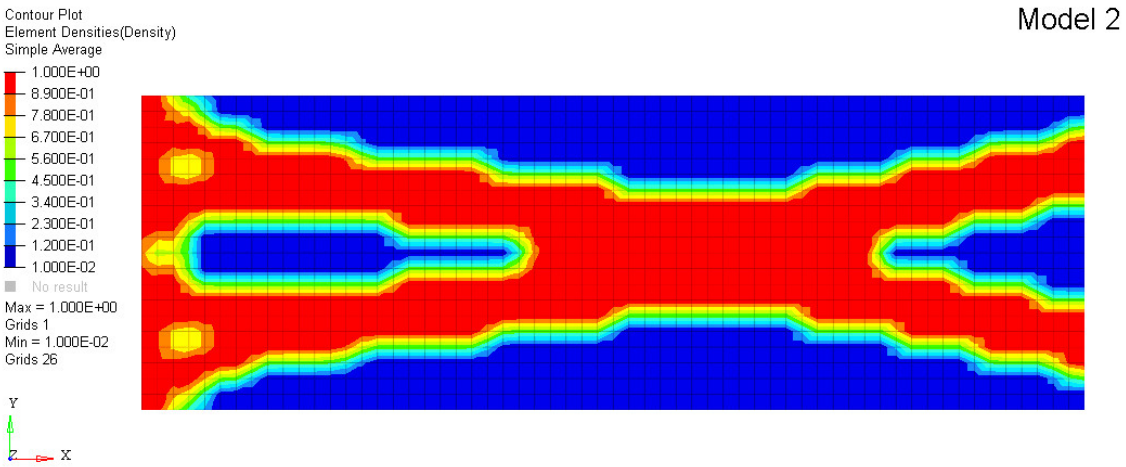

Figure 5.64 : Model 2 density distribution (with simple averaging filter applied)

Although there are similarities between the two results, specifically at the loading and SPC edges of the structures, there are clear differences between the "optimal" material distributions suggested. The topology obtained in Figure 5.63 contains "straighter" structural members linking the forces and SPCs, most likely due to a more homogeneous load load distribution across the left hand edge. This in itself is not a surprise as the BCs of the problem have changed, and reiterates the findings from the discussions in chapter 3 about the dependency of TO on boundary conditions. Furthermore, it could also have an influence on the hybrid optimisation results.

In order to verify this, Model PS_M10 is re-run, with the updated force distribution method applied for Method 1. However, it should be stated that method 1 only applies to the first linear optimisation loop in the hybrid process, as once elements are removed from the model, then the force is no longer considered constant through the interface, in which case method 2 is used (i.e. individual cross sections), which correctly divides the forces at the interface. Therefore, Figure 5.65 below illustrates the density distribution comparison between PS_M10 with and without the updated forces after the first linear optimisation iteration:

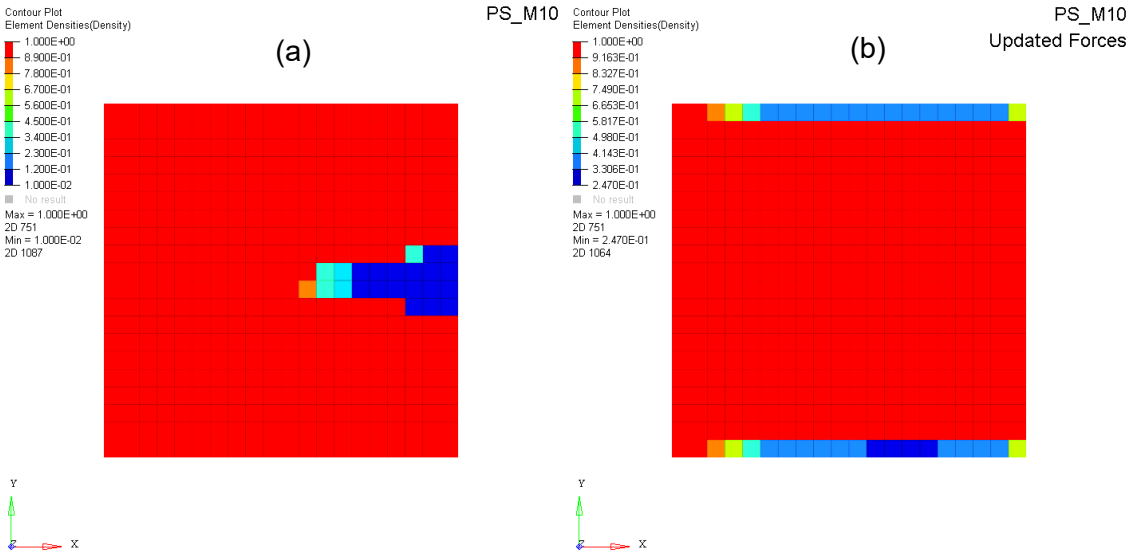

Figure 5.65 : PS_M10 density distribution (a) Original (b) Updated Forces

Figure 5.65 illustrates that the change in force distribution has had a big impact on the density distribution at the first linear optimisation "loop". For the subsequent steps, method 2 is employed to transfer the forces at the interfaces between the non-linear and linear models. Figure 5.66 below illustrates the final structures obtained for PS_M10 with and without the updated forces:

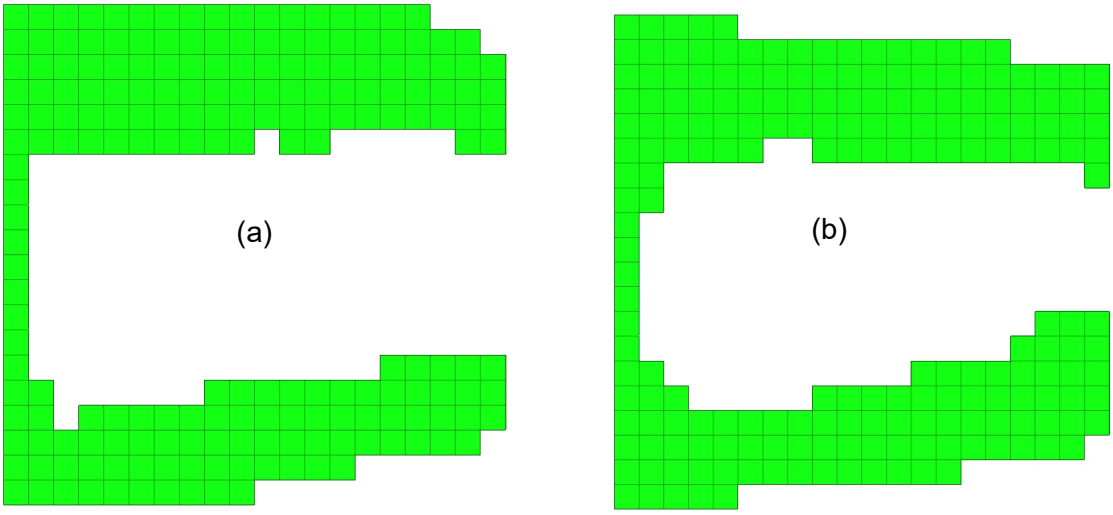

Figure 5.66 : PS_M10 final iteration topologies (a) Original (b) Updated Forces

While the 1st iteration displayed vastly different density distributions, the final topologies obtained for the "linear" sections are very similar. This is likely due to the iterative nature of the hybrid optimisation process, and the relatively low number of elements removed at each iteration (5%). Figure 5.67 below illustrates the behaviour of the overall PS_M10 structure when the updated linear structure is attached to the non-linear structure:

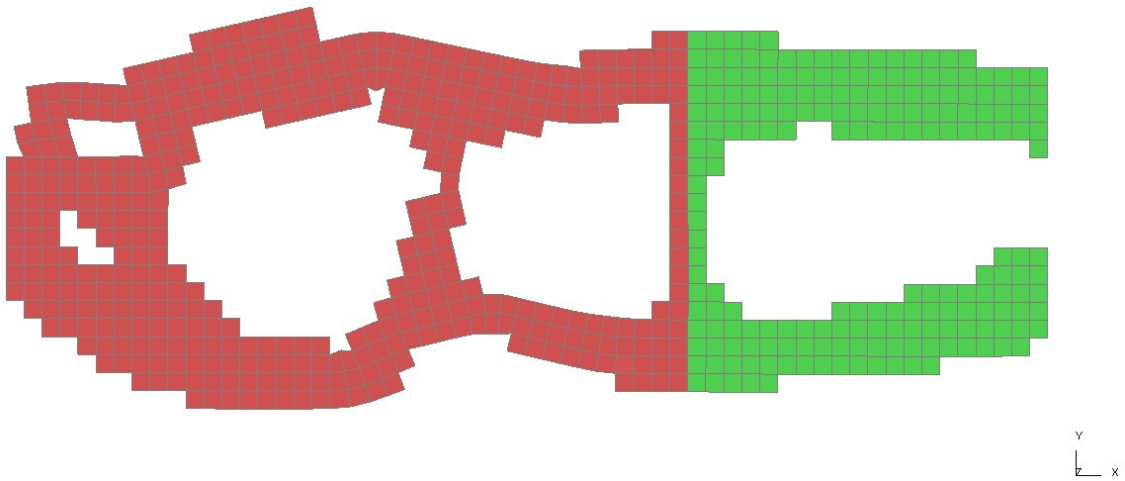

Figure 5.67 : PS_M10 updated forces final topology deformed state

As with the original PS_M10 final structure (Figure 5.21), there is a distinct difference in behaviour between the sections optimised via non-linear and linear optimisation. Furthermore, the maximum plastic strain in the "linear" section was measured at 0.3%, similar to the negligible levels measured for the original model (1%). While this suggests the differences in approaches for transferring interface forces using method 1 from chapter 4 are minimal, the following points should also be remembered:

- The ER value could have an influence on the different approaches. As discussed, method 1 for transferring interface forces only occurs at the first linear optimisation "loop". If the ER value were to be increased, then the "starting" points for the subsequent iterations using method 2 would increase in "differences". By extension, this could have a greater influence on the final iteration topologies obtained.
- The example used to evaluate the updated force exchange was based off a model where the interface BCs (i.e. in the non-linear model) were modelled via SPCs. If the method with the zero length beams were employed, then that could also have an influence, as the different "linear" structure would translate to

different stiffness values for the interface beams (if the variable stiffness method is employed), and by extension different forces at the interface.

- The erroneous force distribution for Method 1 identified is only valid for 2D structures that are not “closed”. For example, for thin-walled box-like structures modelled using 2D elements, if we consider quad elements at the interface similar to the 2D plate in this chapter, then each node would be attached to two elements.

Overall, while the example shows limited difference in the outcome due to the iterative approach of the hybrid optimisation method, method 2 is in fact a better overall approach for both a constant and non-constant force at the interface, contrary to the approach in Chapter 4.

It should be noted that these conclusions are not definitive and constitute an initial overview using a simplified structure to demonstrate the initial trends and validity of the hybrid TO method compared to the studies conducted in chapter 3. Therefore, the following chapter will introduce a second case study more relevant to vehicle components based on industry standard crashworthiness requirements within the front end of a vehicle structure.

6. Case study 2: RCAR bumper impact

The previous chapter provided an initial investigation into the different parameters that make up the hybrid topology optimisation (TO) methodology. However, it was concluded that additional work was needed to further understand this novel methodology, and specifically a load case more closely linked with vehicle dynamic behaviour and crashworthiness requirement standards. Therefore a second case study was set up based on the Research Council for Automobile Repairs (RCAR) vehicle bumper test (Research Council for Automobile Repairs 2010) and the public domain 2010 Toyota Yaris sedan finite element (FE) model, developed by the National Crash Analysis Center (NCAC) for the National Highway Traffic Safety Administration (NHTSA) (Marzougui et al. 2012). This test was established to encourage vehicle manufacturers to design the bumper system in such a way that the impact energy in a low speed impact is absorbed by the bumper system, i.e. no damage to other vehicle structural components. The aim of such a design is to reduce repair costs of the vehicle by restricting damage to easily replaceable parts (bumper and crush cans). This test, while having no impact on the Euro New Car Assessment Program (NCAP) rating of a vehicle has been implemented in several countries for insurance rating purposes (RCAR Damageability Working Group 2016). In order to be eligible for the RCAR bumper test, the bumper must first fulfil certain geometric requirements. Effectively, the test encourages the design of bumper systems that are relatively tall and that are fitted to common heights to improve on compatibility between various vehicle models (Research Council for Automobile Repairs 2010). The geometric requirements are as follows:

1) The bumper beam must engage the RCAR test bumper by at least 75mm (Figure 6.1).

Figure 6.1 : RCAR bumper test engagement measurement (Research Council for Automobile Repairs 2010)

The RCAR bumper test procedure states that a lower overlap between the vehicle and test bumper is an indication of a bumper that is likely to be insufficient (Research Council for Automobile Repairs 2010). With regards to the 2010 Yaris model, the measurement as per Figure 6.1 was 67 mm.

2) Should the first requirement not be met, RCAR will consider bumper beams that have a weighted average “qualifying bumper beam height” (Figure 6.1) from the three “measurement zones” (Figure 6.2) above 100 mm. Measurements in the Yaris FE model showed an average bumper height of 110 mm. These geometric assessments demonstrate that the Yaris FE model is suitable for the RCAR dynamic test.

Some materials have been removed due to 3rd party copyright. The unabridged version can be viewed in Lancester Library - Coventry University.

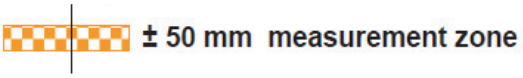

Figure 6.2 : RCAR test vehicle bumper height measurement zones
(Research Council for Automobile Repairs 2010)

Figure 6.3 displays the original bumper system from the Toyota Yaris FE model, which includes the crush cans and longitudinals:

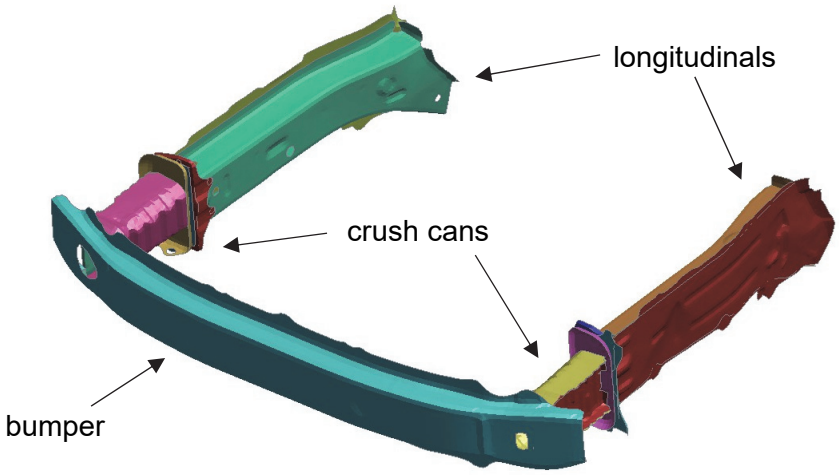

Figure 6.3 : 2010 Toyota Yaris sedan original bumper system
(a) bumper (b) crush can (c) longitudinal

The Toyota Yaris FE model was developed and validated for a 35 mph front crash as required by the NHTSA NCAP (The National Crash Analysis Center 2011). Subsequently the model's robustness was evaluated with a series of further tests such as a 25 mph front impact and a centreline pole impact (Marzougui et al. 2012). The FE model is therefore deemed adequate for a front end impact at reduced velocity.

By considering the requirements of the RCAR bumper test, it can be stated that the longitudinals cannot sustain any permanent damage as a "good bumper beam" must

"restrict damage to the bumper system only", which includes both the bumper beam and crush cans (Research Council for Automobile Repairs 2010). Therefore, in the context of the hybrid optimisation methodology, there is a clear requirement for coupled linear/non-linear behaviour within the bumper system (Figure 6.3) for this particular load case. The longitudinals are the major load paths through the structure for a front end impact and absorb approximately 50% of the energy in a high speed front end crash (Seiffert and Wech 2003). In the context of the RCAR bumper scenario, considering the longitudinals as "linear" components could impact their behaviour at higher velocities. At this stage this is acceptable to demonstrate the capabilities of hybrid optimisation.

Due to the number of components in the full vehicle model, and therefore the relatively high analysis run time (approximately 3h30 on a high performance computer), the first task involves creating a reduced model that replicates the vehicle behaviour for the purposes of the optimisation process.

6.1. Reduced model creation and correlation

Firstly, note that due to the required linear behaviour of the longitudinals, these are not included in the LS-DYNA model, but will be modelled in a separate Optistruct model for linear optimisation. The reduced Yaris model is required to behave in a similar manner to the full FE model. The main characteristics monitored were:

- Global energy levels
- Rebound time
- Energy levels within the crush cans
- Vehicle mass and centre of gravity (CoG)
- Vertical pitching behaviour upon barrier impact

Essentially, there is a trade-off needed between analysis time, accuracy of results and suitability for TO. Figure 6.4 displays the final reduced model created:

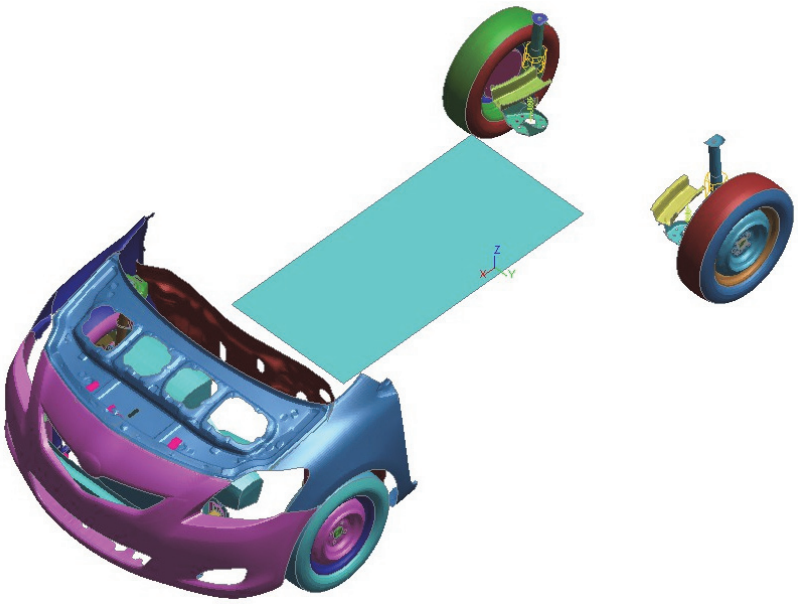

Figure 6.4 : 2010 Toyota Yaris reduced FE model for TO

The main components of the middle vehicle section have been replaced by a rigid plate. The position of the plate and the density of the material were modified in such a way to obtain identical CoG locations for the reduced and full model (Table 6.1):

Table 6.1 : Full and reduced Toyota Yaris model CoG and mass properties

	Full model	**Reduced model**
CoG – x axis (mm)	-1844	-1844
CoG – y axis (mm)	-2.4	-2.4
CoG – z axis (mm)	548	548
Mass (kg)	1254	1254

Overall, the mass of both models was the same measured at 1254 kg. The wheels and suspension sub-systems were retained to represent the overall pitching behaviour of the vehicle upon impact with the barrier, similar to the full model.

Figure 6.5 illustrates the kinetic, internal and total energy graphs for the reduced and full FE models, and Figure 6.6 plots the velocities of the vehicle during impact to verify their respective rebound times:

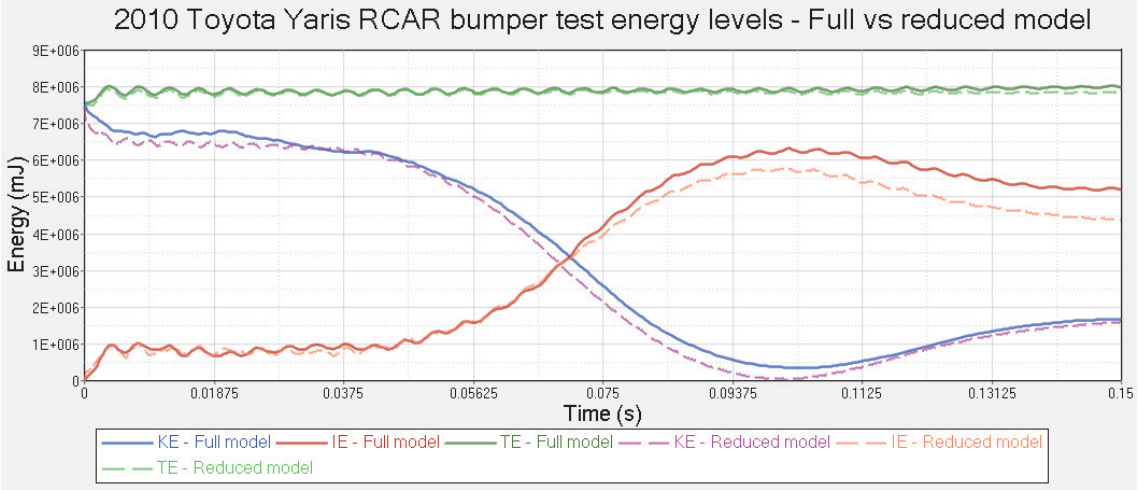

Figure 6.5 : 2010 Toyota Yaris RCAR bumper test energy levels - Full vs reduced model

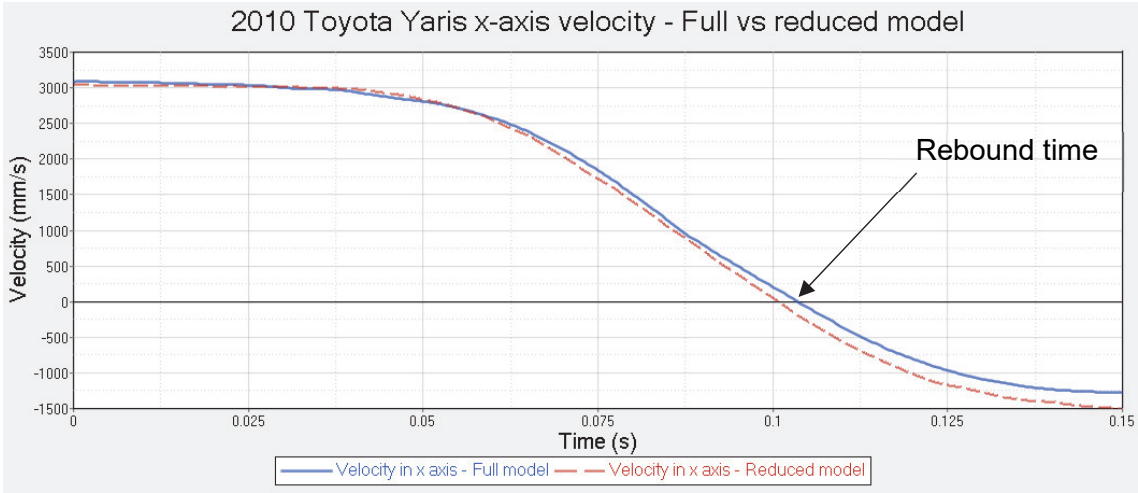

Figure 6.6 : 2010 Toyota Yaris x-axis velocity - Full vs reduced model

The x-axis corresponds to the direction of the impact. Observing the energy levels in Figure 6.5, it is noticeable that the internal and kinetic energy curves are very similar for both models up to the rebound time, and then deviate somewhat. This is due to an increased “bounce” phenomenon in the reduced vehicle which is not visible in the full FE model. However for the purposes of TO only the active deformation phase, i.e. before the rebound, of the bumper system is of interest. The oscillations present in the energy curves arise from the presence of suspension elements in the model, which were included to allow for the “pitching” movement described above. These oscillations are small compared to the main signal, therefore the phenomenon is insignificant. Furthermore, the results suggest a slightly stiffer response from the reduced model as

the internal energy absorbed is slightly lower (Figure 6.5) and the rebound time slightly earlier (Figure 6.6). This is also to be expected, as the reduced model contains more rigid connections and the rigid plate to simulate the vehicle mass.

Taking into account the above statements and the velocity curves in Figure 6.6, the reduced model was deemed to be an acceptable representation of the Toyota Yaris FE model from (Marzougui et al. 2012).

With an acceptable reduced model determined, the next operation consisted of simplifying the crush can geometries for TO. The original crush cans (Figure 6.7) are relatively detailed geometries compared to typical TO cases.

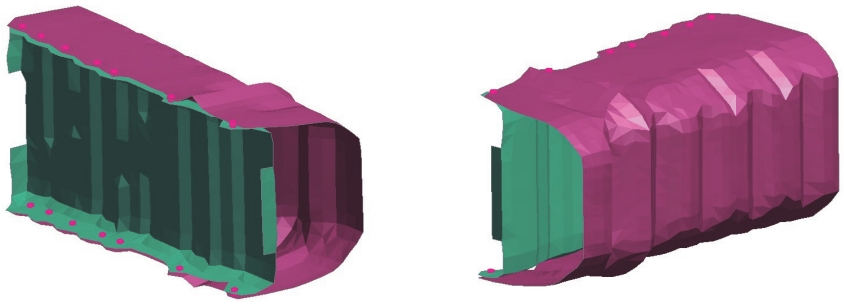

Figure 6.7 : 2010 Toyota Yaris original crush can geometry

They consist of two separate parts connected via spot-weld elements, as well as swages and crush initiators to aid in the energy absorption process. For the purposes of TO, each crush can was simplified into one single part with the removal of the swages and crush initiators, as illustrated in Figure 6.8.

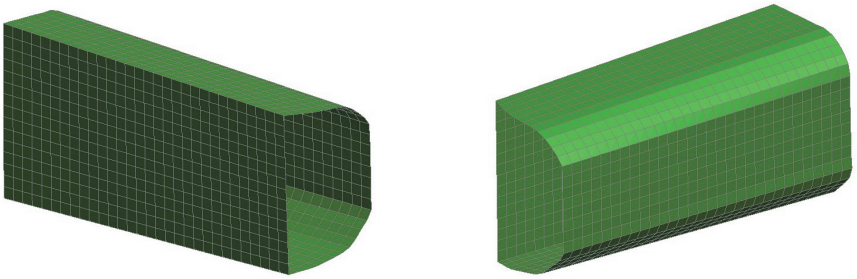

Figure 6.8 : 2010 Toyota Yaris simplified crush can geometry

The longitudinals were likewise simplified (Figure 6.9 and Figure 6.10).

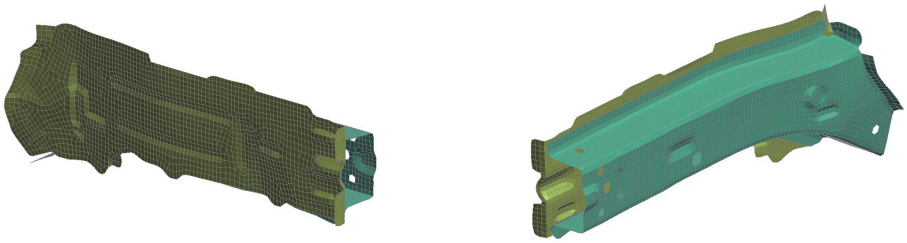

Figure 6.9 : 2010 Toyota Yaris original longitudinal geometry (right hand)

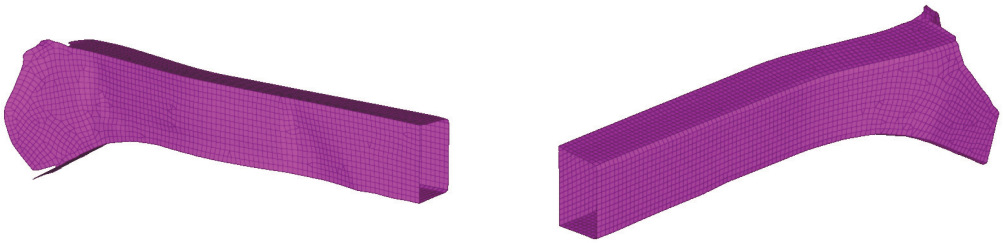

Figure 6.10 : 2010 Toyota Yaris simplified longitudinals geometry (right hand)

It should be noted that the simplification of the crush cans / longitudinals does not reduce the mass, as *ELEMENT_MASS_PART keywords present in the original model were also used in the reduced model to match the component masses. The simplification of the crush cans / longitudinals was to better represent a typical; TO design volume, which would be devoid of flanges, swages, crush initiators, etc., which would result from other optimisation methods such as topography optimisation. Figure 6.11 below illustrates the plastic strain plots of the crush can / longitudinal system integrated into the original Yaris vehicle to determine whether the initial designs are compliant with the RCAR requirement:

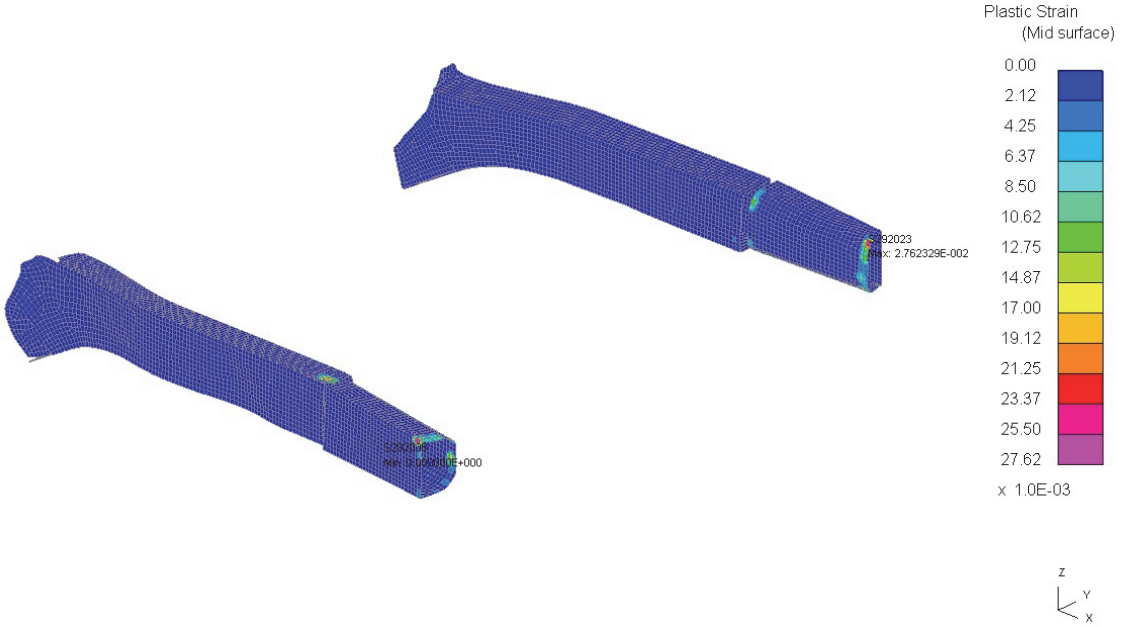

Figure 6.11 : Plastic strain plot of initial simplified crush can / longitudinal system

This plot shows a maximum plastic strain value of 2.7% in the crush can, and the maximum value in the longitudinal is measured as 1.7% located around a spotweld connection. The structure is therefore deemed suitable as a starting design volume for TO, subject to RCAR design requirements.

Similary to chapter 3 and chapter 5, type 16 fully integrated elements are used for the crush can models. In addition to the reasons discussed in chapter 3 on using type 16 elements for the LS-DYNA model, this element formulation was also used in the original Yaris model, and therefore is not modified for the simplified geometries. However, type 16 elements were also used for the longitudinals in the original Yaris model. In this instance, the longitudinals are modelled for linear optimisation in Hypermesh. Furthermore, based on the requirements of the RCAR bumper test, the longitudinals are not expected to exhibit high levels of deformation, significantly less than the levels of a 35mph frontal crash used to correlate the original model (The National Crash Analysis Center 2011). Therefore, 1st-order elements are used for the linear model. Figure 6.12 below illustrates the effect on internal energy levels within the crush cans caused by the change in geometry.

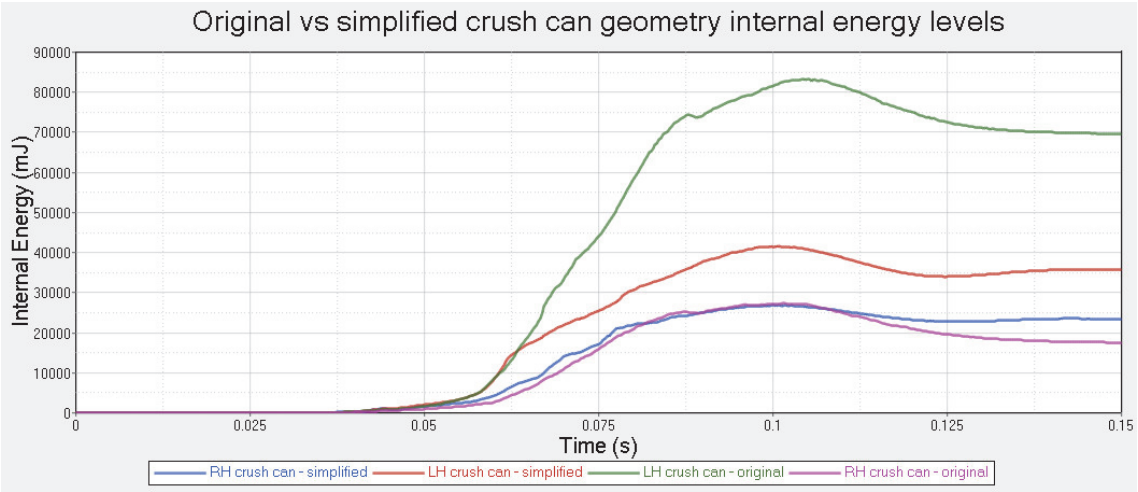

Figure 6.12 : Original vs simplified crush can geometry internal energy comparison

The graph demonstrates that for the right hand crush can the internal energy is very similar between the full and reduced models, however a difference appears between the left hand crush can (the energy levels are lower in the reduced model). Overall, Figure 6.12 shows a lower response for the simplified crush cans compared to the original crush cans. This is to be expected, as the swages have been removed and so there is no "crush initiation" design. Figure 6.13 below illustrates this by showing the internal energy within the bumper beam (Figure 6.3) for both the full and reduced models:

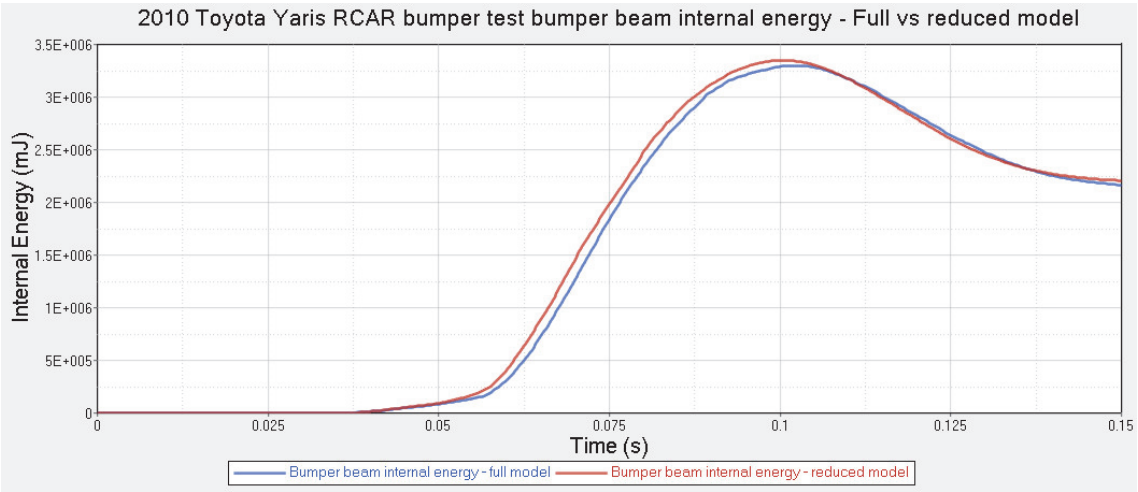

Figure 6.13 : 2010 Toyota Yaris RCAR bumper test bumper beam internal energy - full vs reduced model

This shows that the internal energy, i.e. deformation, levels within both bumper beams are very similar, and by extension the “input” energy into the crush cans is similar. The difference in internal energy highlighted in Figure 6.12 is then caused by a stiffening of the geometry caused by the simplification process. Some of the differences could also

be due to the slight change in FE connections used due to the change in geometry. Figure 6.14 illustrates the connections created between the crush cans and the firewall in the reduced model:

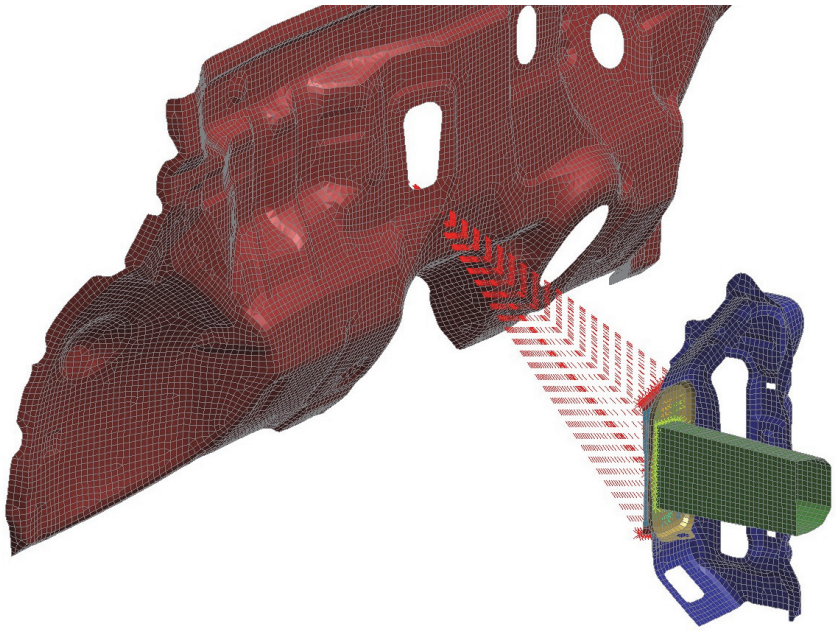

Figure 6.14 : Reduced model connections between crush cans and firewall

The crush can edges are connected to the plates by means of *CONSTRAINED_EXTRA_NODES in LS-DYNA, i.e. rigid connections. In turn, the plates are connected to the firewall via rigid connections. Therefore, a stiffer response from the crush cans is to be expected, as the relative compliance provided by the longitudinals in the original Toyota FE model is replaced by rigid connections. This is analogous to the SPC constraints applied to the non-linear section of the 2D plate in Case study 1 (Chapter 5). However as previously mentioned this is necessary as the longitudinals are not part of the non-linear LS-DYNA model, but in a separate linear Optistruct FE model. Figure 6.12 demonstrates a difference in energy between the left and right hand side, although this is the case for both the reduced model and, to a lesser extent, the full model. This difference in energy levels can be used to analyse the sensitivity and stability of the hybrid optimisation process to asymmetrical loading. Despite the differences with the validated full Yaris model, the behaviour is deemed representative for demonstrating the capabilities of hybrid optimisation.

The force extraction process was discussed in chapter 4 (Figure 4.5), by the means of a user-defined search radius to determine equivalent nodes between the non-linear and the linear models. Figure 6.15 below illustrates the search sphere for case study 2:

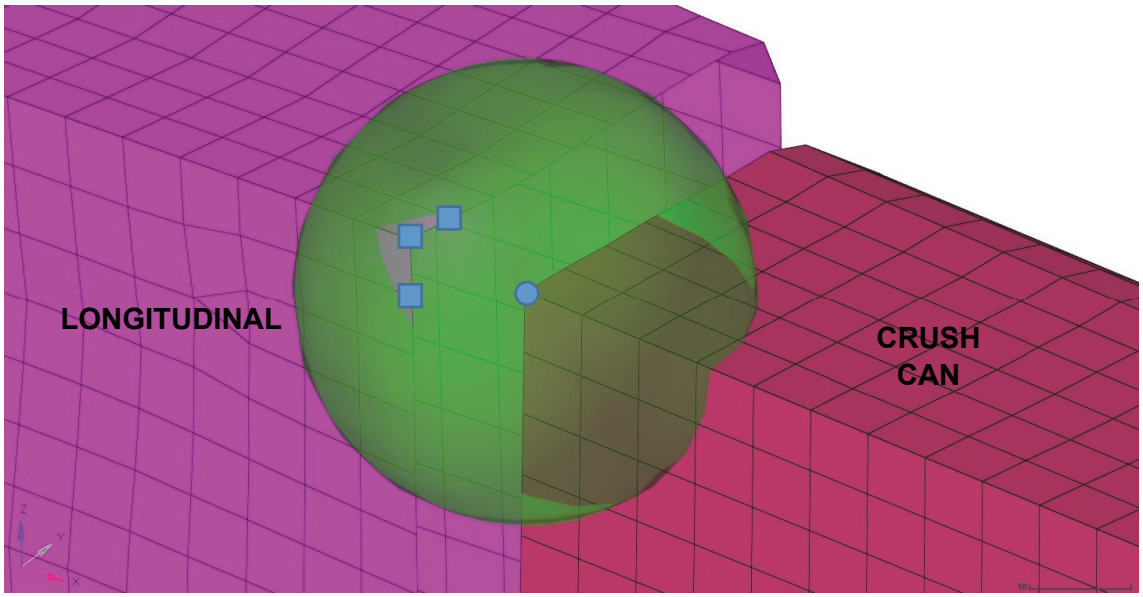

Figure 6.15 : Case study 2 interface nodes search sphere

The use of a search sphere was implemented, as discussed in chapter 4, to allow for different mesh sizes or different nodal locations, as is the case here. Whereas in case study 1, the linear and non-linear sections shared nodes at the interface, this is not true for case study 2, where the crush cans and longitudinals are separated. The circle point at the centre of the sphere in Figure 6.15 represents the non-linear node from the crush can and is the centre of the search space. The square points illustrate the linear nodes identified as inside the search sphere, and therefore the interface forces from the non-linear node will be transferred to those nodes in the longitudinal model (i.e. the linear Optistruct model) as per section 4.2.1 in chapter 4.

Overall, the behaviour of the reduced model with the simplified geometries mirrors to an acceptable level the full model, and the reduced model is therefore accepted for use in the hybrid optimisation study. It should also be noted, the main advantage and indeed the need for a reduced model is the decrease in analysis time. As previously stated the original model required a run time of 3h30 per analysis, whereas the reduced model has a run time of around 45 minutes, which represents a significant decrease.

6.2. Case study hybrid optimisation and modelling parameters

Due to the relatively detailed models, i.e. thin walled structures, and the load case studied, it was expected that less volume could be removed from the structure than the previous case study (50% volume target) before the structure becomes unstable. Therefore for this study the volume target selected is 85% of the initial volume. Case study 1 in chapter 5 helped develop an initial understanding of the hybrid optimisation parameters and their influence on the topology. The following parameters are retained for further analysis in the present case study:

- **Rate of exchange**: In this study, the DESMAX value which formed one part of the rate of exchange will not be modified but be maintained at the default value of 30, i.e. a maximum of 30 iterations per linear optimisation process, a high enough value to allow for the optimisation process to converge as concluded from chapter 5. Therefore, the only parameter to be varied will be the frequency of exchange from the non-linear to the linear solver. Two values will be considered, 1, i.e. data exchanged after every non-linear process, and 4, i.e. data exchanged after every 4th non-linear optimisation iteration.
- **Interface size**: The previous study determined that a too large interface size would be detrimental to the hybrid optimisation process, and produce inefficient topologies. In this case study, three different interface sizes, i.e. three different non-design domain sizes, are selected: “0”, “89” and “445” non-design elements at the interface. The interface size of “445” is used to determine whether the previous trend regarding large interface sizes is replicated here. In the previous case study the largest interface size of “120” elements produced a non-design domain of 15% of the model size. In the case of the crush cans, the largest interface size results in a non-design domain of around 16% of the component volume.
- **Linear model boundary conditions (BC)**: Case study 1 demonstrated that the optimised topologies obtained when using Inertia Relief (IR) depended significantly on the locations of the mass points in the linear model. For case study 2, the linear model corresponds to the longitudinals in the bumper system. The value of the mass points used for IR is therefore the mass of the vehicle subsystems located from the firewall backwards, which using the original Yaris model is approximately 0.86 tonnes. As for the location, the longitudinals are fixed to the firewall and also a section of the floor supports (Figure 6.16):

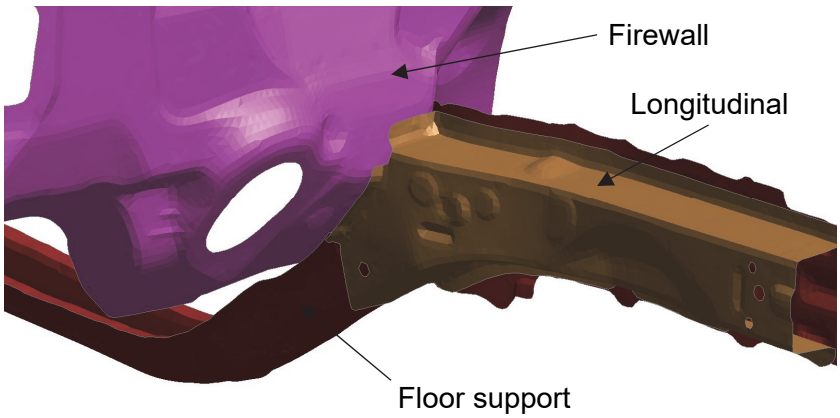

Figure 6.16 : Yaris longitudinals attachment

Therefore, a mass point will be created at an equal distance from both longitudinals, with rigid body elements (RBE2) connecting it to the nodes along component edges. The mass point created (CONM2) is given the mass of 0.86 tonnes previously determined. Figure 6.17 illustrates the setup of the mass points for IR models.

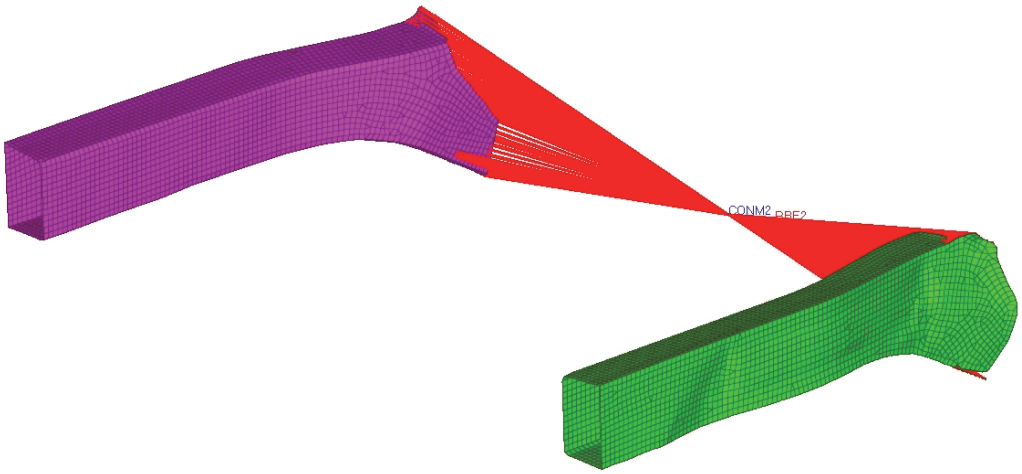

Figure 6.17 : Yaris longitudinals IR FE setup

As the mass of the vehicle is distributed to the nodes as depicted by Figure 6.17, the resistance to the input forces provided by the vehicle body is added to the rear sections of the longitudinal. In essence, the attached nodes will display very little displacement in the $-\vec{x}$ direction (Figure 6.4), which is consistent with the "physical" boundary conditions, i.e. attached to the firewall. As per chapter 5 (case study 1), Single Point Constraints (SPCs) are also used. The same nodes

attached to the mass element for the IR model in Figure 6.17 are this time constrained in all degrees of freedom, as illustrated by Figure 6.18 below:

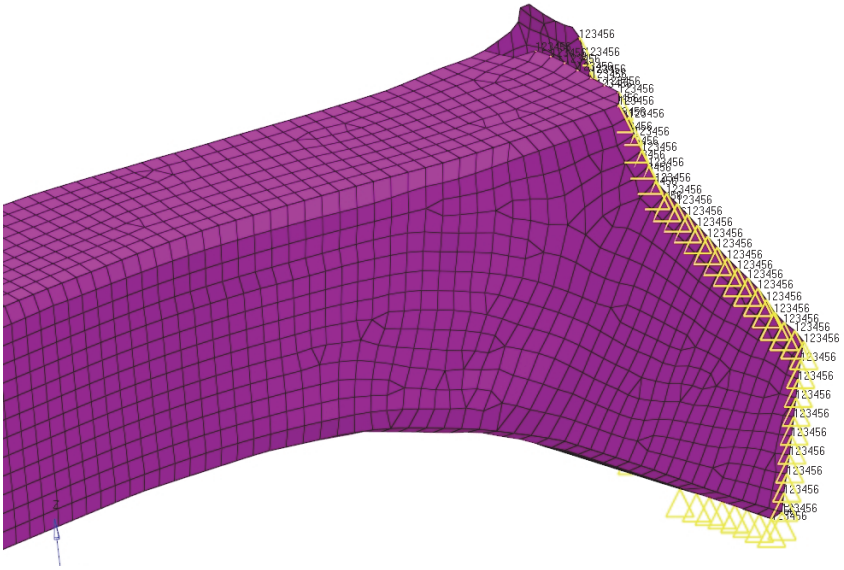

Figure 6.18 : Yaris longitudinals SPC FE setup

- **Linear optimisation objective/constraint**: The objectives and constraints used in the linear optimisation process will also be analysed in similar fashion to case study 1. The first combination will analyse the combination of minimising compliance with the volume target of 85% previously mentioned, and the second combines minimising mass with a stress constraint which is set to the Yield strength of the steel material applied in the original Yaris model, 350 MPa.

Furthermore, the effects of different levels of non-linearity will be analysed. Therefore the impact speed will be modified, with an initial value of 10 km/h (L) as per the RCAR bumper test (Research Council for Automobile Repairs 2010). A second impact velocity of 16 km/h (H) is used, which represents over twice the kinetic energy of the initial load case. Finally, the evolutionary ratio (ER) which was kept constant in the previous case study will be varied. The load case and behaviour of the models is expected to be more unstable than the 2D plate, therefore a lower ER may be needed to avoid removing critical areas of the crush cans. A second value of 2.5% will be used. Table 6.2 below summarises the parameters studied in case study 2:

Table 6.2 : Hybrid optimisation and modelling parameters for case study 2

Parameters	**Value 1**	**Value 2**	**Value 3**
Degree of non-linearity	10 km/h (L)	16 km/h (H)	-
Rate of exchange	Every NL iteration (1)	Every 4 NL iterations (4)	-
Interface Size	0 (0 elements)	1 (89 elements)	5 (445 elements)
Linear model objective	Minimise compliance	Minimise mass	-
Linear model constraint	Volume Target = 85%	von Mises stress = 350 MPa	-
Linear model BC	SPC	IR	-
ER	5%	2.50%	-

From these parameters, Table 6.3 lists the models considered in the case study:

Table 6.3 : Hybrid optimisation bumper study models

Model Number	Degree of non-linearity	ER (%)	Interface size (Number of elements)	Rate of exchange		Linear BC	Linear model objective	Linear model constraint *Volume fraction = 85% von Mises stress = 350MPa*
				BEETS	Optistruct			
BUS_M01	L	5	0	1	30	SPC	Min. comp	Volume fraction
BUS_M02	L	2.5	0	1	30	SPC	Min. comp	Volume fraction
BUS_M03	L	5	0	1	30	IR	Min. comp	Volume fraction
BUS_M04	L	2.5	0	1	30	IR	Min. comp	Volume fraction
BUS_M05	L	5	0	1	30	SPC	Min. mass	von Mises stress
BUS_M06	L	2.5	0	1	30	SPC	Min. mass	von Mises stress
BUS_M07	L	5	0	1	30	IR	Min. mass	von Mises stress
BUS_M08	L	2.5	0	1	30	IR	Min. mass	von Mises stress
BUS_M09	L	5	89	1	30	SPC	Min. comp	Volume fraction
BUS_M10	L	2.5	89	1	30	SPC	Min. comp	Volume fraction
BUS_M11	L	5	89	1	30	IR	Min. comp	Volume fraction
BUS_M12	L	2.5	89	1	30	IR	Min. comp	Volume fraction
BUS_M13	L	5	89	1	30	SPC	Min. mass	von Mises stress
BUS_M14	L	2.5	89	1	30	SPC	Min. mass	von Mises stress
BUS_M15	L	5	89	1	30	IR	Min. mass	von Mises stress
BUS_M16	L	2.5	89	1	30	IR	Min. mass	von Mises stress
BUS_M17	L	5	445	1	30	SPC	Min. comp	Volume fraction
BUS_M18	L	2.5	445	1	30	SPC	Min. comp	Volume fraction
BUS_M19	L	5	445	1	30	IR	Min. comp	Volume fraction
BUS_M20	L	2.5	445	1	30	IR	Min. comp	Volume fraction
BUS_M21	L	5	445	1	30	SPC	Min. mass	von Mises stress
BUS_M22	L	2.5	445	1	30	SPC	Min. mass	von Mises stress
BUS_M23	L	5	445	1	30	IR	Min. mass	von Mises stress
BUS_M24	L	2.5	445	1	30	IR	Min. mass	von Mises stress
BUS_M25	L	5	0	4	30	SPC	Min. comp	Volume fraction
BUS_M26	L	2.5	0	4	30	SPC	Min. comp	Volume fraction
BUS_M27	L	5	0	4	30	IR	Min. comp	Volume fraction
BUS_M28	L	2.5	0	4	30	IR	Min. comp	Volume fraction
BUS_M29	L	5	0	4	30	SPC	Min. mass	von Mises stress
BUS_M30	L	2.5	0	4	30	SPC	Min. mass	von Mises stress
BUS_M31	L	5	0	4	30	IR	Min. mass	von Mises stress
BUS_M32	L	2.5	0	4	30	IR	Min. mass	von Mises stress
BUS_M33	L	5	89	4	30	SPC	Min. comp	Volume fraction
BUS_M34	L	2.5	89	4	30	SPC	Min. comp	Volume fraction
BUS_M35	L	5	89	4	30	IR	Min. comp	Volume fraction
BUS_M36	L	2.5	89	4	30	IR	Min. comp	Volume fraction
BUS_M37	L	5	89	4	30	SPC	Min. mass	von Mises stress
BUS_M38	L	2.5	89	4	30	SPC	Min. mass	von Mises stress
BUS_M39	L	5	89	4	30	IR	Min. mass	von Mises stress
BUS_M40	L	2.5	89	4	30	IR	Min. mass	von Mises stress

Model Number	Degree of non-linearity	ER (%)	Interface size (Number of elements)	Rate of exchange		Linear BC	Linear model objective	Linear model constraint *Volume fraction = 85% von Mises stress = 350MPa*
				BEETS	Optistruct			
BUS_M41	L	5	445	4	30	SPC	Min. comp	Volume fraction
BUS_M42	L	2.5	445	4	30	SPC	Min. comp	Volume fraction
BUS_M43	L	5	445	4	30	IR	Min. comp	Volume fraction
BUS_M44	L	2.5	445	4	30	IR	Min. comp	Volume fraction
BUS_M45	L	5	445	4	30	SPC	Min. mass	von Mises stress
BUS_M46	L	2.5	445	4	30	SPC	Min. mass	von Mises stress
BUS_M47	L	5	445	4	30	IR	Min. mass	von Mises stress
BUS_M48	L	2.5	445	4	30	IR	Min. mass	von Mises stress
BUS_M49	H	5	0	1	30	SPC	Min. comp	Volume fraction
BUS_M50	H	2.5	0	1	30	SPC	Min. comp	Volume fraction
BUS_M51	H	5	0	1	30	IR	Min. comp	Volume fraction
BUS_M52	H	2.5	0	1	30	IR	Min. comp	Volume fraction
BUS_M53	H	5	0	1	30	SPC	Min. mass	von Mises stress
BUS_M54	H	2.5	0	1	30	SPC	Min. mass	von Mises stress
BUS_M55	H	5	0	1	30	IR	Min. mass	von Mises stress
BUS_M56	H	2.5	0	1	30	IR	Min. mass	von Mises stress
BUS_M57	H	5	89	1	30	SPC	Min. comp	Volume fraction
BUS_M58	H	2.5	89	1	30	SPC	Min. comp	Volume fraction
BUS_M59	H	5	89	1	30	IR	Min. comp	Volume fraction
BUS_M60	H	2.5	89	1	30	IR	Min. comp	Volume fraction
BUS_M61	H	5	89	1	30	SPC	Min. mass	von Mises stress
BUS_M62	H	2.5	89	1	30	SPC	Min. mass	von Mises stress
BUS_M63	H	5	89	1	30	IR	Min. mass	von Mises stress
BUS_M64	H	2.5	89	1	30	IR	Min. mass	von Mises stress
BUS_M65	H	5	445	1	30	SPC	Min. comp	Volume fraction
BUS_M66	H	2.5	445	1	30	SPC	Min. comp	Volume fraction
BUS_M67	H	5	445	1	30	IR	Min. comp	Volume fraction
BUS_M68	H	2.5	445	1	30	IR	Min. comp	Volume fraction
BUS_M69	H	5	445	1	30	SPC	Min. mass	von Mises stress
BUS_M70	H	2.5	445	1	30	SPC	Min. mass	von Mises stress
BUS_M71	H	5	445	1	30	IR	Min. mass	von Mises stress
BUS_M72	H	2.5	445	1	30	IR	Min. mass	von Mises stress
BUS_M73	H	5	0	4	30	SPC	Min. comp	Volume fraction
BUS_M74	H	2.5	0	4	30	SPC	Min. comp	Volume fraction
BUS_M75	H	5	0	4	30	IR	Min. comp	Volume fraction
BUS_M76	H	2.5	0	4	30	IR	Min. comp	Volume fraction
BUS_M77	H	5	0	4	30	SPC	Min. mass	von Mises stress
BUS_M78	H	2.5	0	4	30	SPC	Min. mass	von Mises stress
BUS_M79	H	5	0	4	30	IR	Min. mass	von Mises stress
BUS_M80	H	2.5	0	4	30	IR	Min. mass	von Mises stress

Model Number	Degree of non-linearity	ER (%)	Interface size (Number of elements)	Rate of exchange		Linear BC	Linear model objective	Linear model constraint *Volume fraction = 85% von Mises stress = 350MPa*
				BEETS	Optistruct			
BUS_M81	H	5	89	4	30	SPC	Min. comp	Volume fraction
BUS_M82	H	2.5	89	4	30	SPC	Min. comp	Volume fraction
BUS_M83	H	5	89	4	30	IR	Min. comp	Volume fraction
BUS_M84	H	2.5	89	4	30	IR	Min. comp	Volume fraction
BUS_M85	H	5	89	4	30	SPC	Min. mass	von Mises stress
BUS_M86	H	2.5	89	4	30	SPC	Min. mass	von Mises stress
BUS_M87	H	5	89	4	30	IR	Min. mass	von Mises stress
BUS_M88	H	2.5	89	4	30	IR	Min. mass	von Mises stress
BUS_M89	H	5	445	4	30	SPC	Min. comp	Volume fraction
BUS_M90	H	2.5	445	4	30	SPC	Min. comp	Volume fraction
BUS_M91	H	5	445	4	30	IR	Min. comp	Volume fraction
BUS_M92	H	2.5	445	4	30	IR	Min. comp	Volume fraction
BUS_M93	H	5	445	4	30	SPC	Min. mass	von Mises stress
BUS_M94	H	2.5	445	4	30	SPC	Min. mass	von Mises stress
BUS_M95	H	5	445	4	30	IR	Min. mass	von Mises stress
BUS_M96	H	2.5	445	4	30	IR	Min. mass	von Mises stress

Throughout this chapter, the model numbering scheme (BUS_Mxx) will be used, “BUS” specifying the bumper study and “Mxx” the model number where “xx” is replaced by and integer. The following section will analyse the final iteration topologies from a “geometric” point of view, i.e. before any reanalysis, to identify any trends in the optimised final iteration topologies and any limitations of the hybrid optimisation method.

6.3. Optimisation results – geometric analysis

The analysis of TO geometries is separated into two parts. Firstly, the different crush can configurations, i.e. non-linear behaviour, will be analysed. According to the different optimisation parameters analysed (Table 6.2), there are a total of twelve different configurations (two different impact velocities, three different interface sizes and two different ERs). Secondly, the trends in the longitudinals, i.e. linear behaviour, will be analysed.

6.3.1. Crush can configurations

Figure 6.19 – Figure 6.30 displays the twelve different optimised crush can final iteration topologies obtained prior to any “smoothing” for reanalysis:

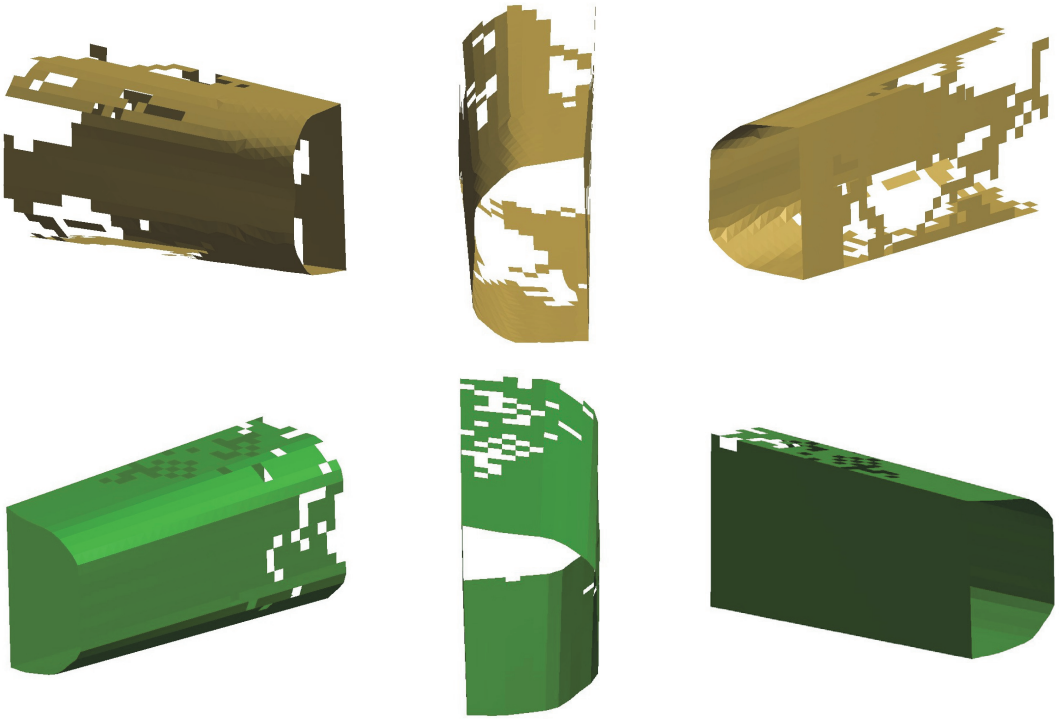

Figure 6.19 : BUS_M01 optimised crush cans (Interface size = 0; Impact velocity = 10 km/h; ER = 5%) – Top = LH crush can, Bottom = RH crush can

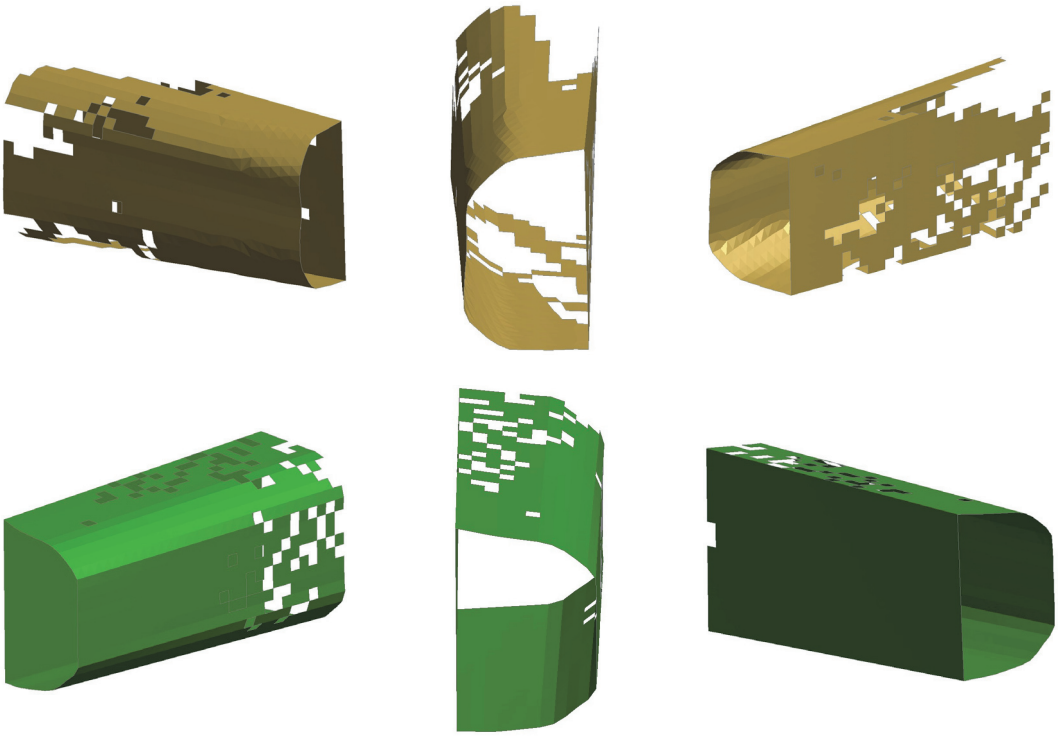

Figure 6.20 : BUS_M02 optimised crush cans (Interface size = 0; Impact velocity = 10 km/h; ER = 2.5%) – Top = LH crush can, Bottom = RH crush can

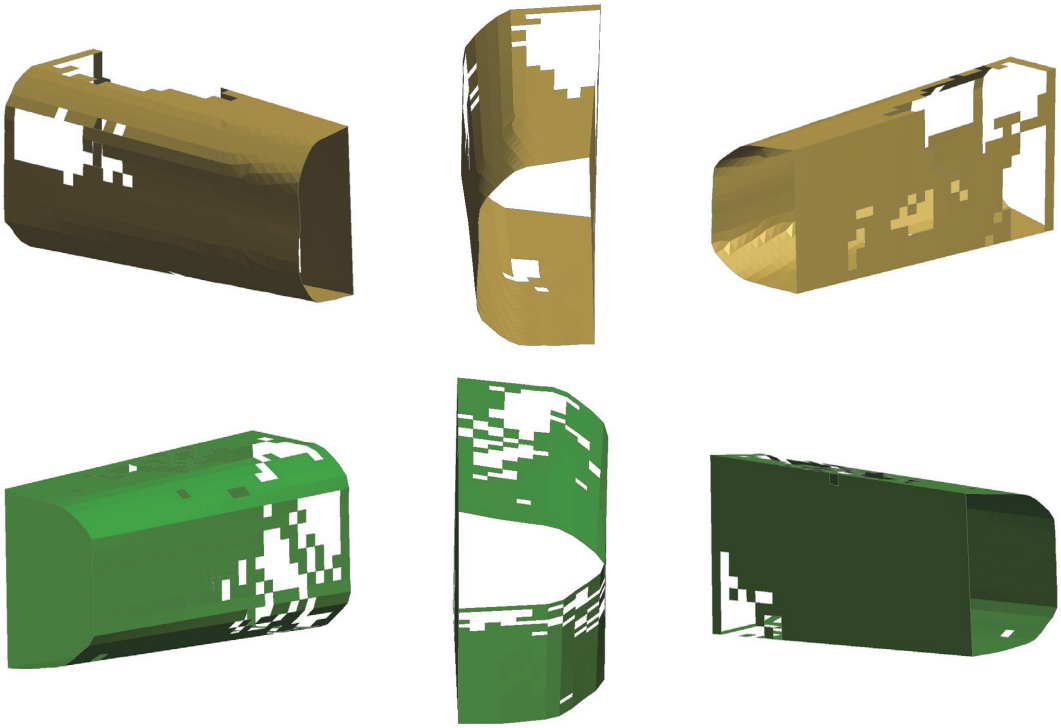

Figure 6.21 : BUS_M09 optimised crush cans (Interface size = 1; Impact velocity = 10 km/h; ER = 5%) – Top = LH crush can, Bottom = RH crush can

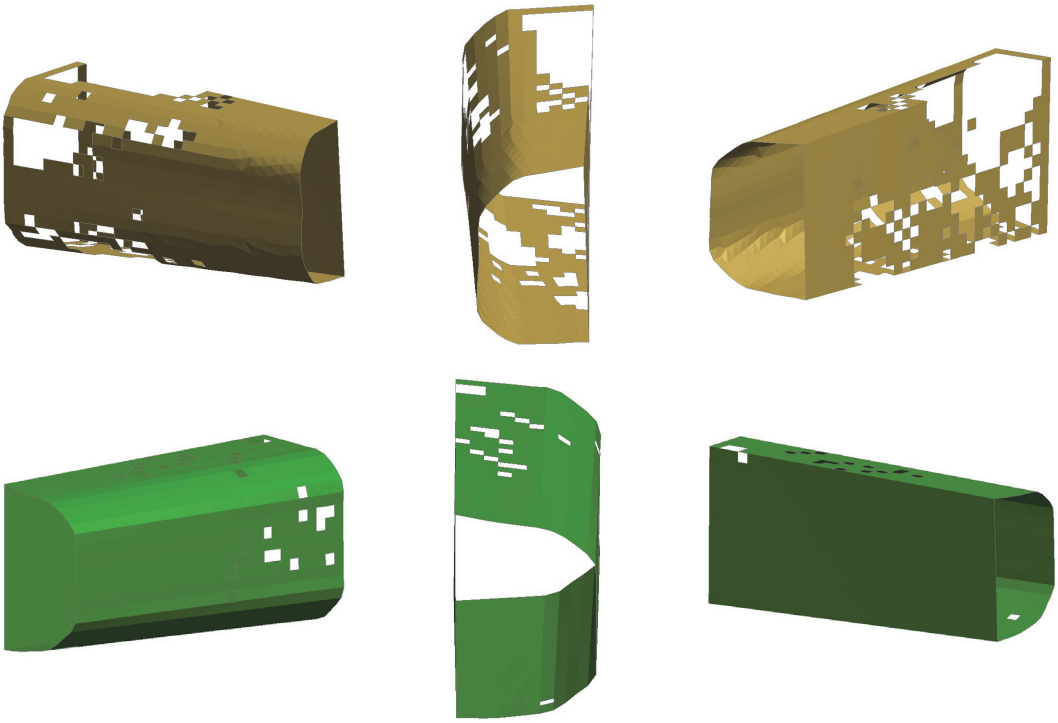

Figure 6.22 : BUS_M10 optimised crush cans (Interface size = 1; Impact velocity = 10 km/h; ER = 2.5%) – Top = LH crush can, Bottom = RH crush can

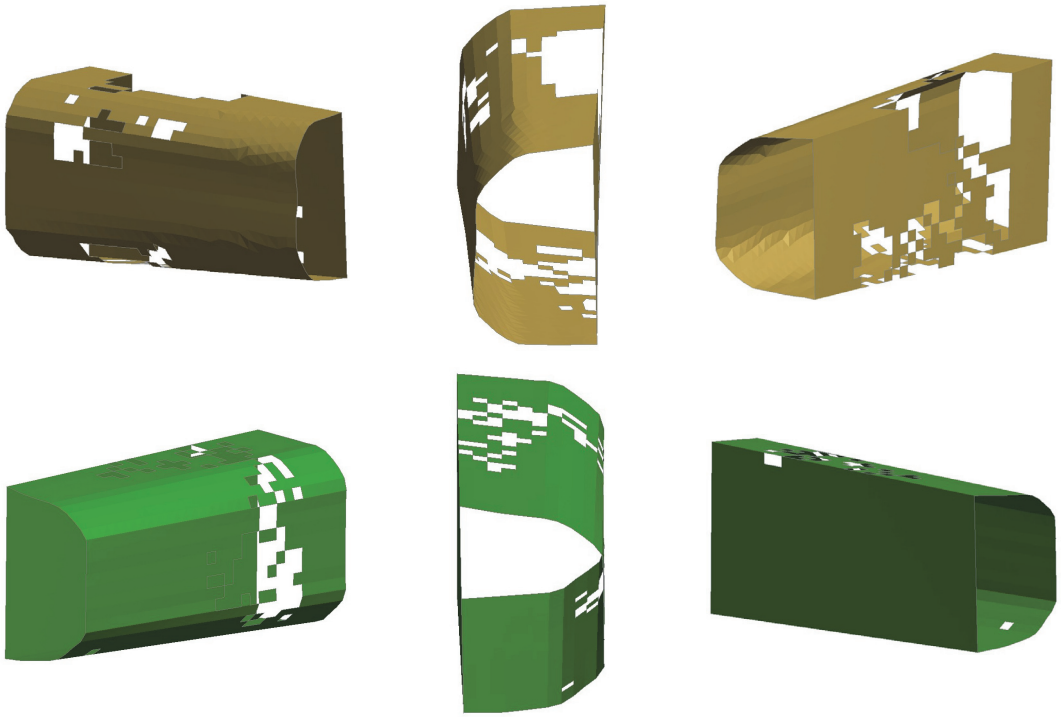

Figure 6.23 : BUS_M17 optimised crush cans (Interface size = 5; Impact velocity = 10 km/h; ER = 5%) – Top = LH crush can, Bottom = RH crush can

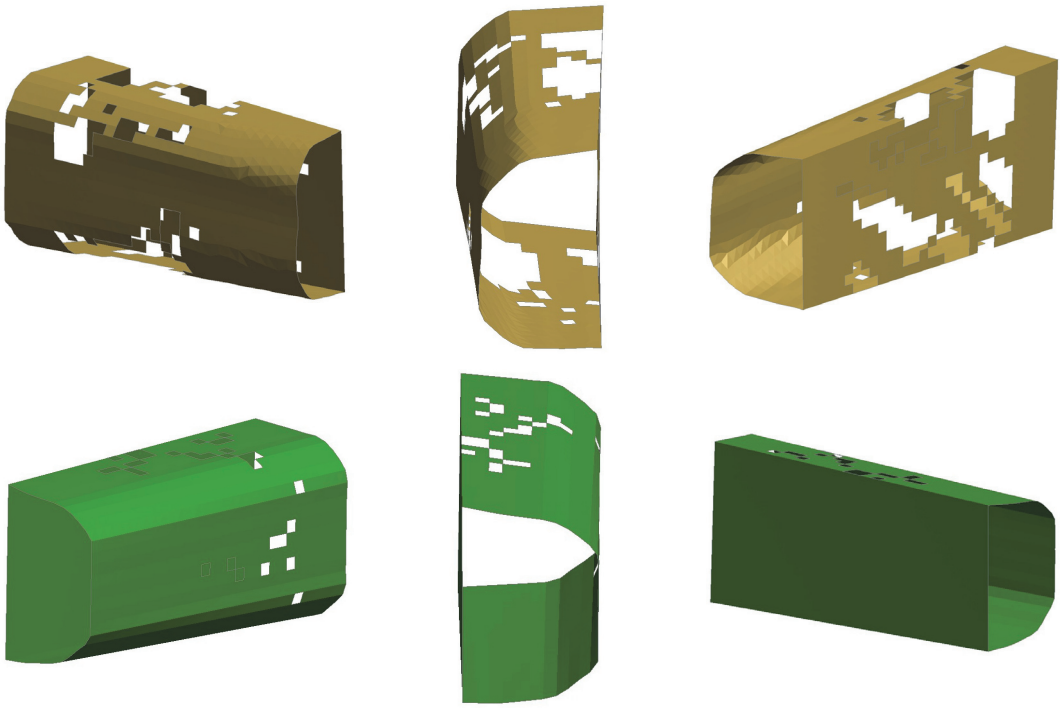

Figure 6.24 : BUS_M18 optimised crush cans (Interface size = 5; Impact velocity = 10 km/h; ER = 2.5%) – Top = LH crush can, Bottom = RH crush can

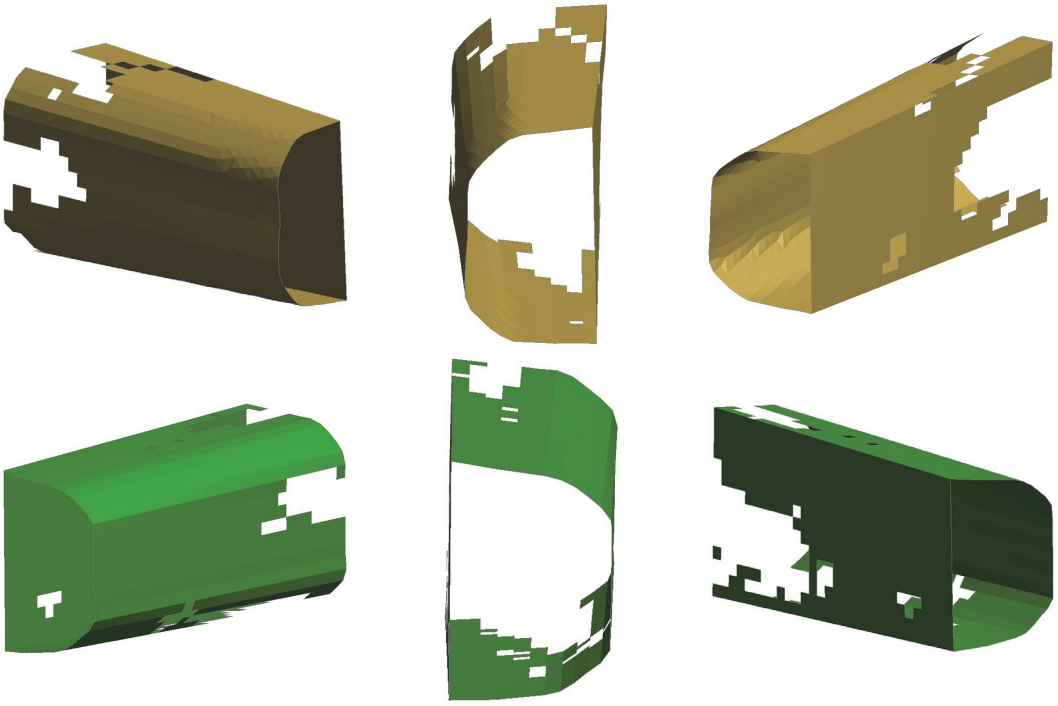

Figure 6.25 : BUS_M49 optimised crush cans (Interface size = 0; Impact velocity = 16 km/h; ER = 5%) – Top = LH crush can, Bottom = RH crush can

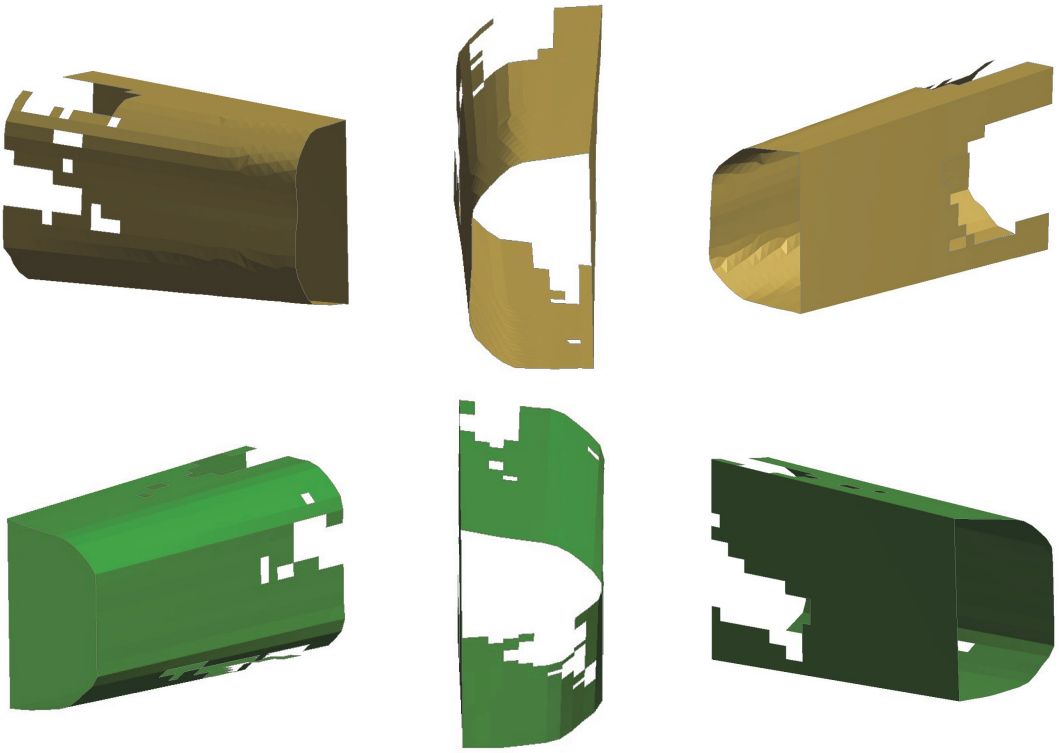

Figure 6.26 : BUS_M50 optimised crush cans (Interface size = 0; Impact velocity = 16 km/h; ER = 2.5%) – Top = LH crush can, Bottom = RH crush can

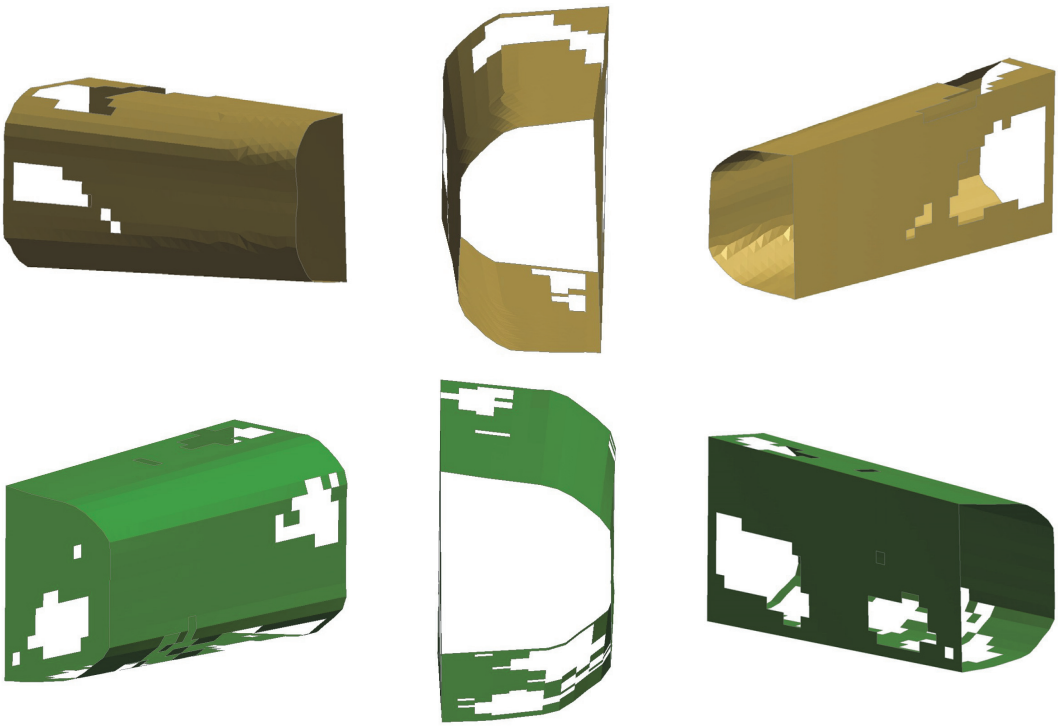

Figure 6.27 : BUS_M57 optimised crush cans (Interface size = 1; Impact velocity = 16 km/h; ER = 5%) – Top = LH crush can, Bottom = RH crush can

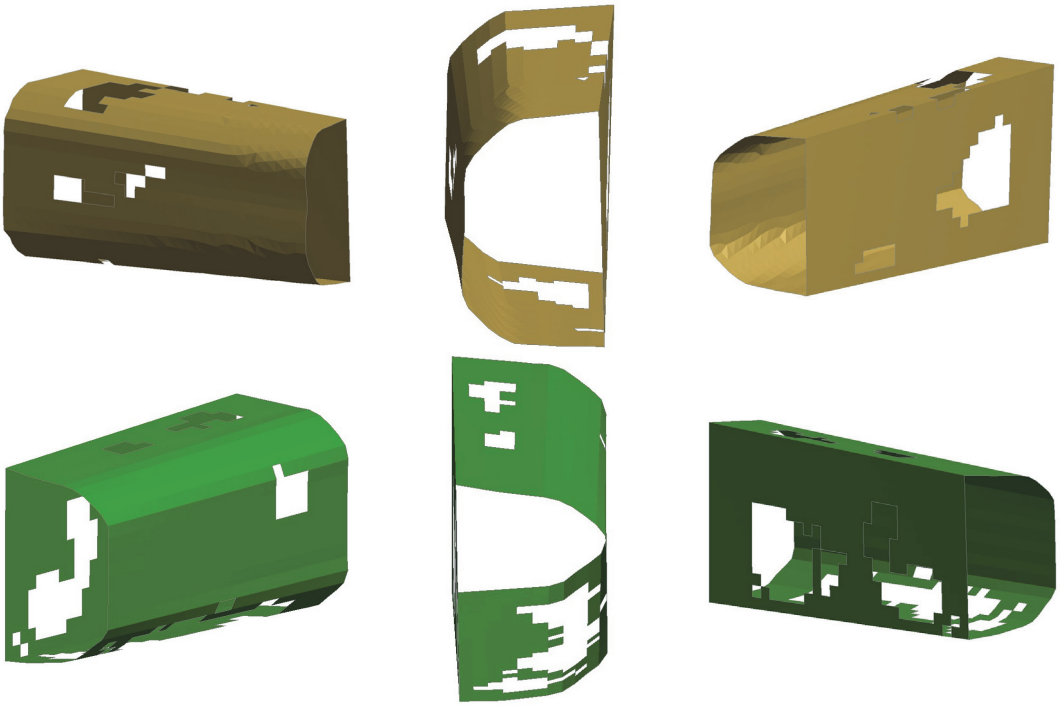

Figure 6.28 : BUS_M65 optimised crush cans (Interface size = 5; Impact velocity = 16 km/h; ER = 5%) – Top = LH crush can, Bottom = RH crush can

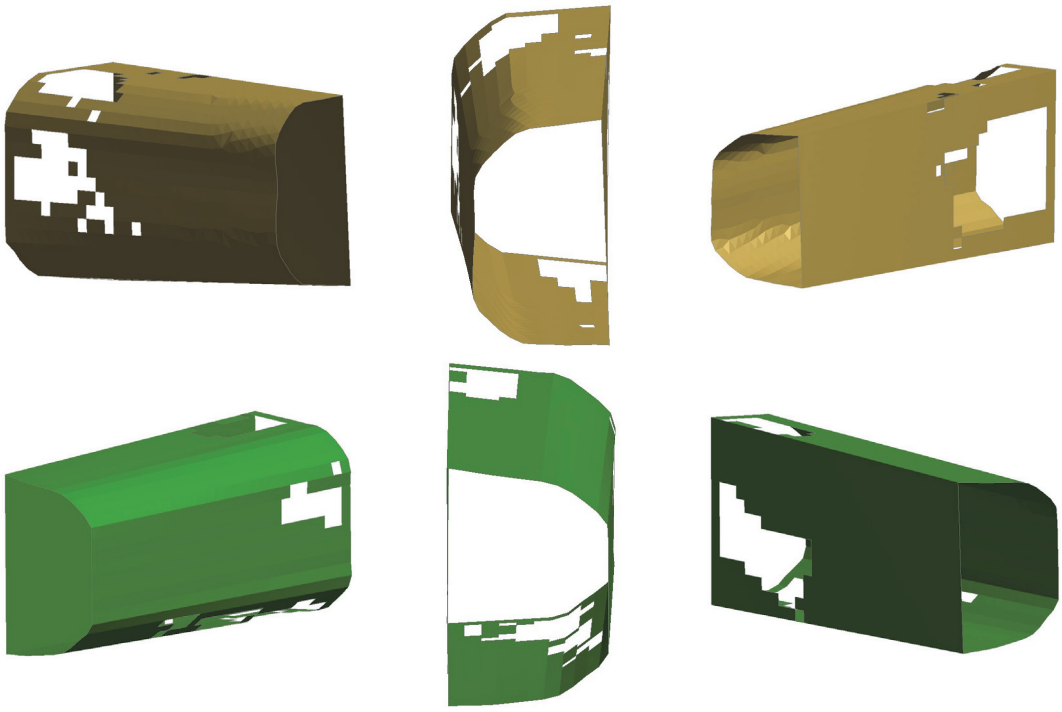

Figure 6.29 : BUS_M58 optimised crush cans (Interface size = 1; Impact velocity = 16 km/h; ER = 2.5%) – Top = LH crush can, Bottom = RH crush can

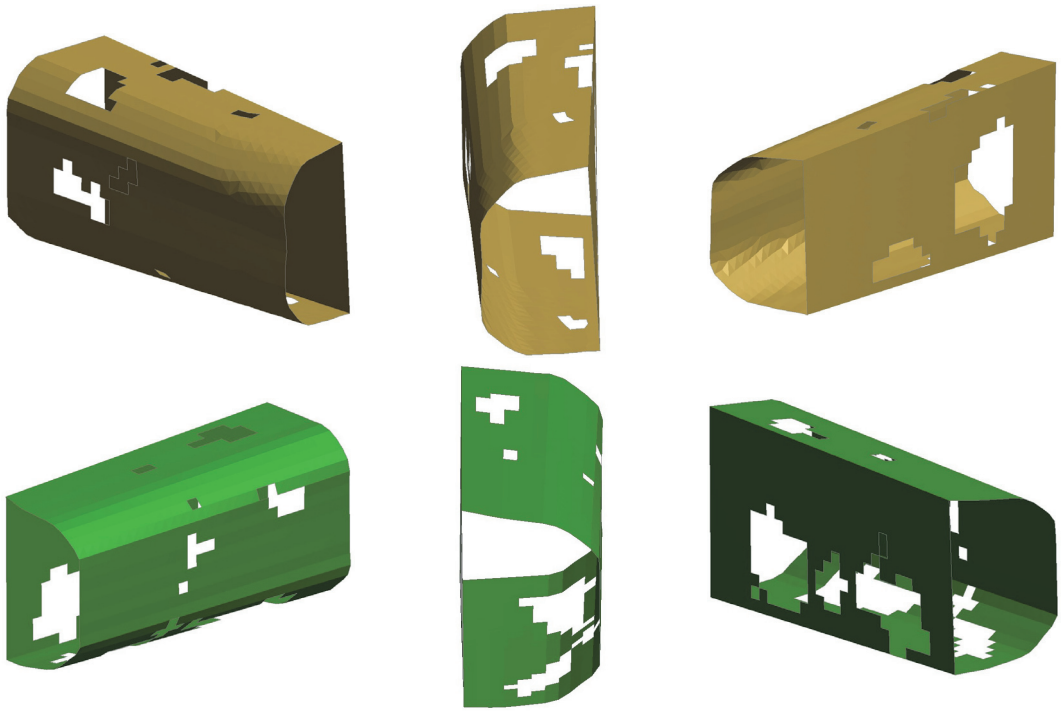

Figure 6.30 : BUS_M66 optimised crush cans (Interface size = 5; Impact velocity = 16 km/h; ER = 2.5%) – Top = LH crush can, Bottom = RH crush can

Firstly, the topologies can be compared according to the impact velocity. Figure 6.19 – Figure 6.24 illustrate the effects of the lower velocity (10 km/h) and Figure 6.25 – Figure 6.30 the effects of the higher velocity (16 km/h). At this stage it is important to reiterate that the difference in velocities constitutes an initial kinetic energy ratio of approximately 1:2.5.

The first noticeable difference regarding this parameter is the higher presence of disconnected elements or “checkerboarding” in the optimised crush cans where the velocity was low. In some cases, for example Figure 6.20, the checkerboarding effect is present to the extent where it is difficult to determine an optimum load path through the structure. Figure 6.31 displays the initial plastic strain plot through the left hand crush can for BUS_M02 (corresponding to Figure 6.20).

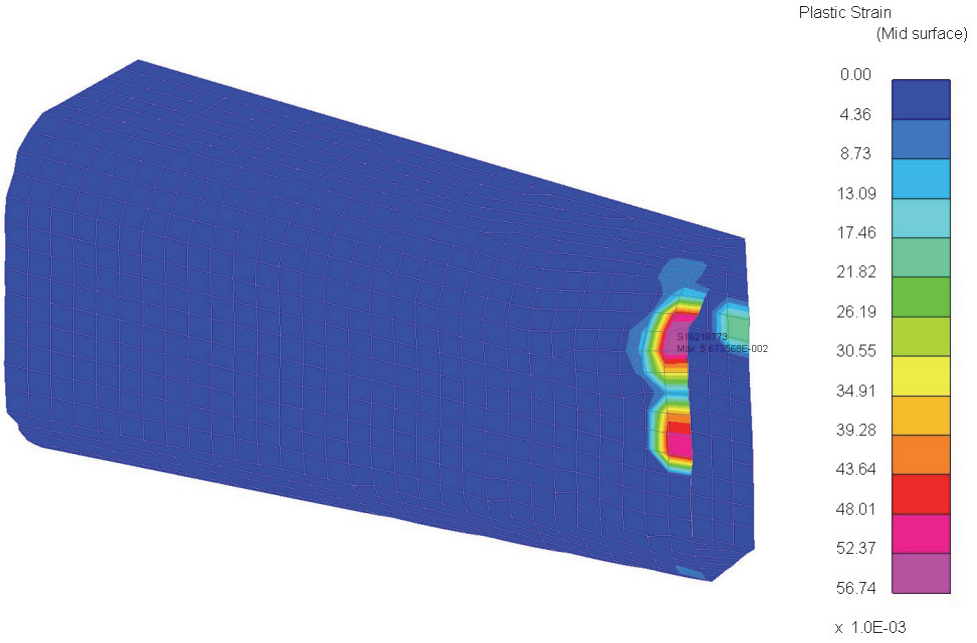

Figure 6.31 : BUS_M02 left hand crush can plastic strain plot

The plastic strain distribution illustrates that the maximum plastic strain is located at the front of the crush cans. This in itself is logical as the front end of the crush cans are connected to the bumper beam which absorbs much of the impact. However, a closer look reveals that the maximum plastic strain is 5.7 %. This in itself is very low, and effectively the behaviour in the rest of the crush can could be considered as linear in this case. The Bi-directional Evolutionary Entropy Tabu search Simulated annealing (BEETS) algorithm uses the “strain tensor” data from the .elout file produced during the non-linear FEA process. LSTC describes the tensorial strain data written in the .elout file as the total state of deformation, i.e elastic + plastic strain (Livermore Software

Technology Corporation 2017). Therefore, in order to verify the observed low plastic strain, the next step is to analyse the total strain distribution in the zone affected by checkerboarding in BUS_M02. This "zone" is highlighted in Figure 6.32 below:

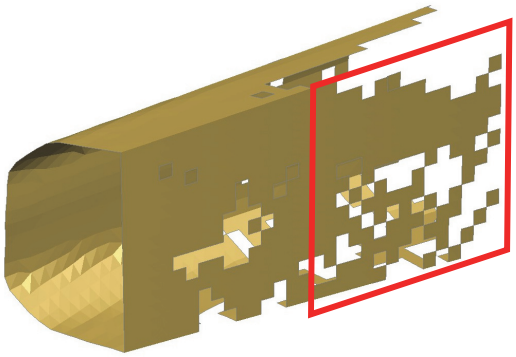

Figure 6.32 : BUS_M02 checkerboard affected zone

Figure 6.33 displays the strain distribution in the local x,y,z (normal strain), xy, xz and yz (shear strain) directions for the section highlighted in Figure 6.32 after iteration 1. The plots represent the values for the upper integration point in each element, which is part of the values written out in the .elout file (the other part being the lower integration point). These values are then translated by the BEETS algorithm into element sensitivities.

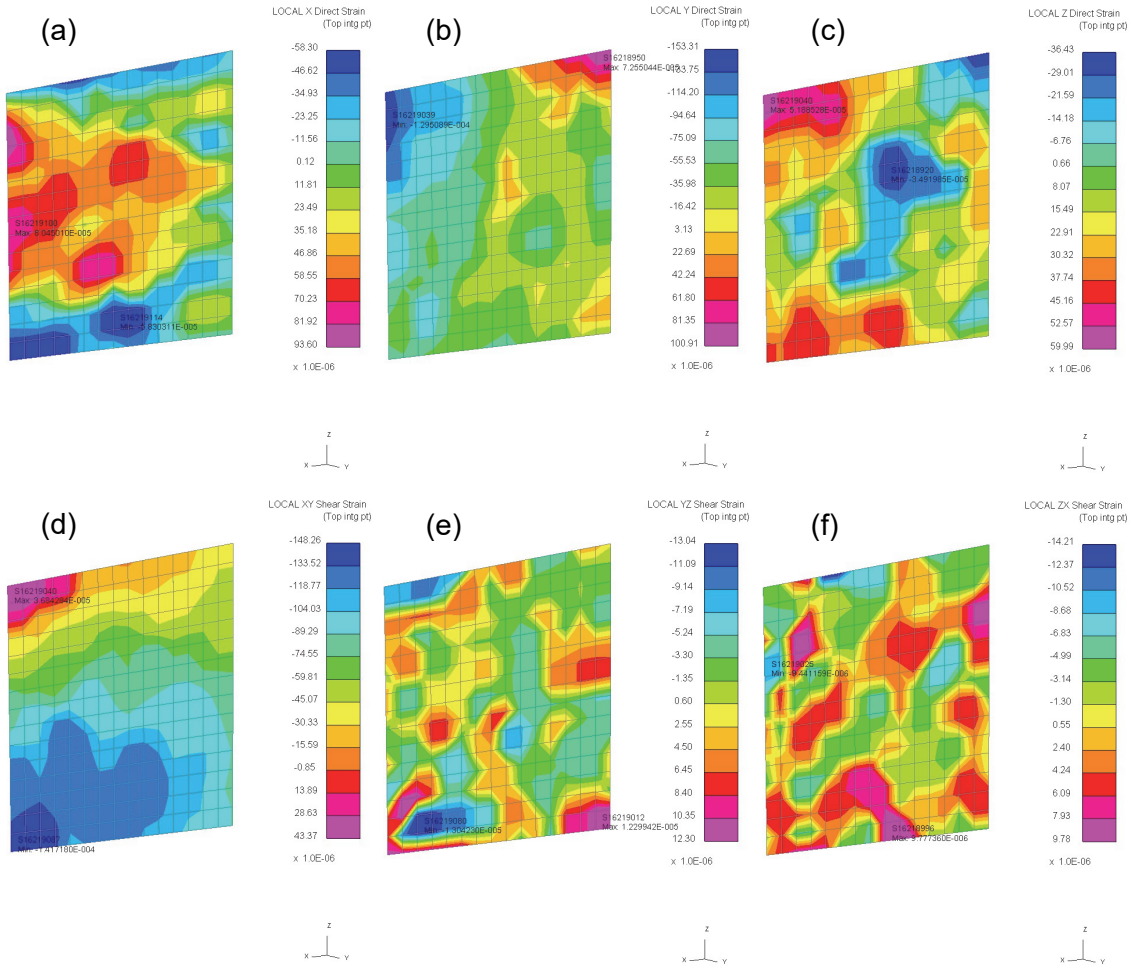

Figure 6.33 : BUS_M02 left hand crush can iteration 1 total strain plots in local element directions (a) Normal X (b) Normal Y (c) Normal Z (d) Shear XY (e) Shear YZ (f) Shear ZX

Firstly, the different order of magnitudes for each strain plot. Overall, the strain levels are in the region of 10^{-5} for each direction / type of strain behaviour, including in the direction of impact. This is despite a clear direction of impact in the global X axis. These means that, for each of the six strain values taken into account in the element sensitivity calculation, there isn't a clear load path or direction through the crush cans. In non-linear optimisation terms, this means that with similar strain values, the algorithm may find it difficult to make an informed decision as to which elements are the least efficient, and by extension the elements to remove. This results in the checkerboard pattern observed in Figure 6.20. By contrast, Figure 6.34 displays the initial plastic strain in the left hand crush can for BUS_M50, which corresponds to the same hybrid optimisation parameters but at the higher velocity of 16km/h, and Figure 6.35 displays the total strain plots for BUS_M50.

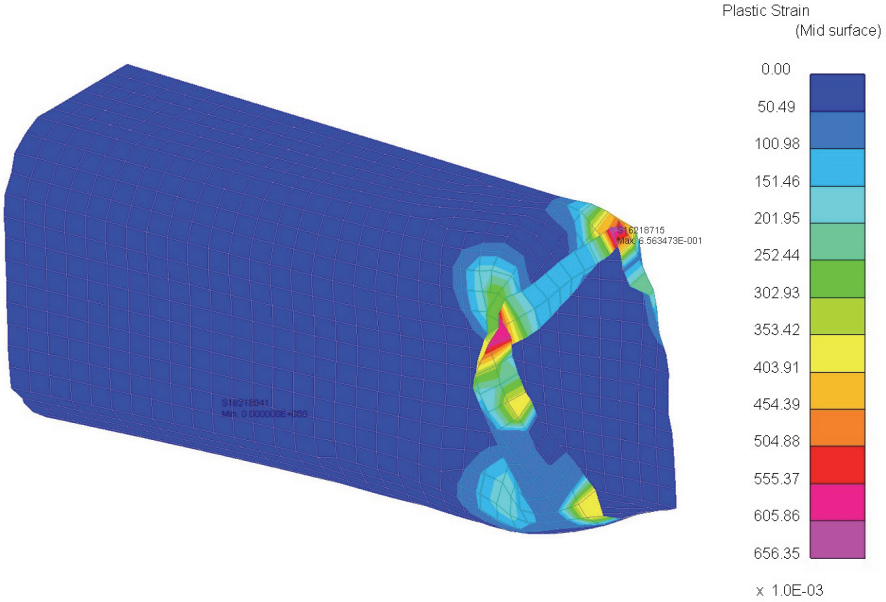

Figure 6.34 : BUS_M50 left hand crush can plastic strain plot

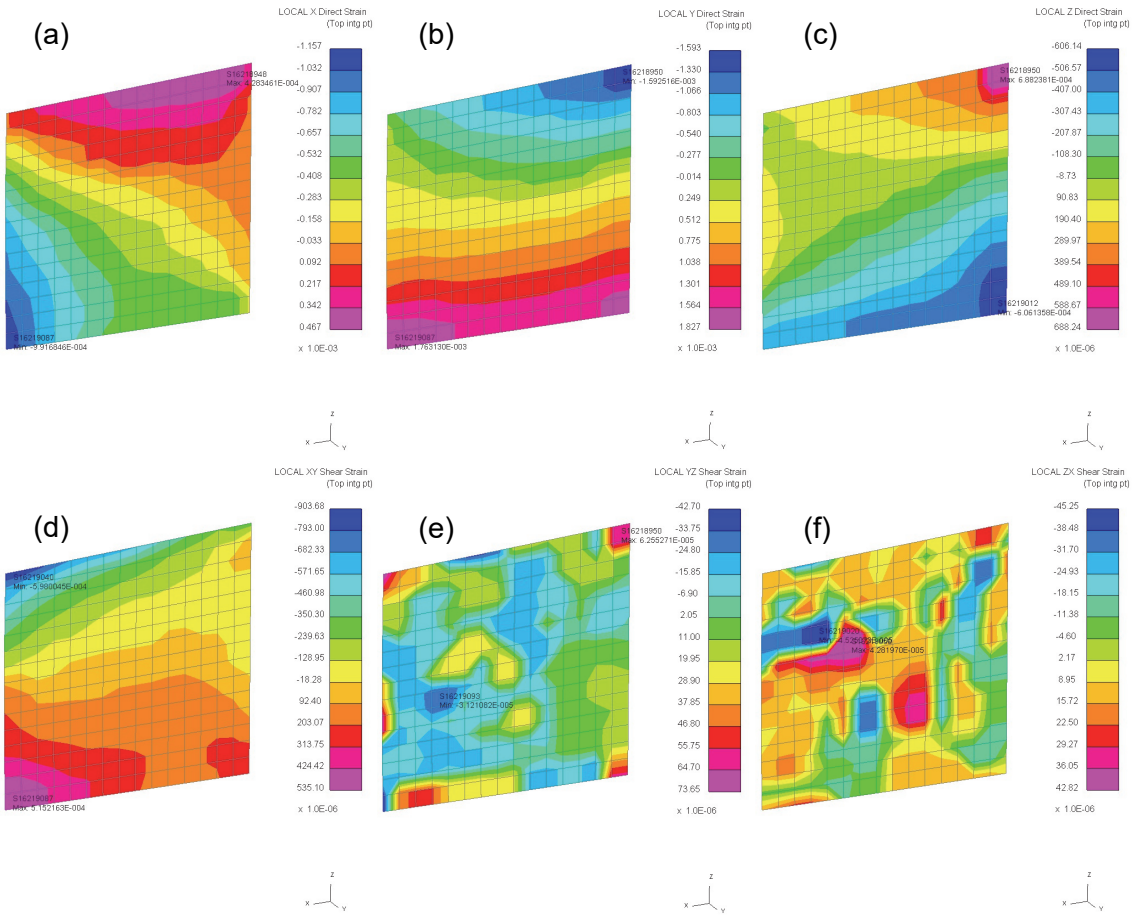

Figure 6.35 : BUS_M50 left hand crush can iteration 1 total strain plots in local element directions (a) Normal X (b) Normal Y (c) Normal Z (d) Shear XY (e) Shear YZ (f) Shear ZX

The strain plots further demonstrates the reasons behind the checkerboard pattern at lower velocity. The normal x, y and the shear xy strain values are an order of magnitude of around 10^{-3}, considerably higher than for the low velocity scenario but more importantly significantly higher than the other local element direction strain. Furthermore, the strain distribution in the x, y and xy strain plots ((a), (b) and (d) in Figure 6.35) demonstrates a more defined load path, i.e. the higher strain magnitudes are on the edges of the surface. This results in elements being removed from the middle section of the crush can, as illustrated in Figure 6.26. Overall, the models with the higher velocity impact produced more clearly defined load paths through the non-linear structure. It could be argued that this indicates that the optimisation process (and in this case the non-linear solver used BEETS) is good for non-linear dynamic scenarios.

Secondly, the optimised crush cans can be compared against the variation of ER. Overall, the areas of elements removed around the structure haven't been influenced by the reduction in the ER. Theoretically, reducing the ER value could add stability to the optimisation process by avoiding large volume reductions in any given iteration. The obvious drawback relates to an increased optimisation run time (for a given target volume). While the overall topologies are very similar, in the lower velocity scenarios reducing the ER has increased the checkerboard pattern discussed above. In the higher velocity cases, the reduced ER hasn't provided clearer loadpaths through the structure, as the original ER of 5% produced optimised final iteration topologies with very little to no checkerboard effect. It is difficult to make a suggestion as to the exact value of the ER for every case of hybrid optimisation, or even just non-linear optimisation, as it is very much dependent on the original structure and the loadcase applied. However, adding to the conclusion from the previous case study that the ER needs to be low enough not to cause instabilities in the structure, it could be suggested that once a suitable ER has been found, reducing it further provides very little in terms of geometric differences.

Finally, the final iteration topologies are compared with varying interface sizes, the final influential parameter on the crush can topologies. At first glance, the overall topologies change only slightly with the variation of the interface size. A closer look at the high velocity models (Figure 6.25 - Figure 6.30) reveals however that the increase in interface size produced final iteration topologies where more elements had been removed in the right hand crush can. Modifying the interface size has therefore affected the element removal process, which in itself is not surprising as the design volume has been changed. However, it is interesting to note that, contrary to the findings of case study 1,

the final iteration topologies obtained with an interface size equal to five times the element size hasn't affected the overall feasibility of the topology in the same manner as the previous case study. This is despite the fact that, in terms of design volume to total volume ratio, the models in case study with the large interface sizes are slightly more restrictive than the models in case study 1. Effectively, in case study 1, the most restrictive of the design volumes / interface sizes, i.e. six times the element size, translated into a design volume 85% of the total volume. In the case of the crush cans, with an interface size five times the element size, the design volume equalled 80% of the total volume. Therefore, while case study 1 concluded in the need to avoid large interface sizes, case study 2 hasn't identified, at least from a geometric/feasibility point of view, a consistent "threshold" value for the interface size. Essentially, similarly to the ER, the value of the interface size is case-dependent.

The next section will analyse the optimised longitudinal geometries.

6.3.2. Longitudinal configurations

The longitudinal topologies depend on all the variable parameters discussed in section 6.2. Therefore, each model has its own "unique" longitudinal geometry, for a total of 96 longitudinal topologies. This section will focus on the main geometry trends that emerge in the longitudinals, with a clear hybrid optimisation parameter influence. Firstly however, several combinations of hybrid optimisation or modelling parameters should be singled out for creating unfeasible and/or inefficient topologies, with in some cases the emergence of detached elements which in linear static optimisation causes error terminations.

The first issue relates back to the volume target calculation combined with the rate of exchange and ER, a problem highlighted in case study 1. For models with an ER of 5%, it takes 4 iterations for the non-linear optimisation process to converge and terminate successfully. Therefore, this is compatible with both rates of exchange of 1 (exchange of data every iteration) and 4 (exchange of data every 4 iterations). In the case of the latter, linear optimisation is performed once before the hybrid optimisation process terminates. In the case of an ER of 2.5%, the hybrid optimisation process terminates after 7 iterations. For models with a rate of exchange of 1, this causes no issues as the force data at the interface is exchanged at every iteration, in effect there is a "loop" of non-linear optimisation followed by linear optimisation, and the volume reductions for both models remains the same (when the volume constraint is specified in the linear models).

However for models with a rate of exchange of 4, linear optimisation occurs only at the 4th hybrid optimisation iteration, and would have occurred again at the 8th iteration. This of course doesn't take place as the non-linear optimisation has converged in the previous iteration, which terminates the hybrid optimisation process. This means that the longitudinals with a combination of ER = 2.5% and a rate of exchange of 4 contain more material than the "analogous" ER = 5% (when the minimise compliance / volume constraint optimisation parameters are used). This "issue" was also present in case study 1, and indicates simply that at this stage of the algorithm, a relationship exists between the rate of exchange and ER. The user therefore needs to specify an ER/rate of exchange pairing where the final volume reduction ratios (for minimise compliance / volume constraint) for both linear and non-linear models are similar.

The second issue concerns the appearance of detached elements in three specific models: BUS_M52, BUS_M60 and BUS_M68. These models correspond to the three different interface sizes, and a combination of high velocity impact, IR, ER = 2.5% and a "minimise compliance" objective. Detached elements appear after the first linear optimisation iteration, this is despite the optimisation process converging. Figure 6.36 displays the element density plot for BUS_M52, and Figure 6.37 the objective function convergence graph for iteration 1 of BUS_M52:

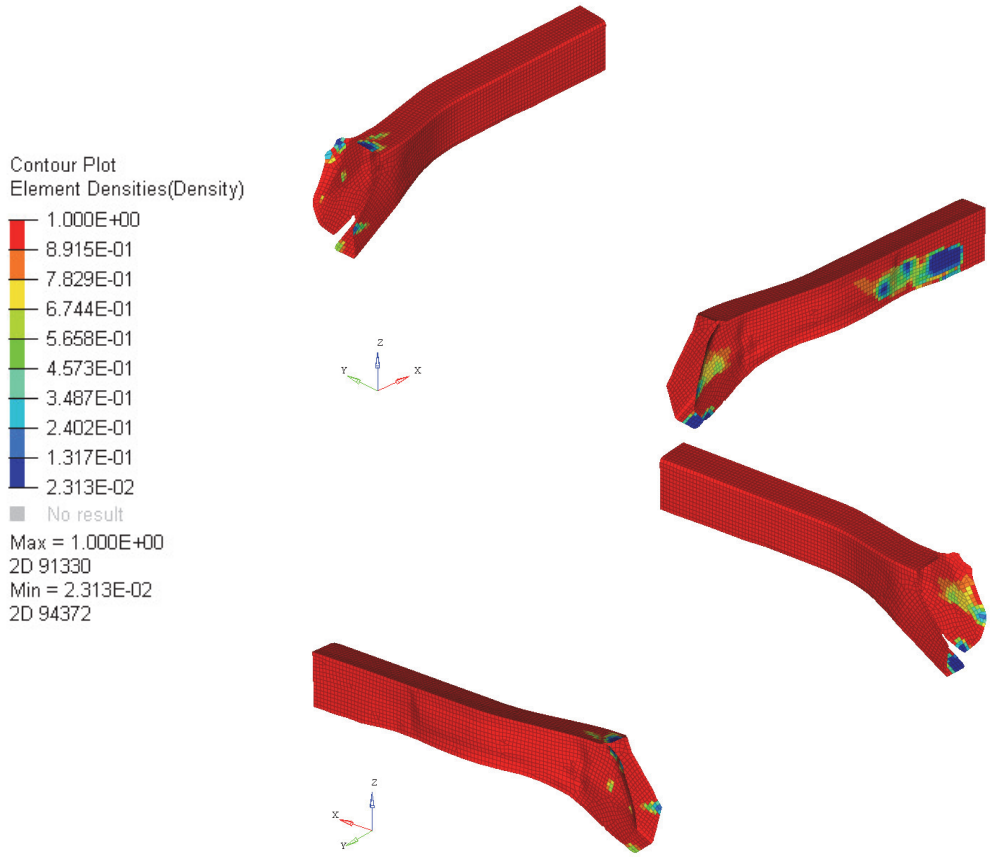

Figure 6.36 : BUS_M52 longitudinals iteration 1 element density plot

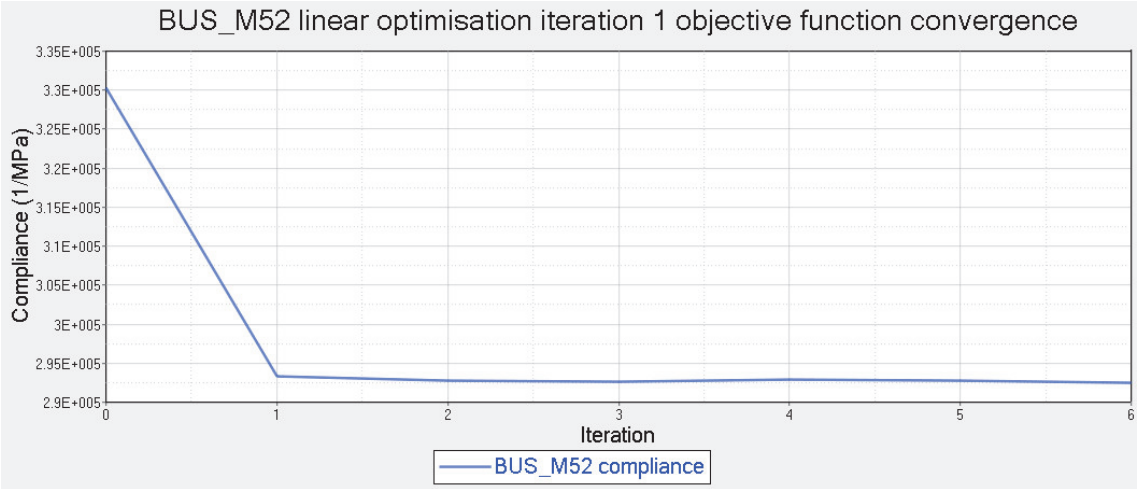

Figure 6.37 : BUS_M52 linear optimisation iteration 1 objective function convergence

Figure 6.36 and Figure 6.37 illustrate that in terms of optimisation process, there are no clear issues. Figure 6.36 demonstrates distinct areas of low density areas within the longitudinals. However, Figure 6.38 depicts the right hand longitudinal from the linear

model used in iteration 2, i.e. after the element densities have been extracted and the structure updated accordingly.

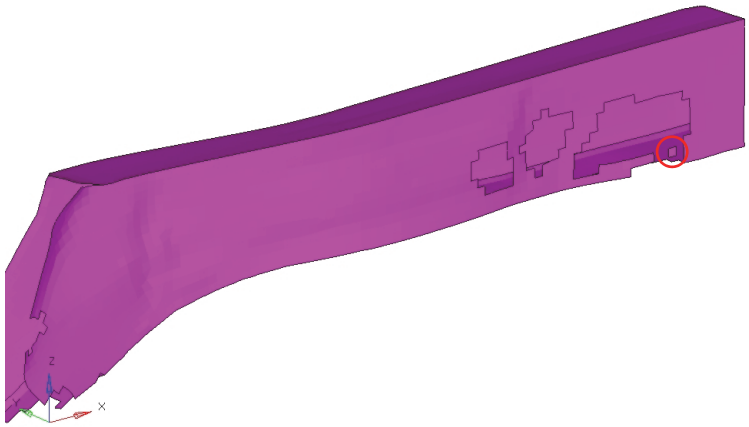

Figure 6.38 : BUS_M52 right hand longitudinal iteration 2 geometry

Circled in Figure 6.38 is the detached element in question. In terms of element removal, the void areas in the longitudinal correspond to the low density areas identified in Figure 6.36. However, the issue here lies with the implementation of the Variable Density Method / Solid Isotropic Material with Penalisation (VDM/SIMP) method within the overall hybrid optimisation methodology. Essentially, for the minimise compliance/volume target optimisation parameters, the ER dictates how many elements are removed per iteration, and the lowest density elements are removed until the iteration volume target is reached. As manufacturing constraints are not implemented, there is no element connection check prior to the next linear optimisation iteration in the hybrid methodology. This only occurs for the ER = 2.5% cases, as with ER = 5% more elements are removed per linear optimisation iteration (which included the detached element circled in Figure 6.38). Also, this problem doesn't arise when applying a "minimise mass" optimisation objective, as the element removal process doesn't depend on ER but rather the "Design volume fraction" provided by Optistruct in the optimisation information (.out) file.

While the issue doesn't occur for higher ERs, and indeed the "minimise mass" models, theoretically this is an issue that could occur for any ER, especially if many intermediate densities are present. Essentially, VDM/SIMP, as implemented in Optistruct is designed to be performed once, and at the end of the process the final iteration topology is interpreted and re-analysed by the user. The automatic process programmed in for hybrid optimisation (and the iterative non-linear / linear "loop" process) doesn't account

for detached elements. This issue is alleviated by using a high enough DISCRETE value to eliminate many of the intermediate densities, ensuring that the optimisation process has converged (increasing the maximum number of iterations with MAXITER) and by avoiding very low ERs. This however is on a case by case basis, as illustrated by the occurrence of this issue in “only” 3 of the 96 models.

The first clear geometry differences emerge as a function of the optimisation setup parameters (objective function / constraint). As with case study 1, the first combination minimises compliance with a target volume constraint. This means that the structural volume at the end of the optimisation process is the same or very similar for each model using these optimisation criteria, regardless of any structural performance values (such as stress or displacement). The second combination consists of minimising mass with a stress constraint applied. Overall, for the models using these optimisation parameters, less material is removed than for the “minimise compliance” cases. Figure 6.39 and Figure 6.40 display the longitudinal element density plots for BUS_M01 and BUS_M05 respectively

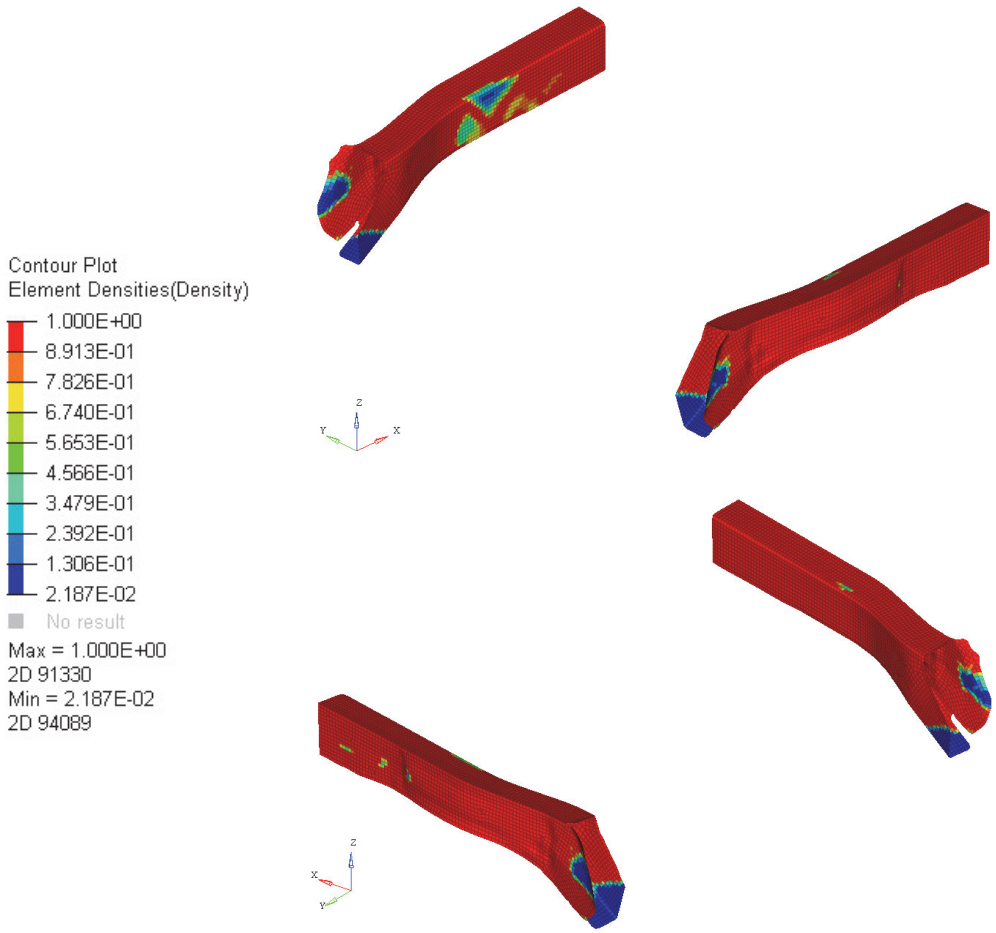

Figure 6.39 : BUS_M01 iteration 1 longitudinals element density plot

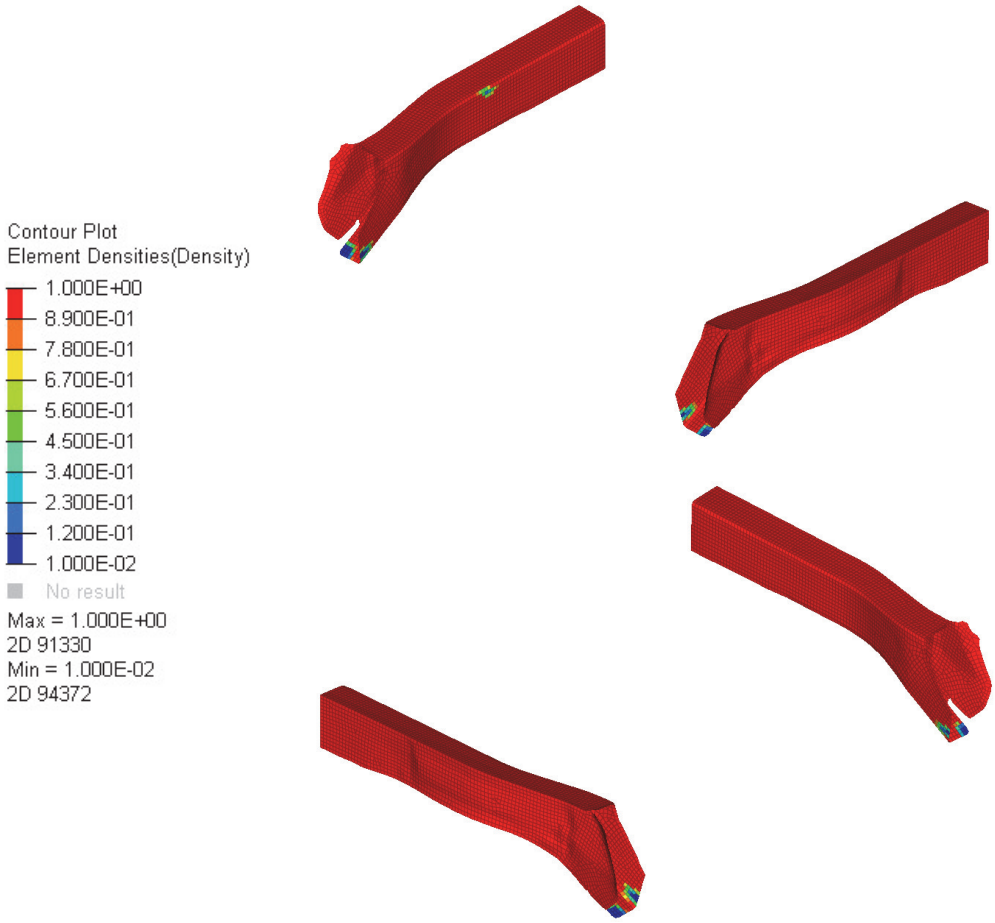

Figure 6.40 : BUS_M05 iteration 1 longitudinals element density plot

These models illustrate how little material can be removed from BUS_M05 (minimise mass) compared to BUS_M01 (minimise compliance). As a stress constraint is applied to BUS_M05, the stress plot at iteration 1 is displayed in Figure 6.41 to identify the reason behind the low number of low density elements in Figure 6.40

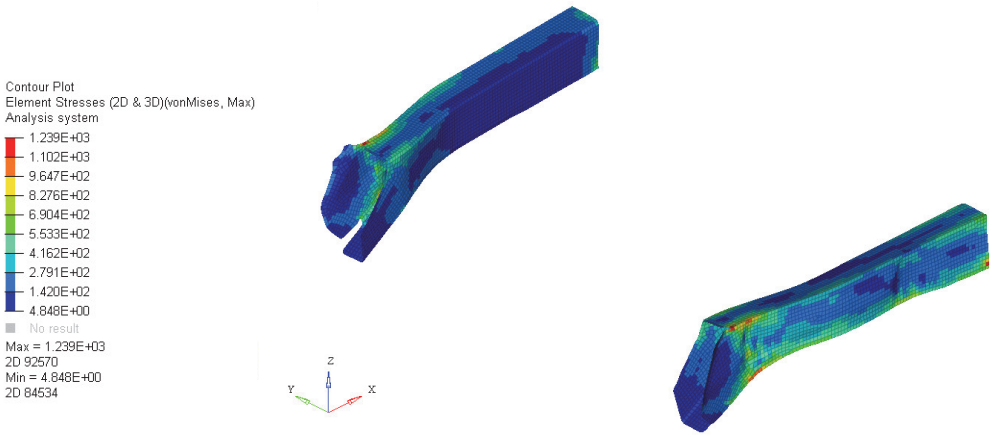

Figure 6.41 : BUS_M05 iteration 1 Von Mises stress plot (MPa)

Figure 6.41 displays very high, localised von Mises stress values above the stress constraint applied to BUS_M05 (350 MPa). However, Altair define the stress constraint implemented in Optistruct's TO solver as a global constraint, and therefore the optimisation process doesn't target localised stress concentrations (Altair University 2015). Essentially, these stress concentrations are targeted during later design stages, using shape and/or size optimisation. Nevertheless, it is clear from the element density plots that there are fewer low density areas for a "minimise mass" objective compared to a "minimise compliance" objective. This results in the final iteration topologies illustrated in Figure 6.42 (minimise compliance) and Figure 6.43 (minimise mass).

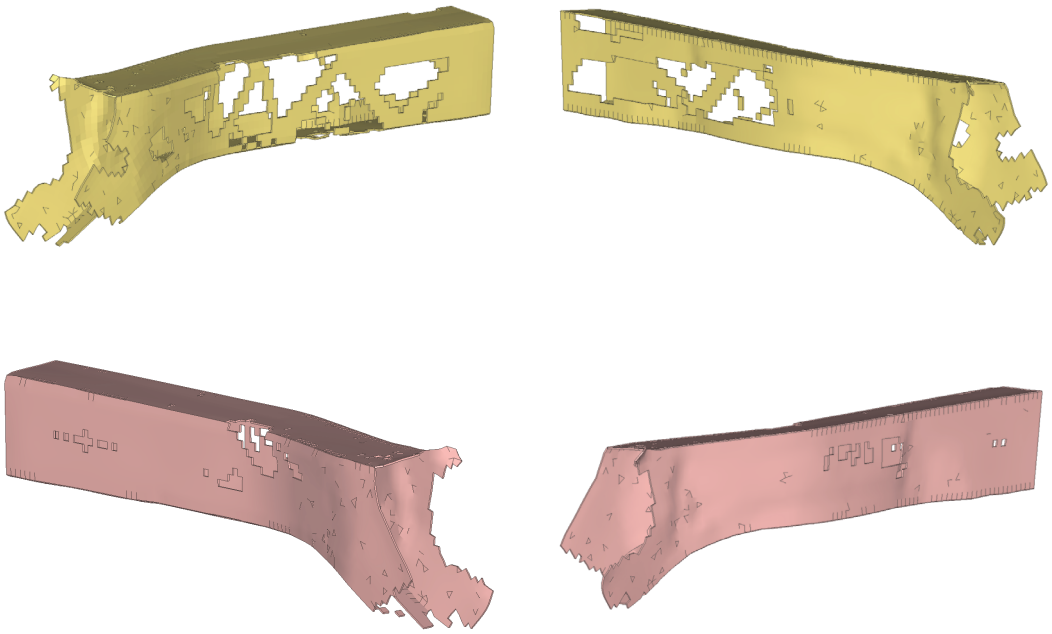

Figure 6.42 : BUS_M01 longitudinals final iteration topologies
Top = LH longitudinal, Bottom = RH longitudinal

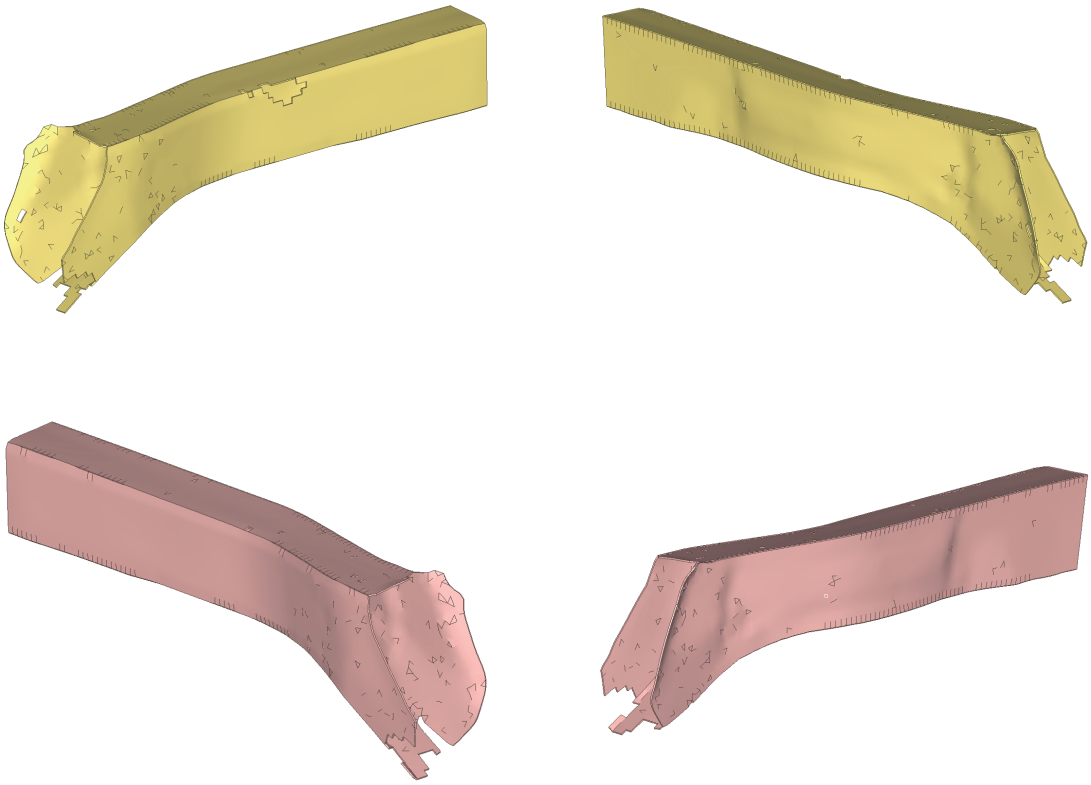

Figure 6.43 : BUS_M05 longitudinals optimised final iteration topologies
Top = LH longitudinal, Bottom = RH longitudinal

While this phenomenon appears in many “minimise mass” models, there are instances where more material is removed from the structure than the example given in Figure 6.43. These instances can be separated into 6 groupings based on the material removal trends in the longitudinals. Examples of these groupings are illustrated in Figure 6.44 – Figure 6.49, while Table 6.4 lists the models included in each grouping:

Table 6.4 : "Minimise mass" longitudinal geometry trend groupings

Grouping 1	Grouping 2	Grouping 3	Grouping 4	Grouping 5	Grouping 6
BUS_M08	BUS_M21	BUS_M23	BUS_M53	BUS_M55	BUS_M95
BUS_M16	BUS_M45	BUS_M47	BUS_M54	BUS_M56	
BUS_M24			BUS_M61	BUS_M63	
			BUS_M62	BUS_M64	
			BUS_M69	BUS_M71	
			BUS_M70	BUS_M72	
				BUS_M79	
				BUS_M87	

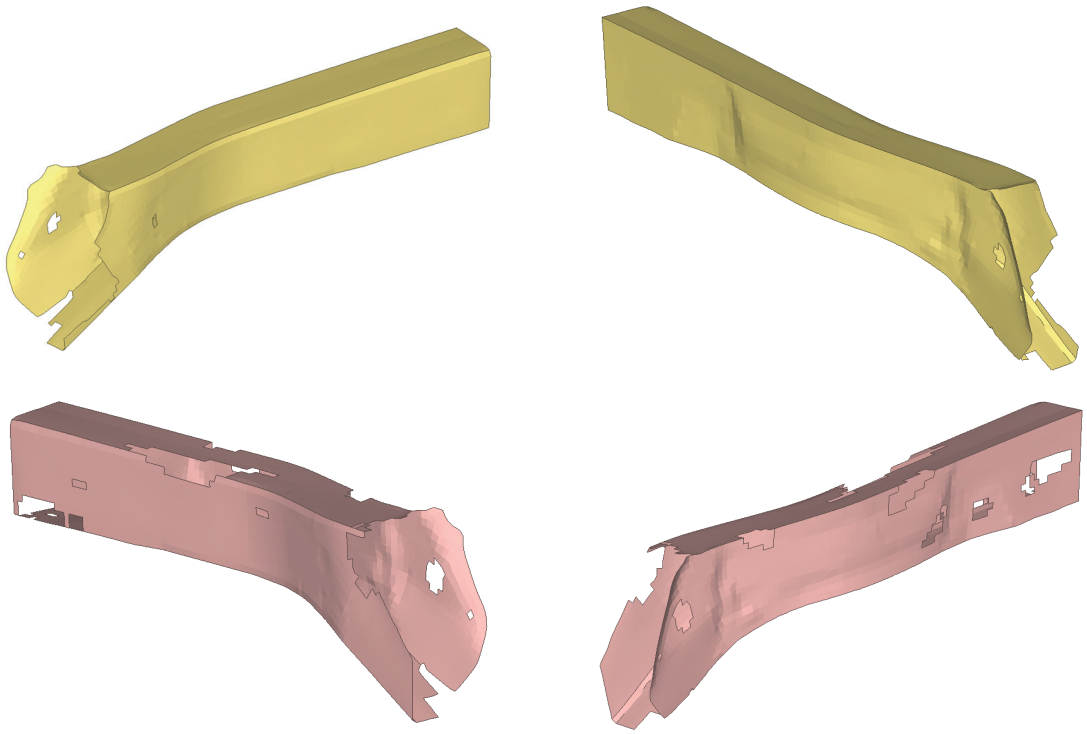

Figure 6.44 : BUS_M16 longitudinals final iteration topologies (Grouping 1)
Top = LH longitudinal, Bottom = RH longitudinal

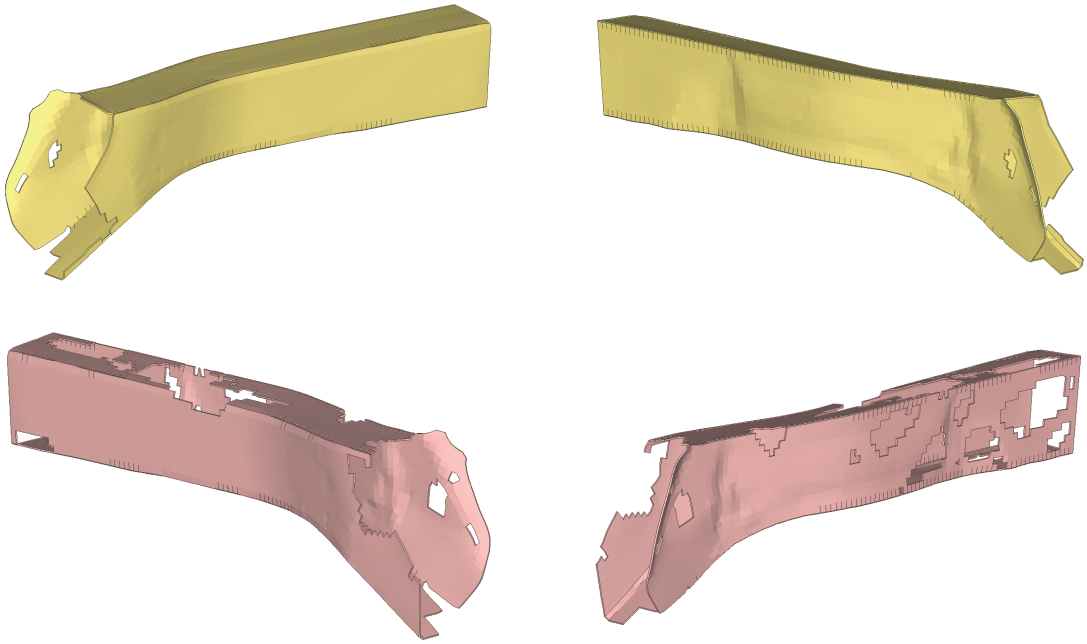

Figure 6.45 : BUS_M23 longitudinals final iteration topologies (Grouping 3)
Top = LH longitudinal, Bottom = RH longitudinal

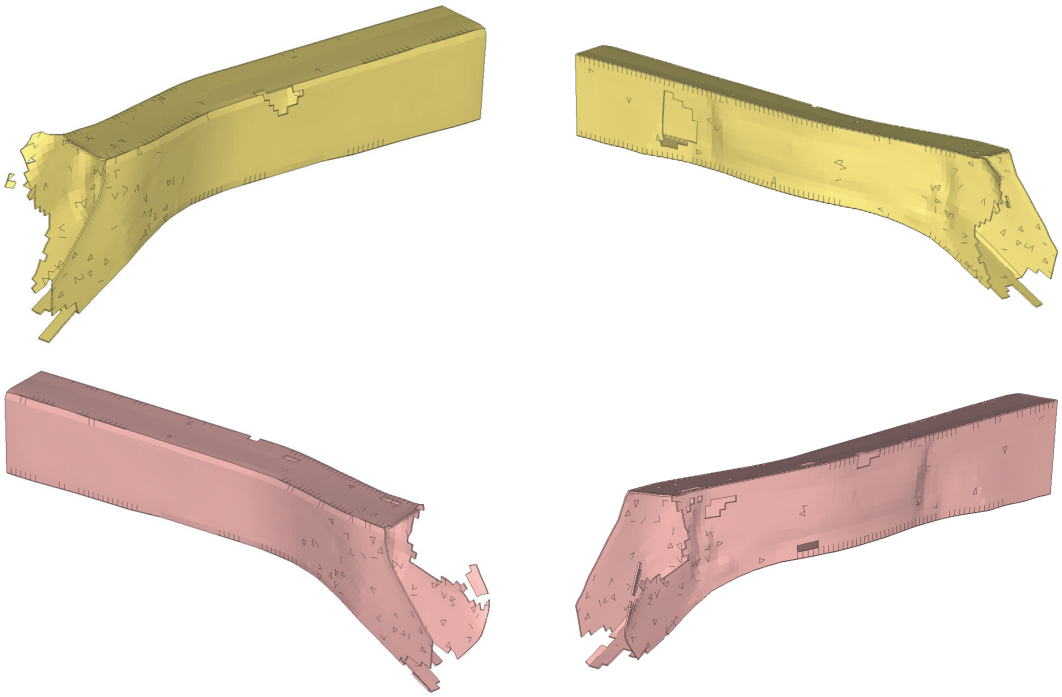

Figure 6.46 : BUS_M21 longitudinals final iteration topologies (Grouping 2)
Top = LH longitudinal, Bottom = RH longitudinal

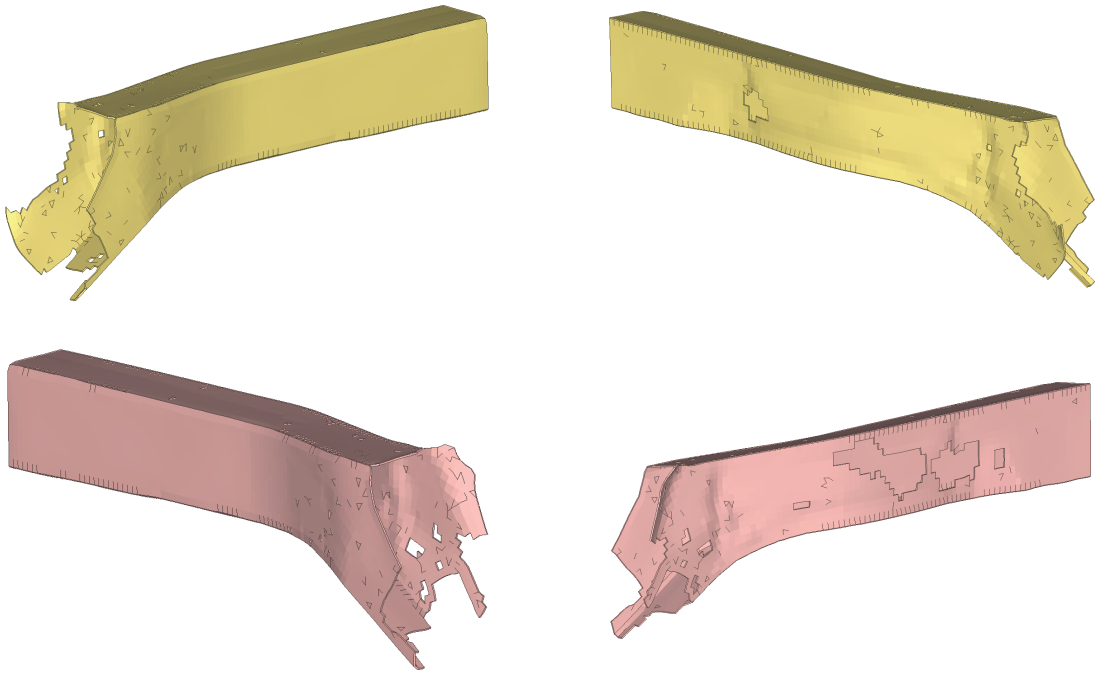

Figure 6.47 : BUS_M53 longtudinals final iteration topology (Grouping 4)
Top = LH longitudinal, Bottom = RH longitudinal

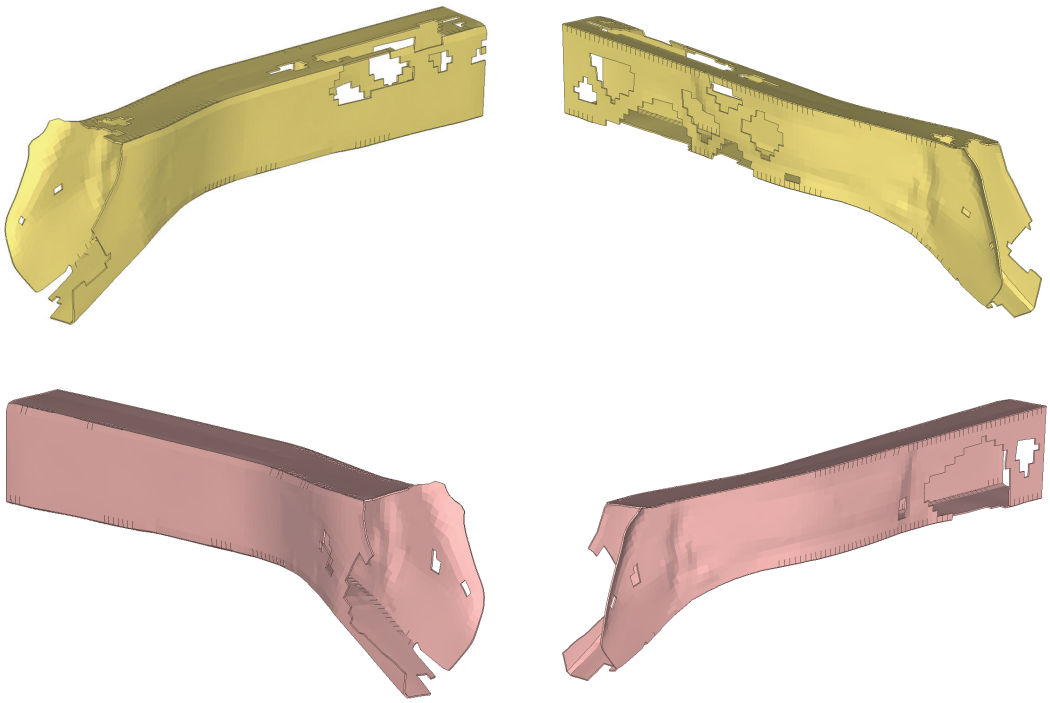

Figure 6.48 : BUS_M55 longitudinals final iteration topology (Grouping 5)
Top = LH longitudinal, Bottom = RH longitudinal

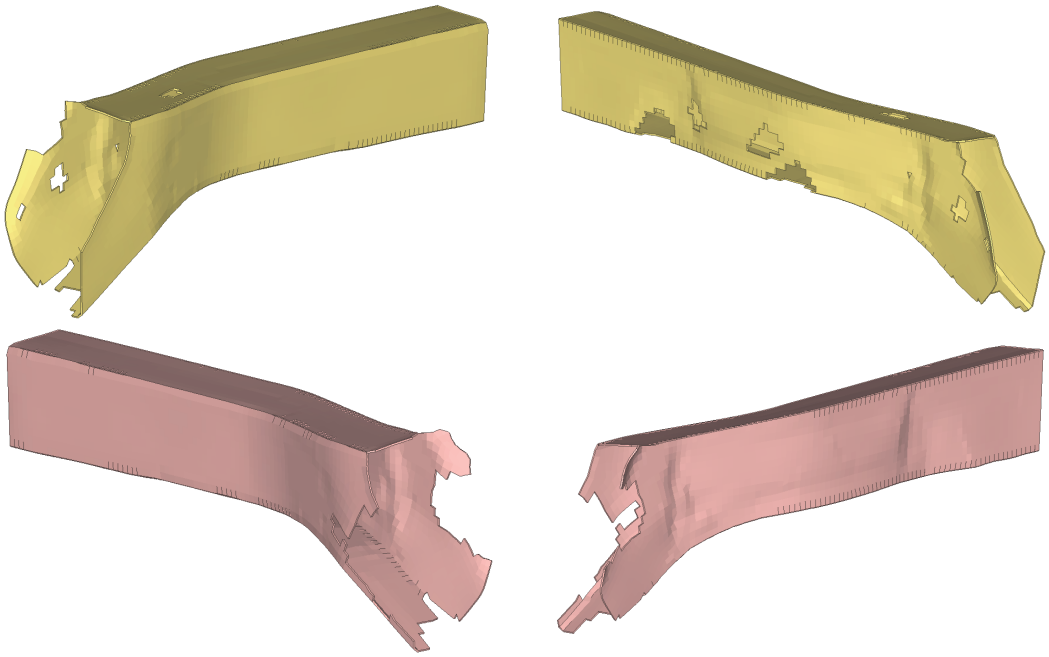

Figure 6.49 : BUS_M95 longitudinals final iteration topology (Grouping 6)
Top = LH longitudinal, Bottom = RH longitudinal

In order determine the hybrid optimisation or modelling parameters that have an influence in combination with the “minimise mass” objective”, Table 6.5 - Table 6.10 summarise the hybrid optimisation and modelling parameters associated with the models in each grouping:

Table 6.5 : Grouping 1 hybrid optimisation and modelling parameters

Model Number	Degree of non-linearity	ER (%)	Interface size (Number of elements)	Rate of exchange		Linear BC	Linear model objective	Linear model constraint
				BEETS	Optistruct			
BUS_M08	L	2.5	0	1	30	IR	Min. mass	von Mises stress
BUS_M16	L	2.5	89	1	30	IR	Min. mass	von Mises stress
BUS_M24	L	2.5	445	1	30	IR	Min. mass	von Mises stress

Table 6.6 : Grouping 2 hybrid optimisation and modelling parameters

Model Number	Degree of non-linearity	ER (%)	Interface size (Number of elements)	Rate of exchange		Linear BC	Linear model objective	Linear model constraint
				BEETS	Optistruct			
BUS_M21	L	5	445	1	30	SPC	Min. mass	von Mises stress
BUS_M45	L	5	445	4	30	SPC	Min. mass	von Mises stress

Table 6.7 : Grouping 3 hybrid optimisation and modelling parameters

Model Number	Degree of non-linearity	ER (%)	Interface size (Number of elements)	Rate of exchange		Linear BC	Linear model objective	Linear model constraint
				BEETS	Optistruct			
BUS_M23	L	5	445	1	30	IR	Min. mass	von Mises stress
BUS_M47	L	5	445	4	30	IR	Min. mass	von Mises stress

Table 6.8 : Grouping 4 hybrid optimisation and modelling parameters

Model Number	Degree of non-linearity	ER (%)	Interface size (Number of elements)	Rate of exchange		Linear BC	Linear model objective	Linear model constraint
				BEETS	Optistruct			
BUS_M53	H	5	0	1	30	SPC	Min. mass	von Mises stress
BUS_M54	H	2.5	0	1	30	SPC	Min. mass	von Mises stress
BUS_M61	H	5	89	1	30	SPC	Min. mass	von Mises stress
BUS_M62	H	2.5	89	1	30	SPC	Min. mass	von Mises stress
BUS_M69	H	5	445	1	30	SPC	Min. mass	von Mises stress
BUS_M70	H	2.5	445	1	30	SPC	Min. mass	von Mises stress

Table 6.9 : Grouping 5 hybrid optimisation and modelling parameters

Model Number	Degree of non-linearity	ER (%)	Interface size (Number of elements)	Rate of exchange		Linear BC	Linear model objective	Linear model constraint
				BEETS	Optistruct			
BUS_M55	H	5	0	1	30	IR	Min. mass	von Mises stress
BUS_M56	H	2.5	0	1	30	IR	Min. mass	von Mises stress
BUS_M63	H	5	89	1	30	IR	Min. mass	von Mises stress
BUS_M64	H	2.5	89	1	30	IR	Min. mass	von Mises stress
BUS_M71	H	5	445	1	30	IR	Min. mass	von Mises stress
BUS_M72	H	2.5	445	1	30	IR	Min. mass	von Mises stress
BUS_M79	H	5	0	4	30	IR	Min. mass	von Mises stress
BUS_M87	H	5	89	4	30	IR	Min. mass	von Mises stress

Table 6.10 : Grouping 6 hybrid optimisation and modelling parameters

Model Number	Degree of non-linearity	ER (%)	Interface size (Number of elements)	Rate of exchange		Linear BC	Linear model objective	Linear model constraint
				BEETS	Optistruct			
BUS_M95	H	5	445	4	30	IR	Min. mass	von Mises stress

Interestingly, these results highlight that the impact velocity but also the linear model BCs differentiate each grouping. The ER also has a minor effect, as BUS_M23 and BUS_M24 are in different groupings (Grouping 3 and Grouping 1 respectively). However, there are some similarities between the final iteration topologies in these two groupings (Figure 6.44 and Figure 6.45), hence why this parameter is less influential on the topologies compared to impact velocity and linear BCs.

Grouping 7, illustrated in Table 6.11 below, groups all the remaining “minimise mass” models that had little or no material removed from the longitudinals, essentially models similar to Figure 6.43. Introducing this grouping will allow further analysis into the parameters that have the most effect when combined with the “minimise mass” optimisation objective.

Table 6.11 : "Minimise mass" longitudinal grouping 7

Grouping 7 Models	
BUS_M05	BUS_M29
BUS_M06	BUS_M31
BUS_M07	BUS_M37
BUS_M13	BUS_M39
BUS_M14	BUS_M77
BUS_M15	BUS_M85
BUS_M22	BUS_M93

The remaining “minimise mass” models are not included in this analysis, as due to the ER/Rate of exchange relationship discussed earlier in this section, only a single linear optimisation “loop” is performed. As a reminder, models with an ER of 2.5% terminate after 7 non-linear iterations, which controls the termination of the overall hybrid process. Coupled with a BEETS rate of exchange parameter of 4 (i.e. one linear optimisation iteration every four non-linear iterations), only a single linear optimisation process is performed at iteration 4. Therefore, these models are inherently “heavier” than other ER/Rate of exchange combinations. Figure 6.13 summarises the hybrid optimisation and modelling parameters for grouping 7:

Table 6.12 : Grouping 7 hybrid optimisation and modelling parameters

Model Number	Degree of non-linearity	ER (%)	Interface size (Number of elements)	Rate of exchange		Linear BC	Linear model objective	Linear model constraint
				BEETS	Optistruct			
BUS_M05	L	5	0	1	30	SPC	Min. mass	von Mises stress
BUS_M06	L	2.5	0	1	30	SPC	Min. mass	von Mises stress
BUS_M07	L	5	0	1	30	IR	Min. mass	von Mises stress
BUS_M13	L	5	89	1	30	SPC	Min. mass	von Mises stress
BUS_M14	L	2.5	89	1	30	SPC	Min. mass	von Mises stress
BUS_M15	L	5	89	1	30	IR	Min. mass	von Mises stress
BUS_M22	L	2.5	445	1	30	SPC	Min. mass	von Mises stress
BUS_M29	L	5	0	4	30	SPC	Min. mass	von Mises stress
BUS_M31	L	5	0	4	30	IR	Min. mass	von Mises stress
BUS_M37	L	5	89	4	30	SPC	Min. mass	von Mises stress
BUS_M39	L	5	89	4	30	IR	Min. mass	von Mises stress
BUS_M77	H	5	0	4	30	SPC	Min. mass	von Mises stress
BUS_M85	H	5	89	4	30	SPC	Min. mass	von Mises stress
BUS_M93	H	5	445	4	30	SPC	Min. mass	von Mises stress

Firstly, a trend regarding the rate of exchange is apparent. 77% of the models where material has been removed, i.e. groupings 1 – 6, exchange the interface force data at every iteration. This strengthens the conclusion of case study 1, where the same phenomenon was observed, where essentially by decreasing the exchange of forces (and by extension the number of linear optimisation “loops”), vital information could be missed and an iteration where material could have been removed may be neglected. Figure 6.50 illustrates the element removal per linear optimisation iteration for BUS_M16:

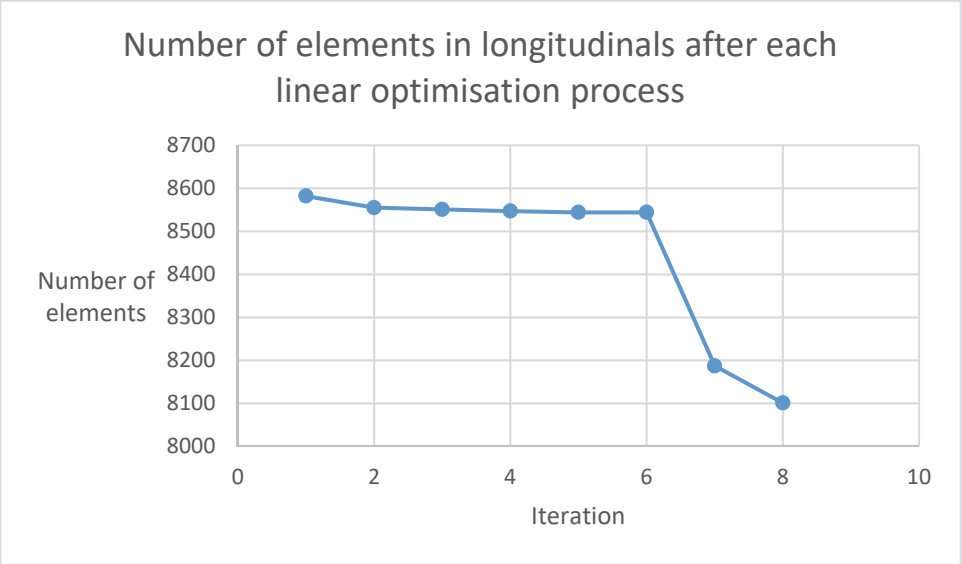

Figure 6.50 : Graph depicting number of elements in longitudinals after each hybrid optimisation iteration (BUS_M16)

Figure 6.50 reveals that the vast majority of element removal occurs after iteration 6 in the hybrid optimisation process for BUS_M16. Therefore, an exchange of data at the interface every 4 iterations would not be able to capture this phenomenon. Overall, for BUS_M16, approximately 5.5% of the material has been removed in the longitudinals by the end of the optimisation process. By analysing the element removal in the analogous model (with the rate of exchange of 4), BUS_M47, only 2.6% of material is removed at the end of the optimisation process. This further highlights the effect of the rate of exchange when combined with the “minimise mass” optimisation objective.

A further trend regarding the combination of impact velocity with the rate of exchange of 1, i.e. interface force data exchanged at every iteration, is also identified. In grouping 7, all the models are low velocity impacts, whereas in groupings 1-6 where more material is removed the models undergo a high velocity impact. At first glance, this is illogical given the optimisation setup includes a stress constraint, and a higher velocity impact should translate into higher interface forces and by extension higher magnitude force inputs into the linear model. Figure 6.51 displays the element removal per iteration in the longitudinals for BUS_M07 and BUS_M55 (analogous models with different impact velocities). BUS_M07 is included in grouping 7 while BUS_M55 is included in grouping 5.

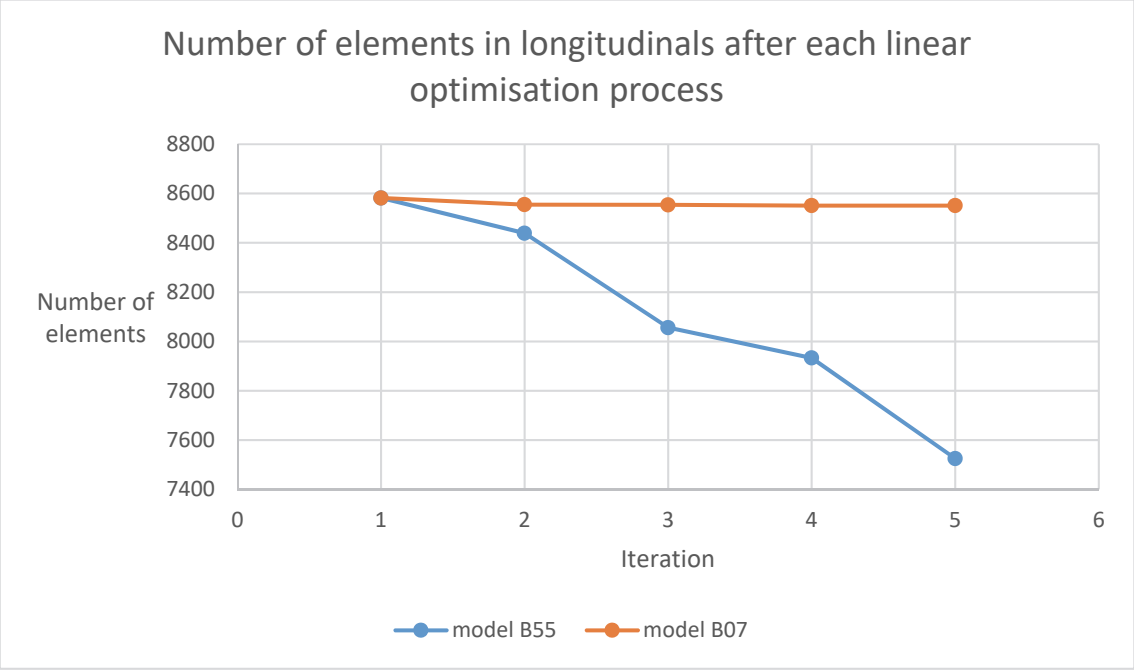

Figure 6.51 : Graph depicting number of elements in longitudinals after each hybrid optimisation iteration (BUS_M07 and BUS_M55)

The graph above illustrates that there is far more element removal in BUS_M55 than in BUS_M07, despite the higher impact velocity in BUS_M55. Figure 6.52 and Figure 6.53 illustrate the input FE models for linear optimisation at iteration 1 for BUS_M07 and BUS_M55 respectively.

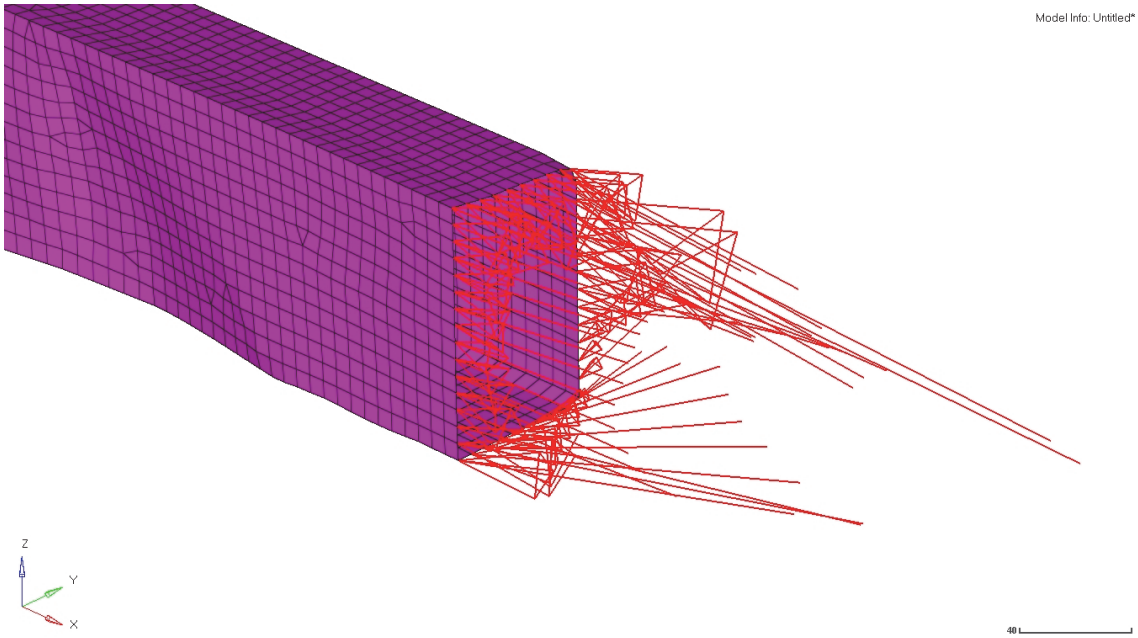

Figure 6.52 : BUS_M07 iteration 1 linear optimisation input (right hand longitudinal)

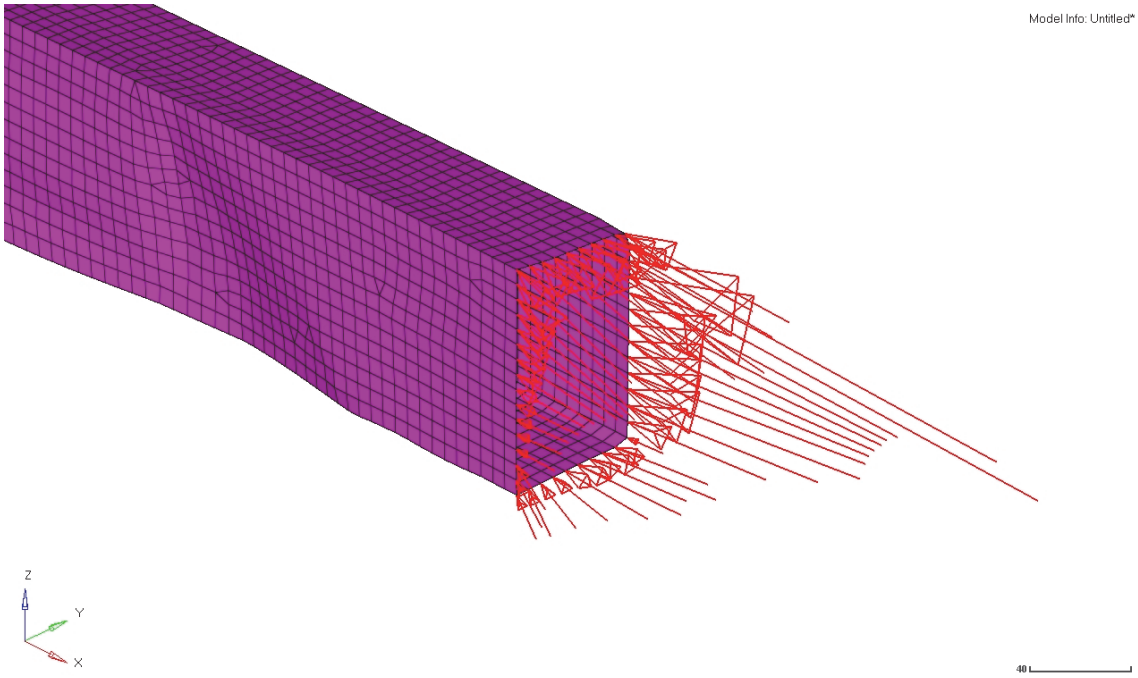

Figure 6.53 : BUS_M55 iteration 1 linear optimisation input (right hand longitudinal)

The force magnitudes do not appear in the figures for clarity, but the arrow length represents the force intensity. It should also be stated that the force magnitudes are higher for BUS_M55 (maximum nodal force of 7706 N) compared to BUS_M07 (maximum nodal force of 2313 N), which is to be expected given the difference in impact

velocity. The visible difference however is in the direction of the forces in the linear model. Figure 6.53 illustrates a clearer overall direction of the input forces in the $-\vec{x}$ direction, whereas this is less clear in Figure 6.52. This relates back to the velocity issues previously mentioned, and at lower velocity the overall loading direction is less well defined. To appreciate the effect this has on the optimisation process, Figure 6.54 and Figure 6.55 display the relative element densities and stress plot at iteration 1 for both BUS_M07 and BUS_M55 respectively. The stress plot is structured so that only areas below the stress constraint value of 350 MPa are displayed. This illustrates the potential for material removal from the longitudinals, however it does not indicate that the elements highlighted will be removed for certain. In essence, these stress plots indicate the less "important" areas for structural performance.

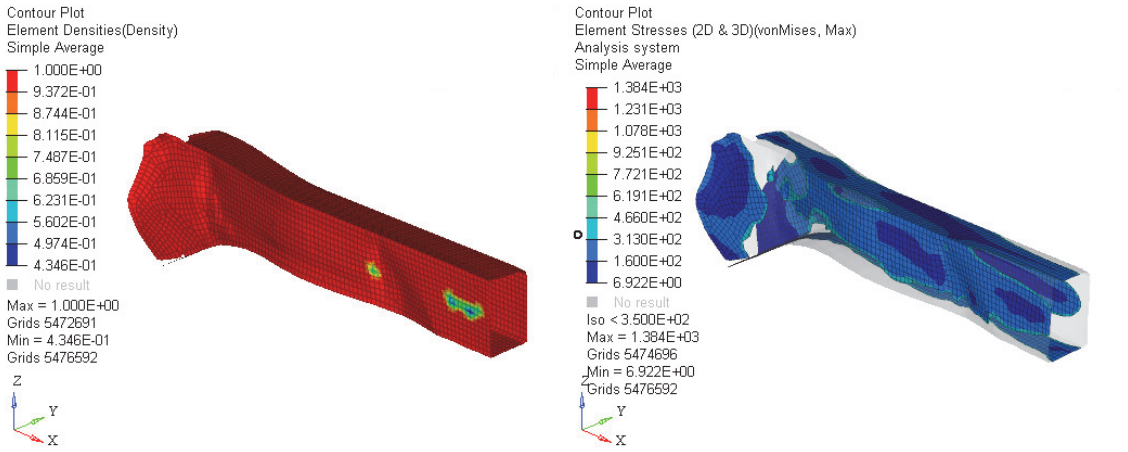

Figure 6.54 : BUS_M07 iteration 1 element density distribution and Von Mises stress plot

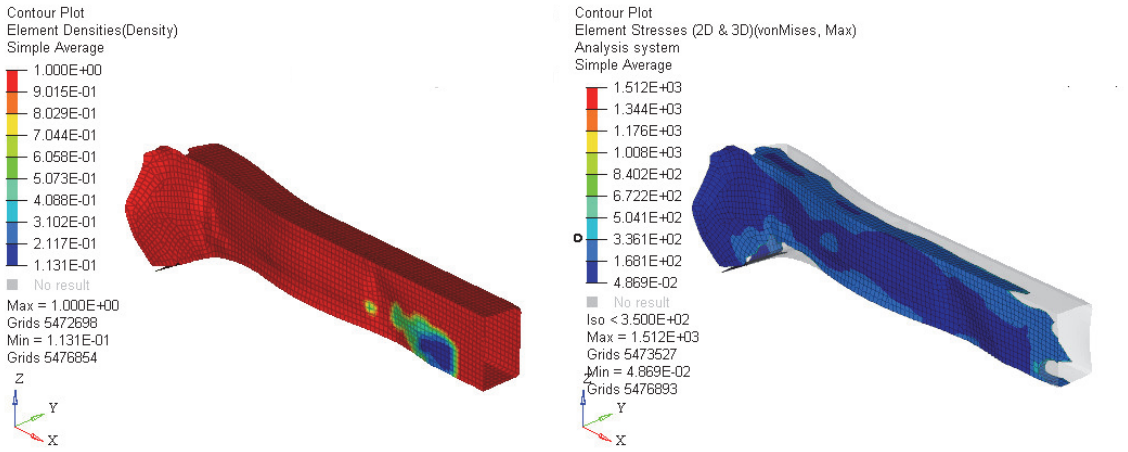

Figure 6.55 : BUS_M55 iteration 1 element density distribution and Von Mises stress plot

Figure 6.54 and Figure 6.55 illustrate why more material is removed where the impact velocity was highest. Essentially, the stress plots show that the areas where the von Mises stress values are below 350 MPa are more frequent for BUS_M07 than BUS_M55. This in itself is not surprising given the loading input, i.e. different velocity. However, for BUS_M55, the area for low stresses, i.e. below 160 MPa, is larger and more continuous than for BUS_M07. Observing the values reveals that for the most part, the stress values are situated between 20 and 250 MPa for BUS_M55. For BUS_M07, while there are some small areas where the stresses are very low (between 4 and 158 MPa), there are some areas where the stresses are between 158 and 311 MPa. At this point it is essential to remember that Optistruct does not take into account stress concentrations when an optimisation stress constraint is applied. Therefore from a “global” viewpoint, the stresses in the right hand longitudinal faces visible in Figure 6.54 and Figure 6.55 are lower for BUS_M55 than BUS_M07. This is illustrated in Figure 6.56 below, where the threshold for visualising the stresses is reduced to 160 MPa, i.e. only areas of the topology where the stresses are below 160 MPa appear:

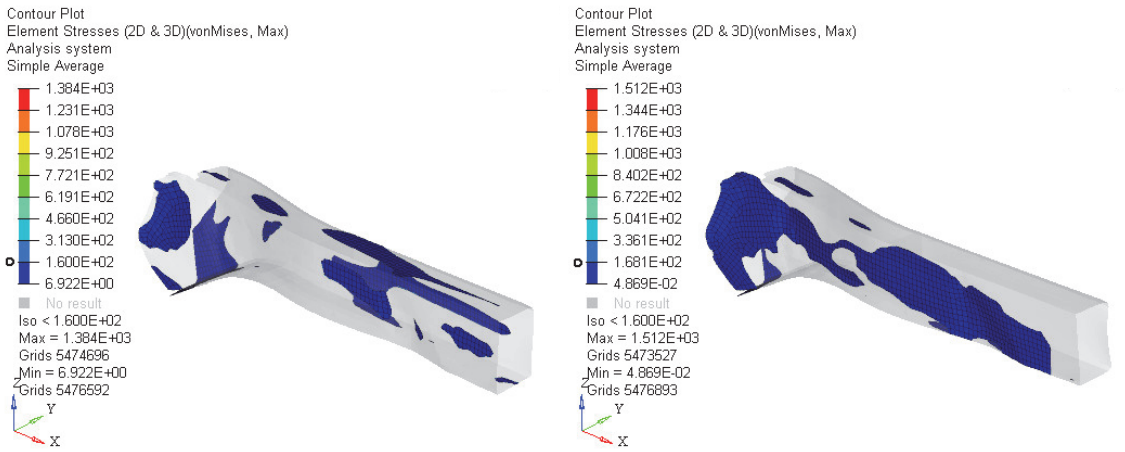

Figure 6.56 : BUS_M07 and BUS_M55 Von Mises stress plot with 160 MPa threshold applied

The stress plots highlight how more material can be removed from BUS_M55 compared to BUS_M07, with larger “available” low stress areas. This is also reflected in the relative element density plots in Figure 6.54 and Figure 6.55.

The “linear optimisation objective” parameter has illustrated a significant influence on the final iteration topologies (from a visual view point). Another hybrid optimisation parameter to that appears to have impacted the optimisation process is the rate of exchange. The issues regarding the combination of the rate of exchange with the “minimise mass”

objective, specifically when the interface force data isn't exchanged every iteration, have been discussed above, as have the "target volume" issues when combined with the lower ER value. Another phenomenon can be observed regarding the rate of exchange, specifically the "clarity" of the final iteration tropologies. The models were the rate of exchange is lower, i.e. "4", produce results that are clearer than when the force is exchanged at every iteration, i.e. "1". This could somehow seem contradictory, as the more the data is exchanged, the more accurate the FE setup for linear optimisation reflects the state of the non-linear structure, in this case the crush cans. However, this can be explained by the non-linear optimisation procedure. Element removal is controlled by the ER, which is typically kept relatively low to avoid instabilities in the FE model. Therefore, a relatively small number of elements are removed at each optimisation iteration, which by extension indicates continuously evolving interface forces as the load path through the crush can changes. This means that the force input into the longitudinals is also continuously evolving. In linear static optimisation, even the smallest changes to the force input profile (distribution across the interface, magnitudes and angles) can have a large effect on the "optimal" load path through the structure. If this load path changes at every hybrid optimisation iteration, different elements could be removed from the linear structure at different times in the optimisation process, hence the overall "optimised" topology could have unclear loadpaths. An example of this phenomenon is displayed for BUS_M01 and BUS_M25, where the same hybrid optimisation parameters are used (see Figure 6.2 and Figure 6.3) with a different rate of exchange used (Figure 6.42 and Figure 6.57).

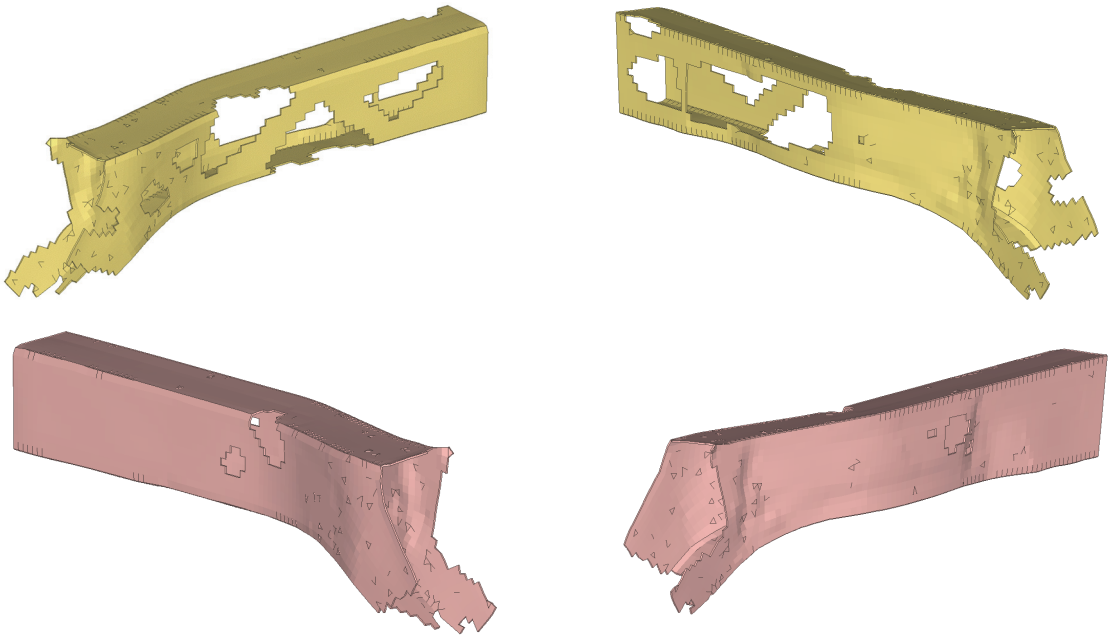

Figure 6.57 : BUS_M25 longitudinals final iteration topologies
Top = LH longitudinal, Bottom = RH longitudinal

Comparing the two final iteration topologies illustrates that, especially in the left hand longitudinal, the load paths are better defined. This could also be due to the MINDIM parameter (minimum dimension) activated during the linear optimisation process. Furthermore, this phenomenon is more visible in the low velocity impact models, which could indicate that this ties in with the checkerboard issues displayed at low velocity in the crush cans. Figure 6.58 and Figure 6.59 display the longitudinals for BUS_M49 and BUS_M73, analogous to BUS_M01 and BUS_M25 but with a high velocity impact.

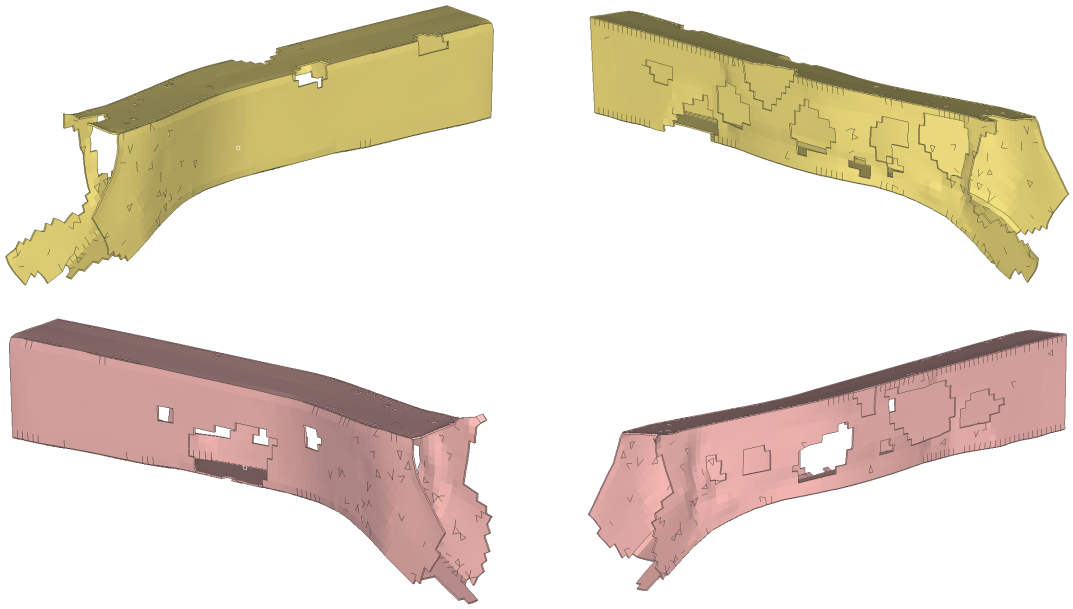

Figure 6.58 : BUS_M49 longitudinal final iteration topologies
Top = LH longitudinal, Bottom = RH longitudinal

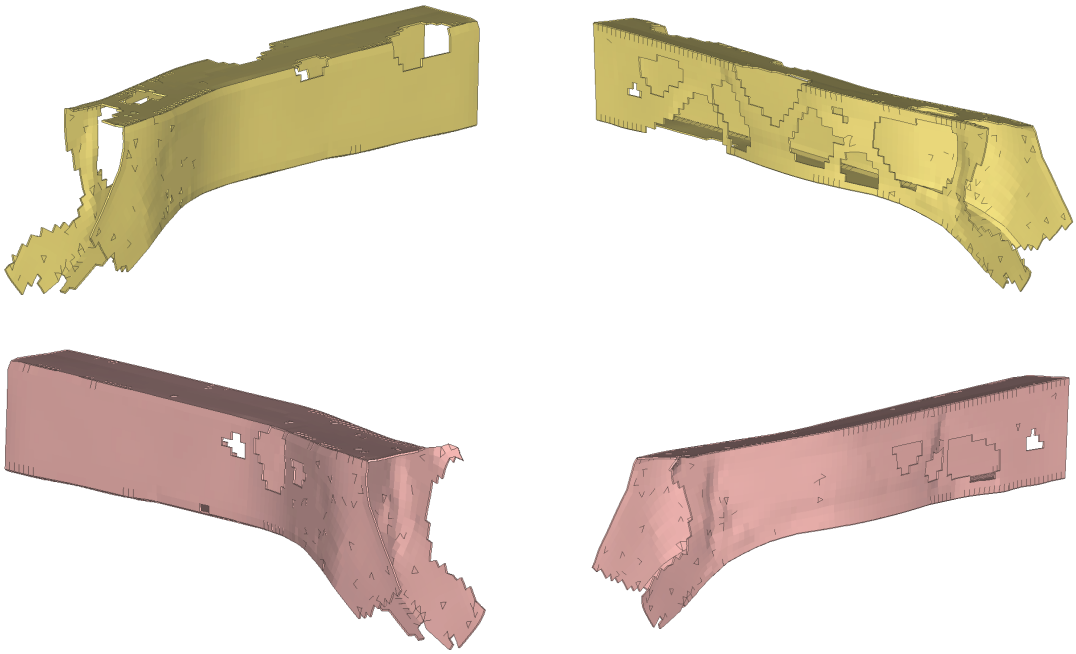

Figure 6.59 : BUS_M73 longitudinals final iteration topologies
Top = LH longitudinal, Bottom = RH longitudinal

Compared to BUS_M01 and BUS_M25, these results demonstrate less difference in the topologies due to the rate of exchange. This can most likely be explained by the fact that at higher velocity, the direction of the forces at the interface are influenced more by a

single direction, i.e. the $-\vec{x}$ in this case, therefore the loadpath through the structure is by default more clear (as displayed by Figure 6.52 and Figure 6.53). Therefore the change in the non-linear crush cans has less influence on the load directions at the interface, and by extension the rate of exchange will have less influence. Furthermore, with a vastly decreased checkerboard effect at high velocity, the load path through the crush cans is clearer. Nevertheless for some high velocity impacts there still exists an influence (e.g. the right hand longitudinal in Figure 6.58 and Figure 6.59), and overall the less frequent rate of exchange results in clearer optimum load paths through the structure. Essentially this could mean that allowing the non-linear optimisation process to form load paths through the crush cans is necessary before transferring the loads at the interface for linear optimisation. There is a limitation to this observation however, which resides in the final volume target of 85%. As has been explained, with an ER of 5%, 4 hybrid optimisation iterations are necessary in order to reach the target. Therefore, with a force exchange every 4 iterations, linear optimisation is performed at the very end of the hybrid optimisation process. If a lower volume target was selected such that more than one linear optimisation “loop” was performed (e.g. 8 hybrid optimisation loops, and therefore 4 linear optimisation “loops”), would the conclusions be the same, i.e. the best results are obtained when linear optimisation is performed only at iteration 8, or would intermediate linear optimisation processes be beneficial. These initial results would suggest that is not the case, and by extension this could signify that the optimisation processes, both linear and non-linear, could be performed separately.

This section has analysed topology trends of the hybrid optimisation results for the Toyota Yaris bumper system. While these conclusions are useful to establish an overview of the hybrid optimisation process when applied to an automotive industry example, it would also be beneficial to establish whether the resulting final iteration topologies fulfil the requirements stipulated by the RCAR bumper test standards. This is investigated in the following section.

6.4. Optimisation results – RCAR bumper test re-analysis

The previous section evaluated the final iteration topologies, both linear and non-linear, from a geometric viewpoint by identifying any trends in topology, identifying the influential hybrid optimisation and modelling parameters and the reasons behind the trends observed. This section evaluates the same topologies according to the RCAR bumper

test requirements. The fundamental “performance” requirement of the RCAR bumper test is for permanent damage, i.e. plastic deformation, to only occur in the bumper beam and/or crush cans.

To test the final iteration topologies obtained during the hybrid optimisation process, they are inserted into the full Toyota Yaris FE model, and the simulation is performed at the impact velocity used during the optimisation process. This in itself means that the final iteration topologies obtained with the higher impact velocity, i.e. 16 km/h, will most likely not fulfil the RCAR requirements, as the standard test is performed at 10 km/h.

The crush cans and longitudinals geometries are “smoothed” before re-analysis to remove detached elements, any major checkerboarding and essentially prepare the structure for remeshing and re-analysis. Firstly, the models are grouped together according to trends and similarities in the final iteration topologies. In total, the 96 models were separated into 26 groupings, firstly by crush can geometry (12 different crush can geometries) followed by the longitudinal geometries. Table 6.13 – Table 6.15 summarises the groupings and the models included in each grouping:

Table 6.13 : RCAR bumper test re-analysis groupings (a)

Grouping 1	Grouping 2	Grouping 3	Grouping 4	Grouping 5	Grouping 6	Grouping 7	Grouping 8	Grouping 9
BUS_M01	BUS_M04	BUS_M05	BUS_M08	BUS_M09	BUS_M11	BUS_M13	BUS_M16	BUS_M17
BUS_M02		BUS_M06		BUS_M10	BUS_M12	BUS_M14		BUS_M18
BUS_M03		BUS_M07			BUS_M33	BUS_M15		BUS_M41
BUS_M25		BUS_M29			BUS_M35	BUS_M37		
BUS_M27		BUS_M31				BUS_M39		

Table 6.14 : RCAR bumper test re-analysis groupings (b)

Grouping 10	Grouping 11	Grouping 12	Grouping 13	Grouping 14	Grouping 15	Grouping 16	Grouping 17	Grouping 18
BUS_M19	BUS_M21	BUS_M23	BUS_M24	BUS_M49	BUS_M51	BUS_M53	BUS_M77	BUS_M57
BUS_M20	BUS_M22	BUS_M47		BUS_M50	BUS_M55	BUS_M54		BUS_M58
BUS_M43	BUS_M45			BUS_M73	BUS_M56			BUS_M81
					BUS_M75			
					BUS_M79			

Table 6.15 : RCAR bumper test re-analysis groupings (c)

Grouping 19	Grouping 20	Grouping 21	Grouping 22	Grouping 23	Grouping 24	Grouping 25	Grouping 26
BUS_M59	BUS_M61	BUS_M85	BUS_M65	BUS_M67	BUS_M69	BUS_M93	BUS_M95
BUS_M63	BUS_M62		BUS_M66	BUS_M71	BUS_M70		
BUS_M64			BUS_M89	BUS_M72			
BUS_M83				BUS_M91			
BUS_M87							

Highlighted in the tables are the models re-analysed as part of each grouping. Figure 6.60 and Figure 6.61 below illustrate the “smoothing” of the crush can and longitudinal final iteration topologies prior to the reanalysis process for BUS_M25:

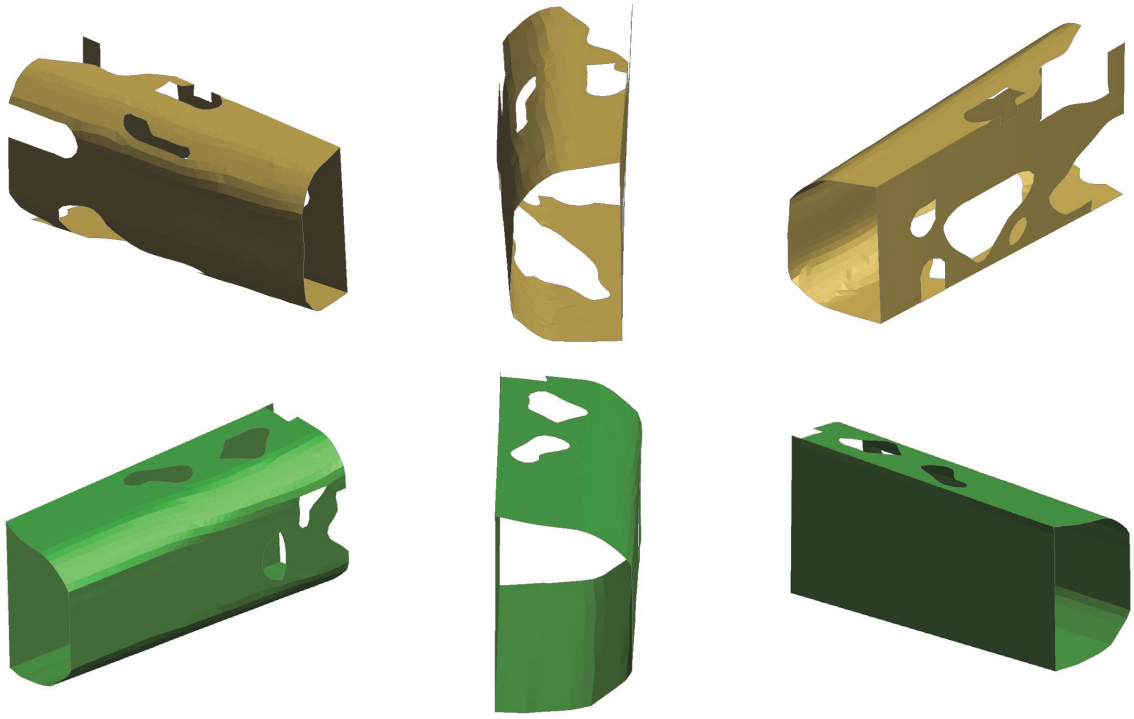

Figure 6.60 : BUS_M25 (BUS_M01) crush cans for re-analysis

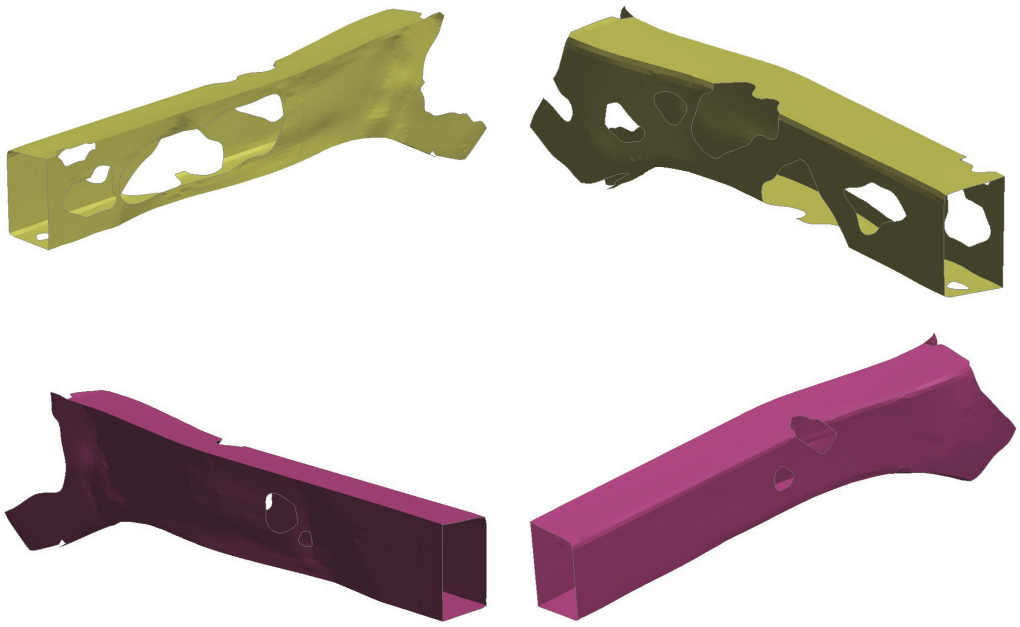

Figure 6.61 : BUS_M25 longitudinals for re-analysis

These structures should be compared to Figure 6.19 and Figure 6.57 respectively. As illustrated, the angles have been smoothed out (to avoid any excessive stress concentrations) and the detached elements have been removed, as has the checkerboard effect. Where the crush cans have displayed extensive checkerboarding, i.e. when the impact velocity was low, it has already been mentioned how the optimum load path can be difficult to determine. Without any manufacturing constraints applied, it is therefore up to the user's discretion when creating the structures for reanalysis.

Table 6.16 summarises the reanalysis data for each "low-velocity" model considered from the groupings in Table 6.13 - Table 6.15. The maximum plastic strain and maximum von Mises stress is extracted for both the crush cans and the longitudinals, as well as the volume reduction for both sections of the bumper system.

Table 6.16 : RCAR bumper test re-analysis results data (Low Velocity)

Model number	Volume reduction crush can (%)	Volume reduction longitudinal (%)	Maximum von Mises stress crush cans (MPa)	Maximum von Mises stress longitudinals (MPa)	Maximum plastic strain crush cans (%)	Maximum plastic strain longitudinals (%)
BUS_M04	15.5	14.5	782	442	23.1	1.8
BUS_M08	15.5	4.1	754	352	38.2	5.6
BUS_M09	15.1	16.5	513	463	7.7	2.1
BUS_M13	15.1	0	620	450	12.6	5
BUS_M16	15.1	4.3	640	436	12.7	4.1
BUS_M17	12.8	16.5	590	434	10	2.6
BUS_M23	12.8	8.2	438	640	3	10
BUS_M24	12.8	3.1	425	352	3.4	2.7
BUS_M25	15.5	17.8	639	520	11.2	6.4
BUS_M31	15.5	0	617	399	12.2	1.9
BUS_M35	15.1	17.4	560	465	11.5	4.5
BUS_M43	12.8	17.2	430	568	11.3	5.3
BUS_M45	12.8	3.8	520	354	3.7	3.4

Comparing the results would initially suggest that BUS_M23 is not efficient, as more plastic strain is apparent in the longitudinal than the crush cans. Figure 6.62 illustrates the behaviour of the optimised right hand longitudinal topology for BUS_M23 after re-analysis:

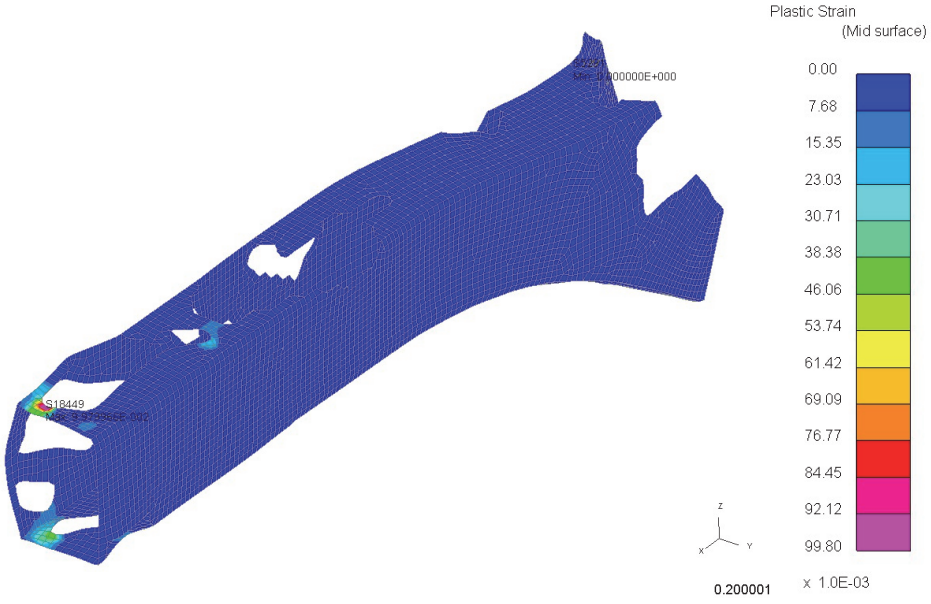

Figure 6.62 : BUS_M23 optimised right hand longitudinal plastic strain plot

As the plastic strain plot illustrates, there is a strain concentration around the hole on the top surface of the longitudinal, near the front end. While TO is an initial design phase, and shape optimisation could attempt to modify stress/strain concentration areas in the topology, there is also noticeable localised buckling near the front end of the longitudinal structure. Therefore in its current state, this structure could be deemed inefficient according to the RCAR bumper test standards.

The table also highlights plastic strain in all longitudinals. This would suggest that there is permanent damage in the longitudinals, and therefore the RCAR requirements are not fulfilled. However, the maximum value in the longitudinals (bar BUS_M23) is 6.4%, which is a relatively low value. The nature of the plastic strain must be therefore be determined, as in certain cases it may be due to a LS-DYNA *SPOTWELD connection point or as BUS_M23 displayed, localised strain concentrations around holes that could be modified through shape optimisation in subsequent design phases. Therefore, the maximum plastic strain may not be a true indicator of the overall longitudinal behaviour. Figure 6.63 - Figure 6.66 displays the behaviour of the BUS_M04 bumper system components, while Figure 6.67 - Figure 6.70 illustrates the analogous behaviour for BUS_M25, i.e. lowest and highest longitudinal maximum plastic strain, bar BUS_M23, respectively:

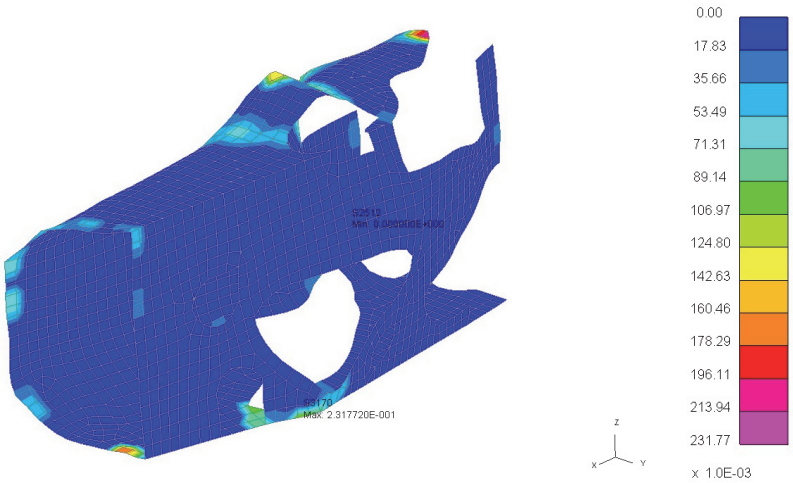

Figure 6.63 : BUS_M04 optimised left hand crush can plastic strain plot

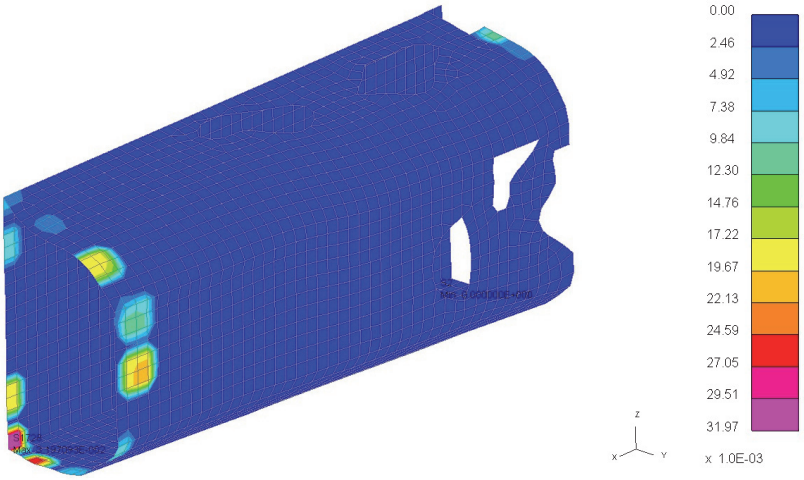

Figure 6.64 : BUS_M04 optimised right hand crush can plastic strain plot

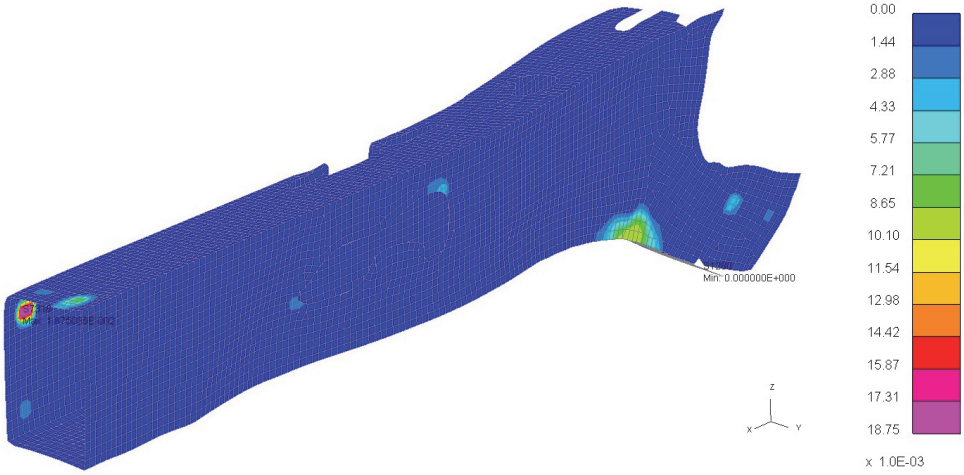

Figure 6.65 : BUS_M04 optimised left hand longitudinal plastic strain plot

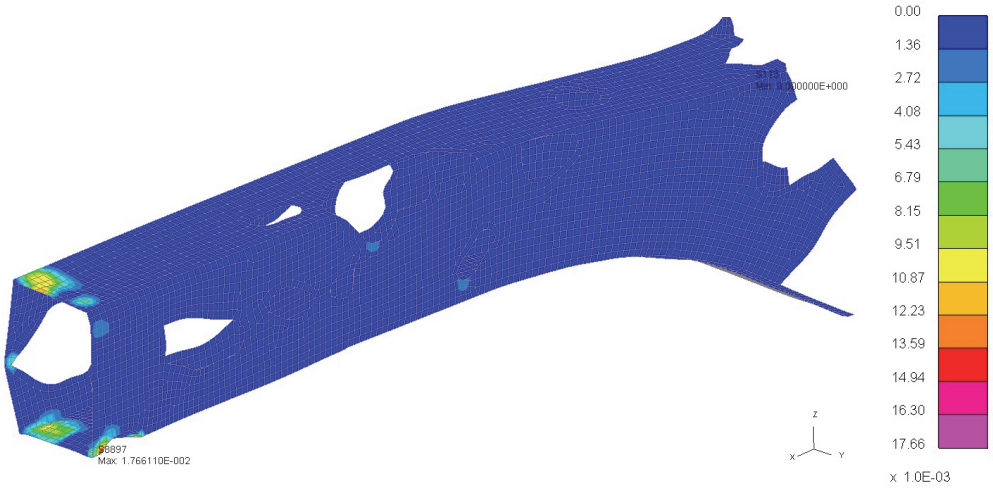

Figure 6.66 : BUS_M04 optimised right hand longitudinal plastic strain plot

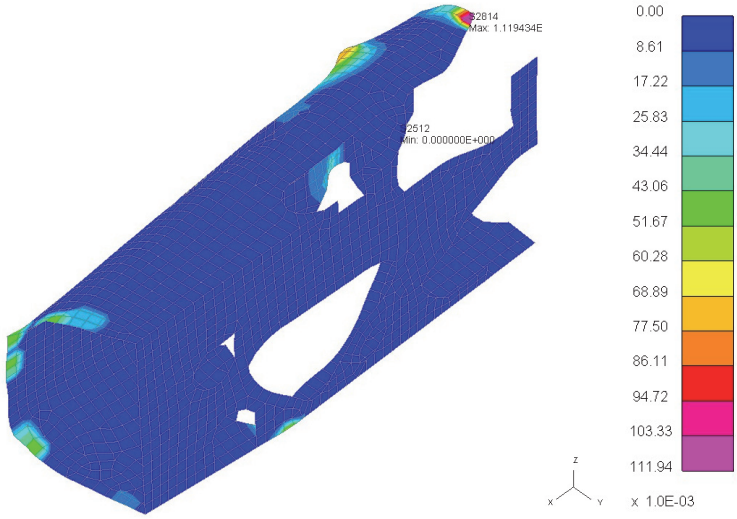

Figure 6.67 : BUS_M25 optimised left hand crush can plastic strain plot

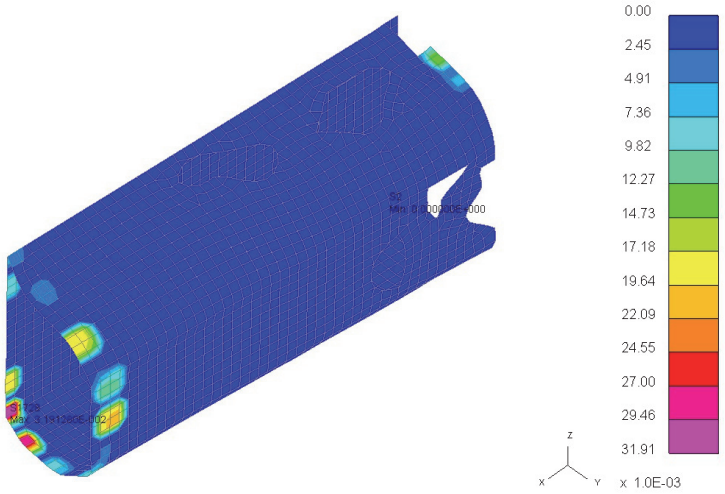

Figure 6.68 : BUS_M25 optimised right hand crush can plastic strain plot

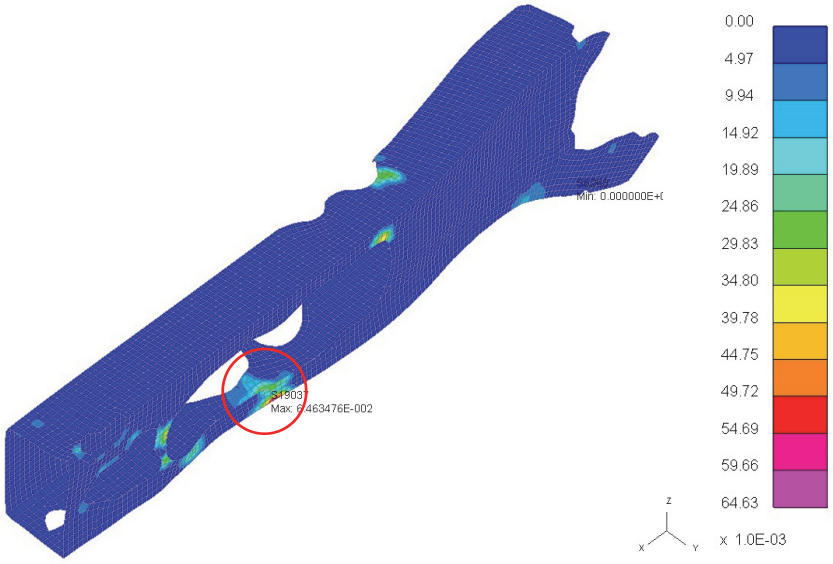

Figure 6.69 : BUS_M25 optimised left hand longitudinal plastic strain plot

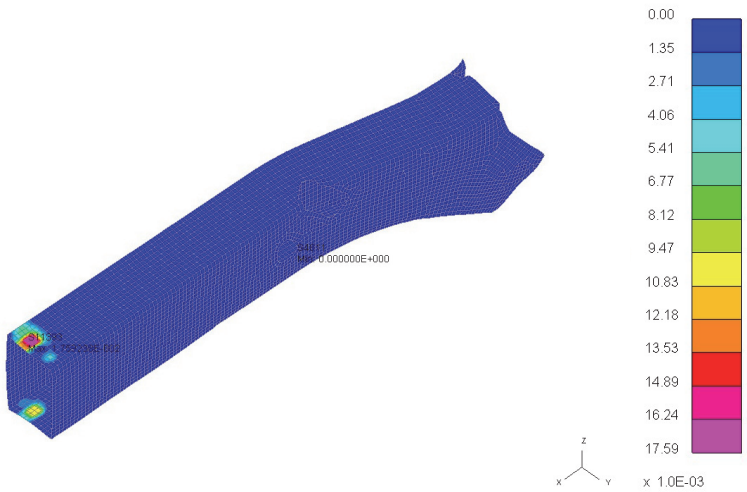

Figure 6.70 : BUS_M25 optimised right hand longitudinal plastic strain plot

Firstly observing the plastic strain plots for BUS_M04, some local buckling is visible in the left hand crush can (Figure 6.63). This however is not an issue, on the contrary this indicates that the crush can is fulfilling its role in absorbing the impact energy. Of more importance, as previously mentioned, is the location, magnitude and nature of the plastic strain in the longitudinals. In the case of BUS_M04, the maximum plastic strain in the left hand longitudinal occurs near the front end (Figure 6.65). However, this plastic strain is due to the use of a spotweld element between the longitudinal and a bracket component. Therefore it is not “representative” of the damage sustained by the right hand longitudinal, where no localised buckling is visible, but more a representation of the rigid connection between the longitudinal and bracket. The same is true of the right hand longitudinal (Figure 6.66), despite the maximum strain being located near a hole created during the optimisation process. There is also evidence of plastic strain as a result of rigid connections to bracket components. Overall the behaviour of BUS_M04 is deemed to be within the requirements of the RCAR bumper test standard. Regarding BUS_M23, there is slight evidence of buckling in the crush cans. However there is also evidence of this in the left hand longitudinal (circled in Figure 6.69). Figure 6.71 offers a close up view of this effect:

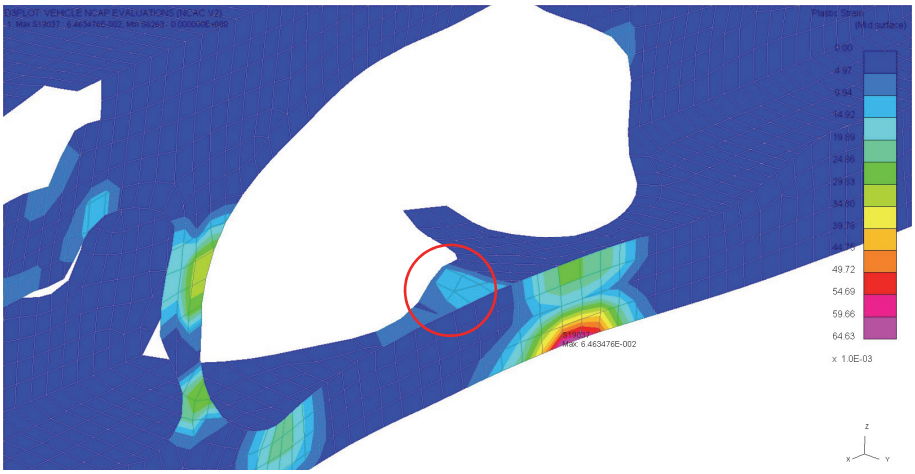

Figure 6.71 : BUS_M25 optimised left hand longitudinal localised buckling

Much like BUS_M23, the structure in this case suffers from permanent damage and therefore does not fulfil the RCAR bumper test standard. Initial observations have shown that the two models (BUS_M25 and BUS_M23) with the highest plastic strain in the longitudinals do not meet the requirements. The reason behind some of the structures' inefficiency could be the dissymmetry identified in the loading before the case study (Figure 6.12). Effectively, the volume target of 85% includes both longitudinals, however this could theoretically result in 30% being removed from one longitudinal and no material removed from the other. This could result in poor performing final iteration topologies. Table 6.17 extends on Table 6.16 by demonstrating the volume reduction, this time differentiating between the left and right hand components. The models are ranked according to the maximum longitudinal plastic strain, and the percentage difference between the left and right hand volume reduction is also displayed:

Table 6.17 : RCAR bumper test volume reduction data (Low Velocity)

Model number	Vol. reduction LH crush can (%)	Vol. reduction RH crush can (%)	Vol. reduction LH longitudinal (%)	Vol. reduction RH longitudinal (%)	LH/RH crush can percentage difference (%)	LH / RH longitudinal percentage difference (%)	Average distribution percentage difference (%)	Maximum plastic strain longitudinals (%)
BUS_M04	26.8	4.2	13	16.1	146	21	84	1.8
BUS_M31	26.8	4.2	0	0	146	0	73	1.9
BUS_M09	18.7	11.6	20	13	47	42	45	2.1
BUS_M17	18.8	6.8	15.8	17.2	94	8	51	2.6
BUS_M24	18.8	6.8	1.8	4.3	94	82	88	2.7
BUS_M45	18.8	6.8	5	2.6	94	63	78	3.4
BUS_M16	18.7	11.6	2.4	6.3	47	90	68	4.1
BUS_M35	18.7	11.6	21.2	13.7	47	43	45	4.5
BUS_M13	18.7	11.6	0	0	47	0	23	5
BUS_M43	18.8	6.8	15.6	18.8	94	19	56	5.3
BUS_M08	26.8	4.2	1.2	7	146	141	144	5.6
BUS_M25	26.8	4.2	26.6	8.6	146	102	124	6.4
BUS_M23	18.8	6.8	1.8	14.5	94	156	125	10

The table reveals two interesting aspects. Firstly, the three models with the highest average percentage difference between the left and right hand components of the structure (BUS_M08, BUS_M23 and BUS_M25) are the worst performing models. Interestingly, this is despite contrasting dissymmetries in the longitudinals for the aforementioned models. Secondly, for the rest of the models where the symmetry isn't as pronounced, there doesn't seem to be a pattern which would indicate increased dissymmetry causing poorer results. For example, for BUS_M04 and BUS_M31, which according to Table 6.16 have the lowest plastic strain levels in the longitudinals, the levels of dissymmetry in the crush cans are also the highest. Comparing BUS_M04 and BUS_M31, Table 6.17 indicates very different levels of material removal in the longitudinals (no material was removed in BUS_M31). However, what both have in common is very little dissymmetry in the longitudinals. This could suggest that dissymmetry in the longitudinals, and not the crush cans, is an important factor in the overall structural performance. However, this is not the case when comparing BUS_M45 and BUS_M43. BUS_M45 shows significantly more dissymmetry in the longitudinals than BUS_M43, but less plastic strain. This would suggest that dissymmetry is not the only issue to consider, but must be taken into account in combination with the actual amount of material removed from the structures. In this regard, BUS_M45 has much less material removed compared to BUS_M43.

Therefore, in order to identify any potential patterns between the hybrid optimisation and modelling parameters and the performances of the structures, Table 6.18 displays the parameters for the models considered during the re-analysis:

Table 6.18 : RCAR bumper test re-analysis models hybrid optimisation and modelling parameters (Low Velocity)

Model Number	Degree of non-linearity	ER (%)	Interface size (Number of elements)	Rate of exchange		Linear BC	Linear model objective	Linear model constraint
				BEETS	Optistruct			
BUS_M04	L	2.5	0	1	30	IR	Min. comp	Volume fraction
BUS_M31	L	5	0	4	30	IR	Min. mass	von Mises stress
BUS_M09	L	5	89	1	30	SPC	Min. comp	Volume fraction
BUS_M17	L	5	445	1	30	SPC	Min. comp	Volume fraction
BUS_M24	L	2.5	445	1	30	IR	Min. mass	von Mises stress
BUS_M45	L	5	445	4	30	SPC	Min. mass	von Mises stress
BUS_M16	L	2.5	89	1	30	IR	Min. mass	von Mises stress
BUS_M13	L	5	89	1	30	SPC	Min. mass	von Mises stress
BUS_M35	L	5	89	4	30	IR	Min. comp	Volume fraction
BUS_M43	L	5	445	4	30	IR	Min. comp	Volume fraction
BUS_M08	L	2.5	0	1	30	IR	Min. mass	von Mises stress
BUS_M25	L	5	0	4	30	SPC	Min. comp	Volume fraction
BUS_M23	L	5	445	1	30	IR	Min. mass	von Mises stress

These models are ordered according to the plastic strain levels in the longitudinals (similarly to Table 6.17) but also with an additional analysis on the nature of the plastic strain levels (as previously conducted on BUS_M04, BUS_M23 and BUS_M25). This resulted in BUS_M13 and BUS_M35 effectively “swapping” positions compared to Table 6.17, as the plastic strain in the longitudinals of BUS_M35 was deemed to be more “representative” of the structure’s behaviour, as illustrated by Figure 6.72 – Figure 6.73 (BUS_M35) and Figure 6.74 – Figure 6.75 (BUS_M13):

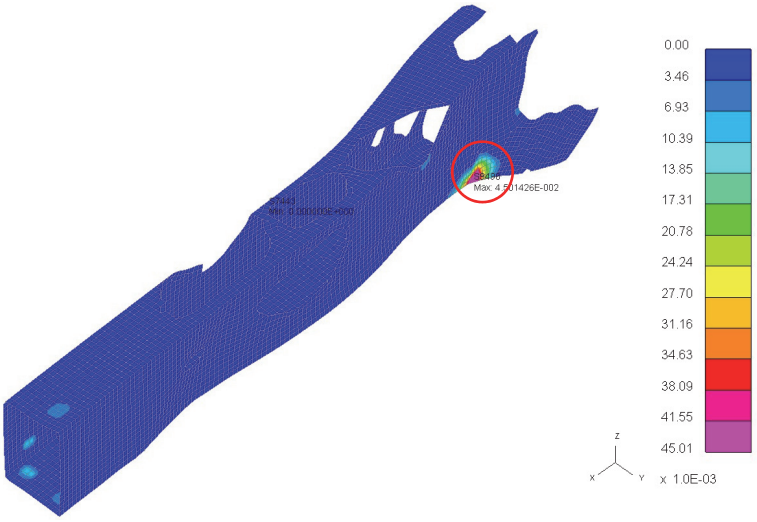

Figure 6.72 : BUS_M35 optimised left hand longitudinal plastic strain plot

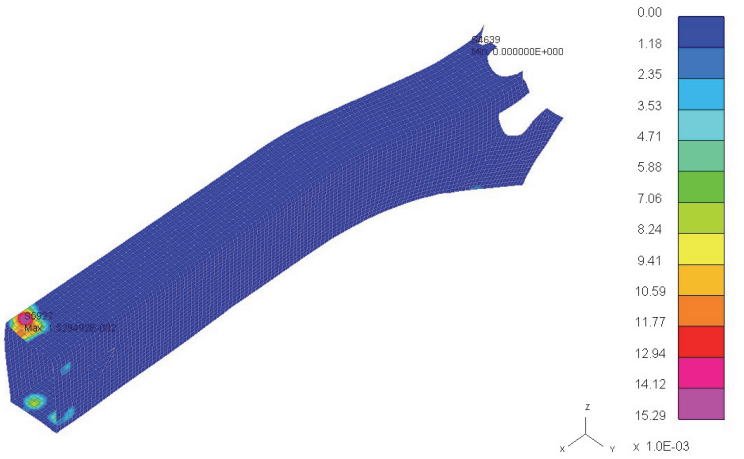

Figure 6.73 : BUS_M35 optimised right hand longitudinal plastic strain plot

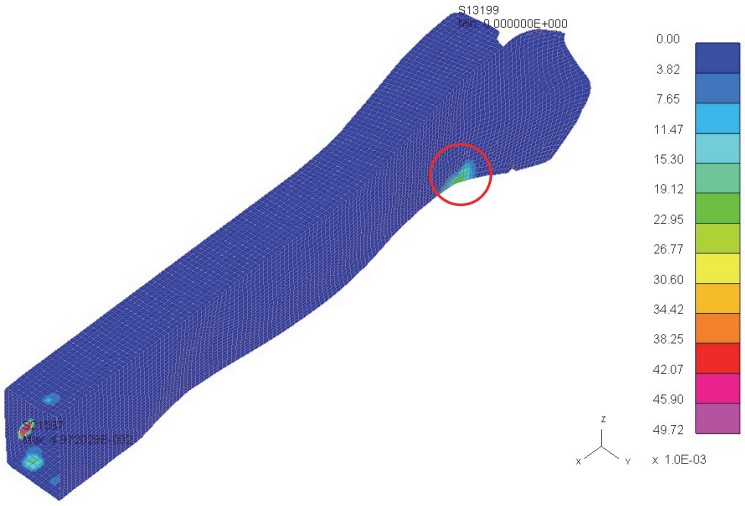

Figure 6.74 : BUS_M13 optimised left hand longitudinal plastic strain plot

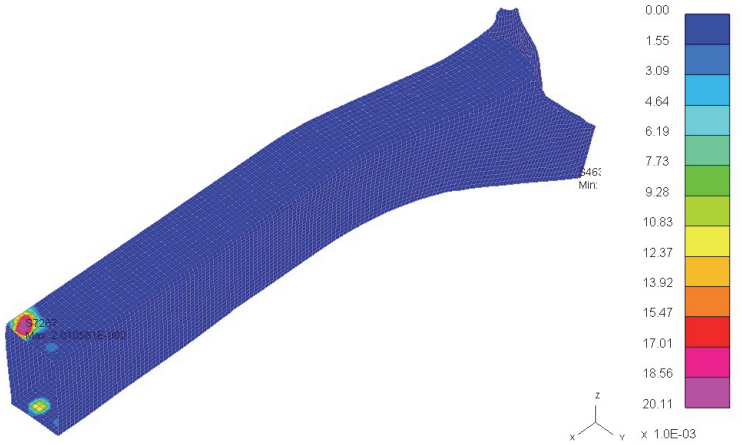

Figure 6.75 : BUS_M13 optimised right hand longitudinal plastic strain plot

The area of interest is circled on the left hand longitudinal for both BUS_M35 and BUS_M13 (Figure 6.72 and Figure 6.74 respectively). For BUS_M35, this area represents the maximum plastic strain zone, and very slight damage sustained. However, in BUS_M13, the maximum plastic strain plotted represents the connection points with the bracket, and so is not representative of the overall longitudinal behaviour. Therefore the area circled in Figure 6.74, where the plastic strain is around 2% is more representative, hence why in Table 6.18 BUS_M13 is ranked above BUS_M35.

Table 6.18 also highlights the “threshold” between models that meet the RCAR bumper standard and those that do not, i.e. the dashed line. Three interesting trends arise from this ranking and the associated hybrid optimisation parameters:

- **Trend 1:** This trend includes BUS_M08, BUS_M13, BUS_M16, BUS_M24, BUS_M31 and BUS_M45. The common trend around these models is the low or non-existent removal of material in the longitudinals (4.3% the maximum for BUS_M13). This results from the use of the “minimise mass / stress constraint” linear optimisation parameters. It has already been discussed during the geometric analysis in section 6.3.2 the effect of modifying the optimisation objectives and constraints. The majority of the models with a “minimise mass” objective displayed the same low levels of element removal as the models above. Of these models, only one was unable to satisfy the RCAR bumper test requirements. Therefore, overall it has been advantageous to include a “performance” based constraint in the optimisation process, as opposed to the “minimise compliance” case which relies solely on a final volume target.
- **Trend 2:** The second trend includes BUS_M04, BUS_M09 and BUS_M17 from the valid models, and BUS_M35, BUS_M43 and BUS_M25 from the “ineffective” models. The hybrid optimisation parameters demonstrate that there could be a link between the rate of exchange and the validity of the optimisation solutions when combined with a “minimise compliance” objective function (Table 6.18). What this trend suggests is that for a “minimise compliance” objective, but also a “volume target” constraint, exchanging the interface force data at a higher frequency has improved the performance of the final iteration topology. Interestingly this goes against the observations made in case study 1, i.e. chapter 5, where a lower rate of exchange created clearer load-paths through the 2D plate structure. There is a trade-off here, in that the final iteration topology must be clear enough to extract a geometry for future analysis or optimisation. However, enough information needs to be provided so that the linear final iteration topology reflects the evolving behaviour and configuration of the non-linear model. Even with a rate of exchange of 1, i.e. exchanging at every iteration, the final iteration topology results in the case of BUS_M04, BUS_M09 and BUS_M17 were clear enough to extract and create a geometry for re-analysis. This phenomenon will need further study in the case of more “generic” initial design volumes such as a block of solid elements, where the differences in

design due to rate of exchange modifications may vary compared to the observations of this case study.

- **Trend 3:** The final trend involves BUS_M23 and the models considered in Trend 1. As previously mentioned one of the reasons behind the poor performance of the longitudinals was the high level of dissymmetry in the final iteration topology. The crucial dissymmetry is that in the longitudinals, and as Table 6.17 demonstrates, 8.2% of the material was removed from the structure. Table 6.18 also illustrates that BUS_M23 is based on a “minimise mass” linear optimisation objective. This is interesting, as the first trend identified models with the same linear optimisation objective where the longitudinals performed within the RCAR standards. This is more a reflection of the constraint, i.e. maximum von Mises stress, than the objective function. As previously discussed, when a stress constraint is activated in Optistruct, the solver evaluates the stresses from a global point of view, and does not take into account local stresses. While this has allowed for varying degrees of volume reduction, as revealed in section 6.3.2, in the case of BUS_M23 the final iteration topology suffers from permanent deformation in the longitudinals. While this is an isolated case when observing the results from Table 6.16, other linear optimisation constraints could be considered to improve the “robustness” of the hybrid methodology.

Owing to the 50% increase in impact velocity compared to the RCAR bumper standard, the high velocity cases are not assessed in relation to the latter, but are reanalysed nonetheless to determine whether there are trends similar to the low velocity cases. Table 6.19 displays the results analogous to Table 6.16, ordered by lowest to highest maximum plastic strain in the longitudinals:

Table 6.19 : RCAR bumper test volume reduction data (High Velocity)

Model number	Volume reduction crush can (%)	Volume reduction longitudinal (%)	Maximum von Mises stress crush cans (MPa)	Maximum von Mises stress longitudinals (MPa)	Maximum plastic strain crush cans (%)	Maximum plastic strain longitudinals (%)
BUS_M53	17	6.24	749	810	110	19
BUS_M85	16.4	0	827	828	76	22
BUS_M49	17	17.4	720	871	82	32
BUS_M89	13.4	17.4	752	825	47	36
BUS_M77	17	0	750	973	94	41
BUS_M61	16.4	6	766	843	145	44
BUS_M91	13.4	16.9	733	922	34	45
BUS_M69	13.4	7.3	697	985	43	49
BUS_M81	16.4	17.3	711	851	73	50
BUS_M93	13.4	0	848	971	118	54
BUS_M95	13.4	4.7	717	980	30	55
BUS_M83	16.4	17.5	597	804	13	61
BUS_M55	17	11.4	701	850	103	63

The results, unsurprisingly, demonstrate high levels of von Mises stress and high levels of plastic strain in the longitudinals, beyond the acceptable levels. Figure 6.76 - Figure 6.79 illustrates the deformation of BUS_M53, i.e. the model with the lowest plastic strain in the longitudinals from the high velocity cases, and the levels of damage sustained by the system:

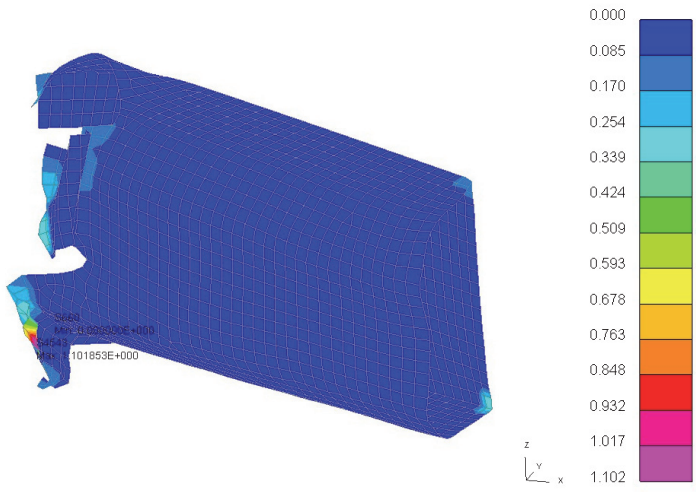

Figure 6.76 : BUS_M53 optimised left hand crush can plastic strain plot

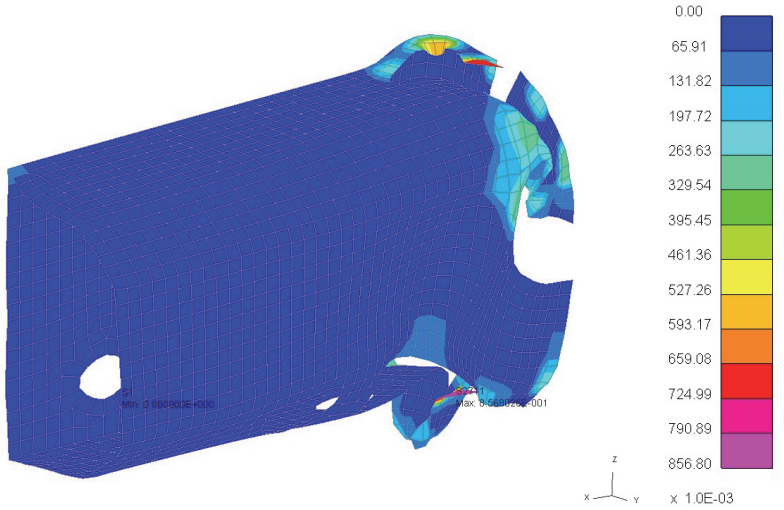

Figure 6.77 : BUS_M53 optimised right hand crush can plastic strain plot

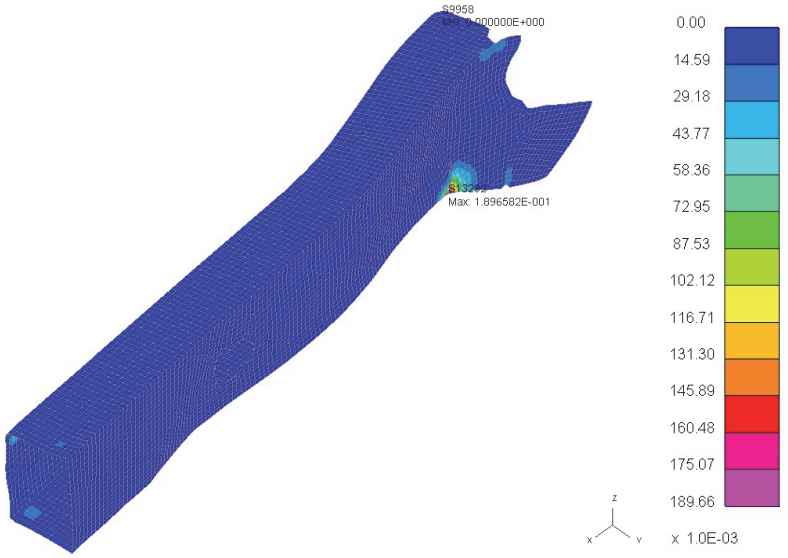

Figure 6.78 : BUS_M53 optimised left hand longitudinal plastic strain plot

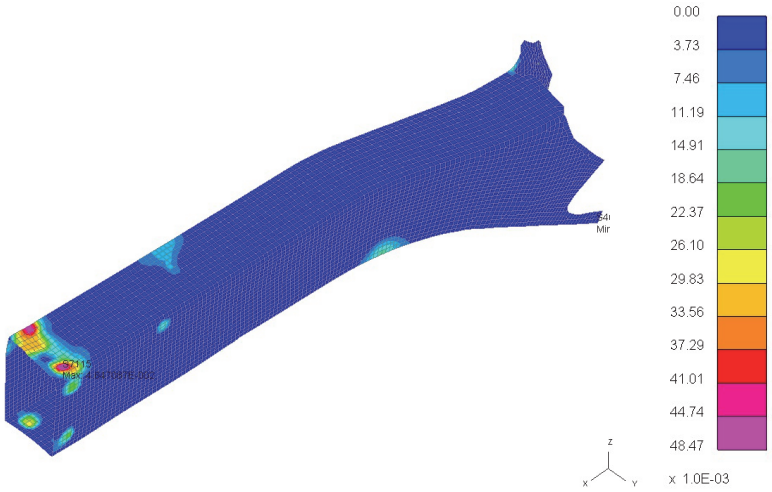

Figure 6.79 : BUS_M53 optimised right hand longitudinal plastic strain plot

The crush cans demonstrate high levels of deformation, but as previously mentioned this behaviour is acceptable and even desired. In terms of longitudinal behaviour, the results display similar behaviour to BUS_M35 and BUS_M13 (Figure 6.72, Figure 6.73 and Figure 6.74, Figure 6.75 respectfully). The left hand longitudinal displays the same plastic strain area near the rear of the crush can, but as Figure 6.80 below illustrates, the “kink” in the structure is more pronounced:

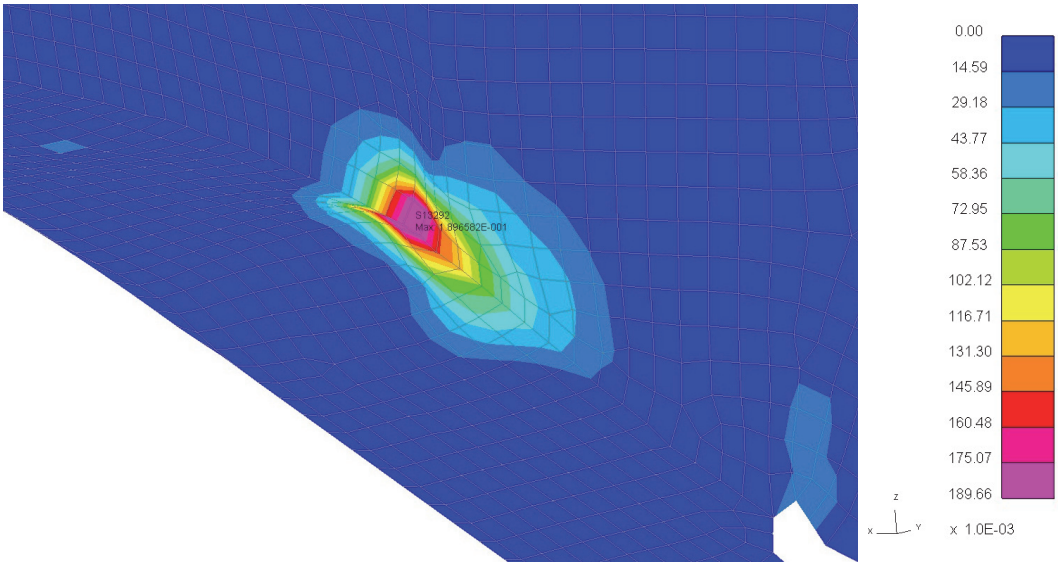

Figure 6.80 : BUS_M53 optimised left hand longitudinal maximum plastic strain area

This model represents a “minimise mass” case where very little material is removed. Conversely, where “minimise compliance” is used (and by extension more material is removed than BUS_M53). In this case, the permanent deformation sustained by the longitudinals is much larger, as illustrated in Figure 6.81 and Figure 6.82 below which displays the deformation of the left hand longitudinal for BUS_M83:

Figure 6.81 : BUS_M83 optimised left hand longitudinal undeformed

Figure 6.82 : BUS_M83 optimised left hand longitudinal deformed

This also why the final iteration topologies obtained from the higher velocity cases weren’t evaluated with regards to satisfying the RCAR requirements. However, this isn’t a surprise given the increase in kinetic energy, i.e. more than twice the energy from the lower velocity cases, and the higher velocity is beyond the scope suggested by the bumper test requirements.

Interestingly, Table 6.19 suggests very different levels of non-linearity in the longitudinals after optimisation, from 19% to 61% maximum plastic strain. Therefore, Table 6.20 lists the hybrid optimisation and modelling parameters of the high velocity re-analysis models, ordered by lowest to highest maximum plastic strain in the longitudinals (Table 6.19):

Table 6.20 : RCAR bumper test re-analysis models hybrid optimisation parameters (High Velocity) and maximum plastic strain in longitudinals

Model Number	Degree of non-linearity	ER (%)	Interface size (Number of elements)	Rate of exchange		Linear BC	Linear model objective	Linear model constraint
				BEETS	Optistruct			
BUS_M53	H	5	0	1	30	SPC	Min. mass	von Mises stress
BUS_M85	H	5	89	4	30	SPC	Min. mass	von Mises stress
BUS_M49	H	5	0	1	30	SPC	Min. comp	Volume fraction
BUS_M89	H	5	445	4	30	SPC	Min. comp	Volume fraction
BUS_M77	H	5	0	4	30	SPC	Min. mass	von Mises stress
BUS_M61	H	5	89	1	30	SPC	Min. mass	von Mises stress
BUS_M91	H	5	445	4	30	IR	Min. comp	Volume fraction
BUS_M69	H	5	445	1	30	SPC	Min. mass	von Mises stress
BUS_M81	H	5	89	4	30	SPC	Min. comp	Volume fraction
BUS_M93	H	5	445	4	30	SPC	Min. mass	von Mises stress
BUS_M95	H	5	445	4	30	IR	Min. mass	von Mises stress
BUS_M83	H	5	89	4	30	IR	Min. comp	Volume fraction
BUS_M55	H	5	0	1	30	IR	Min. mass	von Mises stress

The table above illustrates that for most of the parameters, there is no discernible pattern that emerges in terms of their influence on the structural performance of the overall bumper structure. However, observing the “lin model BC” parameter, i.e. the BCs used in the linear model, would indicate that using SPCs instead of IR results in better performing final iteration topologies, i.e. lower plastic strain in the longitudinals. This is further highlighted by comparing “analogous” models in Table 6.20 where only the “lin model BC” parameter changes. Comparing BUS_M53 with BUS_M55, BUS_M81 with BUS_M83 and BUS_M89 with BUS_M91, the three models that use SPCs (BUS_M53, BUS_M81 and BUS_M89) perform better than their IR counterparts.

To illustrate this point, Figure 6.83 - Figure 6.84 and Figure 6.85 - Figure 6.86 below depict the von Mises stress values located in the initial longitudinal designs for both BUS_M53 and BUS_M55 respectively (as both models use a “minimise mass” objective and stress constraint):

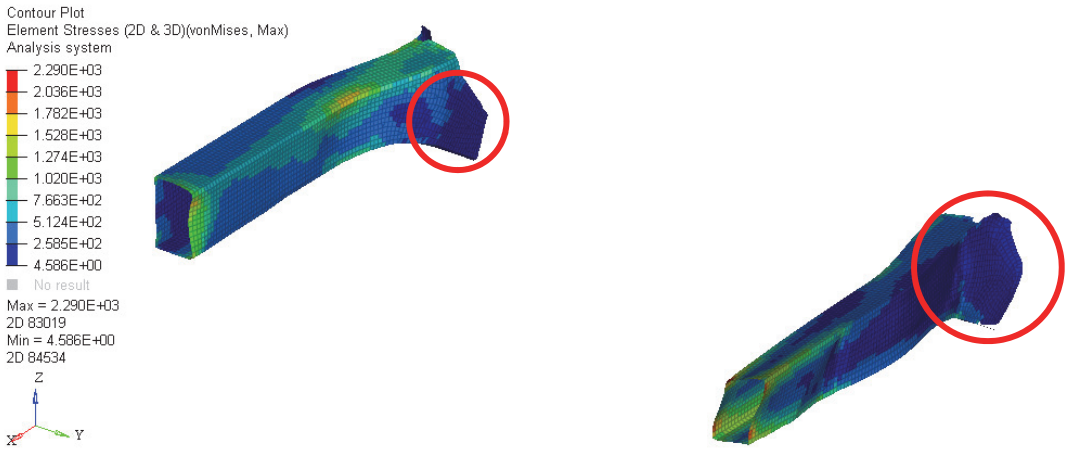

Figure 6.83 : BUS_M53 longitudinals Von Mises stress distribution (MPa) at iteration 1 (1)

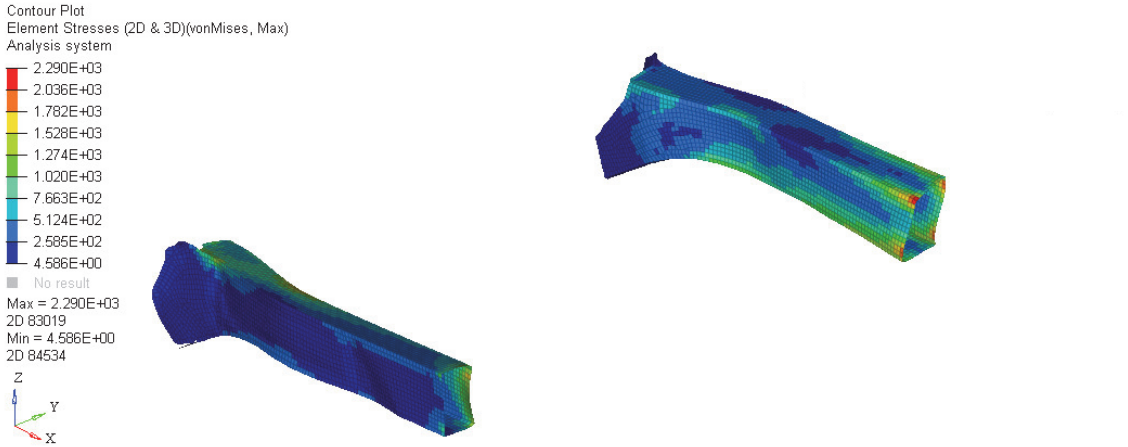

Figure 6.84 : BUS_M53 longitudinals Von Mises stress distribution (MPa) at iteration 1 (2)

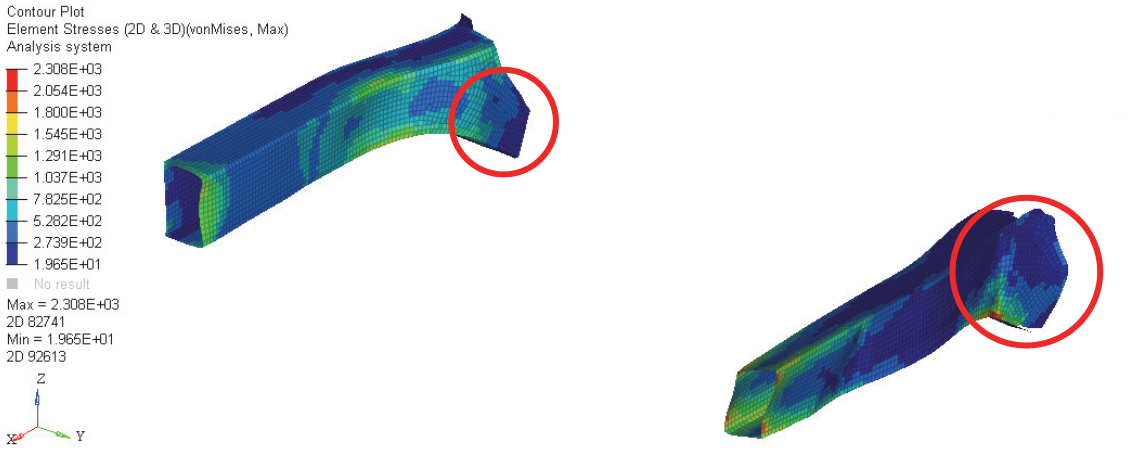

Figure 6.85 : BUS_M55 longitudinals Von Mises stress distribution (MPa) at iteration 1 (1)

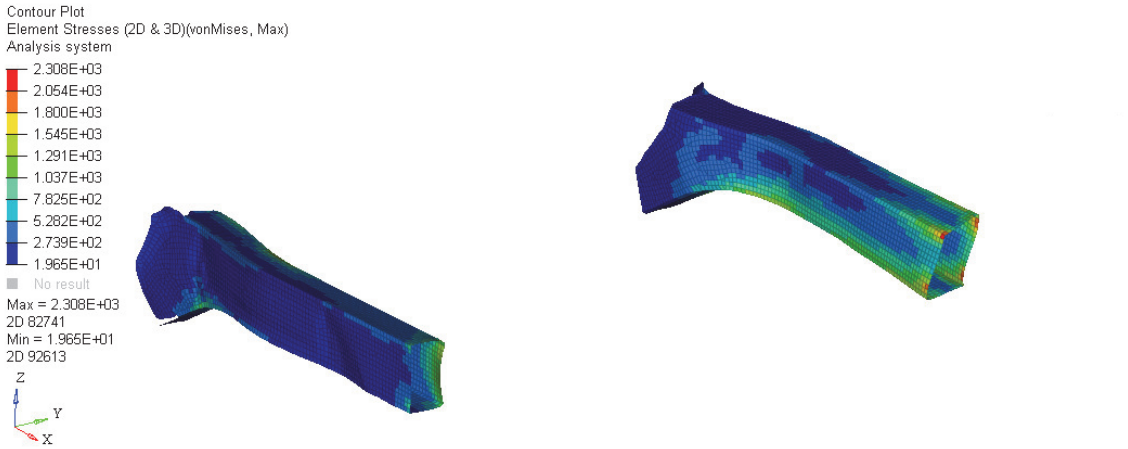

Figure 6.86 : BUS_M55 longitudinals Von Mises stress distribution (MPa) at iteration 1 (2)

At first glance, the stress distributions and magnitudes are very similar. There are some differences, as highlighted in Figure 6.83 and Figure 6.85. However, observing Figure 6.47 and Figure 6.48, i.e. the final iteration topologies for BUS_M53 and BUS_M55, demonstrates the vast difference in the longitudinal final iteration topology. One reason behind the difference could be the increase in stress levels as a result of the element removal locations in both models. Figure 6.87 – Figure 6.88 and Figure 6.89 – Figure 6.90 below illustrate the von Mises stress distribution in the longitudinals at iteration 2, i.e. after one element removal process has been performed.

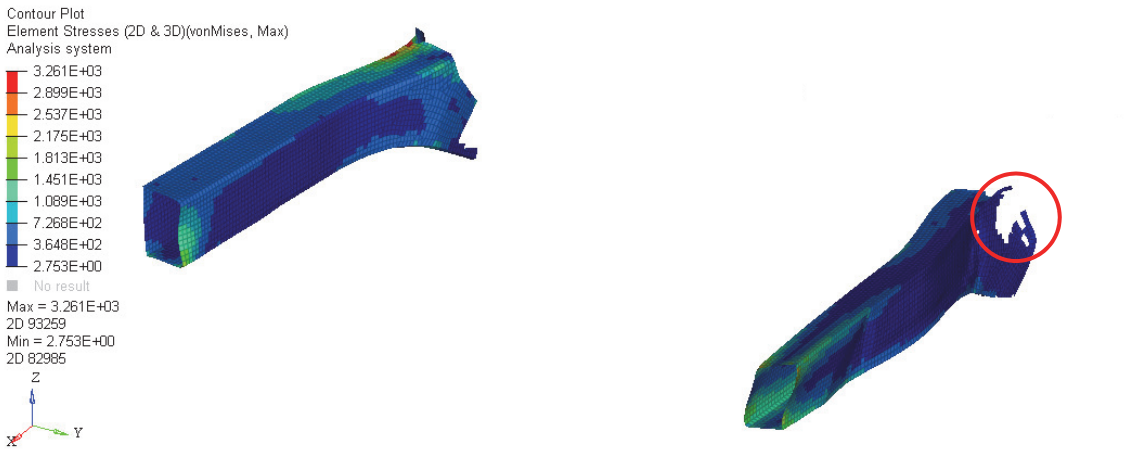

Figure 6.87 : BUS_M53 longitudinals Von Mises stress distribution (MPa) at iteration 2 (1)

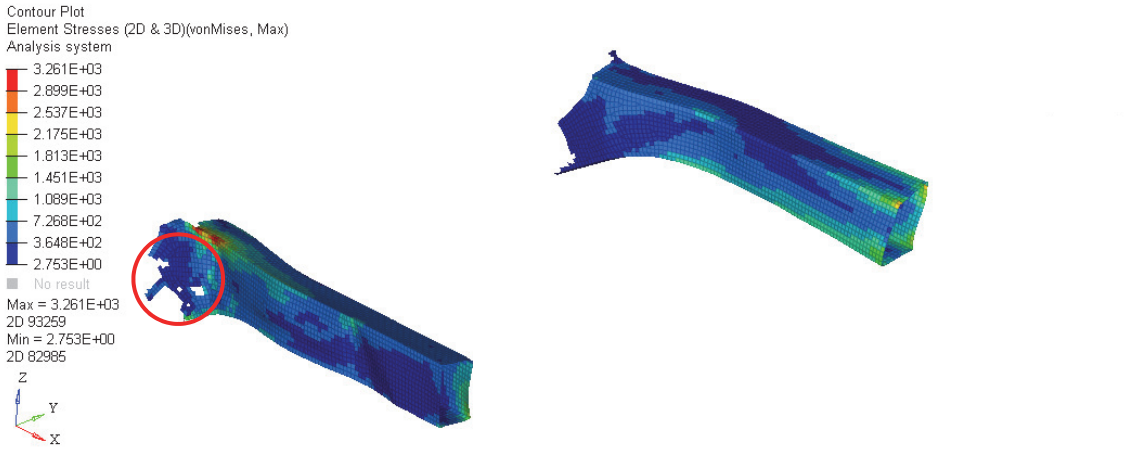

Figure 6.88 : BUS_M53 longitudinals Von Mises stress distribution (MPa) at iteration 2 (2)

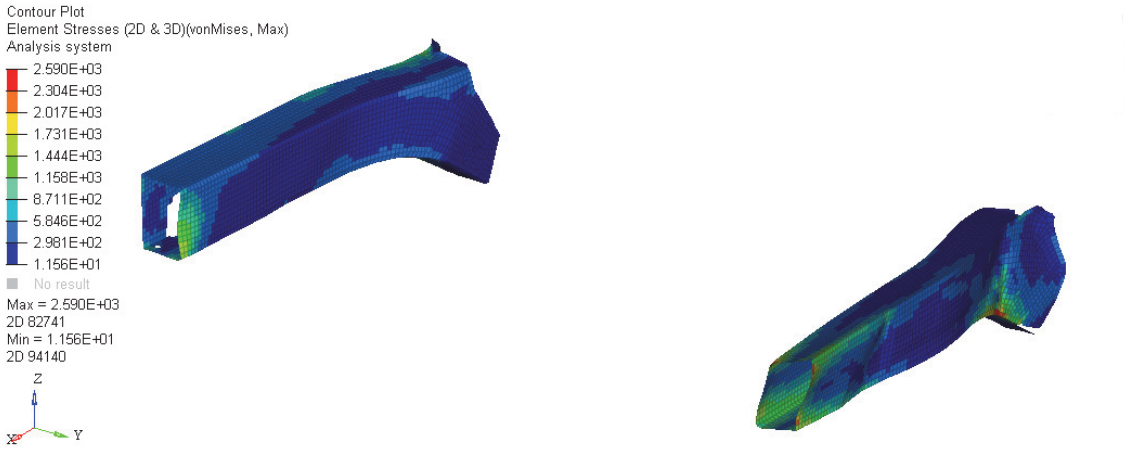

Figure 6.89 : BUS_M55 longitudinals Von Mises stress distribution (MPa) at iteration 2 (1)

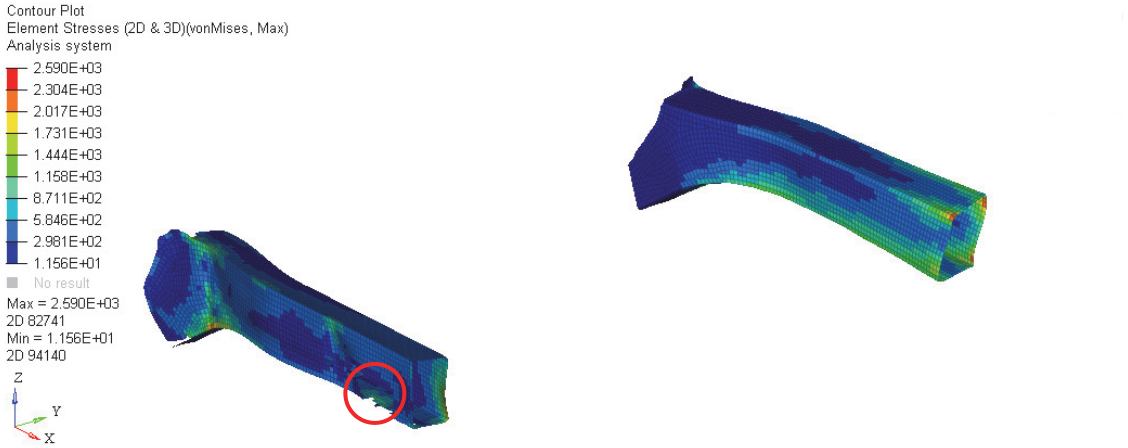

Figure 6.90 : BUS_M55 longitudinals Von Mises stress distribution (MPa) at iteration 2 (2)

The areas where the elements were removed are circled in Figure 6.87 - Figure 6.90. From these figures, it is clear that after the first optimisation iteration, elements have been removed from different location in BUS_M53 (near the rear of both longitudinals) and BUS_M55 (near the front of the left hand longitudinal). This has resulted in the similar initial stress levels illustrated in Figure 6.83 - Figure 6.86 between both models diverging, with the stress levels in BUS_M53 substantially higher. This results in the very different final iteration topologies as illustrated in Figure 6.47 and Figure 6.48 and also the different levels of total volume reduction as stated in Table 6.19. Therefore, the higher velocity cases have revealed a potential influence of the linear BCs, in that IR reduces the stress levels in the linear model throughout the optimisation process, i.e. less

"severe" than using SPCs locked in all directions, and allows for more material reduction. However, this could also be more a further indication of the limitations of using a von Mises stress limit as the sole optimisation constraint, as indicated by the low velocity cases and also Case study 1. Further study could therefore be conducted to determine whether the use of a second constraint, such as a global compliance or local nodal displacement values, could improve the robustness of the linear optimisation portion of the hybrid methodology.

6.5. Conclusion

This second case study has analysed the hybrid optimisation methodology developed during this PhD within the context of a real-world crashworthiness problem. This has allowed for further observations relating to the hybrid optimisation parameters considered after case study 1. These findings are summarised below:

- ***Interface size:*** The crashworthiness example selected for this case study indicated the interface size had very little influence on the final iteration topology. The location of the removed elements however were globally located within the same region (as illustrated for example by the similarity in BUS_M09 (Figure 6.21) and BUS_M17 (Figure 6.23) visually and in terms of performance), with an offset governed by the non-design volume. This is in contrast to the findings of case study 1, where the interface size, when too large, did have an effect on the final iteration topology. This would suggest that, while this parameter can be important in the context of hybrid optimisation, it is also model-dependent, and therefore requires the good judgement of the user in defining an interface size that isn't too restrictive.
- ***Degree of non-linearity:*** The degree of non-linearity, which alludes to the impact velocity, had a large influence on the hybrid optimisation methodology. Firstly, this parameter impacted the clarity of the crush can optimisation results, where a higher velocity significantly reduced the presence of checkerboarding and detached elements. From an engineering point of view, this facilitated the post-processing of the results and the extraction of the optimum load paths. However, as demonstrated by the strain tensor study in section 6.3.1, the impact velocity is not the only influence, but also the absence of a "dominant" loading direction, making it difficult for the BEETS algorithm to make an informed decision on the

deletion of elements. At higher velocity, the optimisation results became clearer, and the degree of non-linearity's influence was increased, as it dictated the direction of mass reduction with little influence from the other hybrid optimisation and modelling parameters. Early indications would suggest this isn't confined to non-linear optimisation, as illustrated by the force input differences in the longitudinals at low (Figure 6.52) and high (Figure 6.53) velocity and the resulting stress plots (Figure 6.54 - Figure 6.56).

- ***Rate of exchange:*** The rate of exchange demonstrated conflicting influences when comparing the clarity of the optimisation results against the performance. Based on a visual interpretation of results (e.g. Figure 6.42 compared to Figure 6.57), a lower rate of exchange, i.e. more non-linear optimisation loops before exchanging the interface force data, created clearer topologies. As suggested during case study 2, this could be caused by the exchange of data only taking place once the non-linear topology has become well defined, and therefore the load input into the linear optimisation process is also better defined. Essentially, the lower rate of exchange in this case, i.e. every 4 non-linear iterations, resulted in only a single linear optimisation process taking place. Therefore, this value essentially evaluates performing both optimisation processes "separately". However, from a structural performance viewpoint, the "better" final iteration topologies, i.e. more resistant to deformation, were mainly obtained (from the low velocity cases) when the interface force data was exchanged after every non-linear optimisation iteration (where a minimise compliance / volume target was used for the linear optimisation process). This is an indication of the need for the hybrid methodology developed throughout this PhD, as the increased link between the two optimisation solvers / models has produced a more efficient final iteration topology when subjected to the RCAR bumper test standard.
- ***Linear model optimisation parameters:*** In the previous chapter, two different combinations of linear optimisation parameters were analysed: minimise compliance subject to a volume constraint and minimise mass subject to a von Mises stress constraint. The results were reflected in case study 2. This in itself isn't a surprise as the mechanisms for element removal are the same. For a "minimise compliance" objective, the elements in the linear structure are removed to reflect the ER in the non-linear optimisation process. For a "minimise mass" objective, as much material is removed subject to a stress constraint. The results demonstrate that once again, less volume is removed from the linear structures

when a performance based constraint, i.e. von Mises stress, is included in the optimisation process. By extension, the majority of the models with a "minimise mass" objective and stress constraint that were re-analysed satisfied the RCAR bumper standards. However, BUS_M08 and BUS_M23 illustrate that this isn't consistent. This is due to the fact that, as stated by (Altair 2017), the stress constraint doesn't cater for local stresses. To improve robustness, future work could determine whether the stress constraint could be paired with another constraint, such as local nodal displacements or component compliance values.

- ***Linear model BCs:*** This parameter had a greater effect upon the results of models with higher non-linearity, i.e. higher impact speed, cases. The two linear model BCs analysed were SPCs and IR. As an example, consider Figure 6.83 - Figure 6.90, which represents the results from an IR model (BUS_M55) and an SPC model (BUS_M53). From the results of the former, it can be seen that in initial iterations, elements are removed in different locations (compared to the latter), causing the optimisation topology history to become vastly different. IR had a tendency to remove material towards the front and rear of the longitudinals, where the loading occurs and the connection to the firewall is located respectfully. This phenomenon is amplified when using a "minimise mass" objective, as the element removal also depends on the stress constraint specified. IR was able to remove more material (as the stress levels were reduced), however in the high velocity load cases this wasn't beneficial. It should however be noted that none of the high velocity cases satisfied the RCAR bumper test as the impact velocity was higher than that prescribed by the standard. Conversely, at lower velocity there was no discernible trend regarding the linear BCs. These observations do not dismiss completely the use of IR. It could be that IR isn't adapted to component level optimisation, or in this case it could be that, due to the size of the firewall compared to the longitudinals, SPCs better represent the spotweld connections.
- ***Evolutionary ratio (ER):*** The effect of the ER was analysed in case study 2 using two values, 5% and 2.5%. In this instance, the reduction of the ER, had very little effect on the final iteration topology. Essentially, as demonstrated in chapter 3, the reduction of the ER can allow for greater "feasibility", i.e. avoiding disconnections within the topology, of the non-linear topology by not removing as many elements in a single iteration. However, as the 5% iterative volume reduction is shown to be stable enough, further reducing the ratio has very little

effect as it offers no consistent improvement in the structural performance of the bumper system, at a cost of increasing the run time of the process, i.e. 4 hybrid optimisation iterations for ER = 5% against 7 for ER = 2.5%. Overall, this means that the ER should be set at the highest possible "stable" value, which offers the best performance vs CPU time compromise. Throughout this PhD, and as seen in the literature review, a value of 5% has consistently offered a stable optimisation process and is therefore suggested as an initial value to consider when running the hybrid optimisation process.

A limitation of this study is the relatively coarse mesh size used for the FE models. The mesh size used for the longitudinals and crush cans was the same as the original in the Toyota Yaris model, i.e. 7mm. For the purposes of TO, a smaller mesh size could have allowed for greater "freedom" in the optimisation process by generating a larger number of design variables and helped create topologies with a greater resolution. Furthermore, as mentioned throughout this chapter, the longitudinals displayed stress concentrations in several examples as a result of the mesh resolution. However, two important points highlight why the mesh size was kept at 7mm. Firstly, mesh size is important in explicit FEA in determining the timestep of the analysis, and by extension the CPU time. This limits the possibility of reducing the mesh size. More importantly however, is the CPU time of the BEETS solver when analysing element information. The BEETS solver is very sensitive to the number of design variables, i.e. number of elements, owing to a large number of "for" and "while" loops that scan all elements/nodes within it. The CPU time is difficult to determine with this case studies, as the LS-DYNA analysis was run on a HPC, and in some instances the FE analysis can be "queued". However, taking the example of BUS_M01, the total run time was approximately 6h and 30 minutes. The Optistruct optimisation process run time is insignificant compared to the total run time (around 11 seconds per iteration for a total of 4 iterations). The total LS-DYNA FEA run time, across all iterations, is approximately 104 minutes or around 1h and 40 minutes. What this means is that the remaining 5h is assigned to sorting and manipulating the element/node data, despite a relatively small design volume (a total of 2682 elements for the crush cans and 8582 elements for the longitudinals). Firstly, part of this issue could be down to the efficiency of the programming, and future development of the tool could improve its performance. Additionally, another potential avenue for future work, the use of so-called "Super Folding Elements" or SFEs (Hanssen et al. 2007) and the "Macro Element Method" (Georgiou and Zeguer 2017), could be explored. In essence, the methods can

be applied to thin-walled structures to predict their folding behaviour during impact without the use of finite elements and are especially useful in early design phases. Therefore the run time is significantly less than that of FEA. In the context of the work done throughout this PhD, SFEs could be used in combination with BEETS, in which case only areas of interest would need to be modelled in FEA for the optimisation solver (for example at the interfaces), and the rest of the model could use SFEs, saving on CPU time.

It must also be reiterated that the bumper system was subjected to a higher velocity than stated in the RCAR bumper test standard, i.e. 16km/h for the higher velocity cases. Despite this limitation, it allowed conclusions to be made about the effects of increased non-linearity on the hybrid optimisation process, specifically the BEETS algorithm.

Finally, as mentioned in the earlier discussions in this chapter, the bumper study is not representative of structures where TO would typically be employed. TO is a tool used for initial design generation, however the crush cans and longitudinals evaluated were already well developed structures. As a result, the crush cans and longitudinal structures were simplified to remove stiffening topography, swages and connect the two sections making up each component into a single, “box-like” section. At this point, it is important to discuss the feasibility of optimising the original, well-developed crush cans and longotudinals, In essence, this would have been possible, subject to some further considerations. The sections making up the components are attached via spotweld elements, as shown by Figure 6.91 below:

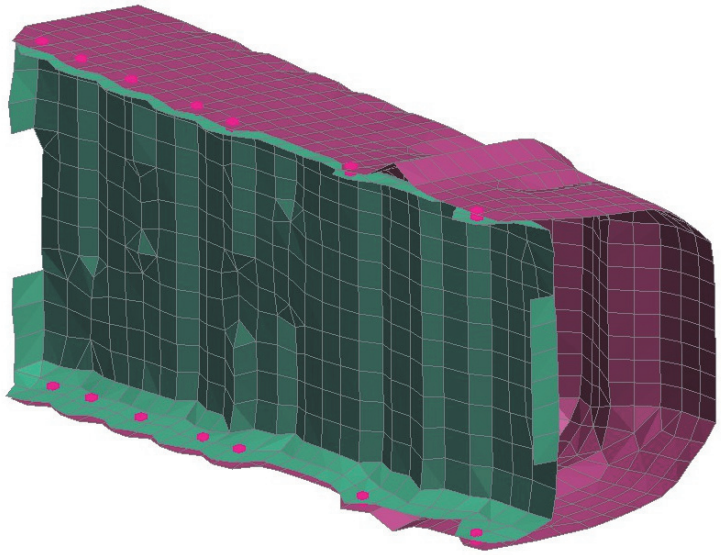

Figure 6.91 : Original Toyota Yaris crush can with spotwelds

There would be several options to cater for the spotwelds. They could be considered fixed, and therefore the surround shell elements either side of the spoweld would become non-design. The second option would be to allow the deletion of the spotwelds, which in this case would require an extra step to monitor the connecting shell elements, with a spotweld "status", similar to the statuses of the individual cross sections. The swages and stiffening "shapes" would be able to be catered for without modification of the code, as they are simply shell elements like the simplified components. However, as previously discussed, the aim of simplification of the components was to "mirror" more typical initial design volumes. Therefore, this bumper study was sufficient as a proof of concept of the hybrid methodology.

The credibility of the optimised designs must also be discussed. This relates back to two main points, the use of TO and the loadcase. As discussed above, the structures were simplified for TO as it is typically a tool used in initial design phases. However, the swages and crush initiators removed are critical to the controlled energy absorption capabilities of the components (Christensen and Bastien 2015). These features would be expected to appear through further design refinement iterations. The topology optimised designs obtained in this chapter should therefore be considered as "main" loadpath suggestions requiring refinement.

Secondly, the structures obtained fulfil to varying degrees the RCAR requirements at 10 km/h. However, the designs are specific to that loadcase and therefore it is unknown what the performance would be like at higher velocities, such as the Euro NCAP full frontal 64 km/h test. This is specifically true for the longitudinals, as the crush cans have little load bearing capabilities in such scenarios. The longitudinals are one of the main loadpaths and energy absorbing structures in such an event. Due to the very different levels of non-linearity, differences in strain rate, it is an entirely different problem to consider for TO. Therefore, it can only be concluded that the credibility of the optimised bumper systems obtained in this chapter is limited to the RCAR bumper test selected.

Overall, the hybrid methodology throughout this PhD has shown potential in providing lightweight and safe vehicle structures when applied to an RCAR bumper test example. The following chapter will present possible future directions of the research.

8. Conclusions

This PhD has presented the development and implementation of a hybrid topology optimisation (TO) methodology for vehicle structures. This chapter summarises the overall findings and contributions to knowledge.

An evaluation of current, commercially available TO algorithms was conducted (Chapter 3) which specifically focused on the lack of capability for dealing with coupled linear/non-linear behaviour. Following this, a novel hybrid optimisation methodology was presented (Chapter 4) which included creating and implementing within a Powershell program "hybrid optimisation parameters", focusing on the interface between the linear and non-linear solvers. A benchmarking study regarding these hybrid optimisation parameters was then completed (Chapter 5), where a total of 108 simulations were performed and analysed to determine the parameters that influenced the final topologies the most. Validation of the need for the novel hybrid methodology was given (Chapter 6) by applying it to an industry relevant scenario, a low velocity bumper test developed by the Research Council for Automotive Repairs (RCAR). The contributions to knowledge addressing the objectives of this PhD are summarised below:

- Investigation into limitations of current TO methodologies for optimisation of combined linear and non-linear behaviour (Chapter 3)
- Development of a novel, hybrid methodology for TO (Chapter 4), proof-of-concept benchmarking (Chapter 5) and application to relevant, industry-based case study (Chapter 6).
- Demonstrated advantage of simultaneous linear and non-linear optimisation, challenging current methods of considering the optimisation processes separately (Chapter 5 & 6).

The main benefit of the hybrid methodology relates to the CPU time. As discussed in Chapter 5, the relative analysis times for the FEA are very different. An LS-DYNA analysis for case study 2 takes approximately 1h40, with the linear FEA terminating after 11 seconds. The gains could potentially be larger if expanding to topology optimisation of solid element structures, as solid elements require a smaller timestep compared to shell elements (Jacob and Goulding, 2002). Therefore, using the hybrid methodology developed throughout this PhD, only the necessary components / systems would need

to be modelled in explicit FEA and optimised using non-linear TO and by extension the consequences of the smaller timestep could be reduced.

There is, however, a limitation compared to using a fully explicit, non-linear model as opposed to the hybrid process. As there are two models in the latter (i.e. linear and non-linear), there must be a change in how the non-linear model is setup to account for this "separation". For example, in case study 2 the "compliant" longitudinals in the bumper system were replaced by rigid connections. This adds artificial stiffness to the response, but may also modify the stress wave propagation through the structure. Therefore, this needs to be taken into consideration when comparing the analysis responses, and ultimately, the optimisation results. Further work on the interface boundary conditions could be conducted to help alleviate the additional stiffness "issue".

By using the hybrid process, it could also be possible to use different objectives for the different models. For example, energy absorption / compliance could be maximised for the non-linear structure, subject to a volume or displacement constraint. The linear structure could however use a minimum compliance case, i.e. maximise stiffness, which in essence would be the opposite the non-linear objective. Presently, LS-TaSC only provides a single objective function, i.e. achieving a uniform internal energy distribution (Livermore Software Technology Corporation, 2013), with displacement constraints possible for stiffness. Therefore, hybrid optimisation could potentially open up in the future avenues for multi-objective or even multi-disciplinary optimisation.

Overall, the main conclusion from the body of work conducted is that a hybrid TO methodology, combining linear and non-linear optimisation within the same process, can be advantageous, highlighting the importance of work in this field. The work has also uncovered several exceptions to this conclusion underlining that additional work is required, and perhaps a "rethink" as to when and how these methods are applied in the pursuit of obtaining lightweight and safe vehicle structures. It was found that the most influential optimisation parameter upon the "usefulness" of TO results is the rate of exchange between the linear and non-linear models/solvers. An increased exchange between linear and non-linear solvers improved structural performance when analysed against the RCAR standard requirements (case study 2).

Case study 2 also uncovered that the non-linear optimisation process (Bi-directional Evolutionary Entropy Tabu search Simulated Annealing or BEETS) suggested clearer topologies at higher impact velocities due to a greater difference in strain distribution

throughout the structure. This is an important finding and, as mentioned in the previous chapter, will constitute a main axis of future work for the hybrid optimisation methodology.

7. Future Work

The work produced throughout this PhD has revealed some areas of interest for future development. These are separated into two parts. Firstly, there are areas of future work relating to the improvement of the methodology's robustness and versatility. Secondly, there are areas of future work in terms of the application of the hybrid methodology.

7.1.1. Future work – hybrid methodology versatility and robustness

Overall, the two case studies demonstrated the potential in applying the hybrid methodology within a vehicle crashworthiness context. However, the current version of the Bi-directional Evolutionary Entropy Tabu search Simulated annealing (BEETS) algorithm, i.e. the non-linear optimisation aspect, operates on a final target volume criteria, and the optimisation process removes elements with the lowest strain. In order to enhance the capabilities of the methodology for crash structures, additional constraints could be considered, such as maximum allowable acceleration levels, and/or maximum displacement values. This could also be extended to the linear optimisation process, which can currently manage a minimise mass or minimise compliance objective, with stress or volume targets respectfully. This could be implemented using the constraints / objectives featured in the Optistruct package, and incorporating them within the hybrid methodology.

As concluded in Chapter 5, the "zero length beams" interface BCs could be investigates further if an automation of the BCs creation process is implemented. This would allow the verification of initial results that indicated "compliant" BCs at the interface could increase energy absorption. There are some limitations to these findings, specifically that the energy absorption indicated was from a "component" point of view. A measure of Specific Energy Absorption (SEA), where the internal energy is divided by the mass of the structure, could be more indicative. For example, models with similar plastic strain results PS_M11 (SPCs) and PS_M75 (variable zero length beams) resulted in internal energy values of 238.04J and 241.35J respectively. However, when taking into account their respective masses, both obtained SEA values of 514J/kg. Furthermore, as previously mentioned, typical structures would have smoothed boundaries as opposed to the "sharp" edges obtained from element removal which could have had an effect on

the results. Therefore this, and BCs in general, will constitute an important avenue of future work and analysis for the hybrid methodology.

One of the interesting aspects revealed throughout the case studies was the link between the rate of exchange and the evolutionary ratio (ER), when a “minimise compliance / target volume” combination is used in the linear optimisation model. For example, when ER is set to 2.5%, in order to reach the target volume of 85% in case study 2, the non-linear optimisation process (BEETS) requires 7 iterations. In the case where the rate of exchange is set to 4 for case study 2, i.e. the interface force data is exchanged every 4 non-linear iterations, the linear optimisation process will only occur once. The volume target for the linear optimisation process will be set to four times ER (as it occurs after 4 non-linear iterations), which in this instance would be 90%. As the linear optimisation process only occurs once, the final linear structure will only be 90% of the initial volume, despite the overall target volume of 85%. Therefore, a modification needs to be made to reflect the link between rate of exchange and ER. This could be that, after the final non-linear iteration occurs, a final linear optimisation process is “forced”, which would remove any remaining material necessary to reach the overall final target. Another proposal could be that the rate of exchange is not a direct user input, but a selection from algorithm suggestions, where the ratio between the number of non-linear iterations to reach the volume target and the rate of exchange is an integer, i.e. a linear optimisation process will occur at the final iteration.

The crush can structures, and indeed the 2D plate structures, optimised using the BEETS algorithm displayed some instances of detached elements. One improvement to the BEETS algorithm could be to detect these detached elements before any other elements within the structure are removed, and those detached elements be eliminated. This would of course improve the clarity of the optimisation results produced, but it could also have an impact on the hybrid methodology. By having clearer structures, the load paths also become clearer and by extension, the forces exchanged at the interface could produce better results in the linear optimisation process. This process could also be applied for Optistruct, to eliminate the detached structures that appeared on some occasions during both case studies and resulted in error terminations the following linear iteration.

7.1.2. Future work – applications of the hybrid methodology

Case study 2 revealed that, at low velocity, the resolution of the results was quite poor, i.e. very little difference between strain results, which create problems in terms of checkerboard effect. Therefore, an area of future work could be to modify the way in which the hybrid methodology functions, by having the program switch between either linear or non-linear optimisation, depending on certain performance criteria. A good example of the merits of such an application would be the optimisation of a typical 3D block of solids, such as illustrated in Figure 7.1 below.

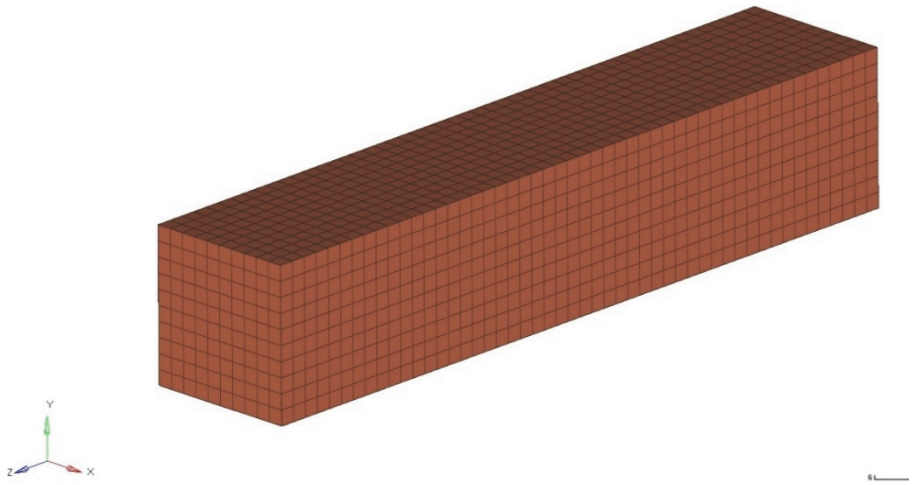

Figure 7.1: Example block of solid elements

Even if the final optimised structure must behave in a non-linear manner, the initial design volume even under impact will not behave in a non-linear manner. Furthermore, the further away an element is from the impact area, the less varied the strain data will be compared to neighbouring elements, which of course determines which elements are removed from the non-linear structure. Therefore, initially, linear optimisation could be run, until a certain threshold is reached (Yield strength or strain levels). At that stage, the hybrid methodology could automatically switch from linear to non-linear optimisation, until the overall objective is reached.

Another possible axis of future work for the hybrid methodology resides around novel thin-walled crash structures. These box-like thin-walled structures contain internal “cells”, as illustrated by Figure 7.2 (Duddeck et al. 2016).

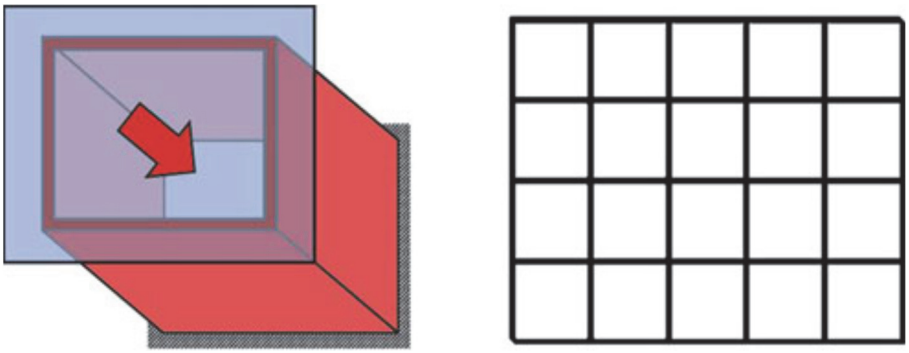

Figure 7.2: Rectangular box-section with internal "cells" (Duddeck et al. 2016)

The thickness of these cells is modified to find the best thin-walled structure “cross-section” for crashworthiness applications. An example of such a cross section from Duddeck et al. (2016) is illustrated in Figure 7.3 below

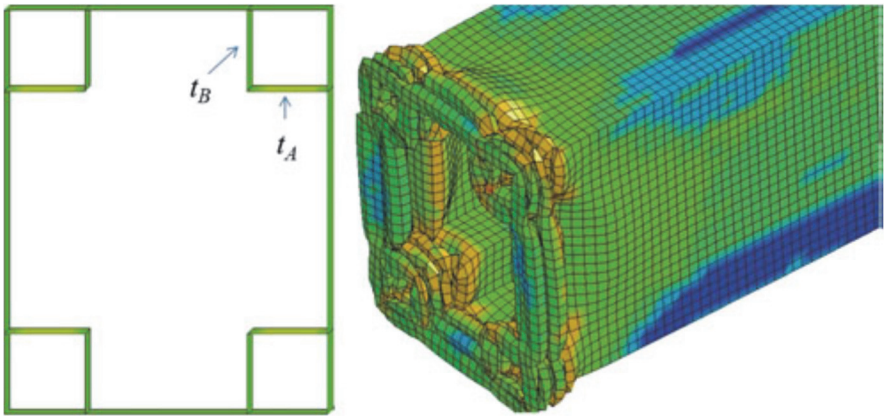

Figure 7.3: Example optimised cross section of thin-walled structure and crashworthiness behaviour

This setup essentially increases the design space, while retaining the possibility of using 2D elements, thus reducing the run time compared to 3D elements and initial design volumes as illustrated by Figure 7.1. The use of the hybrid methodology could be interesting, as the non-linear optimisation solver BEETS is a hard kill method, which could provide different results compared to the Hybrid Cellular Automata (HCA) method used by Duddeck et al. (2016). As only the inner “cells” are modified, i.e. there is no change in the topology of the outer box section, this could also provide added stability to the linear optimisation process, if such a box section was for example used in the RCAR bumper test example of case study 2.

The following chapter will present the overall conclusions relating to the objectives of the PhD.

References

Altair (2017) *Altair Connect* [online] available from <https://connect.altair.com> [14 September 2017]

Altair Engineering (2009) *Concept Design with Topology and Topography Optimization*. available from <http://blog.altair.co.kr/wpcontent/uploads/2011/03/optistruct_optimization_10-0.pdf> [9 June 2015]

Altair Engineering (2011) *Non-Linear Response Optimization with OptiStruct* [online] available from <http://www.altair.de/(S(h0x2ua3daifgpjppgsxodn3u))/ResLibDownload.aspx?file_id2=4903&from_page=/ResourceLibrary.aspx?category=Presentations#3351> [24 August 2015]

Altair University (2015a) *Practical Aspects of Finite Element Simulation* [online] 3rd Editio. available from <http://www.altairuniversity.com/free-ebooks-2/free-ebook-practical-aspects-of-finite-element-simulation-a-study-guide/> [25 April 2016]

Altair University (2015b) *Practical Aspects of Structural Optimization* [online] 2nd Editio. available from <http://www.altairuniversity.com/free-ebooks-2/free-ebook-practical-aspects-of-structural-optimization-a-study-guide/> [17 August 2015]

Bendsøe, M.P. (1989) 'Optimal Shape Design as a Material Distribution Problem'. *Structural Optimization* [online] 1 (4), 193–202. available from <http://link.springer.com/article/10.1007/BF01650949> [27 October 2014]

Bendsøe, M.P. and Kikuchi, N. (1988) 'Generating Optimal Topologies in Structural Design Using a Homogenization Method'. *Computer Methods in Applied Mechanics and Engineering* [online] 71 (2), 197–224. available from <http://www.sciencedirect.com/science/article/pii/0045782588900862> [27 October 2014]

Bendsøe, M.P. and Sigmund, O. (2003) *Topology Optimization: Theory, Methods and Applications*. Berlin, Heidelberg: Springer Berlin Heidelberg

Bianchi, L., Dorigo, M., Gambardella, L.M., and Gutjahr, W.J. (2009) 'A Survey on Metaheuristics for Stochastic Combinatorial Optimization'. *Natural Computing* [online] 8 (2), 239–287. available from http://link.springer.com/10.1007/s11047-008-9098-4

Du Bois, P., Chou, C., Fileta, B., Khalil, T., and King, A. (2004) *Vehicle Crashworthiness and Occupant Protection* [online] American Iron and Steel Institute. available from <http://www.autosteel.org/~/media/Files/Autosteel/Research/Safety/safety_book.pdf> [10 June 2015]

Bruns, T.E. (2005) 'A Reevaluation of the SIMP Method with Filtering and an Alternative Formulation for Solid-Void Topology Optimization'. *Structural and Multidisciplinary Optimization* [online] 30 (6), 428–436. available from <http://link.springer.com/article/10.1007/s00158-005-0537-x> [19 November 2014]

Casadei, A. and Broda, R. (2008) *Impact of Vehicle Weight Reduction on Fuel Economy for Various Vehicle Architectures* [online] available from <http://www.drivealuminum.org/research-resources/PDF/Research/2008/2008-Ricardo-Study.pdf> [1 February 2016]

Christensen, J. (2015) *Topology Optimisation of Structures Exposed to Large (Non-Linear) Deformations* [online] Coventry University. available from <https://www.researchgate.net/publication/284419329_Topology_Optimisation_of_Structures_Exposed_to_Large_non-linear_Deformations> [24 November 2015]

Christensen, J. and Bastien, C. (2015) *Nonlinear Optimization of Vehicle Safety Structures*. 1st editio. Butterworth-Heinemann

Christensen, J., Bastien, C., and Blundell, M. (2013) 'The Feasibility of ESLM for BIW Roof Structure Development and Optimisation'. *International Journal of Crashworthiness* [online] 1, 34–47. available from <http://www.academicpub.org/jmra/paperInfo.aspx?PaperID=14490> [28 July 2015]

Christensen, J., Bastien, C., Blundell, M., Gittens, A., and Tomlin, O. (2011) 'Lightweight Hybrid Electrical Vehicle Structural Topology Optimisation Investigation Focusing on Crashworthiness'. *International Journal of Vehicle Structures and Systems* [online] 3 (2), 113–122. available from <https://curve.coventry.ac.uk/open/file/988e1db1-993c-7d15-e14f-1e2d011c0d9a/1/Lightweight hybrid electrical vehicle.pdf> [17 October 2014]

Chuang, C.H. and Yang, R.J. (2012) 'Benchmark of Topology Optimization Methods for Crashworthiness Design'. in *12th International LS-DYNA® Users Conference* [online] held 2012. 1–10. available from <http://www.dynalook.com/international-conf-2012/optimization-metal-forming18-a.pdf> [23 October 2015]

Department for Business Innovation & Skills (2016) *Driverless Cars Technology Receives £20 Million Boost* [online] available from <https://www.gov.uk/government/news/driverless-cars-technology-receives-20-million-boost> [15 February 2016]

Department for Transport, Driver & Vehicle Standards Agency, Office for Low Emissions Vehicles, and Vehicle Certification Agency (2015) *2010 to 2015 Government Policy: Transport Emissions* [online] available from <https://www.gov.uk/government/publications/2010-to-2015-government-policy-transport-emissions/2010-to-2015-government-policy-transport-emissions> [28 January 2016]

Duddeck, F., Hunkeler, S., Lozano, P., Wehrle, E., and Zeng, D. (2016) 'Topology Optimization for Crashworthiness of Thin-Walled Structures under Axial Impact Using Hybrid Cellular Automata'. *Structural and Multidisciplinary Optimization* [online] 54 (3), 415–428. available from <http://dx.doi.org/10.1007/s00158-016-1445-y>

Dunning, P.D. and Kim, H.A. (2014) 'Introducing the Sequential Linear Programming Level-Set Method for Topology Optimization'. *Structural and Multidisciplinary Optimization* [online] 51, 631–643. available from <http://opus.bath.ac.uk/41750/1/Dunning_Kim.pdf> [18 June 2015]

Euro NCAP (2015) *Assessment Protocol - Adult Occupant Protection*. available from <http://www.euroncap.com/files/Euro-NCAP-Frontal-Protocol-Version-6.0.2---0-0ba7731f-4866-40c8-8dc5-31db64d92f8d.pdf> [2 February 2016]

Euro NCAP (2012) *Assessment Protocol - Overall Rating*. available from <http://www.euroncap.com/en> [17 February 2016]

Euro NCAP (2009) *New Rating to Play Starring Role in Improving Car Safety* [online] available from <http://www.euroncap.com/en/press-media/press-releases/new-rating-to-play-starring-role-in-improving-car-safety/> [18 February 2016]

Forsberg, J. and Nilsson, L. (2006) 'Topology Optimization in Crashworthiness Design'. *Structural and Multidisciplinary Optimization* [online] 33 (1), 1–12. available from <http://link.springer.com/10.1007/s00158-006-0040-z> [23 October 2014]

Garcia-Lopez, N.P., Sanchez-Silva, M., Medaglia, A.L., and Chateauneuf, A. (2011) 'A Hybrid Topology Optimization Methodology Combining Simulated Annealing and SIMP'. *Computers and Structures* [online] 89 (15–16), 1512–1522. available from <http://dx.doi.org/10.1016/j.compstruc.2011.04.008> [15 January 2015]

Genta, G., Morello, L., Cavallino, F., and Filtri, L. (2014) 'Body and Car Architecture'. in *The Motor Car* [online] 13–36. available from <http://link.springer.com/10.1007/978-94-007-8552-6> [5 August 2015]

Georgiou, G. and Zeguer, T. (2017) 'On the Assessment of the Macro-Element Methodology for Full Vehicle Crashworthiness Analysis'. *International Journal of Crashworthiness* [online] 8265 (May 2017), 1–18. available from <https://doi.org/10.1080/13588265.2017.1328723>

Grimes, O., Bastien, C., Christensen, J., Rawlins, N., Hammond, W., Bell, P., Brown, B., and Beal, J. (2013) 'Lightweighting of a Hydrogen Fuel Cell Vehicle Whilst Meeting Urban Accident Criteria'. *World Electric Vehicle Journal* [online] 6 (2), 452–463. available from <http://ieeexplore.ieee.org/xpl/login.jsp?tp=&arnumber=6914946&url=http://ieeexplore.ieee.org/xpls/abs_all.jsp?arnumber=6914946> [5 August 2015]

Guha, S., Bhalsod, D., and Krebs, J. (2008) *LSTC Hybrid III Dummies Positioning and Post-Processing* [online] available from <http://www.oasys-software.com/dyna/en/fe-models/lstc_dummies/LSTC.H3.103008_v1.0_Documentation.pdf> [6 April 2016]

Hanssen, A.G., Artelius, A., and Langseth, M. (2007) 'Validation of the Simplified Super Folding Element Theory Applied for Axial Crushing of Complex Aluminium Extrusions'. *International Journal of Crashworthiness* 12 (6), 591–596

Hellen, T.K. and Becker, A.A. (2013) *Finite Element Analysis for Engineers - A Primer*. Glasgow: NAFEMS

Huang, X. and Xie, Y.M. (2010) *Evolutionary Topology Optimization of Continuum Structures*. Chichester, UK: John Wiley & Sons, Ltd

Huang, X. and Xie, Y.M. (2009) 'Bi-Directional Evolutionary Topology Optimization of Continuum Structures with One or Multiple Materials'. *Computational Mechanics* [online] 43 (3), 393–401. available from <http://link.springer.com/article/10.1007/s00466-008-0312-0> [27 October 2014]

Huang, X. and Xie, Y.M. (2008a) 'A New Look at ESO and BESO Optimization Methods'. *Structural and Multidisciplinary Optimization* [online] 35 (1), 89–92. available from <http://link.springer.com/article/10.1007/s00158-007-0140-4> [27 October 2014]

Huang, X. and Xie, Y.M. (2008b) 'Topology Optimization of Nonlinear Structures under Displacement Loading'. *Engineering Structures* [online] 30 (7), 2057–2068. available from <http://www.sciencedirect.com/science/article/pii/S0141029608000205> [13 October 2014]

Huang, X. and Xie, Y.M. (2007) 'Convergent and Mesh-Independent Solutions for the Bi-Directional Evolutionary Structural Optimization Method'. *Finite Elements in Analysis and Design* [online] 43 (14), 1039–1049. available from <http://www.sciencedirect.com/science/article/pii/S0168874X07000777> [13 October 2014]

Huang, X., Xie, Y.M., Lu, G., Huang, X., Xie, Y.M., and Lu, G. (2007) *Topology Optimization of Energy-Absorbing Structures Topology Optimization of Energy-Absorbing*. [online] 12 (6), 663–675. available from <https://www.tandfonline.com/doi/pdf/10.1080/13588260701497862>

Jacob, P. and Goulding, L. (2002) *An Explicit Finite Element Primer*. Glasgow: NAFEMS

Kiani, M., Gandikota, I., Rais-Rohani, M., and Motoyama, K. (2014) 'Design of Lightweight Magnesium Car Body Structure under Crash and Vibration Constraints'. *Journal of Magnesium and Alloys* [online] 2 (2), 99–108. available from <http://www.sciencedirect.com/science/article/pii/S2213956714000395> [11 June 2015]

Krog, L., Tucker, A., and Rollema, G. (2011) *Application of Topology , Sizing and Shape Optimization Methods To Optimal Design of Aircraft Components* [online] available from <http://www.altairproductdesign.com/ResourceLibrary.aspx?category=Papers#details> [2 February 2016]

Lane, B. (2016) *Electric Car Market Statistics* [online] available from <http://www.nextgreencar.com/electric-cars/statistics/> [18 February 2016]

Litman, T.A. (2015) *Autonomous Vehicle Implementation Predictions: Implications for Transport Planning* [online] available from <www.vtpi.org> [1 February 2016]

Liu, X., Yi, W.-J., Li, Q.S., and Shen, P.-S. (2008) 'Genetic Evolutionary Structural Optimization'. *Journal of Constructional Steel Research* [online] 64 (3), 305–311. available from <http://www.sciencedirect.com/science/article/B6V3T-4PRRHBF-1/2/08198c19aacc122dd4e49136056c3f3e> [11 August 2015]

Livermore Software Technology Corporation (2013) *The LS - TaSC™ Software - User's Manual* [online] available from <http://www.lsoptsupport.com/documents/manuals/ls-tasc/3.0> [9 June 2015]

Livermore Software Technology Corporation (2016a) *LS-DYNA Keyword User's Manual Volume I*. vol. I

Livermore Software Technology Corporation (2016b) *LS-DYNA Keyword User's Manual Volume II Material Models*. vol. II

Livermore Software Technology Corporation (2017) *Effective Plastic Strain* [online] available from <http://www.dynasupport.com/howtos/general/effective-plastic-strain> [21 November 2017]

Livermore Software Technology Corporation (2018a) *Energy Data - LS-DYNA Support* [online] available from <https://www.dynasupport.com/tutorial/ls-dyna-users-guide/energy-data> [20 November 2018]

Livermore Software Technology Corporation (2018b) *Internal Energy - LS-DYNA Support* [online] available from <https://www.dynasupport.com/howtos/general/internal-energy/> [20 November 2018]

Macauly, M.A. (1987) *Introduction to Impact Engineering*. 1st Editio. London: Chapman and Hall

Marzougui, D., Radwan Samaha, R., Cui, C., Kan, C.-D., and Opiela, K.S. (2012) *Extended Validation of the Finite Element Model for the 2010 Toyota Yaris Passenger Sedan* [online] available from <https://www.nhtsa.gov/crash-simulation-vehicle-models#12101>

Malen, D.E. (2011) *Fundamentals of Automobile Body Structure Design*. Warrendale, Pa: SAE International

Nha Chu, D., Xie, Y.M., Hira, A., and Steven, G.P. (1997) 'On Various Aspects of Evolutionary Structural Optimization for Problems with Stiffness Constraints'. *Finite Elements in Analysis and Design* [online] 24 (4), 197–212. available from <http://linkinghub.elsevier.com/retrieve/pii/S0168874X96000492> [25 August 2015]

Patel, N.M. (2007) *Crashworthniness Design Using Topology Optimization* [online] University of Notre Dame. available from http://mechanicaldesign.asmedigitalcollection.asme.org/article.aspx?articleid=1450060

Penfield, P. (2003) 'Principle of Maximum Entropy'. in *Principle of Maximum Entropy* [online] available from http://www-mtl.mit.edu/Courses/6.050/notes/chapter9.pdf

RCAR Damageability Working Group (2016) *Informational Document Regarding Effects of the Introduction of the RCAR Bumper Test* [online] available from <http://www.rcar.org/Papers/MemberPapers/Effects of RCAR Bumper Test issue 1_0.pdf>

Reed, C. (2002) *Applications of Optistruct Optimization to Body in White Design* [online] available from <http://www.altairhyperworks.co.uk/html/en-GB/Tech_Conf/papers/2002/paper5_final.pdf> [28 May 2015]

Research Council for Automobile Repairs (2010) *RCAR Bumper Test* [online] available from <http://www.rcar.org/Papers/Procedures/BumperTestProcedure.pdf>

Roux, W. (2011) *Topology Design Using LS-TaSC ™ Version 2 and LS-DYNA*. available from <https://www.dynamore.de/de/download/papers/konferenz11/papers/session4-paper4.pdf>

Rozvany, G.I.N. (2009) 'A Critical Review of Established Methods of Structural Topology Optimization'. *Structural and Multidisciplinary Optimization* [online] 37 (3), 217–237. available from <http://link.springer.com/10.1007/s00158-007-0217-0>

Rozvany, G.I.N., Zhou, M., and Birker, T. (1992) 'Generalized Shape Optimization without Homogenization'. *Structural Optimization* [online] 4 (3–4), 250–252. available from <http://link.springer.com/10.1007/BF01742754>

Safety Wissen (2018) *Euro NCAP / ANCAP Rating 2018 - 2020* [online] available from https://www.safetywissenapp.de/download/docs/B04.24v7367235aw8uf65ak47834mbpnld63652828634.pdf

Seiffert, U. and Wech, L. (2003) *Automotive Safety Handbook*. SAE International

Sigmund, O. (1994) *Design of Material Structures Using Topology Optimization* [online] Technical University of Denmark. available from <https://etd.ohiolink.edu/ap/10?0::NO:10:P10_ACCESSION_NUM:wright1401302982>

Sigmund, O. and Petersson, J. (1998) 'Numerical Instabilities in Topology Optimization: A Survey on Procedures Dealing with Checkerboards, Mesh-Dependencies and Local Minima'. *Structural Optimization* [online] 16 (1), 68–75. available from <http://link.springer.com/10.1007/BF01214002>

Svanberg, K. (1987) 'The Method of Moving Asymptotes—a New Method for Structural Optimization'. *International Journal for Numerical Methods in Engineering* [online] 24 (2), 359–373. available from http://doi.wiley.com/10.1002/nme.1620240207

The National Crash Analysis Center (2011) *Development & Validation of a Finite Element Model for the 2010 Toyota Yaris Passenger Sedan* [online] available from <http://www.hengstar.com/examples/NCAC-2011-T-001.pdf>

Tovar, A. (2004) *Bone Remodeling As a Hybrid Cellular Automaton Optimization Process*. University of Notre Dame

Van der Sluis, J. (2000) 'Vehicle Compatibility in Car-to-Car Collisions'. *SWOV Publication D-2001-01* 1, 42

Venkayya, V.B. (1989) 'Optimality Criteria: A Basis for Multidisciplinary Design Optimization'. *Computational Mechanics* [online] 5 (1), 1–21. available from <http://link.springer.com/10.1007/BF01046875>

World Health Organization (2013) *Global Status Report on Road Safety 2013* [online] available from http://www.who.int/violence_injury_prevention/road_safety_status/2013/en/

Xie, Y.M. and Steven, G.P. (1993) 'A Simple Evolutionary Procedure for Structural Optimization'. *Computers & Structures* [online] 49 (5), 885–896. available from <http://linkinghub.elsevier.com/retrieve/pii/004579499390035C>

Zhou, M. and Rozvany, G.I.N. (2001) 'On the Validity of ESO Type Methods in Topology Optimization'. *Structural and Multidisciplinary Optimization* [online] 21 (1), 80–83. available from <http://link.springer.com/10.1007/s001580050170>

Zhou, M. and Rozvany, G.I.N. (1991) 'The COC Algorithm, Part II: Topological, Geometrical and Generalized Shape Optimization'. *Computer Methods in Applied Mechanics and Engineering* [online] 89 (1–3), 309–336. available from <http://linkinghub.elsevier.com/retrieve/pii/0045782591900469>

APPENDIX A - BEETS / Optistruct parameter tests

Based on models from the study performed in chapter 3, the first section will analyse the effects of the Optistruct parameters, while the second section will analyse the influence of the Bi-directional Evolutionary Entropy Tabu search Simulated annealing (BEETS) parameters.

I. Optistruct tests

Figure A.1 displays the basic finite element (FE) setup used for the Optistruct parameter tests. It corresponds to the FE setup used for model 52 in chapter 3, with a loading angle of 45°. This is due to the increased presence of intermediate densities, and therefore a greater possibility of illustrating the effects of the Optistruct parameters on the final topology.

Figure A.1 : FE setup for Optistruct parameter tests

Four Optistruct parameters will be modified, to evaluate their influence on the optimised structure obtained, the differences with the original optimisation run (model 52) and crucially any improvements on feasibility and load path definition. By analysing the Optistruct documentation (Altair 2017), four parameters were identified as having direct influence on negative aspects of linear optimisation highlighted in previous chapters such as checkerboard effect and intermediate densities:

- ***DISCRETE:*** The “DISCRETE” parameter is equivalent to the penalisation factor defined in the VDM/SIMP method, the basis of the Optistruct method. By default, the DISCRETE value is equal to 1 (i.e. a linear relationship between relative element density and stiffness). However, as discussed in the literature review, a

penalisation factor between 2 and 4 is recommended in order to avoid intermediate densities (Altair University 2015). Therefore the DISCRETE value will be increased to 3 in order to evaluate its effect on the topology.

- ***MINDIM:*** This parameter is in effect a “member size control” parameter, used to limit the formation of thin members during the optimisation process and also plays a role in reducing the checkerboard effect (Altair University 2015). In this case, a MINDIM value of around three times the element mesh size is suggested (Altair 2017). For the following parameter tests, the MINDIM value when activated will be set to 30mm.
- ***CHECKER:*** This parameter is simply an in-built, checkerboard reducing option. However, a potential drawback to activating this parameter is the possibility of an increase in intermediate densities (Altair 2017). This side effect can however be mitigated by activating the member size control (MINDIM). The effect of activating CHECKER will therefore be analysed.
- ***MMCHECK:*** Finally, this parameter, similar in its function to CHECKER corresponds to a checkerboard control parameter used in conjunction with MINDIM. Furthermore, it also has the undesired effect of achieving results with intermediate densities (Altair 2017).

The models used in this parameter study are listed in Table A.1 below:

Table A.1 : Models for Optistruct parameter tests

Model number	DISCRETE	MINDIM	CHECKER	MMCHECK
52_1	1	Yes	Yes	No
52_2	1	Yes	No	Yes
52_3	3	Yes	No	No
52_4	1	No	Yes	No
52_5	3	No	No	No
52_6	1	No	No	Yes
52_7	3	No	Yes	No
52_8	3	No	No	Yes
52_9	3	Yes	Yes	No
52_10	3	Yes	No	Yes

Results

Table A.2 summarises the optimisation run details in terms of CPU time, number of iterations and convergence verification:

Table A.2 : Optistruct parameter test optimisation run data

Model number	CPU time (s)	Number of iterations	Convergence	Compliance value (mm/N)
52_1	11	39	Yes	8.91E+05
52_2	10	37	Yes	1.14E+06
52_3	12	45	Yes	8.94E+05
52_4	2	7	Yes	1.09E+06
52_5	7	25	Yes	1.09E+06
52_6	2	8	Yes	1.07E+06
52_7	8	30	Yes	1.17E+06
52_8	6	25	Yes	1.09E+06
52_9	12	45	Yes	8.94E+05
52_10	11	41	Yes	1.27E+06

In this instance, “convergence” relates to the optimisation process terminating due to a small change in the objective function (i.e. minimise compliance) and not a maximum number of iterations reached. Furthermore, the CPU time itself is not important here (as it is relatively small all around), but the relative difference between models that is of interest. At first glance, there are clear differences in CPU time and number of iterations depending on the parameters used, with a particular trend emerging regarding applying minimum dimension restrictions to the optimisation process. Where MINDIM is activated, the CPU time and the number of iterations to convergence increases. This however is not surprising as activating MINDIM is in essence adding a level of complexity to the optimisation process, an additional constraint.

However, when observing the density plots for each solution (Figure A.2 – Figure A.11), it becomes clear that several solutions are unsuitable in terms of “manufacturability” and display the same issues as the original model 52 (Figure 3.17(c) in chapter 3). The criteria for “good manufacturability” in this instance relates to the lack of intermediate densities and checkerboarding in the optimum solutions (i.e. clear load paths through the structure). The resulting structure could be produced using laser cutting for example. The aim therefore is for solid/void designs as introduced in chapter 2.

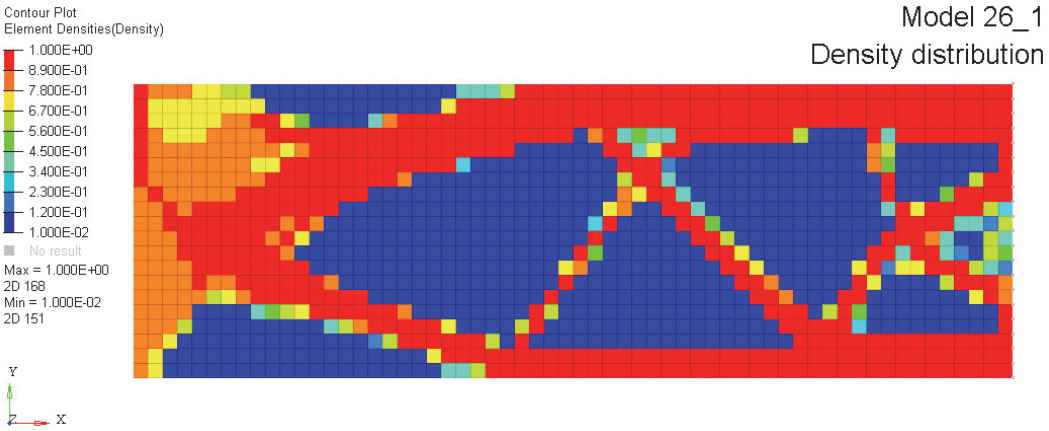

Figure A.2 : Model 52_1 density distribution

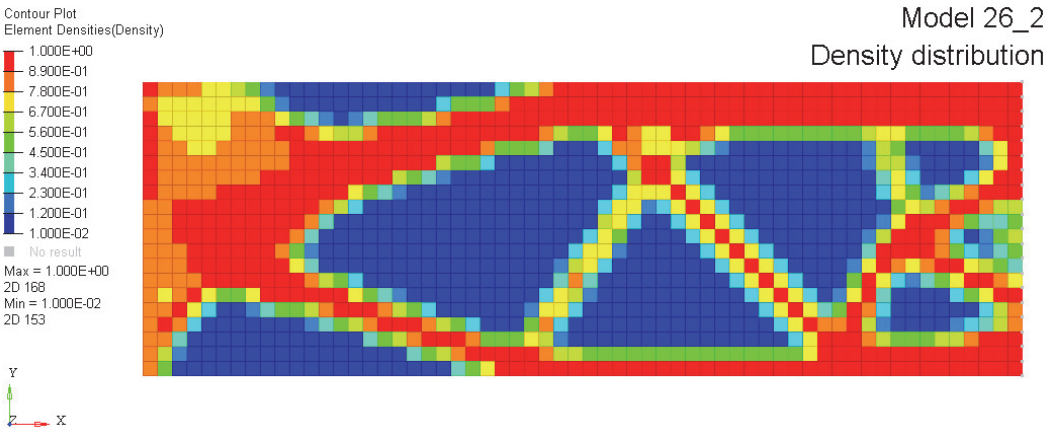

Figure A.3 : Model 52_2 density distribution

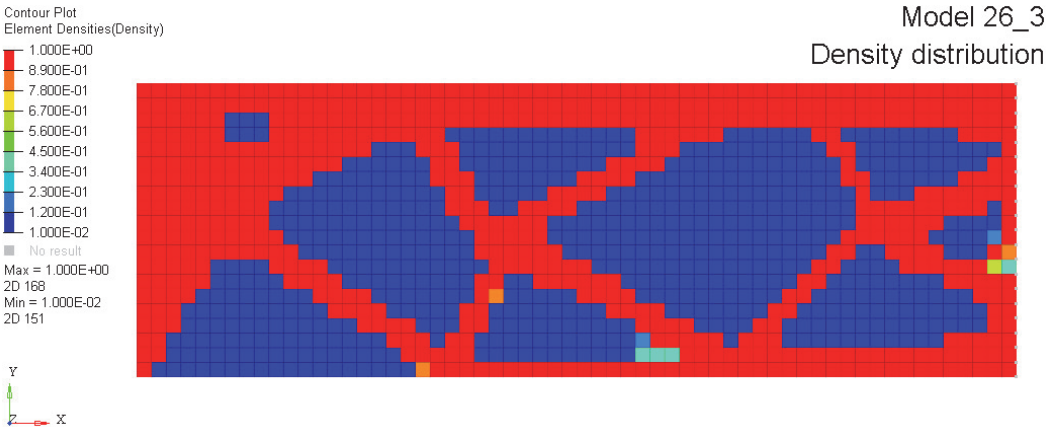

Figure A.4 : Model 52_3 density distribution

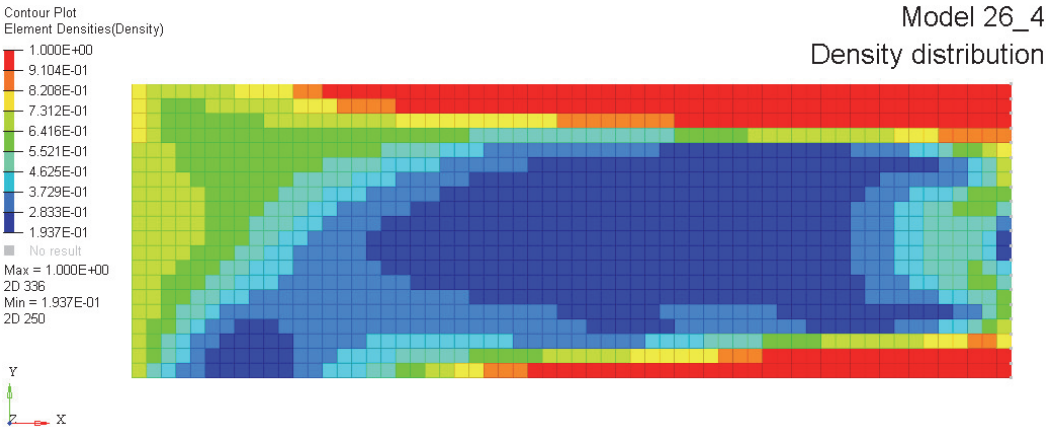

Figure A.5 : Model 52_4 density distribution

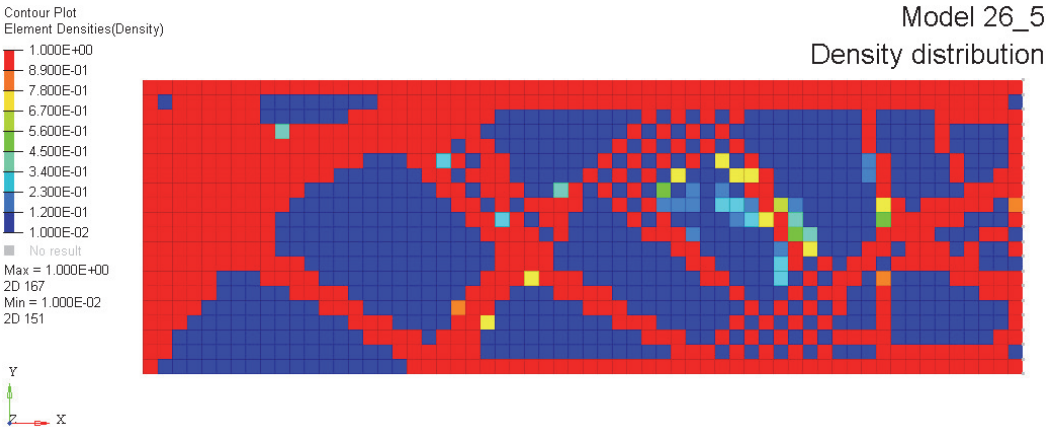

Figure A.6 : Model 52_5 density distribution

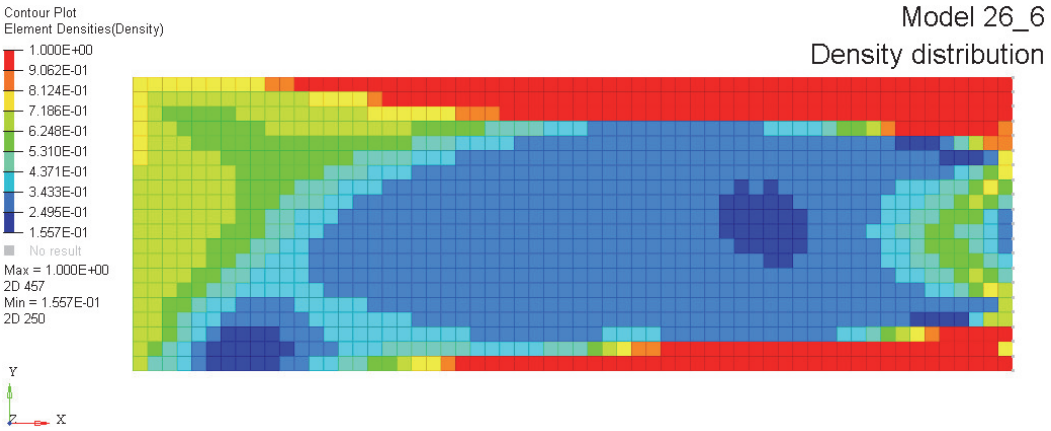

Figure A.7 : Model 52_6 density distribution

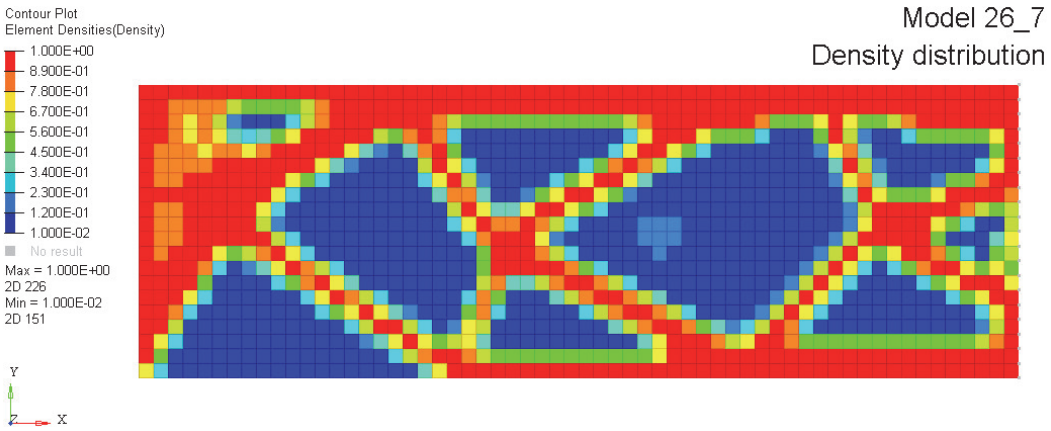

Figure A.8 : Model 52_7 density distribution

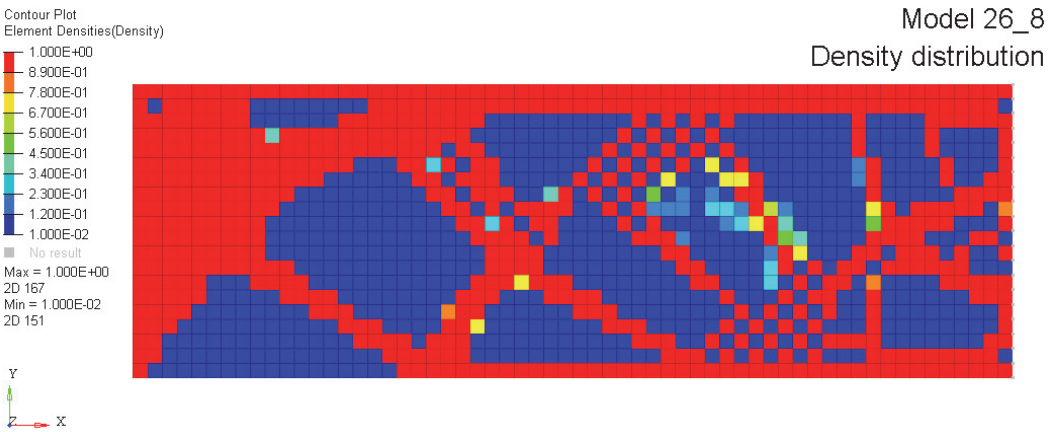

Figure A.9 : Model 52_8 density distribution

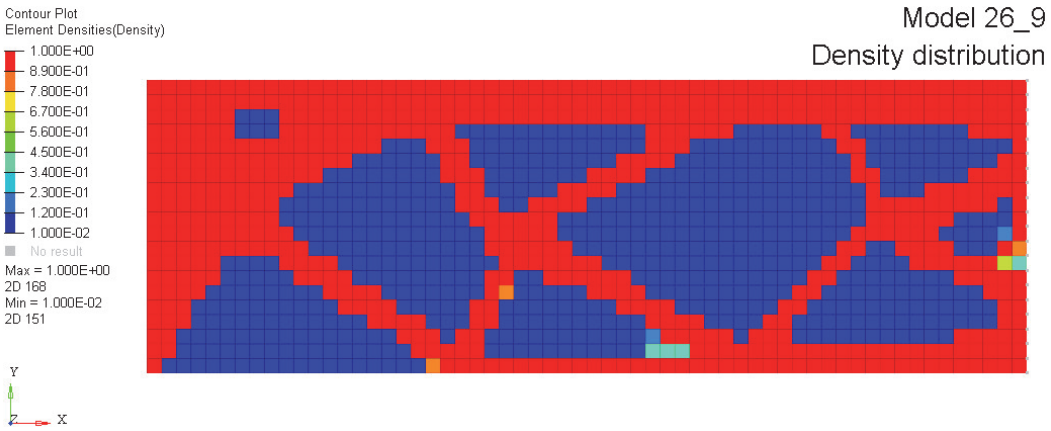

Figure A.10 : Model 52_9 density distribution

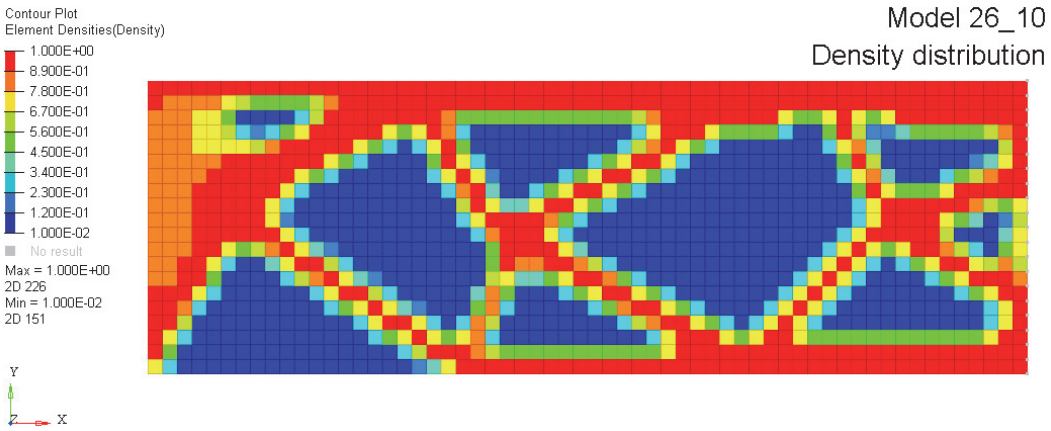

Figure A.11 : Model 52_10 density distribution

Several observations can be made regarding selecting default Optistruct parameters for hybrid optimisation:

- The minimum dimension parameter has a major impact on obtaining clearly defined, checkerboard free solutions. Model 52_4 and model 52_6 (Figure A.5 and Figure A.7) for example have a number of intermediate densities in the centre of the optimised structure, whereas model 52_5 and 52_8 (Figure A.6 and Figure A.9 respectively) have clear checkerboard patterns. Therefore, for future models and hybrid optimisation runs, a minimum member size will be specified, typically chosen as 3 times the mesh size.

- Modifying the DISCRETE parameter to 3 as opposed to the default setting of 1 also seems to have a positive effect by eliminating intermediate densities from the structure. The value of 3 is therefore chosen for future models.
- In model 52_9 (Figure A.10), the CHECKER parameter seems to have had a positive effect on the overall structure, as in terms of compliance the structure has the lowest of all the models. Furthermore, it displays a clear loadpath through the structure, similar to model 52_3 (Figure A.4). However this isn't consistent throughout all the models where CHECKER has been activated. Effectively, MINDIM and DISCRETE seem to have the greater effect as when these are not activated, the CHECKER parameter does not improve the topology optimisation (TO) results. The data from Table A.2 illustrates this point further, as the run time, number of iterations and final compliance value for model 52_3 and model 52_9 are identical. MMCHECK seems to have very little positive effect on the structure. Overall, these findings for MMCHECK and CHECKER may be due to the relatively simple structure and load case set up. Nevertheless, these results and Optistruct literature (Altair 2017) suggests the use of CHECKER and MMCHECK is on a case by case basis. Therefore, both these parameters will not be activated for the following case study.

The Optistruct parameters selected for case study 1 are summarised in Table A.3:

Table A.3 : Summary of Optistruct parameters for case study 1

Parameter	Value
DISCRETE	3
MINDIM (mm)	30
CHECKER	No
MMCHECK	No

II. BEETS tests

The BEETS parameters tested relate specifically to the number of elements removed per optimisation iteration: the evolutionary ratio (ER) and the cooling parameters COOLIT and SF, which are used in equation (2.27) and equation (2.28) respectively. Model 30 from chapter 3 is used as the basis for this review and Table A.4 summarises the models tested and their respective parameters:

Table A.4 : Models for BEETS parameter tests

Model number	ER	COOLIT	SF
30	0.05	-	-
30_1	0.1	-	-
30_2	0.2	-	-
30_3	0.05	0.1	0.1
30_4	0.1	0.9	0.1

The first three models are run with no simulated annealing activated. Model 30_3 and model 30_4 each have cooling factors applied during the process. No run with ER = 0.2 and a cooling factor activated is demonstrated as the overly aggressive nature of the element removal process (and the resulting topology) effectively removes any benefit of applying a cooling factor, as the results below will reveal.

Results

Figure A.12 – Figure A.14 displays the optimised topologies obtained through the BEETS algorithm for model 30, model 30_1 and model 30_2.

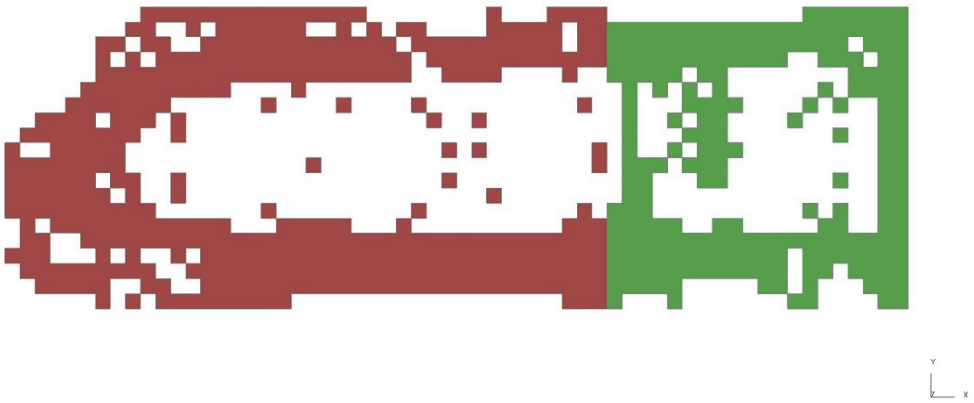

Figure A.12 : Final topology model 30

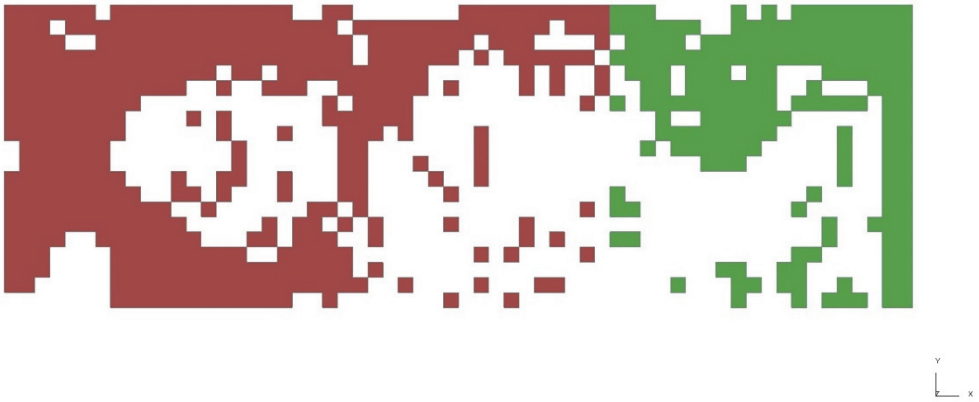

Figure A.13 : Final topology model 30_1

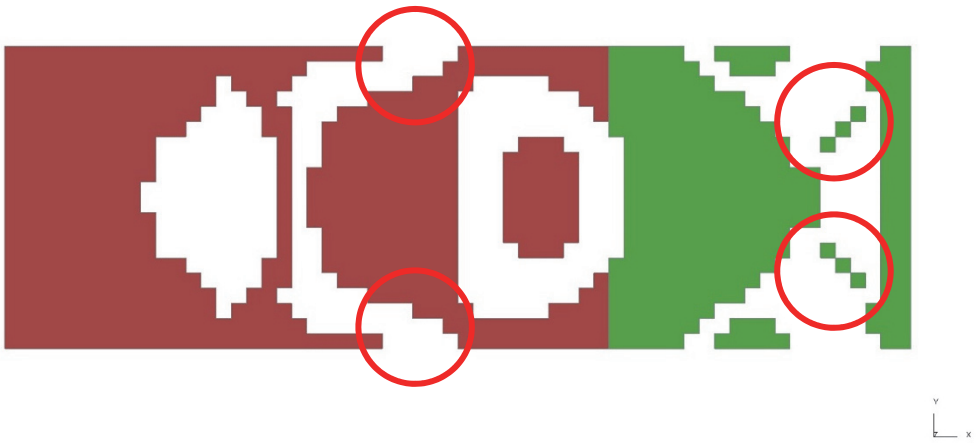

Figure A.14 : Final topology model 30_2

It should be noted that the topology illustrated in Figure A.14 was obtained after only 3 iterations. At first glance, Figure A.14 demonstrates a “clearer” topology in that there are no “individual” disconnected elements. However, it is also clear that the loadpaths through the structure are entirely disconnected in four locations, highlighted in Figure A.14. Figure A.13 also contains many detached elements. These effects are undesirable from a structural design point of view, and indeed a feasibility point of view. This originates from an ER value that is too aggressive. The structures obtained at the end of the optimisation process are very different for each ER value, but if the structures are compared at similar “volume levels” in the optimisation process, it can be demonstrated that they are indeed very similar. Figure A.15 illustrates model 30 after iteration 4, Figure A.16 model 30_1 after iteration 2 and Figure A.17 model 30_2 after iteration 1.

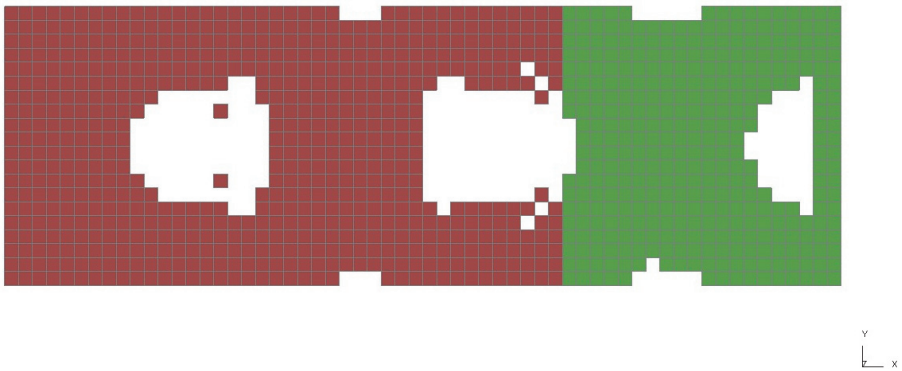

Figure A.15 : Model 30 topology after iteration 4

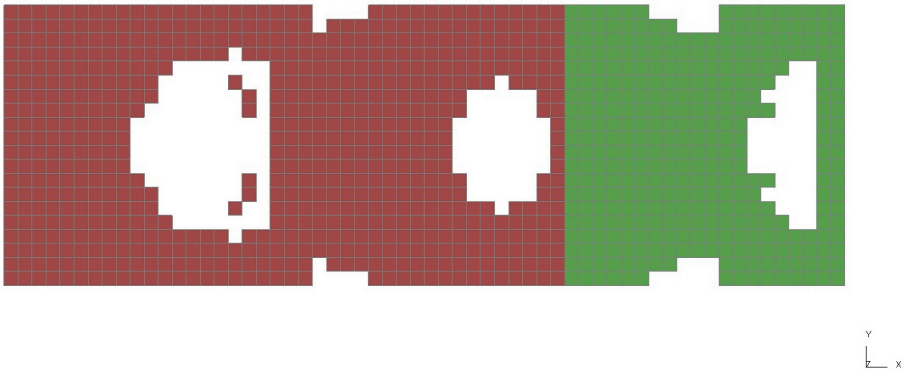

Figure A.16 : Model 30_1 topology after iteration 2

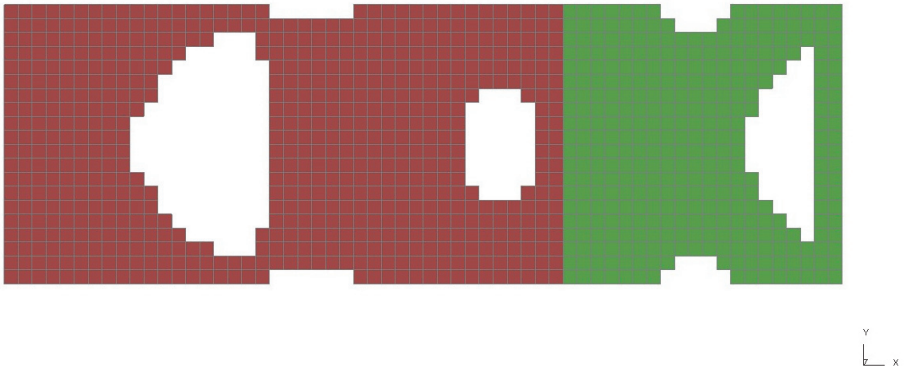

Figure A.17 : Model 30_2 topology after iteration 1

The figures above demonstrate that elements are removed from the same “zones” in the structure, but with different ER values they occur at different instances in the optimisation process. The high ER values lead to the instabilities illustrated in Figure A.13 and Figure A.14.

As discussed in the literature review, simulated annealing (i.e. the cooling factor) is applied to the optimisation process in order to reduce the aggressiveness of element removal when the structural volume nears the final target. The cooling ratio is triggered using the COOLIT parameter, which determines at which volume threshold the ER value should be reduced. However, from the results in Figure A.14, it is clear that the cooling factor will have very little effect on improving the optimised structure, as the discontinuities appear extremely early (after iteration 2) in the optimisation process. Therefore the cooling function is only applied for ER = 0.05 and ER = 0.1 (model 30_3 and model 30_4 respectively).

The first observation is the different COOLIT values for models 30_3 and 30_4 (Table A.4). In essence, the COOLIT parameter activates earlier for model 30_4 (after only 10% of the volume has been removed) due to the instabilities and detached elements appearing a lot earlier in the optimisation process. Figure A.18 and Figure A.19 show the final topology for model 30_3 and model 30_4 respectively:

Figure A.18 : Final topology model 30_3

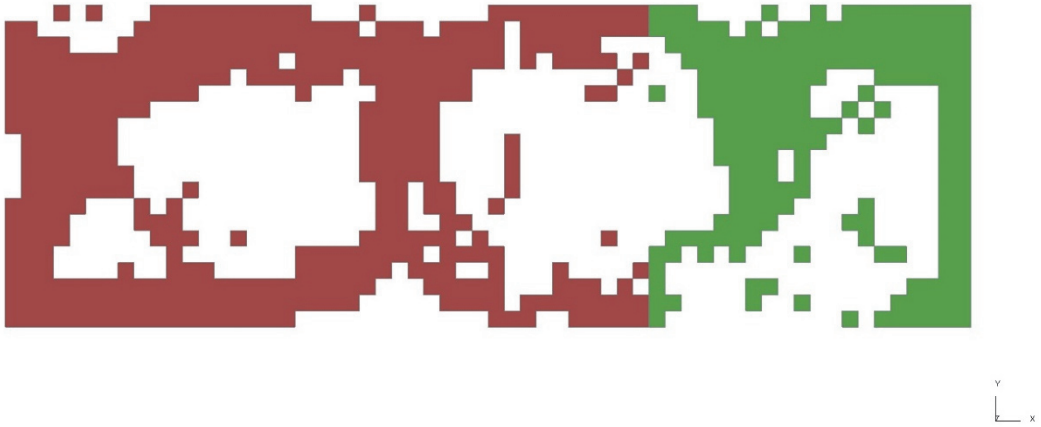

Figure A.19 : Final topology model 30_4

Comparing Figure A.18 to Figure A.12 (ER = 0.05 with and without cooling activated), it is clear that overall, the loadpaths are very similar. The main difference is a slight reduction in detached elements with the cooling factor activated. By contrast, the cooling factor has a more substantial effect on the final topology with model 30_4 (ER = 0.1, Figure A.19). An additional loadpath has appeared in the lower section of the structure, albeit a relatively thin member. As with model 30_3, there is also a noticeable reduction in detached elements.

Overall, the simulated annealing function does seem to improve the optimisation process by creating clearer loadpaths, however the effects seem to reduce when the evolutionary ratio is lower, as the optimisation process is inherently less aggressive. Furthermore, the need to activate the cooling process early on for model 30_4 negates the benefit of the cooling factor, namely enabling a relatively high evolutionary ratio at the beginning of the process, with the reduction applied only close to the target volume in order to save on computation time.

A further drawback to the current implementation of simulated annealing is in the event the optimisation process overshoots the target volume (i.e. current volume < target volume), there is no strategy in place to add elements back into the structure in order to reach the target. Therefore, before the optimisation process, the user would need to calculate the COOLIT and SF parameters to get as close as possible to the target volume, essentially predicting the volume at each iteration. This is obviously a cumbersome process, and would also depend on the target volume and ER. By contrast, without simulated annealing, the BEETS process has a mechanism to always reach the target even in the case of an overshoot.

From the BEETS parameter tests, an evolutionary ratio of ER = 0.05 is selected due to the improved clarity of structural loadpaths. Simulated Annealing does show potential in being able to provide clearer TO results, however the effect is somewhat minimal for ER = 0.05. The mechanism remains at an experimental phase, therefore simulated annealing will be deactivated for subsequent studies. Table A.5 summarises the BEETS paramaters selected for case study 1:

Table A.5 : Summary of BEETS parameters for case study 1

Parameter	**Value**
ER	0.05
COOLIT	No
SF	No

APPENDIX B – Hybrid methodology user recommendations

From the findings throughout this PhD, several initial recommendations can be made to potential users of the hybrid topology optimisation (TO) tool.

1) The first recommendation concerns the finite element (FE) modelling for the TO process. Chapter 5 showed the importance of the sampling rate selected in LS-DYNA on the interface forces that can be transmitted. Therefore the user must first select/determine a sampling rate that allows the LS-DYNA solver to accurately represent the behaviour at the interface. The user must also be aware though that there is a trade-off, as too many data points can have a high negative impact on the tool's run time.

2) A further FE modelling recommendation concerns the size of the design volume. At present, a too high number of elements (i.e. design variables) in the non-linear FE model runs the risk increasing substantially the run time of the non-linear solver (BEETS). The FE model itself can be relatively large, as shown in case study 2, but many of the elements in the non-linear model (the reduced Yaris model) contained non-design elements. These are analysed and placed into a template file only once, at the beginning of the hybrid optimisation process, so have relatively little effect on the total run time compared to the size of the design volume, which as discussed in the conclusion to chapter 6, is relatively small.

3) The importance of an increased rate of exchange has been discussed. However, the user must also be aware that this is of critical importance when selecting a "minimise mass" objective. If a rate of exchange other than 1 (i.e. data exchanged at every iteration) is selected, the user runs the risk of crucial information not being transmitted to the linear solver, and by extension less material than possible could be removed from the linear structure.

4) The DESMAX value was shown, unsurprisingly, to be very important in case study 1. It controls the maximum number of iterations within the Optistruct optimisation solver, and by extension can determine whether the optimisation process can converge (although this only limits the maximum number of iterations, it does not control the convergence of the objective function itself).

Therefore, the user needs to specify a DESMAX value that allows for enough Optistruct iterations until convergence of the objective function. It should be noted, that for every linear optimisation cycle (i.e. every time the hybrid optimisation process returns to linear optimisation), the model may have changed as material may have been removed, and the force input may be different. Therefore it could be that the number of iterations needed to converge is also different. Overall, a value should be selected that compensates for this possible change, specifically rise, in iterations until convergence.

5) The choice of evolutionary ratio (ER) has also shown to be important throughout this thesis. While the “default” value of 5% has consistently performed well throughout this thesis, modifying ER has shown an interesting phenomenon. A too high value, as seen in Appendix A, unsurprisingly is too aggressive and removes too many elements at each iteration, which resulted in detached elements. However, case study 2 interestingly showed that a lower value of 2.5% did not significantly change the results for the non-linear crush cans, and even in some instances created disconnected element issues in the linear longitudinals. Therefore, an ER of 5% is recommended.

APPENDIX C – Ethical Approval review

Hybrid structural algorithm development P32182

REGISTRY RESEARCH UNIT

ETHICS REVIEW FEEDBACK FORM

(Review feedback should be completed within 10 working days)

Name of applicant: Alexis Wilson.....

Faculty/School/Department: [Faculty of Engineering and Computing] Mechanical Automotive & Manufacturing Engi.....

Research project title: Hybrid structural algorithm development

Comments by the reviewer

1. Evaluation of the ethics of the proposal:	
2. Evaluation of the participant information sheet and consent form:	
3. Recommendation: (Please indicate as appropriate and advise on any conditions. If there any conditions, the applicant will be required to resubmit his/her application and this will be sent to the same reviewer).	
	Approved - no conditions attached
	Approved with minor conditions (no need to re-submit)
	Conditional upon the following – please use additional sheets if necessary (please re-submit application)
	Rejected for the following reason(s) – please use other side if necessary
X	Not required

Name of reviewer: Anonymous .....

Date: 06/03/2015.....

Alexis Wilson Page 1 of 1 06 March 2015